Novel Scenarios of Ultracold Lattice Gases

Von der Fakultät für Mathematik und Physik
der Gottfried Wilhelm Leibniz Universität Hannover

zur Erlangung des Grades

Doktor der Naturwissenschaften
Dr. rer. nat.

genehmigte Dissertation von
Dipl. Phys. Sebastian Greschner

geboren am 06. Dezember 1984 in Quakenbrück, Deutschland

2016

To Vivien and Valentin

Abstract

Ultracold gases in optical lattices constitute one of the most active research fields in both quantum optics and condensed matter physics, since they open interesting possibilities for the controlled study of the properties of strongly-correlated many-body systems. Nowadays, due to a variety of experimental and theoretical advances the quantum simulation of frustrated quantum magnetism and synthetic gauge fields has come into experimental reach. In this thesis we examine properties and scenarios of strongly correlated quantum gases in optical lattices by means of numerical and analytical techniques.

Inspired by recent lattice shaking experiments [1], we investigate the quantum groundstate phases of ultracold bosonic particles in frustrated zig-zag optical lattices. The interplay between geometric frustration and contact-, long range dipolar or three body interactions is shown to give rise to a rich manifold of quantum phases, including chiral and two-component superfluids, exotic chiral Mott-insulators, supersolids or topological Haldane-insulator phases. We demonstrate a general analytical technique for the study of frustrated systems in the dilute limit.

The recent experimental realization of synthetic magnetic fields [2] in ultracold gases has attracted a lot of interest. In this context we study the properties of the simple paradigm of bosons in two-leg ladders. For the first time we are able to show the stability of conjectured groundstate phases such as vortex-lattice phases and the biased ladder phase in a numerical unbiased approach. Furthermore we observe and explain a counter-intuitive current-reversal effect.

The realization of the effective models in experiments often relies on the fast modulation of external parameters. We review recent proposals for the generation of non-linear hopping amplitudes by means of a fast modulation of interactions. We further demonstrate how the coherent modulation of interactions and lattice position allows for the emulation of a large class of correlated hopping Hubbard models.

In the context of current attempts for the quantum simulation of dynamical lattice gauge theories, we investigate different schemes for the preparation of density dependent magnetism in optical lattices, which includes a dynamical back-action of the particles on the field. Density dependent gauge fields result in anyon Hubbard models in 1D lattices, including unconventional two-component superfluid phases and statistically driven phase transitions, and a non-trivial interplay between density modulations and effective magnetic fluxes in 2D square lattices.

Finally we examine the groundstate phase diagram of fermionic alkali spinor gases in the presence of strong magnetic fields. By quasi-adiabatically lowering the field strength starting from a high field low entropy band insulator different Mott-insulator phases, including dimer, Néel and Haldane phases, may be prepared.

Keywords: ultracold quantum gases, frustrated quantum magnetism, synthetic gauge fields

Kurzzusammenfassung

Ultrakalte Quantengase sind eines der aktivsten Forschungsfelder in der Quantenoptik wie auch in der Physik der kondensierten Materie, da sie faszinierende Möglichkeiten der kontrollierten Untersuchung stark korrelierter Systeme eröffnen. Heutzutage ist aufgrund vieler experimenteller und theoretische Fortschritte die Quantensimulation von frustriertem Magnetismus und synthetischen Eichfeldern in greifbare Nähe gerückt. In dieser Arbeit untersuchen wir Szenarien für solche stark korrelierten Quantengase mittels analytischer und numerischer Methoden.

Inspiriert von aktuellen Experimenten zur Modulation optischer Gitter [1] analysieren wir die Grundzustandsphasen von Bosonen in frustrierten Zick-Zack-Gittern. Das Wechselspiel von geometrischer Frustration und Kontakt-, langreichweitiger Dipol-Dipol-, oder 3-Körper Wechselwirkung führt zu einer Mannigfaltigkeit verschiedener Quantenphasen, welche chirale und 2-komponentige Supraflüssigkeiten, exotische chirale Mott-Isolatoren, Supersolids sowie topologische Haldane-Isolatoren beinhalten. Wir demonstrieren zudem eine analytische Methode zur Untersuchung frustrierter Systeme im Limes kleiner Dichten.

Die kürzliche experimentelle Realisierung künstlicher Magnetfelder [2] in ultrakalten Gasen hat großes Interesse hervorgerufen. Wir untersuchen hierzu die Eigenschaften eines einfachen Modells von Bosonen in leiterartigen Gittern mit zwei Holmen. Erstmalig zeigen wir mit einer unverzerrten numerischen Methode die Stabilität von Vortexgittern und Biased-ladder-Phasen in diesem Modell. Darüber hinaus beobachten und erklären wir einen ungewöhnlichen Strom-Umkehr Effekt.

Die Realisierung effektiver Modelle im Experiment wird oft durch eine schnelle Modulation äußerer Kontrollparameter möglich. Nach einer Rekapitulation verschiedener Vorschläge für die Erzeugung nicht-linearer Tunnelamplituden durch modulierte Wechselwirkungen zeigen wir, wie durch kohärente Modulation von Wechselwirkung und Gitter eine große Klasse von Hubbard-Modellen mit korrelierten Hüpfamplituden emuliert werden kann.

Im Zusammenhang mit aktuellen Bestrebungen zur Quantensimulation dynamischer Gittereichtheorien, studieren wir verschiedene Schemata für die Erzeugung eines dichteabhängigen Magnetismus in optischen Gittern. Der Effekt dichteabhängiger Eichfelder beinhaltet Anyon-Hubbard-Modelle mit unkonventionellen 2-komponentigen Phasen in 1D sowie einem nicht-trivialen Wechselspiel von Dichtemodulationen mit einem effektiven magnetischem Fluss und verblüffender Dynamik in zweidimensionalen Gittern.

Schließlich untersuchen wir das Grundzustandsphasendiagramm für fermionische Alkali-Spinor-Gase in einem starken Magnetfeld. Durch eine quasi-adiabatische Verringerung der Feldstärke können ausgehend von einem Band-Isolator-Zustand niedriger Entropie verschiedene Mott-Isolatoren, welche Néel und Haldane Phasen beinhalten, präpariert werden.

Schlagwörter: ultrakalte Quantengase, frustrierter Quantenmagnetismus, synthetische Eichfelder

Contents

Chapter 1

Introduction

Scientists typically try (and luckily are able) to describe a large part of our physical world from the reductionists viewpoint, treating phenomena on a single particle level. This has been very successful to explain physical phenomena ranging from planetary motions to chemistry or elementary particle physics (eventually introducing perturbative corrections). However, there are physical conditions in which this situation substantially changes. Such strongly correlated many body systems may develop completely new phenomena and be governed by their own fundamental physical laws, or as summarized by Anderson [3]: "More is different".

Twenty years after the first experimental preparation and observation of Bose-Einstein condensates (BEC) in dilute weakly interacting atomic gases [4–6] the field of ultracold quantum gases has entered and made important progress in the studies of strongly correlated systems. Important beginnings were made by the seminal proposal of the observability of the Mott to superfluid quantum phase transition in cold atoms with optical lattices by Jaksch et al. [7] and its experimental realization few years later by Greiner et al. [8]. During the recent years further important milestones of strongly-correlated gases have been reached, among them the observation of the Tonks–Girardeau gas [9], fermionic Mott insulators [10, 11] or Anderson localization [12]. Nowadays many other strongly correlated quantum gas experiments are being performed including frustrated magnetism [1], gauge fields [13, 14], quantum magnetism with dipolar quantum gases [15, 16] or many-body localization [17].

A deeper theoretical understanding and experimental control of interacting systems apart from being of fundamental interest on its own, may have enormous effects in applications or devices ranging from high temperature superconductors [18], precision metrology [19, 20] to quantum computing [21].

Nowadays, probably the latter point, the engineering of universal quantum computers or specific quantum simulators constitutes one of the most prominent objectives and motivations in the field of ultracold quantum gases. In typical condensed matter systems theoretical ambitions are to describe the (low energy) behavior of the real complex material by an effective model. Unfortunately many such effective - though often simplistic - models are very demanding to tackle theoretically. Even numerically the simulation of complex many body models with classical computers often becomes a hard problem: Quantum Monte Carlo (QMC) simulations suffer from the so called negative sign problem for typical fermionic or frustrated systems [22]. Other approaches such as the density matrix renormalization group (DMRG) techniques [23] are mainly restricted to one dimensional systems. Hence, typically not even groundstate properties can be efficiently simulated let alone non-equilibrium or open systems. Here the idea of quantum simulation as proposed already by Feynman in 1982 [24] offers a possible solution and funda-

mentally changes the relation between theory and experiments.

Quantum simulators may substantially help answering fundamental questions of interacting many body systems such as unveiling the nature of high-temperature superconductivity or the search for spin liquid groundstates in quantum magnetism. But the scope goes far beyond the simulation of traditional solid state or condensed matter systems as one can see in established experimental realizations of high spinor quantum gases [25] or proposed schemes for the emulation of exotic dimensions [26] or lattice gauge theories [27, 28] of high energy physics.

Due to the amazing degree of control, cleanness and observability [29] experiments with ultracold quantum gases could offer the amazing possibility for the quantum engineering of a multitude of further many body models [30], highly correlated states or the simulation of dynamical properties. Compared to alternative approaches such as trapped ions, for which very successfully the control and quantum simulation and the implementation of universal quantum gate operations was proven[31–33], optically trapped neutral particles offer a large degree of scalability ranging from few [34] to many particle systems.

Even though there has been enormous progress, the field may still be considered in its infancy and many open problems have to be answered both by experiment and theory. In this thesis we will both address questions being of a more general interest for strongly correlated systems and various physical effective models and in particular search for possible realizations of those systems with ultracold quantum gases in optical lattices. We will lay a particular focus on one- or quasi one-dimensional systems for which interactions are strongly enhanced but also powerful analytical and numerical techniques are at hand [35].

1.1 Outline

This thesis is structured as follows. After a brief introduction to the physics of ultracold quantum gases trying to review parts of the current experimental situation (chapter 2), we give a short overview of the numerical algorithms, exact-diagonalization and DMRG methods employed in this work (chapter 3). The classical simulation of quantum many body systems such as the considered cold-atom scenarios, during the recent years has received much input from the quantum information community. In chapter 4 we will further introduce some concepts such as entanglement or quantum fidelity that we will employ as useful tools in numerical simulation for the description of in particular quantum phases and phase transitions. Here we will as well present a more specific study of the scaling properties of the so called fidelity susceptibility in certain situations and its connection to conductivity [36].

In the chapters 5 and 10 we will discuss two different many-body systems with ultracold bosons which have been both recently started being studied in experiments in different regimes. Chapter 5 discusses the so called frustrated zig-zag ladder in the context of modulated lattice systems [1]. We will present a careful analysis of quantum phases and phase transitions for many different scenarios and extensions including dipolar and three body interactions or variations in the ladder geometry [37–41].

Chapter 10 is dedicated to the square ladder in which a frustration is introduced by a rectified flux induced by synthetic magnetic fields penetrating the ladder as seen recently in Ref.[2]. We present detailed phase diagrams for ultracold bosons

in such a system, proving the stability of conjectured vortex-lattice and biased ladder phases as well as describe a very surprising counter intuitive current reversal effect [42, 43].

Nowadays the fast modulation of certain degrees of freedom in experiments has been established as a useful tool for the engineering of effective lattice models such as the ones mentioned before. In chapter 7 we focus on the case of a modulated magnetic field which translates to modulated interactions. After a review of the resulting effective models for bosons and fermions[44, 45] we focus on the particular case of a combined periodic modulation of lattice and interactions[46].

So far the realized synthetic gauge fields are static, without dynamical feedback of the particles on the field. In chapter 8 we discuss density depended gauge fields, which may be generated by modulated interactions[47] or laser-assisted hoppings[48, 49]. We will in detail discuss the experimental proposals and the resulting physical consequences, which includes statistically induced phase transitions, exotic quantum phases in one dimensional anyon-models, or intriguing properties of the doublon and holon dynamics.

Chapter 9 extends the viewpoint to a different class of systems. Motivated by recent experiments such as [25] we study dynamics and quantum phases for spin-3/2 fermions [50].

Chapter 2

Ultracold Quantum Gases in Optical Lattices

In this introductory chapter we briefly discuss basic concepts of the description, experimental preparation and observation of ultracold quantum gases in optical lattices. We will explain basic paradigms such as the Bose-Hubbard model and indicate various extensions such as dipolar interactions, dissipation or spinor gases. A particular focus is laid on the emulation of various effective Hamiltonians by fast periodic modulations of system parameters.

2.1 Trapping and cooling of atomic gases

2.1.1 Atom-light interaction

The interaction of neutral atoms with a coherent laser field forms the basis for atomic cooling, manipulation and trapping. Within the electric dipole approximation we may express the light-force induced by a laser driving an atomic transition with a detuning δ by a dissipative and a conservative part [29, 51]. The dissipative part, the radiation pressure force is caused by absorption and subsequent spontaneous emission processes. A spatially inhomogeneous intensity profile gives rise to the conservative optical dipole force $\mathbf{F}_D(R) \sim \delta \frac{\nabla \Omega(\mathbf{R})}{\Omega(\mathbf{R})}$ with the Rabi-frequency $\Omega(\mathbf{R})$ proportional to the intensity of the field $\Omega(R)^2 \propto |E_L|^2$. For a large detuning $|\delta| \gg \Gamma$ and a weak intensity one may approximate the potential by

$$V_{dip}(x) \approx \frac{\Omega(\mathbf{R})^2}{4\delta} \tag{2.1}$$

Interestingly, the sign of the force depends on the detuning δ. Hence, for a blue detuning of the laser with respect to the atomic transition $\delta > 0$ the regions of highest intensity act like a repulsive potential for the atoms. Contrary to that, for a red detuning $\delta < 0$ an attractive potential is realized. This way ultracold neutral atoms can be trapped in optical dipole traps.

2.1.2 Atom-atom interaction

In typical experiments we may describe the interactions by the two-particle scattering properties. For this binary collision problem we have to solve the time independent Schrödinger equation of the relative coordinate $r \left(-\frac{\hbar^2}{2\mu} + V(r) \right) \Psi(r) = E \Psi(r)$, where generally the precise short range form of the interparticle potential is not known and the long range part shows the asymptotic $1/r^6$ behavior of the van-der-Waals interactions. For the spherical symmetric scattering problem the wave function may be split into scattered partial waves with conserved angular momentum l.

Due to symmetry considerations if the scattered particles are identical bosons only even momenta $l = 0, 2, ..$ and for identical fermions only odd $l = 1, 3...$ contribute. Due to the presence of the centrifugal barrier for ultracold gases the scattering to channels $l \neq 0$ is frozen out. This s-wave scattering for low energy may be completely characterized by the s-wave scattering length a which typically has to be determined in experiments [29].

So ultracold one component fermionic atoms are well described by a free Fermi gas. For ultracold bosons in conventional conditions is justified to substitute the actual scattering potential by a contact interaction fully described by the s-wave scattering length a

$$V(x) \rightarrow \frac{4\pi a}{m}\delta(x) \tag{2.2}$$

In 1D the δ-interacting bosons model (Lieb-Liniger-model) may be solved analytically using Bethe-ansatz [52, 53].

The presence of nearby bound states may significantly change the scattering properties. For a model of two scattering channels corresponding e.g. to two internal states of the colliding particles, the admixture of the closed channel can lead to a typical resonant behavior in the scattering cross section. Such Feshbach resonances have been first discussed for nuclear physics [54] and applied to collisions of cold atoms where, remarkably, the scattering length may be changed by magnetically shifting the bound state due to its different Zeeman effect [55]. Typically a Feshbach resonance can be described by its width ΔB and position B_r by

$$a(B) = a_{bg}\left(1 - \frac{\Delta B}{B - B_r}\right) \tag{2.3}$$

where a_{bg} is the off-resonant background scattering length [29]. Feshbach resonances are extensively employed in current cold atom experiments to tune the interaction strength [56, 57]. It is also possible to induce Feshbach resonances optically via one- or two-photon transitions [58, 59].

2.1.3   Cooling of neutral atoms

The radiation pressure force may be exploited to dissipatively trap and cool neutral atoms within Doppler cooling schemes. Temperatures down to the Doppler-temperature $T_D = \frac{\hbar\Gamma}{2k_B}$ can be realized (Γ is the spontaneous emission rate). For typical Alkali experiments T_D is of order of $100\mu K$ [60]. In a magneto optical trap (MOT) a superimposed inhomogeneous magnetic field may be employed to realize trapping potential for neutral atoms.

Sub-Doppler cooling schemes such as the Sisyphus cooling or sub-recoil cooling have been invented to realize $\sim \mu K$ temperatures. Such laser cooling techniques, honored by the Nobel prize to S. Chu, C. Cohen-Tannoudji and W.D. Phillips in 1997, offered an essential step on the way to the first BEC. Due to the photon reabsorption of spontaneously emitted photons such laser cooling schemes cannot be used for reaching lowest temperatures and quantum degeneracy [60].

The groundbreaking realization of a Bose-Einstein condensation [4–6] in alkali atoms was achieved by the so called evaporative cooling technique. Atoms are magnetically trapped. By adiabatically lowering the trap-height atoms with the largest kinetic energy are evaporated from the trap, such that the average temperature after rethermalization has lowered. Since the necessary ingredient for this
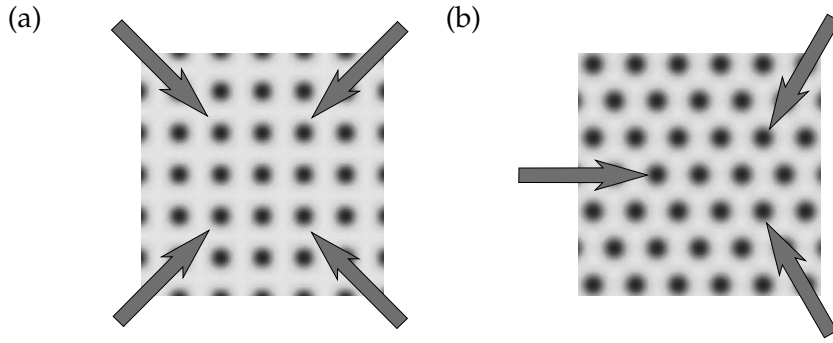
Fig. 2.1: Examples for optical lattice potentials. (a) A 2D square lattice generated by the superposition of two standing waves. (b) Triangular lattice as described in Ref. [66]. The intensity of the shading means lower lattice potential.

is the reaching of a thermal equilibrium through particle scattering processes, this cooling technique is not available to identical fermions with contact interactions.

Fermionic atoms may be cooled sympathetically by another species of atoms. This way Fermi-degeneracy could be reached experimentally [61]. In the presence of strong dipole-dipole interactions low energy elastic collisions between fermions are allowed and this way recently a direct evaporative cooling of fermions was observed[62].

Even though in BEC-experiments incredibly low temperatures have been reported [63], reaching sufficiently low temperatures or entropies per particle for the observation of certain strongly correlated many body phenomena in particular in optical lattice experiments remains challenging. Further schemes in particular for the cooling of quantum many body systems in optical lattices have been proposed[64] an are being actively explored[65].

2.1.4   Optical lattices

In the seminal proposal of Ref.[7] optical lattices have been introduced as a key element for the realization of strongly correlated systems in cold atom experiments without the need to increase the scattering lengths which also affects the condensate lifetime due to inelastic collisions.

The coherent superposition of counter-propagating lasers is used to create a periodic trapping potential for ultracold atoms. Two retro-reflected lasers $\mathbf{E} = \mathbf{e}\sin(kx + \omega t)$ may form according to Eq.(2.1) a standing wave potential

$$V_{lat} = -V_x \sin^2(kx) \, . \tag{2.4}$$

It is favorable to introduce the lattice depth V_x given in units of recoil energies $E_R = \hbar k^2/2m$. The period of the lattice is $d = \pi/k$, half the laser-wavelength λ. Two and three dimensional square-lattices (Fig. 2.1 (a)) may be generated by superimposing different pairs of standing waves with orthogonal polarization such that no interference terms appear[29]. While in the one or two dimensional lattices the radial or axial confinement is given by the overall Gaussian profile of the laser beams, which may be considered as an external (harmonic) trapping potential, for a three dimensional lattice the particles are strongly confined in all three spacial directions

$$V_{lat}(x,y,z) = -V_x \sin^2(kx) - V_y \sin^2(ky) - V_z \sin^2(kz). \tag{2.5}$$
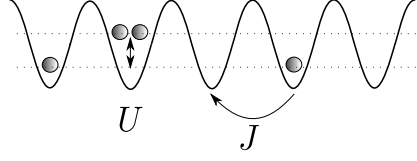
Fig. 2.2: Scheme of the Bose-Hubbard model Eq.(2.10). Particles tunnel with a tunneling rate J. The occupation of two particles per lattice site results in an energy offset U.

In most cases of this work we will consider such situations. The different strengths of the lattice depths $V_{x,y,z}$ may be tuned separately allowing for the emulation of strongly correlated gases in effectively one, two or three dimensions.

Ref. [66] discusses the creation of triangular optical lattices

$$V_{triang}(\mathbf{r} \equiv (x,y)) = V_0 \left[\sin^2(\mathbf{b}_1 \cdot \mathbf{r}/2) + \sin^2(\mathbf{b}_2 \cdot \mathbf{r}/2) + \sin^2((\mathbf{b}_1 + \mathbf{b}_2) \cdot \mathbf{r}/2) \right], \quad (2.6)$$

by superposition of three lasers with the wavevectors $\mathbf{b}_1 = \sqrt{3}k\mathbf{e}_y$, $\mathbf{b}_2 = \sqrt{3}k(\sqrt{3}\mathbf{e}_x/2 - \mathbf{e}_y/2)$ and $\mathbf{b}_3 = \sqrt{3}k(\sqrt{3}\mathbf{e}_x/2 + \mathbf{e}_y/2)$ forming angles of $2\pi/3$ with each other. Choosing a different polarization also hexagonal lattices can be created [66].

Nowadays various further geometries are at hands of the experimentalists. By the incoherent superposition of a blue detuned triangular lattice with wavelength λ and a red detuned triangular lattice with half the wavelength a Kagome lattice has been prepared[67]. In [68] three retro-reflected laser beams where employed for generation of a very tunable lattice configuration including square and honeycomb geometries.

In the future even more flexible lattice configurations and manipulation possibilities might become available using holographic-projection techniques [69].

2.2 The Bose-Hubbard model

2.2.1 Single particle eigenfunctions

Bloch's theorem states that eigenstates of a periodic potential, i.e. the eigenstates of $\hat{\mathcal{H}} = \frac{p^2}{2m} + V(x)$ with $V(x) = V(x+d)$ may be chosen as eigenstates of the translation operator $T_d : x \to x + d$. Hence they are periodic functions $u_q^{(n)}(x) = e^{iqx}u_q^{(n)}(x+a)$, with a quasi momentum q defined in the Brillouin-zone $-\frac{\pi}{a} < q < \frac{\pi}{a}$. $u_q^{(n)}$ is the Bloch-wavefunction of the n-th band of the system. For a finite lattice depth one typically observes a finite energy-gap between the different bands.

While Bloch wavefunctions are completely delocalized over the whole lattice it is favorable to introduce a basis-set of wave-functions, the Wannier-functions $w(x)$, which are strictly localized to a given lattice site [7],

$$w(x) = \sum_q e^{iqx}u_q^{(n)}. \qquad (2.7)$$

For deep lattices we may approximate the lowest Wannier-function by the Gaussian groundstate $w_{harm}(x) = e^{-(x/l)^2/2}/\sqrt{\sqrt{\pi}l}$ of a harmonic oscillator potential with frequency $\omega_0 = \sqrt{4E_R V_x}/\hbar$ and $l = dV_x^{-}1/4/\pi$. In the limit of deep lattices the band gap is of the order ω_0.++

2.2.2   Tight binding approximation

The second quantized form of the Hamiltonian for interacting bosonic particles in a trapping potential is given by

$$\hat{\mathcal{H}} = \int dx^3 \hat{\Psi}^\dagger(x) \left(-\frac{\hbar^2}{2m} \nabla^2 + V(x) \right) \hat{\Psi}(x) \quad + \tag{2.8}$$

$$+ \quad \frac{2\pi a_s \hbar^2}{m} \int dx^3 \hat{\Psi}^\dagger(x) \hat{\Psi}^\dagger(x) \hat{\Psi}(x) \hat{\Psi}(x) \tag{2.9}$$

Following Ref. [7] one may expand bosonic field operator in basis of Wannier-functions $\hat{\Psi}(x) = \sum_i \hat{a}_i w(x - x_i)$ and obtain a tight-binding approximation of the model

$$\hat{\mathcal{H}}_{BH} = -\sum_{\langle ij \rangle} J_{ij} \hat{a}_i^\dagger \hat{a}_j + \sum_i (\epsilon_i - \mu) \hat{n}_i + \sum_i \frac{U}{2} \hat{n}_i (\hat{n}_i - 1) \,. \tag{2.10}$$

This is the Bose Hubbard (BH) Hamiltonian with effective parameters for hopping J_{ij}, interaction U and chemical potential μ. Here the basic assumption is that all of the physics is sufficiently described by the lowest Bloch-band, which is valid for a sufficiently deep lattice depth.

The effective model parameters are given by

$$U = a_S \frac{4\pi\hbar^2}{m} \int dx^3 \|w(x)\|^4 \tag{2.11}$$

and

$$J_{ij} = - \int w^*(x - x_i) \left[-\frac{\hbar^2}{2m} \nabla^2 + V_L(x) \right] w(x - x_j) \,. \tag{2.12}$$

Units are typically given by the recoil energy $E_R = \frac{\hbar^2 k^2}{2m}$. For the one dimensional tunneling an accurate description is given by Mathieu characteristics a and b [29]

$$J = \frac{E_R}{4} \left(b_1 \left(\frac{v_x}{4} \right) - a_0 \left(\frac{v_x}{4} \right) \right) \approx \frac{4}{\sqrt{\pi}} v_x^{3/4} e^{-2\sqrt{v_x}} E_R \,. \tag{2.13}$$

For an optical lattice potential of the form $V_L = E_R \sum_{j=1}^3 v_j \sin^2(k x_j)$ the Wannier-functions separate to $w(x, y, z) = w_x(x) w_y(y) w_z(z)$ and J does not depend on the lattice-dimension. Within the harmonic approximation we find

$$U_{harm} = \sqrt{8}\pi (v_x v_y v_z)^{1/4} (k a_S) E_R \,. \tag{2.14}$$

In Fig. 2.3 we display J and U for a square lattice as obtained by a numerical calculation of the Wannier-functions in a square lattice. The harmonic approximation yields reasonable results.

2.2.3   Mott to superfluid transitions

Contrary to the Fermi-Hubbard model the Bose-Hubbard model (2.10) is not analytically solvable in general. Exceptions are the trivial limits $U \to 0$

$$\hat{\mathcal{H}}_{tun} = -\sum_{\langle ij \rangle} J \hat{a}_i^\dagger \hat{a}_j + \mu \sum_i \hat{n}_i = \sum_k (-2J \cos(k) - \mu) \hat{a}_k^\dagger \hat{a}_k, \tag{2.15}$$
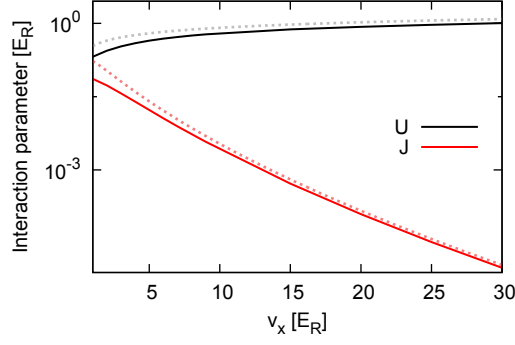
Fig. 2.3: Tight binding model parameters for a typical Alkali lattice gas (here ^{40}K with $a_s \approx 160 a_B$, $\lambda = 1030 nm$, $v_y = v_z = 35 E_R$ and $E_R \approx 4.9 kHz$, see chapter 9). The picture shows U and J from numerically calculated Wannier functions (solid lines). The dotted lines denote the approximations Eq. (2.13) and (2.14).

in which the groundstate is given by a fully delocalized state with a quasi-momentum $k = 0$, and the limit $J \to 0$

$$\hat{\mathcal{H}}_{J=0} = \sum_i \frac{U}{2} \hat{n}_i (\hat{n}_i - 1) - \mu n_i. \tag{2.16}$$

In the latter case the groundstate is completely localized with an integer number of n particles at each site for $n - 1 < \mu/U < n$, i.e. a pure Fock state $|n\rangle_{MI} = \prod_x |n\rangle_x$. These two groundstates are connected to different quantum phases, the superfluid (SF) and the Mott-insulator (MI) phase.

We obtain an intuitive understanding of the phase diagram by some simple mean field treatment. Starting from the MI-groundstate of Eq. (2.16) with energy $E_n^{(0)} = \frac{U}{2} n(n-1) - \mu n$ we calculate the energy correction of the perturbation by $\hat{\mathcal{H}}_{tun}$ which, introducing the condensate density $\psi = \langle a_i^\dagger \rangle = \langle a_i \rangle$ may be written as

$$\hat{\mathcal{H}}_{tun} \approx -\psi (a_j^\dagger + a_j) \tag{2.17}$$

Up to second order in ψ the groundstate energy is given by

$$E_n \approx E_n^{(0)} + r_n \psi^2 + \dots \tag{2.18}$$

with $r_n = 1 + \frac{n+1}{\mu - Un} + \frac{n}{U(n-1) - \mu}$. For $r_n > 0$ a vanishing condensate density $\psi = 0$ minimizes this energy corresponding to the MI phase, for $r_n < 0$ we find $\psi \neq 0$ and the SF phase. From the condition $r_n = 0$ we obtain the second order phase boundary within this Landau paradigm depicted as a dotted line in Fig. 2.4.

Due to the Mermin-Wagner theorem [70] in 1D not even at zero temperature continuous symmetries may be broken spontaneously. Contrary to the mean field statement, hence, there cannot be an ordered phase with a true long range order. In one dimension critical phases are described by conformal field theories. Here all correlations decay algebraically and in the one-dimensional SF phase hence a quasi-long-range order is seen by the slow power-lay decay of single particle correlation functions $\langle b_i^\dagger b_i \rangle$. In the MI phase this correlation function decays exponentially. The MI phase is characterized by the hidden parity order

$$\mathcal{O}_P^2 \equiv \lim_{|i-j| \to \infty} \langle \exp[i\pi \sum_{i<l<j} \delta n_l] \rangle \tag{2.19}$$

with $\delta n = \bar{n} - \hat{n}$.

For one-dimensional systems the groundstate phase diagram obtained by numerical (DMRG) calculations is shown in Fig. 2.4. An accurate description of the phase boundary has been obtained as well by means of higher order perturbation theory [71]. The phase transition at unit filling has been estimated numerically to $U/J \approx 3.37$ [72] using DMRG. This value substantially deviates from the mean-field prediction $U/J \approx 11.7$. For higher dimensions the MI-SF transition has been calculated using QMC techniques (e.g. [73]) and, as expected, both shape and extend of the Mott-lobes are much better reproduced by the mean field treatment.

2.2.4 Bosonization

A more detailed description of the one-dimensional quantum phases may be obtained by means of bosonization techniques, which we will briefly introduce in this subsection. Following [35] and [52] we identify bosonic operators with their collective fields, density $\rho(x)$ and phase fluctuations $\theta(x)$,

$$b_j^\dagger \to \rho(x_j)^{1/2} e^{-i\theta(x_j)} \qquad (2.20)$$

with $\rho(x) \simeq \rho_0 - \frac{1}{\pi}\partial_x\phi$ neglecting the contribution of higher harmonics. ρ_0 is the average density and $x_j = j \cdot a$ the position of site j (in the following we typically set $a = 1$ and, for convenience, $\hbar = 1$). Phase and density fluctuations θ and $\partial_x\phi$ fulfill the commutation relations $[\theta(x), \partial_y\phi] = i\delta(x - y)$.

With this one finds for the BH model assuming a weak coupling $U \ll J$

$$\hat{\mathcal{H}} = \frac{v}{2\pi} \int dx \left[\frac{\pi^2}{K}(\partial_x\phi)^2 + K(\partial_x\theta)^2 \right], \qquad (2.21)$$

with $vK \approx \rho_0/2m$ and $v/K \approx U/\pi^2$. The low energy description Eq. (2.25) generally even holds for the description of the strong coupling superfluid regime, or more generally, any one dimensional critical Luttinger liquid phase. Here, however, the simple identification of sound velocity v and Luttinger liquid parameter K with the microscopic parameters has to be renormalized. For completeness we mention that for few cases v and K may be calculated analytically such as for the (extended)
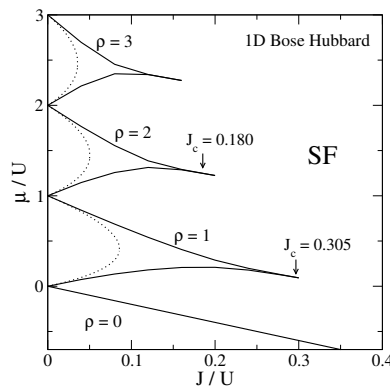
Fig. 2.4: 1D phase diagram of the BH model (2.10) with the SF-phase and Mott-lobes at filling $\rho = 1$, 2 and 3 obtained from DMRG calculations (solid lines) and mean field approach (2.17) (dotted line).

hardcore ($U \to \infty$) Bose-Hubbard model (2.36) restricted to nearest neighbor interactions

$$K = \frac{\pi}{2\arccos\left(-\frac{V}{2J}\right)} \; , \qquad v = \frac{J\pi\sqrt{1 - \frac{V^2}{(2J)^2}}}{2\arccos\left(\frac{V}{2J}\right)} \; , \qquad (2.22)$$

Hence, for the limit $V \to 0$ we obtain $K = 1$, which corresponds to the case of free spinless fermions.

From model (2.25) we may evaluate correlation functions [35]. For the single-particle one obtains

$$\langle \hat{b}_i^\dagger \hat{b}_j \rangle \sim |i - j|^{-1/2K} \; . \qquad (2.23)$$

For the density density correlations the result is

$$\langle n_i n_j \rangle = \rho_0^2 - \frac{K}{2\pi^2 |i - j|^2} + \cdots \qquad (2.24)$$

where the ellipsis includes subleading corrections, including the oscillatory term $\sim \cos(2\pi\rho_0 r)|i - j|^{-2K}$.

In the presence of a lattice the so called Umklapp-processes in which particles are scattered to states with an integer number of reciprocal lattice vectors difference introduce additional terms such as

$$\hat{\mathcal{H}}_{\text{Umklapp}} \sim \int dx \cos\left(2p\phi(x) + \delta x\right) \; . \qquad (2.25)$$

δ describes the doping away from a commensurate particle filling of an integer number of n bosons every p sites. Renormalization group methods for this sine-Gordon models show that for a commensurate density $\delta = 0$ for $K < 2/p^2$ the cos-term dominates and fluctuations of ϕ become strongly suppressed. This case corresponding to a strong localization of the particles is the MI phase. The continuous transition between MI and SF phase is of Berezinskii-Kosterlitz-Thouless (BKT) type [74, 75]. Here universally $K = 2/p^2$ and the gap opens exponentially slow.

Introducing a finite doping $\delta \neq 0$ oscillations in the cos-term annihilate its effect at large distances and the system in the low energy limit returns to a LL/SF phase. The phase transition is of commensurate-incommensurate (C-IC) type which may be analyzed using refermionization techniques. The critical Luttinger-liquid-parameter takes the universal value $K = 1/p^2$.

Conformal field theory offers a powerful tool for the description of Luttinger-liquids in finite size system and finite temperatures. For open boundary condition of a chain of size L the result Eq. 2.23 becomes [76]

$$\langle \hat{b}_i^\dagger \hat{b}_j \rangle \sim \left[\frac{\sqrt{d(2i, 2L)d(2j, 2L)}}{d(i + j, 2L)d(i - j, 2L)} \right]^{1/2K} + \cdots \; , \qquad (2.26)$$

with the cord-function $d(x, L) = L|\sin(\pi x/L)|/\pi$.

2.2.5 External potential

In typical optical lattice experiments the Gaussian-shape laser-beams introduce an external confinement to the finite size system that in most cases may be assumed to be harmonic

$$V_{trap}(x) = \omega_{trap}^2 (x - L/2)^2 \; . \qquad (2.27)$$
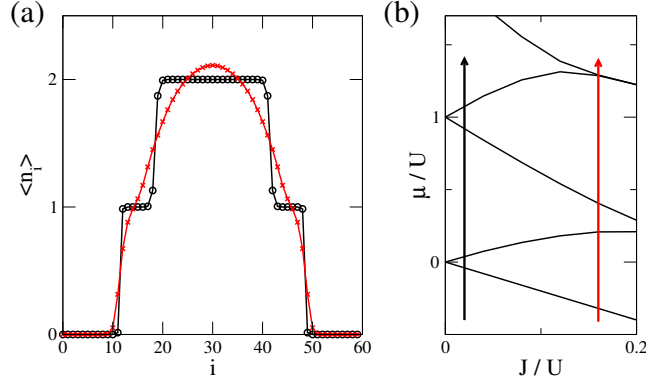
Fig. 2.5: (a) Density profile $\langle n_i \rangle$ of the BH model in an external harmonic confinement (2.27) at different values of the hopping strength $J/U = 0.02$ and 0.16 ($L = 60$ sites). The observed wedding cake structure for strong U/J can be understood within the local density approximation (b).

The external trap has a severe impact on the observability of quantum phases. For a spatial slowly varying trapping potential we may employ the local density approximation assuming a locally homogeneous system with a chemical potential

$$\mu(x) \rightarrow \mu - V_{trap}(x) \tag{2.28}$$

Hence, we observe the so called wedding-cake structure, with different regions and plateaus corresponding to the (gapped and gapless) quantum phases realized at $\mu(x)$ in an homogeneous system (see Fig.2.5).

2.2.6 Observability

Ultracold quantum gases offer fascinating possibilities for the experimental detection and analysis of quantum states and phases prepared in the lattice. Contrary to traditional condensed-matter experiments, it is possible the directly observe the quasi-momentum distribution or even in-situ occupation.

The time of flight (TOF) imaging has become to one of the standard methods for the analysis of quantum gases. After a sudden turning off of the confining and lattice potential a contact interacting gas expands freely according to its initial momentum distribution. The density of atoms of the atomic cloud may be measured using light absorption imaging. The real space density of atoms at position X after a long time of flight is given by the initial momentum distribution [77]

$$n(r) \approx \frac{m}{t} n(Q) \tag{2.29}$$

where $Q = \frac{mx}{t}$. This can be related to the lattice quasi momentum distribution via

$$n(Q) = |\tilde{w}(Q)|^2 n(k) \tag{2.30}$$

Here $k = dQ \bmod 2\pi$ corresponds to the quasi-momentum in the lattice and $\tilde{w}$ is the Fourier transform of Wannier-function of the lattice. The whole TOF picture hence contains several copies of the initial momentum distribution with an overall envelope $|\tilde{w}(Q)|^2$. Similarly, an adiabatic switching off of the lattice depth leads to a conservation of the quasi-momentum k and allows for the direct imaging of the

occupations of different Brillouin-zones. This band mapping technique has been applied to measure the population of higher excited bands and Fermi-surfaces [78, 79]. A detailed analysis of TOF images allows for the detection of higher order correlations [77].

During the recent years the realization of "quantum gas microscopes" [69, 80] has opened the amazing possibility to directly observe on-site particle densities in an optical lattice. The experimental scheme relies on the implementation of a high-resolution optical imaging system. After the state-preparation or experimental sequence a sudden ramping up of lattice depth pins the atoms to fixed lattice sites and projects the many-body wavefunction to a certain Fock-space snapshot. Shining in resonant light causes a fluorescence of the atoms which allows for a cooling and imaging of their positions but also causes strong inelastic light induced collisions and two-body losses. Hence, within this technique it is possible to image precisely the atom number modulo two. This allowed for example for a direct observation of the wedding cake-structure [80] or measurements of complicated correlations such as parity order in MI phases[81] in groundstates or time dependent evolutions [82] by averaging over several snapshots of the quantum phases.

2.3   Extensions

Several extensions or generalizations to the previously introduced scenario of (Bose) Hubbard models have received a large interest in both theory and experiment. In the following we will present few of them including multicomponent Hubbard models, dipolar-quantum gases and models with 3-body interactions.

2.3.1   Spinor gases

Spinor gases, i.e. quantum gases with an additional internal spin degree of freedom, in optical lattices [7, 83] offer a fascinating possibility to study quantum magnetism and lattice models which resemble electronic degrees of freedom in solid state systems but may as well, for more that two internal states, go substantially beyond the standard condensed matter paradigms.

Generically spin S particles in an optical lattice can be described by the Hamiltonian

$$\hat{\mathcal{H}} = J \sum_{\sigma} \sum_{\langle i,j \rangle} c_{\sigma i}^{\dagger} c_{\sigma j} + \hat{\mathcal{H}}_I \tag{2.31}$$

where the interaction part is

$$\hat{\mathcal{H}}_I = \sum_{i} \sum_{\{\sigma_1,\sigma_2,\sigma_4,\sigma_3\}} V_{\sigma_1,\sigma_2,\sigma_4,\sigma_3} c_{\sigma_1 i}^{\dagger} c_{\sigma_2 i}^{\dagger} c_{\sigma_3 i} c_{\sigma_4 i} . \tag{2.32}$$

Here $c_{\sigma_1 i}^{\dagger}$ ($c_{\sigma_1 i}$) creates (annihilates) a particle with spin σ_1 at site i. Since s-wave contact interactions do not break rotational symmetry the total spin F of the two colliding particles is a good quantum number such that $\sigma_1 + \sigma_2 = \sigma_3 + \sigma_4$ and the contact interaction potential of two spin S particles may be decomposed as [84, 85]

$$V_{\sigma_1,\sigma_2,\sigma_4,\sigma_3} = \sum_{F=0..2S} \frac{g_F}{2} \sum_{M=-F...F} \langle M, F | \sigma_1 \sigma_2 \rangle \langle \sigma_3 \sigma_4 | F, M \rangle . \tag{2.33}$$

Here $g_F = U \frac{a_F 4\pi\hbar^2}{m}$ denotes the coupling strength of the F-channel, a_F the corresponding scattering length and $U = \int dx^3 \|w(x)\|^4$ accounts for the lattice on-site wavefunction. Due to the symmetry of the Clebsch-Gordon coefficients $\langle \sigma_3\sigma_4|F, M\rangle$ only certain scattering channels are allowed depending on the statistics of the atoms: For fermions since orbital wavefunction has to be symmetric to allow s-wave scattering, the total spin state has to be antisymmetric. Thus only channels contribute if $F + 2S$ is odd. Analogously for bosons $F + 2S$ has to be even.

Thus the simplest nontrivial interaction Hamiltonians only contain density-density interactions

- Spin 1/2 fermions: $\hat{\mathcal{H}}_I = g_0 n_{-\frac{1}{2}} n_{\frac{1}{2}}$

- Spin 1/2 bosons: $\hat{\mathcal{H}}_I = \frac{g_1}{2}\left(n_{\frac{1}{2}} n_{\frac{1}{2}} + n_{-\frac{1}{2}} n_{-\frac{1}{2}}\right) + g_1 n_{-\frac{1}{2}} n_{\frac{1}{2}}$

- Spin 1 fermions: $\hat{\mathcal{H}}_I = -g_1\left(n_0 n_1 + n_{-1} n_0 + n_{-1} n_1\right)$

However as soon as more components come into play there is also the possibility for spin-changing collisions. For spin-1 bosons the Hamiltonian is given by

$$\hat{\mathcal{H}}_I = \frac{g_0 + 2g_2}{6} n_0 n_0 + \frac{g_2}{2}\left(n_1 n_1 + n_{-1} n_{-1}\right) + g_2\left(n_0 n_1 + n_{-1} n_0\right) + \frac{2g_0 + g_2}{3} n_{-1} n_1$$
$$+ \frac{g_2 - g_0}{3}\left(c_0^\dagger c_0^\dagger c_1 c_{-1} + c_{-1}^\dagger c_1^\dagger c_0 c_0\right) \tag{2.34}$$

For some typical experimentally accessible alkali-species, such as the $F = 1$ manifold of ^{87}Rb both $g_0 \approx g_2$. This case looks - accidentally - like a $SU(N)$-symmetric like spinor gas. In this context recently alkali-earth and similar (e.g. ytterbium) quantum gases have received a lot of attention[86]. Due to their closed shell spin-orbit coupling does not lead to a hyperfine splitting and an almost perfect $SU(N)$-symmetry is realized.

In chapter 9 we will discuss in detail physical properties of spin 3/2 alkali fermions at half filling.

2.3.2 Dipolar quantum gases

Nowadays active research is focused on the understanding and experimental production of dipolar quantum gases [87, 88]. The dipolar interaction due to its anisotropy and long range character decaying as $1/r^3$ adds radically new features to the quantum gas. The interaction potential between two externally aligned dipoles with angle θ between the polarization direction and their position, is given by [87]

$$U_{dd}(r) = \frac{C_{dd}}{4\pi} \frac{1 - 3\cos^2\theta}{r^3} . \tag{2.35}$$

Today various realizations of dipolar gases are being explored in experiments. Several ultracold atom-species with a strong magnetic dipole moment have been brought to quantum degeneracy, such as chromium [89], dysprosium [90] or erbium [91]. Metastable Rydberg–dressed atomic gases [92, 93] exhibit a huge electric dipole moment however present difficulties due to their short lifetime. Recently also ultracold lattice gases of polar molecules have been realized in several experiments [15, 94]. Dipolar interactions give rise to exotic phenomena such as roton-like

dispersion minima [95], d-wave symmetric collapse [96] or Rosenzweig instability in ferrofluids [97].

In one-dimensional lattice systems we are in particular interested in the long range character of the dipole-dipole interactions, which is described by the extended (Bose-)Hubbard model

$$\hat{\mathcal{H}}_{eBH} = -\sum_i J\hat{a}_i^\dagger \hat{a}_{i+1} + H.c. + \sum_i \frac{U}{2}\hat{n}_i(\hat{n}_i - 1) + \sum_{i \neq j} \frac{V}{|i-j|^3}\hat{n}_i\hat{n}_j \, . \qquad (2.36)$$

Recently this model has been realized with erbium atoms [16].

Let us briefly review the quantum phases that may be found in a one-dimensional realization of the extended Bose-Hubbard model at unit filling. This model has been extensively studied for repulsive interactions in Refs.[98–100], which may be understood from an approximate mapping of the model to a spin-1 system [101] by identification of $|0\rangle \to |-\rangle$, $|1\rangle \to |0\rangle$ and $|2\rangle \to |+\rangle$. For the limit $J \to 0$ we may immediately understand the emergence of two regimes depending on the ratio U/V. For dominant on-site interactions a usual MI phase is found, for dominant nearest-neighbor interactions a (charge) density wave (DW or CDW) $\ldots |2020\rangle \ldots$ with a spontaneously broken translational symmetry is stabilized. The latter, corresponding to a Néel phase in the spin-1 system, is characterized by the CDW-order parameter

$$\mathcal{O}_{CDW} \equiv \lim_{j \to \infty} (-1)^j \langle n_i n_{i+j} \rangle \qquad (2.37)$$

The transition between CDW and MI is of first order. Interestingly, for a finite hopping $J > 0$ a gapped intermediate phase with a hidden string order[99]

$$\mathcal{O}_S^2 \equiv \lim_{|i-j| \to \infty} \langle \delta n_i \exp[i\pi \sum_{i<l<j} \delta n_l] \delta n_j \rangle \qquad (2.38)$$

emerges. This so called Haldane-insulator (HI) phase can be understood as a kind of diluted CDW-phase in which the alternating sequence 0 and 2 may be interrupted by a sequence of 1. Parity order $\mathcal{O}_P^2$ vanishes in the HI. In section 3.2.1 we will review a simple archetype of the Haldane phase.

Many other unconventional quantum phases are expected in such kind of models such as supersolids, a devil's staircase of coulomb crystals [88]. Interestingly for non-local interactions the Mermin-Wagner theorem does not hold and continuous symmetry breaking phases may be found in models with long-range interactions [102].

In Ref. [103] creation of exotic effective models with dominant three body interactions between neighboring sites by microwave-dressing of polar molecules was proposed. In chapter 5 we study this possibilities in the context of frustrated lattice models.

2.3.3 Dissipation and the Zeno-effect

Sources of loss or decoherence in cold atom experiments due to the interaction of a quantum system with its environment have been thought to be a severe obstacle in the precise experimental study of quantum states. However, they may be even exploited for the preparation of certain interesting quantum systems [104, 105].

In particular three-body losses, ubiquitous in cold gas experiments, have recently been suggested to allow for the engineering of a three body on-site hard
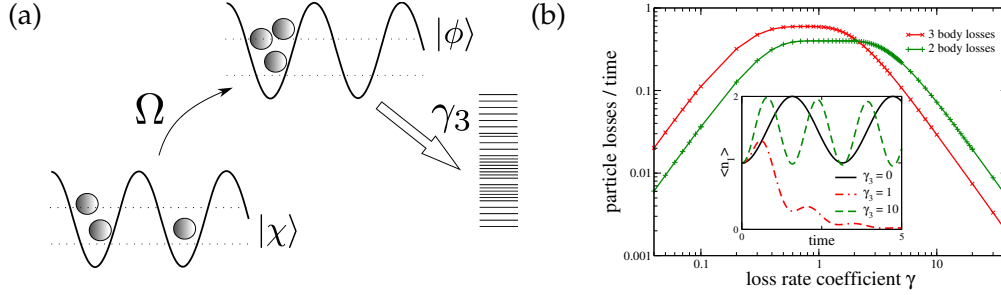
Fig. 2.6: (a) Quantum optical scheme for the loss process. (b) Master equation approach for losses in a 2-site Bose-Hubbard-model ($t = 1, U = 0$). The inset shows change of particle number for the 3-body-loss for different values for $\gamma_3 = 0, 1, 10$. For unconstrained bosons $\langle n_i \rangle$ oscillates like $\frac{1}{2}(3 - \cos 2t)$, while the constraint case the oscillation-period is halved $\frac{1}{2}(3 - \cos 4t)$.

core constraint: Central result of the seminal work by Daley et al. [106] is that a large three body loss processes with decay rate $\gamma_3 \gg |J|$ will give rise to an effective strong three body repulsion

$$(b_i^\dagger)^3 = 0 \,. \tag{2.39}$$

The underlying principle may be understood from the quantum Zeno-effect: A large loss rate, acting as observer of the quantum state, will dynamically suppress the generation of three-body occupation on a given site.

The suppression of three-body occupation has been hinted in recent experiments [107]. Analogously it was shown for a cold gas of Feshbach-molecules [108] that strong two-body losses lead to an effective (two-body) hardcore constraint.

In Fig. 2.6 (a) we sketch a simplified quantum optical picture of the system: Two discrete states are coupled via a process Ω which corresponds the hopping t of one particle. The second state is coupled to the continuum via a loss mechanism - e.g. inelastic 3-body collisions. The effective loss-rate Γ_{eff} has to take into account the probability density of $|3, 0\rangle$ in the new continuum of states, which has a Lorentzian-shape [109]. So for $\gamma_3 \gg 1$ one finds $\Gamma_{eff} \sim \frac{\Omega^2}{\gamma_3}$ [108].

As pointed out in [106] one may formally express three-body losses in the lattice system in the following form of a Lindblad-type master equation

$$\partial_t \rho = -\mathrm{i} \left(\hat{\mathcal{H}}_{eff} \rho - \rho \hat{\mathcal{H}}_{eff} \right) + \frac{\gamma_3}{12} \sum_i 2 b_i^3 \rho (b_i^\dagger)^3 \tag{2.40}$$

with $\hat{\mathcal{H}}_{eff} = \hat{\mathcal{H}} - \mathrm{i} \frac{\gamma_3}{12} \sum_i b_i^3 (b_i^\dagger)^3$. In Fig. 2.6 (b) the master-equation (2.40) is integrated for a given time starting from a pure state $|2, 1\rangle$ (from $|1, 1\rangle$ for the case of two-body-losses) and we display the change in particle number over that period. For small loss-rates we find a steep increase of particle losses with $\gamma_3 \ll 1$. For sufficiently big $\gamma_3 \gg 1$, however, the losses are strongly suppressed.

The three-body constraint opens exciting novel scenarios for Bose-gases with attractive interactions, including color superfluids in spinor Bose gases [110] and pair-superfluid phases [106, 111, 112].

Different proposals [113, 114] involving additional laser-couplings could allow for the generation of fully tunable on-site three-body interactions.

2.4   Real time control

One of the most interesting features of experiments with cold quantum gases is the possibility to almost arbitrarily study and manipulate the behavior of quantum systems in real time [29] which offers unique possibilities for the study of out-of-equilibrium systems. Contrary to the relatively broad understanding of equilibrium properties, the physics of non-equilibrium quantum systems is much less clear [115], since theoretical approaches are often restricted and also numerical simulations can only deal with short time evolutions.

One of the most interesting questions which is subject of a long-standing controversy is how and whether isolated quantum systems once driven out of equilibrium may reach stationary state, i.e. may be described by an thermal equilibrium canonical (Gibbs) ensemble. Cold atom experiments such as [116, 117], which are to a large extent isolated form their environment, help in understanding these fundamental properties of quantum manybody systems. The particular case of integrable models does not reach thermal equilibrium [116], but should rather be described by a generalized Gibbs ensemble including further conservation laws[118]. It has been conjectured that non-integrable systems could first reach a intermediate prethermalized state, described by a generalized Gibbs ensemble [117, 118] and then at larger timescales reach full thermalization.

The breaking of ergodicity in disordered systems due to Anderson–localization [119] has been observed in cold atom systems with random laser potentials in 1D [120], 2D [121] and 3D [12]. Recently many-body localization, i.e. localization in excited states on an interacting many-body system, has turned into the focus of active research [17, 122].

The dynamics and defect creation of a driving through a continuous phase transition between a disordered and an ordered phase is described by the classical Kibble-Zurek mechanism [123, 124] which may be generalized to quantum systems [125]. Among many other experiments e.g. in superfluid Helium [126] the Kibble-Zurek like scaling has been hinted in several experiments in ion crystals [127] or BECs [128, 129].

The observability of single lattice sites [69, 80, 130] has opened the possibility to directly image light-cone like spreading of correlations in a lattice system [82], which allows for example for the possibility of studying open questions of Lieb-Robinson bounds in bosonic quantum systems.

In the chapters 7, 8, and 9 we explicitly study the non-equilibrium properties of some aspects of lattice models implying quasi-adiabatic processes and sudden quench scenarios, relevant for experiments [131, 132].

2.5   Fast periodic modulations

The fast periodic modulation of certain degrees of is an ubiquitous tool in many areas of physics for the engineering and probing of various systems ranging from NMR probes in solid state physics to atom-light interactions or Raman-dressed states. During the recent years lattice shaking techniques have established themselves as toolbox for the creation of effective Hamiltonians in cold atom systems. The idea of Floquet-engineering is based on the effective averaging of fast periodic drivings to obtain a effective time-independent Hamiltonian description with different novel properties. Below we will briefly present the underlying principles for

(a) (b)
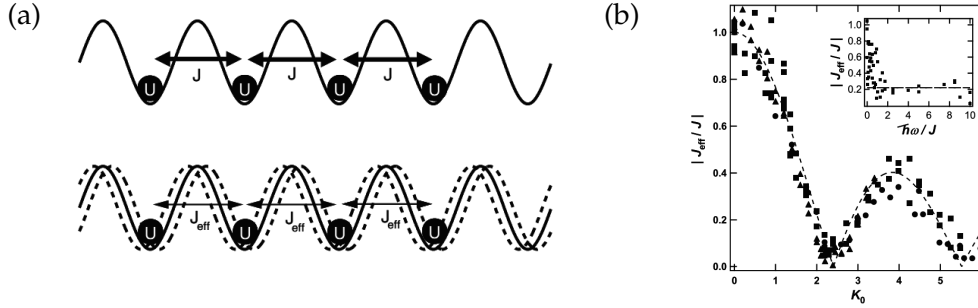
Fig. 2.7: (a) Lattice shaking scheme for the generation of an effective tunneling $J_{eff} = \mathcal{J}_0(K_0)$. (b) Experimentally observed reduction of the modulus of the effective tunneling. Figs. are adapted from Ref. [133].

the resulting effective time independent Hamiltonians and discuss several related properties.

A prominent example is the modulation of the spacial position of optical lattices [134], lattice shaking. By for example direct micro-mechanical modulation of the position of a retro-reflecting mirror of the lattice lasers it is possible to shake the lattice periodically in time

$$V_{lat}(t) = V_{lat}(x - r(t)) \tag{2.41}$$

with e.g. $r(t) = A\cos(\omega t)$. As shown in [133, 135] for a fast modulation this situation may effectively be described by a lattice model with a modified hopping rate

$$J \to J_{eff} = J\mathcal{J}_0(K/\hbar\omega) \,,. \tag{2.42}$$

with the amplitude $K = md^2 A/\hbar$ and the zeroth order Bessel-function $\mathcal{J}_0$. Interestingly tunneling may be strongly reduced or even completely suppressed which allows to drive a superfluid (SF) to Mott insulator (MI) transition [136]. A changing of sign of the hopping rate was successfully shown to emulate frustrated classical magnetism [1] in a 2D-system of bosonic atoms. Experimentally it is possible to modify the shaking function almost at will and a different shaking scheme than a pure sinusoidal modulation Eq. (2.41) may lead to complex effective hopping amplitudes. This way tunable gauge potentials [137] have been demonstrated. We will explore these ideas in chapter 5. In Ref. [138] the coupling of different Bloch-bands via lattice-shaking techniques was exploited for the generation of strong interaction between different spin-components. This particular methods opens interesting properties to create tunable band structures in optical lattices.

Recently, these ideas have been extended to fast periodically modulated interactions [44, 45, 139]. We will discuss these concepts more in detail in chapter 7.

2.5.1 Floquet analysis

The action of time periodic Hamiltonians

$$\hat{\mathcal{H}}(t) = \hat{\mathcal{H}}(t + T) \tag{2.43}$$

with period $T = 2\pi/\omega$ may be formalized employing the Floquet theory. Analog to Bloch-wave functions for a spatially periodic Hamiltonian, the Floquet-theorem [140,
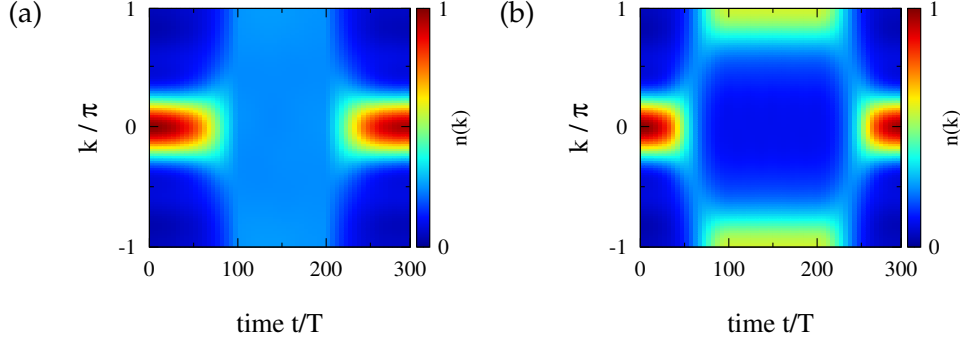
Fig. 2.8: Quasi-momentum distribution for lattice-shaking as demonstrated in [134] for bosons in a $L = 5$ site lattice using Eq.(2.49) with a quasi-adiabatic ramping of the shaking amplitude over 100 cycles ($U/J = 3$, $\omega/J = 14$, unit filling). (a) SF to MI transition for a ramp to $\frac{K}{\hbar\omega} = 2.4$ (b) Inversion of the sign of the tunneling element for $\frac{K}{\hbar\omega} = 3.8$.

141] ensures the existence of a set of solution to the time dependent Schrödinger-equation of the form

$$\Psi_n(t) = u_n(t)e^{i\epsilon_n t/\hbar}. \tag{2.44}$$

with time-periodic functions $u_n(t) = u_n(t + T)$ being the eigenstates of $H(t) - i\hbar\partial_t$. The real quasi-energies ϵ_n are just defined up to a multiple of a photon-energy $m\hbar\omega$. Following [134, 142] it is useful to choose a Floquet basis in a composite Hilbert space of the original lattice problem and time-periodic functions

$$|\{n_j\}, m\rangle = |\{n_j\}\rangle e^{im\omega t} \tag{2.45}$$

One may introduce a scalar product on the composite space which includes a time-averaging

$$\langle\!\langle \cdot|\cdot \rangle\!\rangle = \frac{1}{T} \int_0^T dt \langle \cdot|\cdot \rangle. \tag{2.46}$$

The basis is (ideally) chosen in such a way that the resulting Hamiltonian $\langle\!\langle \{n_j'\}, m'|H(t) - i\hbar\partial_t|\{n_j\}, m\rangle\!\rangle$ becomes time-independent. The matrix consists of several blocks, with the diagonal blocks $m = m'$ corresponding to one Floquet-sector, coupled by off-diagonal blocks. For a fast modulation, if block separation $\hbar\omega$ is larger than any other energy scale of the system, we may neglect the coupling between different Floquet-sectors and describe the system with the time-independent effective Hamiltonian given by $\langle\!\langle \{n_j'\}, m|H(t) - i\hbar\partial_t|\{n_j\}, m\rangle\!\rangle$.

2.5.2 Lattice shaking

For the case of a lattice shaking (2.41), we employ a unitary transformation [143]

$$\tilde{U} = e^{-\frac{i}{\hbar}\int_0^t dt' \frac{m\dot{r}(t')^2}{2} - \frac{i}{\hbar}\dot{r}(t)x} e^{\frac{i}{\hbar}\dot{r}(t)p} \tag{2.47}$$

to the comoving frame

$$\hat{\mathcal{H}} \to \tilde{U}\hat{\mathcal{H}}\tilde{U}^\dagger - i\hbar\tilde{U}\partial_t\tilde{U}^\dagger = \frac{p^2}{2m} + V_{lat}(x) - m\ddot{r}(t)x \tag{2.48}$$

Hence, reintroducing the tight binding approximation and interaction terms in this frame the lattice shaking maps to a force described by a modulation of a lattice tilt

$$\hat{\mathcal{H}} = \hat{\mathcal{H}}_{BH} + K(t) \sum_j j\hat{n}_j \, . \tag{2.49}$$

Note that, since $r(t)$ is time periodic and unbiased this is as well true for its derivatives $\ddot{r}$. For this reason initial phases do not play a role in the creation of complex hopping amplitudes as we will discuss in chapter 7.

We now may employ another unitary transformation

$$\hat{U} = e^{-\frac{i}{\hbar}V(t)\sum_j j\hat{n}_j} \tag{2.50}$$

with $V(t) = \int_0^t K(t')dt'$ and arrive at a time-dependent tunneling phase

$$\hat{\mathcal{H}} \to -J \sum_i \hat{a}_i^\dagger e^{-iV(t)} \hat{a}_{i+1} + \sum_i \frac{U}{2} \hat{n}_i(\hat{n}_i - 1) \tag{2.51}$$

Now we may use the Floquet-formalism as shown above and obtain the Floquet-matrix[134]

$$\langle\!\langle \{n'_j\}, m' | H(t) - i\hbar\partial_t | \{n_j\}, m \rangle\!\rangle = \delta_{m,m'} \left[\langle \{n'_j\} | H_{int} | \{n_j\} | \rangle + \hbar\omega m \right] +$$

$$+ \left(\sum_j j(n'_j - n_j) \right)^{m'-m} \mathcal{J}_{m'-m} \left(\frac{K}{\hbar\omega} \right) \langle \{n'_j\} | H_{tun} | \{n_j\} | \rangle \tag{2.52}$$

Hence, for a high frequency behavior we effectively yield a usual Bose-Hubbard model Hamiltonian Eq.(2.10) with an effective tunneling rate given as in Eq. (2.42).

In Fig. 2.8 we demonstrate the validity and properties of the effective model Hamiltonian for a small system. Following Ref. [134] starting from a SF-groundstate we quasi-adiabatically ramp up the shaking amplitude to a particular value of $\frac{K}{\hbar\omega}$. After keeping the amplitude constant for some cycles and monitoring the momentum distribution of this state we slowly lower the shaking amplitude in order to prove that coherence of the state has not been lost during this scheme. Initially the momentum distribution exhibits a peak at 0 modulo 2π. For $\frac{K}{\hbar\omega} = 2.4$, the first root of the Bessel-function, the momentum distribution becomes flat corresponding to a MI-state with localized particles (see Fig. 2.8 (a)). In Fig. 2.8 (b) we show that the sign of the effective hopping may even be inverted for $\mathcal{J}_0\left(\frac{K}{\hbar\omega}\right) < 0$. Here we find peaks of the momentum-distribution at π.

2.5.3   Lattice depth modulation

We will discuss some further aspects of effective modulated Hamiltonians for the example of lattice depth modulations, as demonstrated in Ref. [144]. The weak modulation of the intensity of the lattice lasers may result in a strong modulation of the tunneling matrix element $J + \delta J(t)$ due to its exponential dependence of the lattice depth. The interaction strength U will basically remain unaffected for typical modulations amplitudes (in [144] the modulation strength around 15% of the original intensity is employed). The model Hamiltonian is given by

$$\hat{\mathcal{H}} = (J + \delta J(t))\, \hat{\mathcal{H}}_{tun} + \hat{\mathcal{H}}_{int} \, . \tag{2.53}$$
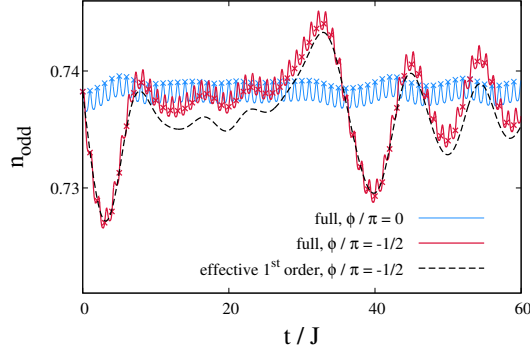
Fig. 2.9: Comparison of the full time evolution (2.53) and the effective model (2.60) for lattice depth modulation ($\delta J = 0.8J$, $U = 4$, $L = 6$ unit filling, $\omega = 80$) for different initial phases.

For a sinusoidal modulation $\delta J(t) = \delta J \sin(\omega t + \phi)$ we obtain the Floquet-Hamiltonian

$$\langle\!\langle \{n_j'\}, m' | \hat{\mathcal{H}}(t) - i\hbar\partial_t | \{n_j\}, m \rangle\!\rangle = \delta_{m,m'} \left[\langle\{n_j'\}| J\hat{\mathcal{H}}_{tun} + \hat{\mathcal{H}}_{int} |\{n_j\}|\rangle + \hbar\omega m \right] +$$

$$+ \delta_{m',m+1} i\frac{\delta J}{2} e^{i\phi} \langle\{n_j'\}|\hat{\mathcal{H}}_{tun}|\{n_j\}|\rangle +$$

$$- \delta_{m',m-1} i\frac{\delta J}{2} e^{-i\phi} \langle\{n_j'\}|\hat{\mathcal{H}}_{tun}|\{n_j\}|\rangle . \tag{2.54}$$

2.5.4 Higher order corrections

So far (and in the remaining part of this work) we have restricted the analysis to one Floquet sector neglecting couplings between the blocks. One may include this influence in a perturbative sense including higher order corrections in $1/\omega$. These higher order terms may play an important role in the model. E.g. they have been employed for the simulation of the next nearest neighbor hopping in the Haldane model[145].

Following the presentation of [145–148] we can express the effective Hamiltonian as a series in $1/\omega$

$$\hat{\mathcal{H}}_{eff} = \hat{\mathcal{H}}_{eff}^{(0)} + \hat{\mathcal{H}}_{eff}^{(1)} + \mathcal{O}\left(\frac{1}{\omega^2}\right) \tag{2.55}$$

The terms of the average effective Hamiltonian employing Magnus expansion[149] may be written as

$$\hat{\mathcal{H}}_{eff}^{(0)} = \frac{1}{T} \int_0^T dt_1 \hat{\mathcal{H}}(t_1) \tag{2.56}$$

$$\hat{\mathcal{H}}_{eff}^{(1)} = \frac{-i}{2T} \int_0^T dt_2 \int_0^{t_2} dt_1 [\hat{\mathcal{H}}(t_2), \hat{\mathcal{H}}(t_1)] \tag{2.57}$$

Expressing the time dependent Hamiltonian as a Fourier series

$$\hat{\mathcal{H}}(t) = \hat{\mathcal{H}}_0 + \sum V^{(k)} e^{ik\omega t} \tag{2.58}$$
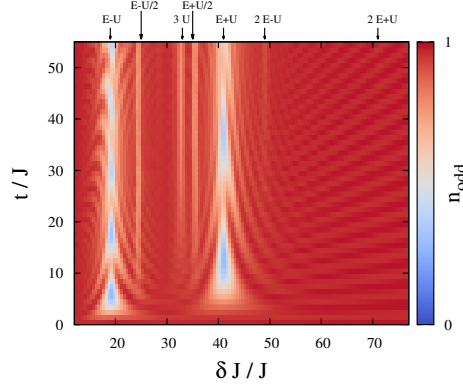
Fig. 2.10: Resonances in a tilted optical lattice with a weak lattice depth modulation ($\delta J = 0.8J$, $U = 11$, $\mu = 30J$ $L = 6$ unit filling) as demonstrated in Ref. [144].

one yields

$$\hat{\mathcal{H}}_{eff}^{(0)} = \hat{\mathcal{H}}_0 \tag{2.59}$$

$$\hat{\mathcal{H}}_{eff}^{(1)} = \frac{1}{\omega} \sum_k \frac{1}{k} \left([V^k, V^{-k}] - [V^k, \hat{\mathcal{H}}_0] + [V^{-k}, \hat{\mathcal{H}}_0] \right) \tag{2.60}$$

Convergence of this expansion may be given far away from low lying resonances. An alternative derivation of effective higher order Hamiltonians is presented in Ref. [146] where the initial phases are treated separately.

   We illustrate the influence of these corrections for the case of lattice depths modulation. For a sinusoidal modulation obviously $V^{(1)} = i/2 e^{i\phi} \hat{\mathcal{H}}_{tun}$ and $V^{(-1)} = -i/2 e^{-i\phi} \hat{\mathcal{H}}_{tun}$ and

$$\hat{\mathcal{H}}_{eff}^{(1)} = \frac{iU\delta J}{\omega} \cos \phi \sum_i b_i^\dagger b_{i+1} - n_i b_i^\dagger b_{i+1} + H.c. \tag{2.61}$$

In Fig. 2.9 we show the time evolution of the occupation with odd numbers of particles per site n_{odd}, as can be studied in lattice microscopes for a system initially prepared in a MI state. At time $t = 0$ the lattice depth modulation is immediately turned on and we compare the results obtained by the full time dependent Hamiltonian (2.53) and the effective model (2.60). Note that this setting implies that the zeroth order effective model would not show any time dependence. Interestingly the effective model depends strongly on the initial phase of the modulation. For a cosine-modulation the first order corrections vanish as shown in Fig. 2.9.

2.5.5   Resonances

In the presence of resonances the Magnus expansion (2.60) breaks down. The effective Hamiltonian may be described by the off-diagonal blocks of Floquet-Hamiltonian. A typical scenario is to exploit such resonance conditions to restore a coherent tunneling behavior in initially tilted lattices. As described e.g. in [150] due to static tilt $\Delta \sum_j j n_j$ the tunneling is strongly suppressed. For the specific choice of a lattice shaking with $\hbar\omega = \Delta$ it may be restored due to the off-diagonal couplings of different Floquet sectors (corresponding to a rotating wave approximation). The effective tunneling is given by

$$J \to J \mathcal{J}_1 \left(\frac{K}{\hbar\omega} \right) \tag{2.62}$$

and the tilt is eliminated due to absorption of emission of photons $\hbar\omega$. We will employ this idea extensively for the generation of synthetic gauge fields in the chapters 10 and 8.

A detailed numerical study of effective and resonant behavior for the case of lattice shaking has been performed in [151] where (multi)photon resonances to particle hole excitations have been identified. In Ref. [144] different resonances are mapped out by the observation of the doublon-occupation in the presence of an additional strong tilt. In Fig. 2.10 we simulate such an scenario using the full time evolution of Eq. (2.53) for a small system. One may clearly observe several resonances in the number of produced doublons.

Chapter 3

Numerical Principles

Main aspects of this work to a large extent rely on numerical simulations. For the study of ground-state physics we will employ exact diagonalization (ED) and density matrix renormalization group (DMRG) techniques in 1D or ladder-like systems with open and periodic boundary conditions. In some cases dynamical properties and quench simulations will be performed using both exact digitalization and the time evolving block decimation (TEBD or tDMRG) algorithm. DMRG and TEBD methods can be readily applied to the simulation of systems in the thermodynamic limit (iDMRG/iTEBD). Connections to two dimensional systems will be made by means of cluster mean field (CMF) techniques.

3.1 Exact diagonalization

One of the main numerical tasks in this work reduces to the solution of the time-independent Schrödinger-equation, i.e. the eigenvalue problem $\hat{\mathcal{H}} |\Psi\rangle = E |\Psi\rangle$. Sufficiently small systems may be diagonalized exactly.

For cases in which we may write down the complete matrix-representation of $\hat{\mathcal{H}}$ in a given basis it is possible to calculate the full energy spectrum with different numerical techniques such as the QR-method [152]. For such full diagonalization problems various highly optimized program libraries such as LAPACK [153] exist. The computational complexity for the full diagonalization of a large $D \times D$ matrix scales typically as $\propto D^3$. However, the fundamental problem of computational many particle quantum physics lies in the exponential growth of Hilbert-space D dimension with the system size L. In Tab. 3.1 we illustrate this property for the simple example of a spin-1/2 system. Without further reductions of Hilbert space dimensions due to symmetries (see below), a full diagonalization of a spin-1/2 system with more than $L = 14$ sites becomes very demanding on modern desktop-computers.

Since we are mainly interested in low energy properties of the ultracold quantum gases, the knowledge of the lowest eigenstate and its first excitations is often sufficient. Iterative methods offer a computationally cheaper way for the approximation of certain parts of the spectrum. In particular Lanczos- or Arnoldi-methods allow for the calculation of eigenstates with the largest or lowest eigenenergy. The underlying principle of the Lanczos-algorithm is the generation of a set of orthonormal basis vectors, similar to a Gram-Schmidt-method, of the Krylov-space belonging to $\hat{\mathcal{H}}$ [154], i.e. the vector-space build from

$$\{v, \hat{\mathcal{H}}v, \hat{\mathcal{H}}^2 v, ...\} ,$$

where v is an (arbitrary) initial state. In this basis $\hat{\mathcal{H}}$ acquires a tridiagonal form $\tilde{\mathcal{H}}$. If we stop this process after few iterations $\#_{it} \ll D$ the eigenvalues of $\tilde{\mathcal{H}}$ ap-

proximate the largest amplitude eigenvalues of $\hat{\mathcal{H}}$ with high precision. The rest of the spectrum is approached with less accuracy, one difficulty being that the multiplicity of eigenvalues is typically not correct. It turns out to be favorable in many cases not to keep the (typically sparse) matrix $\mathcal{H}$ in memory but to evaluate matrix-elements just in time when the matrix-vector multiplication is performed. For such an iterative diagonalization procedure it is sufficient to keep three vectors of full Hilbert-space dimension in computer memory.

Exact-diagonalization techniques can readily be applied to simulate dynamical problems or thermodynamic properties. For a time-independent Hamiltonian we obtain the time evolution operator $\mathcal{U} = \mathrm{e}^{i\hat{\mathcal{H}}t/\hbar}$ solving the Schrödinger-equation $i\hbar|\Psi(t)\rangle = \hat{\mathcal{H}}|\Psi(t)\rangle$, which is given in its diagonal matrix form after a full diagonalization. For an iterative Lanczos process a good approximation is given by $\mathcal{U} \approx \mathrm{e}^{i\tilde{\mathcal{H}}t/\hbar}$ using the initial state of the Lanczos sequence $v = \Psi(0)$. Time-dependent situations can be solved by an approximate integration scheme, such as Crank-Nicholson or Runge-Kutta methods [152].

3.1.1   Symmetries

As illustrated in Tab. 3.1 further symmetries of the underlying Hamiltonian should be exploited to substantially reduce the amount of memory and CPU-time needed for the simulation. With the use of symmetries the Hilbert-space can be restricted to a smaller subspace corresponding to a given (set of) quantum-numbers and the Hamiltonian will acquire a block-diagonal form. Central and possibly involved part of an exact diagonalization algorithm is, hence, the construction of the appropriate set of symmetric basis vectors [154]

Apart form a reduction of computational complexity calculating excited states corresponding to certain quantum-numbers has been exploited as tool for the precise location of phase transitions and properties [155]. This so called level spectroscopy is based on the observation that a quantum phase transition often can be related to a fundamental change in symmetry of ground and excited states. Using exact diagonalization methods we may precisely locate crossing points for several finite system sizes (see chapter 5) and try to extrapolate to the thermodynamic limit.

The (Bose-)Hubbard or spin-chain models discussed in this work typically conserve the total number of particles

$$N = \sum_i n_i \tag{3.1}$$

L	$D = 2^L$	double-vector	$D_{N=L/2} = \binom{L}{N}$	$D_{N=L/2,k=0}$
4	16	128 B	6	2
8	256	2 kB	70	10
16	65 536	512 kB	12 870	810
24	16 777 216	128 MB	2 704 156	112 720
30	1 073 741 824	8 GB	155 117 520	5 170 604

Table 3.1: Full Hilbert-space dimension d and amount of memory needed for the storage of one vector of type "double" for spin-1/2 chains of different length L. $D_{N=L/2}$ and $D_{N=L/2,k=0}$ denote the dimensions of blocks with conserved particle number $N = L/2$, and conserved linear momentum $k = 0$, resp.

or the total magnetization S^z and for periodic boundary conditions a quasi momentum, corresponding to the translational invariance

$$T : b_i^{(\dagger)} \rightarrow b_{i+l}^{(\dagger)} \tag{3.2}$$

with l being the periodicity of the unit-cell. In most cases a spacial inversion symmetry is given

$$I : b_i^{(\dagger)} \rightarrow b_{L-i}^{(\dagger)}, \tag{3.3}$$

which allows to group the eigenstate into symmetric and antisymmetric states with respect to I. Another example of a discrete symmetry group which is important for fermionic Hubbard models is the particle hole transformation

$$Q : c_{i,\sigma}^{\dagger} \rightarrow (-1)^i c_{i,\bar{\sigma}}, \quad c_{i,\sigma} \rightarrow (-1)^i c_{i,\bar{\sigma}}^{\dagger}. \tag{3.4}$$

Many spin or spinor-gas models exhibit higher symmetries and $\hat{\mathcal{H}}$ is invariant under rotational $SU(2)$ or $SU(N)$ operations. Computationally the representation of the Hamiltonian in such non-abelian symmetric forms becomes very involved but allows for the simulation of large and complex systems (e.g. [156]).

3.2   Matrix product states

Even though utilizing symmetries and employing iterative methods the computational complexity still scales exponentially with the system size which defines fundamental limits of these approaches. A way out of this dependence of exploding Hilbert-space dimensions is based on the variational principle. A good approximation of the ground state $|\Psi_0\rangle$ may be found by minimization of the energy over an appropriate choice of a variational manifold,

$$E_0 = \frac{\langle \Psi_0 | H | \Psi_0 \rangle}{\langle \Psi_0 | \Psi_0 \rangle} \leq \frac{\langle \Psi | H | \Psi \rangle}{\langle \Psi | \Psi \rangle} \quad \forall \, \Psi \in \mathcal{H}. \tag{3.5}$$

The variational principle has turned out to be very powerful in the description of various problems ranging from quantum chemistry [157] to fractional quantum Hall physics [158].

A trivial class of ansatz-states for a variational manifold of a lattice problem are product states. E.g. for a Hilbert-space of local dimension d per lattice site a general product state is given by

$$|P\rangle = \sum_{\sigma_1 \ldots \sigma_L} c^{[1]\sigma_1} \cdot c^{[2]\sigma_2} \cdot \ldots \cdot c^{[L]\sigma_L} |\sigma_1 \ldots \sigma_L\rangle = |\alpha_1\rangle |\alpha_2\rangle \ldots |\alpha_L\rangle \tag{3.6}$$

Here we need d complex numbers $c^{[i]\sigma_i} \in \mathbb{C}$ for each site, where $|\alpha_i\rangle = \sum_{\sigma_i} c_{\sigma_i}^i |\sigma_1\rangle$ where we should employ a normalization condition $\sum_{\sigma_i} |c^{[i]\sigma_i}|^2 = 1$. Obviously we just need $L \cdot d \ll d^L$ coefficients to describe this manifold completely. This simple variational class also known as Gutzwiller mean-field approach has been applied to describe the Bose-Hubbard model [7, 159]. Since these states are not entangled in particular their capability for the description of one-dimensional systems is questionable.

A much more general class of ansatz-functions is obtained by choosing the co-efficients $c^{[i]\sigma_i}$ to be matrices instead of complex numbers.

$$|MPS\rangle = \sum_{\sigma_1...\sigma_L} C^{[1]\sigma_1} C^{[2]\sigma_2}...C^{[L]\sigma_L} |\sigma_1...\sigma_L\rangle \ . \tag{3.7}$$

Here $C^{[1]\sigma_1}$ and $C[L]\sigma_L$ are column- or row-vectors resp. such that the total matrix-product is a (complex) number. DMRG and related methods rely on these so called matrix product states (MPS) which have been developed to an important tool of theoretical physics and led to important progress in the fields of quantum information theory and strongly correlated matter during the past decades [23].

Indeed, MPS are the most general variational class on a lattice system with finite local Hilbert-space dimension d [160]. Choosing the matrix-dimension M to be large enough we may recast any arbitrary state

$$|\Psi\rangle = \sum_{\sigma_1...\sigma_L} c_{\sigma_1...\sigma_N} |\sigma_1...\sigma_L\rangle \ .$$

in from of an MPS. Following Ref. [23] we interpret the coefficients as a matrix $c_{\sigma_1,(\sigma_2...\sigma_L)} = c_{\sigma_1...\sigma_N}$ which may be decomposed by a singular value decomposition (SVD)

$$c_{\sigma_1,(\sigma_2...\sigma_L)} = (USV^\dagger)_{\sigma_1,(\sigma_2...\sigma_N)} = \sum_\alpha U_{\sigma_1,\alpha} S_{\alpha,\alpha} V^\dagger_{\alpha,(\sigma_2...\sigma_N)} \ . \tag{3.8}$$

Here U and V are orthogonal matrices of dimensions $(d \times d)$ and $(d^{N-1} \times d^{N-1})$. S is diagonal (but not quadratic) and contains the so called singular values that can be chosen to be real and positive. The SVD of the coefficient matrix corresponds to a Schmidt-decomposition of the state in a left and right part with

$$|\Psi\rangle = \sum_\alpha S_\alpha |\Phi^L_\alpha\rangle \otimes |\Phi^R_\alpha\rangle \ , \tag{3.9}$$

with $|\Phi^L_\alpha\rangle \in U$ and $|\Phi^R_\alpha\rangle \in V^\dagger$. Renaming the column vectors of U as $\Gamma^{[1]\sigma_i}$ and expressing the product V as new coefficients $c_{a_1,\sigma_2...\sigma_L}$ we obtain

$$|\Psi\rangle = \sum_{\substack{\sigma_1,(\sigma_2...\sigma_L), \\ a_1}} \Gamma^{\sigma_1}_{a_1} S^{[1]}_{a_1} c_{a_1,\sigma_2...\sigma_L} |\sigma_1...\sigma_L\rangle \ . \tag{3.10}$$

We may now continue with this process by decomposing the new coefficient matrix $c_{(a_1,\sigma_2),(\sigma...\sigma_L)}$. Finally we yield a MPS-form of $|\Psi\rangle$

$$|\Psi\rangle = \sum_{\substack{\sigma_1,\sigma_2...\sigma_L, \\ a_1,a_2,...a_L}} \Gamma^{[1]\sigma_1}_{a_1} S^{[1]}_{a_1} \Gamma^{[1]\sigma_2}_{a_1,a_2} S^{[2]}_{a_2}...S^{[L-1]}_{a_L} \Gamma^{[L]\sigma_L}_{a_L} |\sigma_1...\sigma_L\rangle \tag{3.11}$$

Obviously this representation is exact and generally the matrix dimension M would show the same exponential scaling as the Hilbert-space dimension. If we restrict the matrix dimension M to a finite number $M \ll D$ we still have a very accurate approximation $|\tilde\Psi\rangle$ of $|\Psi\rangle$ if we keep the Schmidt-vectors $|\Phi^L_\alpha\rangle$ corresponding to the largest M singular values S_α. In fact, as shown in [23], this procedure minimizes the functional

$$\big\||\Psi\rangle - |\tilde\Psi\rangle\big\|^2 = \left\|\sum_{a,b}(\Psi_{a,b} - \tilde\Psi_{a,b}) |\Psi^a_L\rangle |\Psi^b_R\rangle\right\|^2 = \mathrm{Tr}\left((\Psi - \tilde\Psi)^\dagger(\Psi - \tilde\Psi)\right) \ , \tag{3.12}$$

where $\breve{\Psi}_{a,b}$ should a matrix of rank M. Generally such a truncated SVD can be shown [152] that be the best approximation of a matrix A with a matrix A_M of rank M with respect to the spectral norm $\|A - A_M\| = \inf_{\substack{B \in \mathbb{R}^{m \times n}, \\ \text{rank}(B) = M}} \|A - B\|$. For weakly entangled states, in particular describing one dimensional gapped quantum systems, this procedure is highly efficient (see chapter 4). Here it can be shown [160]) that the Schmidt-values decay exponentially with their spectral position α,

$$\lambda_\alpha \propto e^{-\chi \alpha} \, , \chi > 0 \, . \tag{3.13}$$

Different to a simple product-state an MPS may obviously be entangled and correlated. Overlaps or expectation values of two MPS may be efficiently evaluated by contracting iteratively the tensors from the boundary [23]

$$\langle \bar{\Psi} | \Psi \rangle = \sum_{\sigma_L} \bar{C}^{[L]\sigma_L \dagger} \left(\cdots \left(\sum_{\sigma_2} \bar{C}^{[2]\sigma_2 \dagger} \left(\sum_{\sigma_1} \bar{C}^{[1]\sigma_1 \dagger} C^{[1]\sigma_1} \right) C^{[2]\sigma_2} \right) \cdots \right) C^{[L]\sigma_L} \, , \tag{3.14}$$

In DMRG we will typically use a sightly different MPS representation, the mixed canonical form

$$|\Psi\rangle = \sum_{\sigma_1 \ldots \sigma_N} A^{[1]\sigma_1} \ldots A^{[l]\sigma_l} C_l \, B^{[l+1]\sigma_{l+1}} \ldots B^{[N]\sigma_N} |\sigma_1 \ldots \sigma_N\rangle \, . \tag{3.15}$$

The matrices fulfill a normalization condition

$$\sum_{\sigma_i} A^{[i]\sigma_i \dagger} A^{[i]\sigma_i} = \mathbb{1} \, , \quad \sum_{\sigma_i} B^{[i]\sigma_i} B^{[i]\sigma_i \dagger} = \mathbb{1} \, , \quad \text{and } \text{Tr}\left(C^\dagger C \right) = 1 \, . \tag{3.16}$$

During the last years there has been intense activity generalizing MPS to higher dimensional systems [161], operator-products[162, 163], continuum systems[164] and many more [23]. Apart from providing a very general variational class of quantum states that may be used for the approximation of a given state by a product of local matrices, for certain models MPS may describe an analytical ground-state solution. While this can be generalized very much in detail [165], in the following we will just present two simple very common examples.

3.2.1 AKLT

Ian Affleck, Tom Kennedy, Elliott Lieb und Hal Tasaki [166] describe the construction of an analytical ground state to the bilinear-biquadratic spin-1 Hamiltonian

$$H_{AKLT} = J \sum_n \mathbf{S}_n \mathbf{S}_{n+1} - \frac{1}{3} (\mathbf{S}_n \mathbf{S}_{n+1})^2 \, , \tag{3.17}$$

expressed by an MPS (or valence-bond-state) of matrix dimension $M = 2$. The AKLT state is given by

$$C^+ = \frac{1}{2}\sigma_+ \, , \ C^0 = \frac{1}{2}\sigma_- \, , \ C^- = \frac{1}{2}\sigma_z \, , \tag{3.18}$$
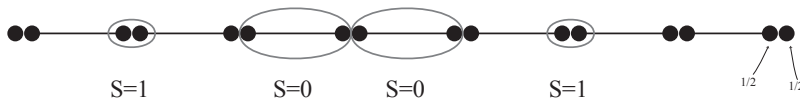

Fig. 3.1: Scheme of AKLT-state.

where $\sigma_\pm$ and σ_z denote the spin-1/2 Pauli-matrices. This state is a paradigm of the ground states of the Haldane-phase. The spectrum of model (3.17) is gapped and the AKLT state exhibits a finite string-order (2.38), that corresponds to a hidden diluted antiferromagnetic order. Indeed one may easily see that the AKLT state just contains non-zero contribution of states like $|\ldots 00 + 00 - 0 + -000 + \ldots\rangle$ in which the states $|+\rangle$ are followed directly by $|-\rangle$ with an intermediate string of an arbitrary number of $|0\rangle$.

In its original interpretation Eq.(3.18) may be understood as follows. Each spin-1 is expressed in form of two symmetrized internal spin-1/2 states (see Fig. 3.1). Due to the antiferromagnetic interaction the spin-1/2 states on neighboring sites prefer to form a singlet state $|\uparrow_1\downarrow_2\rangle - |\downarrow_1\uparrow_2\rangle$. Hamiltonian (3.17) can be written in terms of local projectors to the subspace of total spin $J_i = S_i + S_{i+1} = 2$. Since always two internal spins form a singlet the total spin cannot be 2 and, hence, the AKLT state is ground state of (3.17) with energy $\frac{2JL}{3}$. Interestingly, in this construction the two boundary spin-1/2 remain ungrouped in an open boundary system and lead to a 4-fold degeneracy of the AKLT state. With periodic boundaries all spin-1/2 are grouped and the degeneracy is lifted which illustrates the topological character of the Haldane phase.

3.2.2 Majumdar-Gosh

A very early example of an exact MPS ground-state is the Majumdar-Gosh-state [167] given by

$$C^\uparrow = \begin{pmatrix} 0 & 1 & 0 \\ 0 & 0 & -1 \\ 0 & 0 & 0 \end{pmatrix}, \quad C^\downarrow = \begin{pmatrix} 0 & 0 & 0 \\ 1 & 0 & 0 \\ 0 & 1 & 0 \end{pmatrix} \qquad (3.19)$$

which is ground state of the isotropic spin-1/2 chain with next-nearest neighbor coupling

$$\hat{\mathcal{H}}_{MG} = \sum_i \mathbf{S}_i \mathbf{S}_{i+1} + \frac{1}{2} \mathbf{S}_i \mathbf{S}_{i+2} \ . \qquad (3.20)$$

This state belongs to a gapped dimerized phase build from paired singlets between neighboring sites $|\ldots(\uparrow\downarrow - \downarrow\uparrow)_{i,i+1}(\uparrow\downarrow - \downarrow\uparrow)_{i+2,i+3}\ldots\rangle$.

3.3 DMRG

DMRG in its basic idea is an algorithm for the variational approximation of a quantum (ground-)state by an MPS via the relaxation of the problem to local optimizations. It was invented in 1992 by Steve White [168] as an improvement of the numerical renormalization group. Later it was interpreted as a variational approach for MPS [169] and afterwards it has received important contributions and improvements from the quantum information theory. Today, DMRG has established itself as a quasi-standard for the analysis of low-dimensional systems allowing for the calculation of results with in principle numerical precision.

Through the years DMRG has provided important insight in an enormous class of one-dimensional systems, e.g. spin-chains [170], bosons and fermion Hubbard models, spinor gases [50] and quasi-1D systems e.g. square [42] and triangular ladders [38] with two or more legs [171]. DMRG provides in a natural way information on entanglement properties which have been shown to offer important
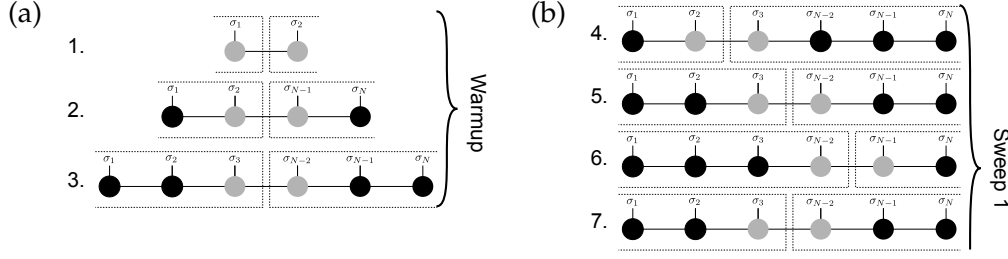
Fig. 3.2: Scheme of the 2-site DMRG algorithm. (a) iDMRG or warmup process. (b) Sweeping through the finite lattice back and forth iteratively the variational ground-state solution is improved.

insight in the properties of a given quantum states and phases [172–174] and will be discussed in chapter 4.

Although with MPS we have an excellent variational class at hand, the minimization of the energy functional (3.5) with respect to the entries of the tensors $C^{[i]\sigma_i}_{a_{i-1},a_i}$ generally results in a high dimensional non-linear problem. The DMRG algorithm searches a solution to this problem by a minimization of the tensors in one or two local sites. For the so called two-site DMRG algorithm we rewrite the Hamiltonian as

$$H = \sum_k H^k_L \otimes H^k_{i,j} \otimes H^k_R \, , \tag{3.21}$$

separated into a left, right and so called system part. Now we can express the local minimization as an eigenvalue problem

$$\tilde{H}^{a'\sigma_i'\sigma_j'b'}_{a\sigma_i\sigma_jb} X_{a\sigma_i\sigma_jb} = E X_{a'\sigma_i'\sigma_j'b'} \tag{3.22}$$

Here the operator $\tilde{H}$

$$\tilde{H}^{a'\sigma_i'\sigma_j'b'}_{a\sigma_i\sigma_jb} = \sum_k \left(\tilde{H}^k_R \right)^{a'}_a \left(\tilde{H}^k_L \right)^{b'}_b \left(H^k_{i,j} \right)^{\sigma_1',\sigma_2'}_{\sigma_1,\sigma_2} \tag{3.23}$$

contains the left and right contractions of the MPS $\tilde{H}_R$ and $\tilde{H}_L$ (which may be obtained from the previous step) and $X_{a'\sigma_i'\sigma_j'b'}$ denotes the local wavefunction. The eigenvalue problem is typically solved using a Lanczos algorithm and may be drastically sped up taking into account an initial guess from previous iterations [175]. As described above we may now use a truncated SVD procedure on $X_{a\sigma_i\sigma_jb}$ to recover an updated MPS representation of this state.

Fig. 3.2 (a) illustrates the first part of a traditional finite system size DMRG procedure that iteratively builds up a mixed canonical MPS representation for an increasing system size. This infinite DRMG (iDMRG) procedure may be employed to approximate bulk-properties of an infinite chain [176]. Alternatively we may start from a randomly chosen initial state. After this initialization we iteratively sweep through the system as illustrated in Fig. 3.2 (b) to obtain a very accurate MPS description of the finite system.

The errors of a DMRG calculation stem from mainly three sources[176]: the iterative numerical diagonalization, a lack of convergence within the class of MPS states and, most importantly, the restriction to a finite matrix dimension M. This,

so called truncation error depends on the weight of the discarded singular values
during the DMRG procedure

$$p = \sum_{\alpha=M+1}^{D} S_\alpha^2 = 1 - \sum_{\alpha=1}^{M} S_\alpha^2 \,. \tag{3.24}$$

It can be shown [176]), that the error of the ground-state energy is proportional to
p.

Although being known to be best implemented in one-dimensional open bound-
ary systems DMRG has been extended to systems with periodic boundaries[177]
and infinite systems for calculations in the thermodynamic limit[175, 178]. In two
dimensional lattices DMRG-calculations being performed along a one dimensional
path covering the lattice introduce fictitious long range interactions and become
extremely costly. However, recently DMRG has been providing important insight
into two dimensional frustrated models where QMC-simulations suffer from the
"negative-sign problem" for example deciding the longstanding question of the
spin-liquid ground state of the Heisenberg antiferromagnet in Kagome lattices by
simulation of large-scale cylinders[179, 180].

As for exact-diagonalization procedures, in DMRG the use of appropriate sym-
metries plays an important role. In the DMRG calculations performed in this work
we will typically restrict to additive abelian quantum numbers [176], as well as
parity and inversion symmetries [181]. During the recent years DMRG has been
extended to SU(2)-symmetries [182, 183] and the possibility to obtain momentum
eigenstates [184] has been shown.

3.4   Time dependent simulations

Within the MPS-framework the simulation of dynamics may be treated in vari-
ous ways. As long as dynamics is restricted to Hamiltonians with a local sup-
port the adaptive time-evolution methods like the time evolving block decima-
tion (TEBD) [160, 185] algorithm, or the adaptive t-DMRG [186] method, allow for
the simulation of real and imaginary time evolutions by application of a Suzuki-
Trotter-decomposed time-evolution operator to a given MPS.

Following the breakthrough work by Vidal [160, 185] an efficient time-evolution
of an MPS may be implemented for Hamiltonians which may be decomposed
to operators acting only locally on neighboring sites (or single sites). Hence the
Hamiltonian may be recast as

$$\hat{\mathcal{H}} = \sum_i \hat{\mathcal{H}}_{2i,2i+1} + \hat{\mathcal{H}}_{2i+1,2i+2} = \hat{\mathcal{H}}_{even} + \hat{\mathcal{H}}_{odd} \tag{3.25}$$

Using a Suzuki-Trotter decomposition of the time-evolution operator $U_{\hat{\mathcal{H}}}(t) = e^{-i\hat{\mathcal{H}}t}$
we may write a time propagation for a short time step δ as

$$|\Psi(t+\delta)\rangle = U_{\hat{\mathcal{H}}_{even}}(\delta) U_{\hat{\mathcal{H}}_{odd}}(\delta) |\Psi(t)\rangle \,, \tag{3.26}$$

or using a second order decomposition

$$|\Psi(t+\delta)\rangle = U_{\hat{\mathcal{H}}_{even}}(\delta/2) U_{\hat{\mathcal{H}}_{odd}}(\delta) U_{\hat{\mathcal{H}}_{even}}(\delta/2) |\Psi(t)\rangle \,. \tag{3.27}$$
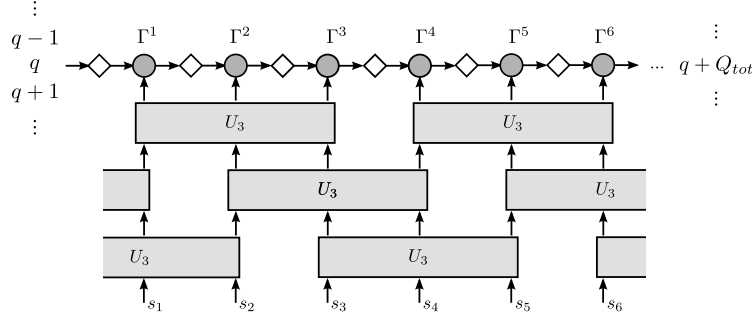
Fig. 3.3: Scheme of the iTBED algorithm for a time-evolution decomposed in 3 site operators. The MPS is represented by circles (for the tensors $\Gamma^{[i],\sigma_i}_{a_{i-1},a_i}$) and diamonds (representing $S^{[i]}_{a_{i-1},a_i}$). Obviously here the (first order) Trotter decomposition has to be applied consecutively in three steps such that all bonds are covered. The arrows indicate the ordering of the (set of) additive quantum numbers. For an iTEBD variant at the edge of an unit cell a shift Q_{tot} has to be introduced.

Since even and odd terms commute the two-site time-evolution operators $U_{\hat{\mathcal{H}}_{i,i+1}}(\delta) = e^{-i\hat{\mathcal{H}}_{i,i+1}t}$ may be applied independent from each other, which allows for a parallelization of the program-code. After the application of one two-site operator we have to restore an MPS representation which is possible using a single SVD as described above (3.10). In practice again the finite matrix dimension M is (compared to the error resulting from the Trotter-decomposition) the main source of errors. The accessible timescale, hence, strongly depends on the amount of entanglement created during the evolution which the variational class has to be able to capture: Thus in this framework sudden quench simulations are typically restricted to small timescales while e.g. slow quasi-adiabatic preparations may be studied for very long times [47]. It is straight forward to apply the TEBD algorithm to more than two site operators allowing for example for the simulation of next-nearest neighbor coupling Hamiltonians [187]. This situation is sketched in Fig. 3.3.

TEBD offers a simple alternative for the calculation of ground states by application of an imaginary time evolution to an arbitrary initial state $|\Psi_0\rangle$

$$|\Psi_{gr}\rangle = \lim_{\tau \to \infty} \frac{e^{-\hat{\mathcal{H}}\tau} |\Psi_0\rangle}{\| e^{-\hat{\mathcal{H}}\tau} |\Psi_0\rangle \|} . \tag{3.28}$$

Ref. [178] introduces an extension of this algorithm to an infinite system with the MPS representing a finite size unit-cell of the system which in this approach should be at least two sites. This technique allows for the calculation of ground-state properties, similar to iDMRG, and time evolutions directly in the thermodynamic limit.

As for the DMRG algorithm we allow for conserved additive quantum numbers in the iTEBD algorithm. As sketched in Fig. 3.3 the quantum numbers q are defined as average per unit-cell, such as Q_{tot}-particles per l sites. The arrows in Fig. 3.3 indicate the monotonic growth of q. As described in [175] we have to introduce at the last site of a unit-cell a shift relating $q + Q_{tot} \to q$.
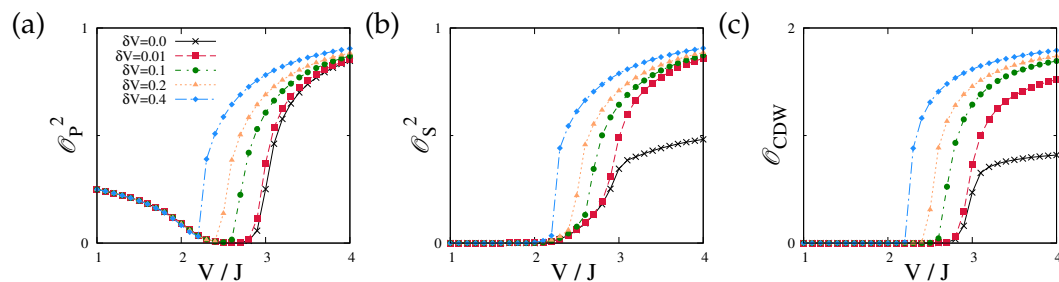
Fig. 3.4: (a) Parity-, (b) string- and (c) CDW order parameters of the extended Bose-Hubbard model the presence a weakly coupled 2D environment ($U = 4$, $L = 80$) for an attractive inter chain coupling δV.

3.4.1   Mixed states

These before mentioned algorithms are generally designed for pure quantum states. However, mixed states may be treated by the so called purification trick [162, 188]: Any mixed quantum state, a density matrix describing an e.g. equilibrium finite temperature system, may be expressed by a pure state in a - by an auxillary system - enlarged Hilbert space. Taking the partial trace over the auxiliary, which may be a copy of the original system, one recovers the original density matrix. The real or imaginary time evolution algorithms for pure states may now be employed: Starting from an infinite temperature state, where the purification is known to be a maximally entangled state of original and auxiliary system, an imaginary time evolution applied to this initial MPS allows for the preparation and study of systems at lower temperatures[189]. Subsequent real time evolutions may be applied to simulate finite temperature dynamical properties, which has been successfully used in 1D and ladder spin systems [190, 191].

3.5   Cluster mean field

In order to study cross dimensional effects and the extension to two and higher dimensional lattice systems beyond the exact study of multiple leg ladder systems one may employ CMF techniques [192]. These approximate methods offer a simple and inexpensive treatment of strongly correlated lattice systems in two or higher dimensions.

The CMF idea describing degrees of freedom by a mean field treatment of an effective cluster of a certain size goes beyond a standard mean field approach including effects of local correlations. Implementing the algorithm we decompose the model Hamiltonian $\hat{\mathcal{H}}$ to clusters of connected sites $\mathcal{C}$ parqueting the (possibly infinite) lattice, with the effective Hamiltonian of a cluster being described by

$$\hat{\mathcal{H}}_{\mathcal{C}} = \hat{\mathcal{H}}_{exact} + \hat{\mathcal{H}}_{mf} \; . \tag{3.29}$$

Here, $\hat{\mathcal{H}}_{exact}$ is the exact Hamiltonian of the cluster and $\hat{\mathcal{H}}_{mf}$ describes the mean-field decoupled terms connecting the cluster to its neighbors. We iteratively calculate the ground state of $\hat{\mathcal{H}}_{\mathcal{C}}$ using e.g. exact diagonalization techniques in order to obain a self consistent solution for the system.

Among many others CMF has been successfully applied to frustrated spin [193] and boson systems [194], Fermions [195] or square lattices with (possibly density dependent) magnetic fields [49]. CMF may be combined with the DMRG

method [196] as a solver, which allows for the treatment of very large clusters. In particular this opens the - for current optical lattice experiments important - possibility of simulating arrays of weakly coupled low dimensional systems, which themselves may be treated in an numerical exact way.

3.5.1 Weakly coupled 1D chains

As an example we study the effect of inter chain coupling in an array of one dimensional chains of dipolar (see chapter 2) particles extending the study of Ref. [99] in which the analysis was restricted to two leg-ladders and bosonization. For the CMF method in combination with DMRG it is favorable to neglect a tunneling coupling between the chains. We assume the dipoles to be oriented in such a way that an attractive inter-chain interaction and a repulsive in-chain interaction is realized. The total Hamiltonian is given by

$$\hat{\mathcal{H}} = \hat{\mathcal{H}}_{chain} + \hat{\mathcal{H}}_{interchain} \tag{3.30}$$

with

$$\hat{\mathcal{H}}_{chain} = \sum_{i,j} a_{i,j}^\dagger a_{i+1,j} + H.c. + \frac{U}{2} n_{i,j}(n_{i,j} - 1) + V n_{i,j} n_{i+1,j} \tag{3.31}$$

$$\hat{\mathcal{H}}_{interchain} = \sum_{i,j} -\delta V n_{i,j} n_{i,j+1} \tag{3.32}$$

In order to perform the CMF technique we decompose the inter chain Hamiltonian as Eq. (3.29)

$$\hat{\mathcal{H}}_{mf} \approx \sum_i -\delta V n_i \langle n_i \rangle \tag{3.33}$$

introducing L mean fields $\{\langle n_i \rangle\}$.

As shown in Ref. [99] the marginal inter chain coupling does not immediately destroy the HI phase. Up to a coupling of $\delta V \approx 0.3$ we observe a region of vanishing parity but non-vanishing string-order as shown in Fig. 3.4. For a stronger inter chain coupling the HI-phase vanishes and a direct apparently first order transition between the MI and CDW phase is found. The effect of repulsive inter-chain interactions is expected to be similar. Further studies have to clarify the robustness of this approach concerning the increase of cluster size (e.g. the simulation on an array of ladders) and map out the complete phase diagram.

Chapter 4

Measurables from Quantum Information Theory

During the recent years important advances in the physics of strongly correlated systems have been obtained by insights originating from quantum information theory. In particular the understanding of quantum entanglement which is the fundamental property of any quantum mechanical system, led to important developments and new algorithms, such as MPS- or PEPS-techniques, suitable for the simulation and understanding of interacting many body systems.

Here, we will concentrate on some quantities relevant for this work: the entanglement entropy and entanglement spectrum as well as the ground-state fidelity-susceptibility. Other ideas which are subject to active research include multi-partite entanglement measures, (pair) concurrence [197], or experimentally relevant aspects such as the quantum Fisher information [198].

4.1 Entanglement spectrum

If we consider a quantum state ρ on subregion A of a quantum (lattice) system the reduced state obtained by tracing out the other sites B of the system

$$\rho_A = \mathrm{Tr}_B \rho \tag{4.1}$$

is in general not a pure state even if this was the case for ρ. The spectrum of eigenvalues $S_i^2(l)$ of the reduced density matrix ρ_A has hence in general more that one non-vanishing value.

It is possible to obtain the eigenvalues $S_\alpha(l)$ by means of the so called Schmidt decomposition as described in Eq. (3.9). For a product state all Schmidt-values except for one vanish. In all other cases the state is defined to be entangled. It is one of the most remarkable properties of quantum mechanics that even a pure quantum state exhibits a non-vanishing entanglement entropy, while in classical systems a finite entropy characterizes the lack of knowledge about the state [199].

The so called entanglement spectrum $S_\alpha(l)$ - has been shown to offer a sensitive probe for quantum phases and quantum phase transitions [173, 174, 200–202]. We compute in particular the gap in the entanglement spectrum,

$$\Delta_{es}(l) = \sum_\alpha (-)^\alpha S_\alpha(l) . \tag{4.2}$$

The entanglement spectrum may offer a sensitive probe for the degeneracy of a ground state in certain cases. In chapter 5 we will observe this property for the example of the chiral superfluid phase which is characterized by the spontaneous symmetry breaking of the Z_2 symmetry apparent from the vanishing of Δ_{es}.

4.1.1 Symmetry protected topological phases

In one dimensional systems topological phases may only exist if they are protected by certain symmetries of the model. Ref. [173] shows that for example the Haldane phase is stabilized by different symmetries, such as a space inversion, rotation and time reflection symmetry. As long as not all of these symmetries are broken the Haldane phase is separate from the large-D (or MI) phase. The degeneracy of the topological phase is characterized by its twofold degenerate entanglement spectrum. We may recover this property from the MPS-representaion of the AKLT state Eq. (3.18) where we find $S_{1,2} = \frac{1}{2}$. Similarly a Majorana-fermion phase [203] is characterized by the doubly degenerate entanglement spectrum [204].

4.2 Entanglement entropy

We may quantify the amount of entanglement by the von-Neumann entropy of the reduced density matrix

$$S_{vN} = -\text{Tr}\rho_A \log \rho_A. \tag{4.3}$$

It has been conjectured that the ground-state entanglement-entropy of gapped local systems satisfies a so called area law, i.e. that the entanglement growth of the a given area is proportional to the length of the boundary of the area [199]. Generally the entanglement entropy of an arbitrary quantum state will grow with the size of the volume of the considered partition of the state [199].

For one dimensional systems the properties of entanglement entropies are to a large extend settled analytically. The area law strictly holds for ground states of local, gapped Hamiltonians. Here the entanglement entropy is bounded by a constant, independent of the system size [205].

In two dimensions the entanglement entropy has received growing interest for the identification of topological quantum phases, which can be characterized by calculation of the non-divergent constant part γ of the entanglement-entropy $S(L) = \alpha L - \gamma + \ldots$ [206, 207].

4.2.1 Critical phases

For one dimensional gapless phases the area law does not hold. The entanglement entropy here diverges logarithmically as has been shown using conformal field theory [208]

$$S_{vN}(L) \sim \frac{c + \bar{c}}{6} \log L \tag{4.4}$$

where L is the partition size. Here c and $\bar{c}$ are central charges for the so called holomorphic and anti-holomorphic sectors of the conformal field theory. In the models studied in this work we always have $c = \bar{c}$. The central charge depends on basic properties of the underlying microscopic model, such as the number of effective degrees of freedom [209]. In Fig. 4.1 (a) we show the logarithmic divergence for a free fermion model, where $c = 1$. Eq. (4.4) has been generalized to finite open and periodic systems [172]

$$S_{vN} = \frac{c}{3} \log \left[\frac{L}{\pi} \sin \frac{\pi l}{L} \right] + g \,. \tag{4.5}$$
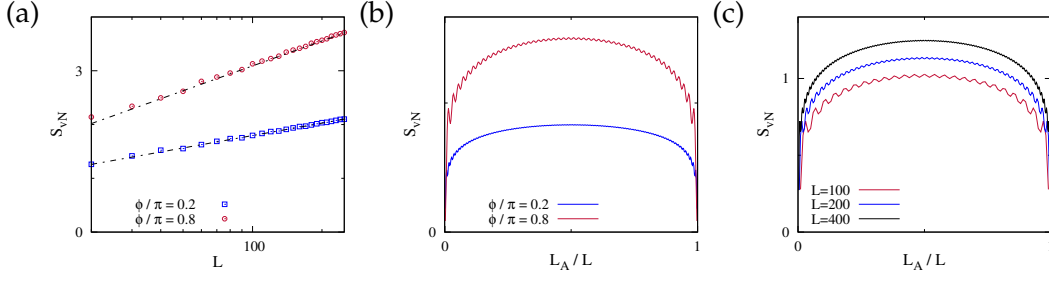
Fig. 4.1: Entanglement entropy for different free fermion models on a ladder (see chapter 10) with central charge $c = 1$ and $c = 2$ ($\phi/\pi = 0.2$ and 0.8, $J_\perp = 1$, $\rho = 1/4$ as defined in Eq. (6.14)). (a) Logarithmic entanglement growth with the system size L. The data are fitted to Eq. (4.4) with $c = 0.94$ and $c = 2.07$. (b) S_{vN} for different partitions of an OBC system with $L = 400$ rungs. (c) Dependence of the finite-size oscillations in the OBC data for different systems sizes ($c = 1$-phase, $\phi/\pi = 0.2$).

For periodic boundary condition the prefactor has to be replaced by $\frac{c}{6}$.

In this work we will frequently calculate the central charge of the system for a detailed characterization of the ground-state phases and phase transitions. In exact diagonalization approaches c may be estimated from the scaling of the ground-state energy

$$\frac{E_g(L)}{L} \simeq \epsilon_\infty - \frac{\pi c v}{6 L^2} \tag{4.6}$$

which requires the additional calculation of the velocity of sound v. In the age of DMRG Eq. 4.5 offers a a very accurate tool for the extraction of c. We study this behavior for the free fermion models, for which we can obtain quasi-analytical results for S_{vN} [209], in Fig. 4.1 (b) and (c). As seen in Fig. 4.1 (b) one may clearly distinguish phases with a $c = 1$ and $c = 2$ from this approach. For OBC $S_{vN}(l)$ exhibits small Friedel-like-oscillation due to the proximity of the boundary. With increasing system size these effects vanish (see Fig. 4.1 (c)).

Interestingly we may also study the entanglement properties directly in the thermodynamic limit using iDMRG or iTEBD approaches. Here the finite system size L of the system is replaced by the matrix-dimension M of the MPS representation which defines an effective correlation length $\xi \propto M^\kappa$ with $\kappa = \frac{6/c}{\sqrt{12/c+1}}$ depends on the central charge c [210]. As shown in [211] we may hence extract c directly from the scaling of the entanglement entropy

$$S_{vN} = \frac{1}{\sqrt{12/c + 1}} \log M . \tag{4.7}$$

4.3 The ground-state fidelity-susceptibility

The ground state fidelity susceptibility (FS) has established itself as a useful computational tool for locating quantum phase transitions in many-body systems [212, 213]. For a general Hamiltonian $\widehat{\mathcal{H}}(\lambda) = \widehat{\mathcal{H}}_0 + \lambda \widehat{W}$ the fidelity susceptibility χ_W is a measure for the change of the wavefunctions respect to the "perturbation" $\widehat{W}$. If we expand the overlap or fidelity of a ground state as $F = \langle \Psi_0(\lambda) | \Psi_0(\lambda + \delta\lambda) \rangle$ we

find

$$F = 1 + \delta\lambda \langle \Psi_0(\lambda) | \frac{\partial}{\partial_\lambda} \Psi_0(\lambda + \delta\lambda) \rangle + (\delta\lambda)^2 \langle \Psi_0(\lambda) | \frac{\partial^2}{\partial_\lambda^2} \Psi_0(\lambda + \delta\lambda) \rangle$$

From the normalization of the wavefunction follows that its absolute values only contains terms in leading order $\delta\lambda^2$

$$|F| = 1 - \frac{(\delta\lambda)^2}{2} \chi_W$$

with the ground state fidelity susceptibility χ_W and thus [214]

$$\chi_W(\lambda) \quad = \quad \lim_{\delta\lambda \to 0} \frac{2(1 - |F|^2)}{\delta\lambda^2} = \lim_{\delta\lambda \to 0} \frac{-2\ln|F|}{(\delta\lambda)^2}$$

Within second order perturbation theory one may express χ_W in terms of Matrix-elements of the unperturbed Hamiltonian

$$\chi_W = \sum_{n \neq 0} \frac{|\langle \Psi_n(\lambda) | W | \Psi_0(\lambda) \rangle|^2}{(E_n(\lambda) - E_0(\lambda))^2}$$

The FS has been extended to finite temperatures [215] and the thermodynamic limit [215].

4.3.1 Fidelity susceptibility as indication of quantum phase transitions

The FS may show intriguing scaling behavior at a quantum phase transition as can be seen from scaling arguments [214, 216] given that the correlation length ξ at a phase transition diverges as $\xi \sim |\lambda - \lambda_c|^{-\nu}$ for $L \to \infty$. Since the fidelity $F(\lambda, \delta\lambda)$ is a dimensionless quantity close to the phase transition it may be written as [214]

$$\chi_W(\lambda \simeq \lambda_c) \sim (\delta\lambda)^{-2} f(L/\xi) = (\delta\lambda)^{-2} f(L(\delta\lambda)^\nu) = (\delta\lambda)^{-2} \tilde{f}(L^{1/\nu}\delta\lambda) \qquad (4.8)$$

Requiring that for finite systems L there may not be singularities one finds that $\tilde{f}(L^{1/\nu}\delta\lambda) \sim (L^{1/\nu}\delta\lambda)^2$ and so

$$\chi_W(\lambda_c) \sim L^{2/\nu} \qquad (4.9)$$

Thus the scaling of χ_F may be used to determine the position and universality class of some phase transitions. In particular Ising type phase transitions may be accurately discriminated by the FS due to its divergence $\chi_F \sim L^2$ with respect to its wings. However, as will be shown in the following there are cases in which this scaling behavior becomes unusual. A prominent counter example of a non-diverging FS is the BKT-phase transition. Here it has been shown recently [217] that χ_F/L converges logarithmically as $\chi/L = \chi_0 - \chi_1/\ln(L/a) + ...$

4.4 Current fidelity susceptibility and conductivity

The following section is based on the publication Ref. [36] developed in collaboration with A. Kolezhuk and T. Vekua. We consider properties of the FS with respect

to particular operators such as the current or twist operator. We will observe un-usual scaling relations of this current fidelity susceptibility (CFS). Carefully analyzing the finite-size scaling of the CFS with respect to the current reveals properties of the corresponding conductivity.

In the following a hardcore boson (spin-1/2 XXZ-) chain will be used as example

$$\hat{\mathcal{H}}(\phi) = \sum_j b_j b_{j+1} e^{i\phi} + H.c. + \Delta n_j n_{j+1} \,. \tag{4.10}$$

For small twist angles ϕ this may be recast in the form of a chain with the Dzyaloshinskii-Moriya like coupling (see chapter 5)

$$\hat{\mathcal{H}}(\phi) = \hat{\mathcal{H}}(0) + \phi \hat{J} \,, \tag{4.11}$$

with the current operator given by $\hat{J} = -\frac{i}{2} \sum_j b_j^\dagger b_{j+1} - b_{j+1}^\dagger b_j$.

4.4.1   Conductivity

An important experimental quantity in the context of transport and currents is the conductivity σ defined as the linear response to an external electric field E: $j(\omega) = \sigma(\omega)E(\sigma)$. From the Kubo-formula one obtains the expression [218]

$$\mathrm{Re}\,\sigma(\omega) = D_0 \delta(\omega) + \sigma_1(\omega)$$

with

$$D_0 = \frac{\pi}{L} \left(-\langle T \rangle - 2 \sum_{m \neq 0} \frac{|\langle m|\hat{J}|0\rangle|^2}{E_m - E_0} \right) = \pi L \left(\frac{\partial^2 E_0(\phi)}{\partial \phi^2} \right)_{\phi=0} \tag{4.12}$$

and

$$\sigma_1(\omega) = \frac{\pi}{L\omega} \sum_n |\langle \Psi_n(\lambda)|\hat{J}|\Psi_0(\lambda)\rangle|^2 \delta\left[\omega - (E_n(\lambda) - E_0(\lambda))\right] \tag{4.13}$$

As discussed in Ref. [219] the $\mathrm{Re}\,\sigma(\omega)$ shows a very different behavior in finite systems with open and periodic boundary conditions. In both cases the total conductivity satisfies the f–sum rule [218, 220, 221]

$$\frac{1}{\pi} \int_0^\infty \sigma(\omega)\,d\omega = -\frac{1}{2L}\langle T_k \rangle, \tag{4.14}$$

The average kinetic energy $\langle T_k \rangle$ is independent of the boundary conditions.

Periodic boundary conditions

For PBC we may identify D_0 with the so-called Drude-weight D. For the interacting case from Bethe-Ansatz one obtains [218] $D(\Delta) = Ku$ with the Luttinger-liquid parameter K and sound-velocity u as defined in Eq.(2.22).

For non-interacting particles the regular part vanishes $\sigma_1(\omega > 0) = 0$ since the current operator is a conserved quantity $[\hat{\mathcal{H}}, J] = 0$ and thus the right part of Eq. (4.13) vanishes. This is not the case for finite interaction. However, for an extensive range of interactions $\sigma_1(\omega > 0)$ is negligible compared to the Drude-weight-contribution. Indeed, one may approximate for $-1 < \Delta \lesssim 1/4$ the average kinetic energy $\langle -T_k \rangle \simeq LKu/\pi$ such that already the Drude-contribution almost exhausts the f-sum-rule (4.14).
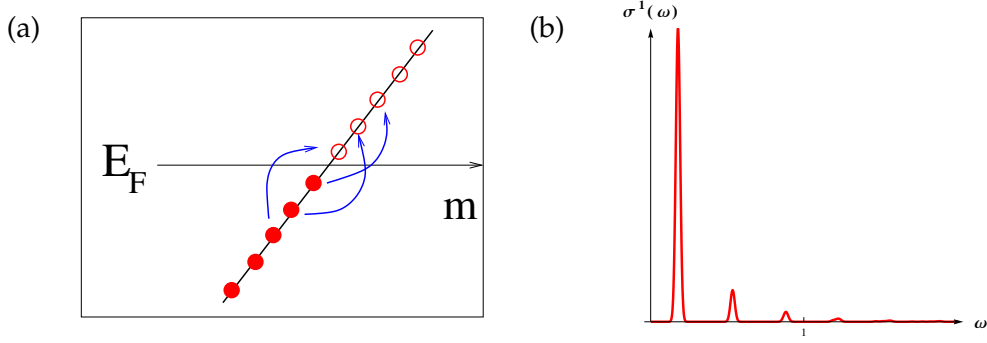
Fig. 4.2: (a) Sketch of the single particle excitations and their degeneracy. The excitation of energy E_m is m-fold degenerate. (b) Conductivity for the XX-model (non-interacting fermions, $L = 37$) as defined in Eq. (4.17) expressing δ-functions as Gaussian distributions.

Open boundary conditions

In the case of OBC one may always gauge out the effect of the twist in Eq. (4.10) by a redefinition of the bosonic operators $b_j \to b_j \exp -i\phi j$. Thus $D_0 = 0$ as in the upper definition (4.12). At first glance this result may seem surprising since the integrated conductivity should be independent of the boundary conditions as can be seen by the f-sum rule. Also we expect that in the thermodynamic limit $L \to \infty$ boundary conditions should not play any role. In fact it may be shown that now the Drude-weight contribution is smeared among several finite frequencies [36, 219].

This may be exemplified for the conductivity of the non-interacting model, which we calculate assuming an approximately linear spectrum of particle-hole excitations $E_m - E_0 \simeq u\pi m/L$, as sketched in Fig. 4.2. For all other excitations the matrix-element of the current operator vanishes and so does its contribution to the conductivity

$$\sigma_1^{OBC} = \frac{\pi}{\omega L} \sum_{m>0} \rho(m) |\langle \psi_0 | \widehat{J} | \psi_m \rangle|^2 \delta(\omega - (E_m - E_0)) \qquad (4.15)$$

The degeneracy of excitations of energy $u\pi m/L$ is $\rho(m) = m$. Due to a parity selection rule the matrix-element is given by

$$|\langle \psi_0 | \widehat{J} | \psi_m \rangle| = \frac{\left[1 - (-1)^m\right] u}{m\pi} \qquad (4.16)$$

This yields the entire conductivity of the non-interacting case

$$\begin{aligned} \sigma_1^o = D(\omega) &= \frac{\pi u^2}{L\omega} \sum_{k=0}^{\infty} \frac{4(2k+1)}{(2k+1)^2 \pi^2} \delta\left(\omega - (E_{2k+1} - E_0)\right) \\ &= \sum_{k=0}^{\infty} \frac{4u}{(2k+1)^2 \pi^2} \delta\left(\omega - \frac{(2k+1)u\pi}{L}\right). \end{aligned} \qquad (4.17)$$

A bosonization calculation with open boundary conditions shows [36] that finite interactions basically just result in a renormalization of the matrix-elements of the current which now include the Luttinger-liquid parameter K and the renormalized sound velocity u and, hence,

$$D(\omega) = \frac{\pi}{L\omega} \sum_{k=0}^{\infty} \frac{4Ku^2}{(2k+1)\pi^2} \delta(\omega - \frac{(2k+1)u\pi}{L}) . \qquad (4.18)$$

The integrated Drude-weight for OBC coincides with the value for PBC $\int_0^\infty D(\omega)\, d\omega =$ $\sum_K \frac{4Ku}{(2k+1)^2\pi^2} = Ku$.

CFS via conductivity

Comparing the current fidelity susceptibility

$$\chi_J = \sum_{n\neq 0} \frac{|\langle \Psi_n(\lambda)|\hat{J}|\Psi_0(\lambda)\rangle|^2}{(E_n(\lambda) - E_0(\lambda))^2} \tag{4.19}$$

and real part of the conductivity

$$\mathrm{Re}\,\sigma(\omega)|_{\omega>0} = \frac{\pi}{L\omega}\sum_n |\langle \Psi_n(\lambda)|\hat{J}|\Psi_0(\lambda)\rangle|^2 \delta\left[\omega - (E_n(\lambda) - E_0(\lambda))\right] \equiv \sigma_1(\omega)\,, \tag{4.20}$$

one obtains the following relation between CFS χ_J and conductivity σ_1

$$\chi_J = \frac{L}{\pi}\int_0^\infty d\omega \frac{\sigma_1(\omega)}{\omega}\,. \tag{4.21}$$

It is crucial to note that we may not include $\omega = 0$ due to the lower bound $E_n - E_0 \sim 1/L > 0$. For systems with periodic boundary conditions χ_J is directly connected to the low frequency behavior of the regular part of the conductivity $\sigma_1(\omega)$. For OBC χ_J is determined by the singular part of the conductivity that is essentially the smeared Drude peak. This leads to different scaling laws in systems with open and periodic boundary conditions.

4.4.2 Open boundary conditions

For open boundary conditions one obtains a universal quadratic scaling of CSF with system size. For the XXZ-model one finds generally $\chi_J^{OBC} \sim L^2$ as can be easily shown with the help of Eq. (4.21) and (4.18)

$$\chi_J^{OBC} = \frac{L}{\pi}\int_0^\infty d\omega \frac{D(\omega)}{\omega} = \sum_{k=0} \frac{4KL^2}{\pi^4(2k+1)^3} = \frac{7\zeta(3)}{2\pi^4}KL^2\,. \tag{4.22}$$

Here ζ denotes the Riemann-zeta-function. The equation above as in most of the cases in this chapter describes the leading order divergence of the CFS. Subleading orders depend on the regular part of the conductivity.

This unusual super-extensive behavior of CSF may obscure the detection of phase transitions. We illustrate such "masking" for the example of the attractive single-component Bose-Hubbard model with an additional 3-body constraint $\left(\left(b^\dagger\right)^3 = 0\right)$ (compare chapter 5)

$$\hat{\mathcal{H}} = -\frac{t}{2}\sum_j \left[b_j^\dagger b_{j+1} + b_{j+1}^\dagger b_j\right] - \frac{\mathrm{i}d}{2}\sum_j \left[b_j^\dagger b_{j+1} - b_{j+1}^\dagger b_j\right]$$

$$+ \frac{U}{2}\sum_j n_j(n_j-1) + U_3\sum_j n_j(n_j-1)(n_j-2)\,. \tag{4.23}$$

As shown in Ref.[106] this model exhibits an Ising-type phase transition between a gapless SF and a pair SF (PSF) phase. Fig. 4.3 depicts the fidelity susceptibility with respect to the usual hopping and the CFS close to this Ising phase transition.
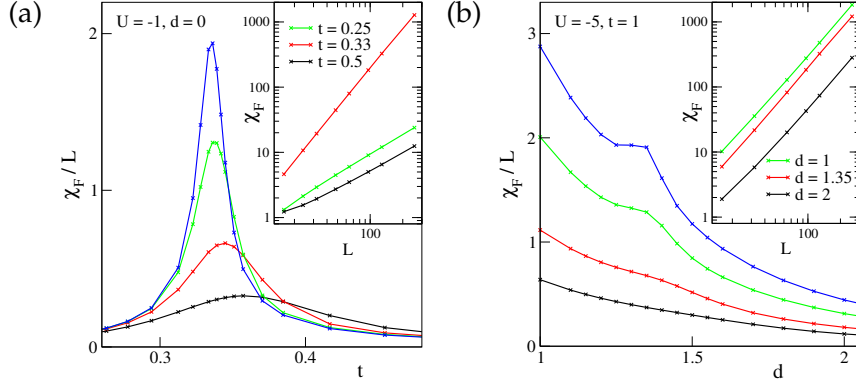
Fig. 4.3: Different fidelity susceptibilities for the attractive Bose Hubbard model 4.23. χ_t/L with respect to the hopping t (a) for different system size of (from bottom to top) $L = 16, 32, 64$ and 96 sites. The inset shows the scaling of χ_t for different fixed parameters of t. Only close to the phase transition point the divergence of χ_t goes with L^2 and thus the Ising type phase transition is nicely reveled. However, for the current fidelity susceptibility (b) the scaling is always as L^2 and thus the divergence at the phase transition is "masked". Sub-leading corrections however lead to a local maximum in χ_J still indicating the phase transition point.

Due to the overall L^2 scaling of the CFS the latter case does not exhibit a significantly divergent peak with respect to the wings as a clear signature of this phase transition.

Similar observations can be made for the polarization operator P (corresponding to an external electric field for charged particles, or to tilting the optical lattice for cold neutral atoms).

$$\chi_{\text{tilt}}^o = \frac{31 K L^4 \zeta(5)}{8u^2\pi^6} \tag{4.24}$$

Note that, interestingly, the CFS in OBC is proportional to the Luttinger-liquid parameter K and may be used as a tool for the calculation of K. Similar the ratio of (4.24) and (4.22) may be used to calculate the sound-velocity of the model.

CFS scaling for OBC from unitary transformation

In the following we present an alternative deviation of the unusual scaling properties of the CFS. One may eliminate the current term by means of a unitary "twist" operator

$$\widehat{U}[\phi] = e^{i\phi\widehat{\mathcal{P}}}, \quad \widehat{\mathcal{P}} = \sum_j j\hat{n}_j . \tag{4.25}$$

Note also, that the current-operator from Eq. (4.11) may be eliminated employing the transformation above introducing renormalized interactions Δ. With this the CFS may be expressed in terms of expectation values of the unperturbed ground state

$$\chi_J^{OBC} \simeq \left(\langle \widehat{\mathcal{P}}^2 \rangle - \langle \widehat{\mathcal{P}} \rangle^2 \right) = \sum_{j,j'=1}^{L} \frac{(j-j')^2}{2} \left(\langle n_j \rangle \langle n_{j'} \rangle - \langle n_j n_{j'} \rangle \right) . \tag{4.26}$$
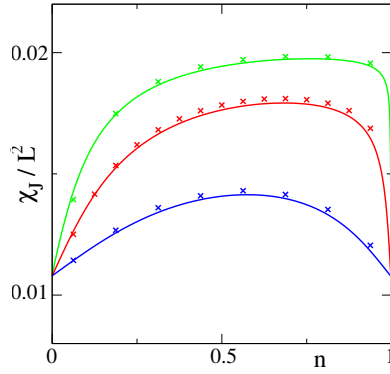
Fig. 4.4: CFS of the fermionic Hubbard model with OBC for (top to bottom) $U/t = 1$, 2 and 6. The symbols denote the DMRG data for Hubbard chains of $L = 128$ sites, solid lines correspond to the analytical expression (4.30).

Using the analytical expressions for the correlation functions [222, 223] whose smooth part essentially decays as $1/|j - j'|^2$ one arrives at a generalized expression of Eq. (4.22)

$$\frac{\chi_J^o(d, M)}{L^2} = \frac{7\zeta(3)}{2\pi^4(1 + d^2)^2} K(M, \widetilde{\Delta}) + \cdots. \tag{4.27}$$

where $K(M, \widetilde{\Delta})$ denotes the Luttinger liquid parameter for a filling M.

Hence, the L^2 dependence of the CFS is a generic feature of gapless models with OBC with conserved n or S^z, a current term that may be eliminated with the unitary transformation of Eq. (4.25), and correlation functions that decay as $1/|j - j'|^2$.

The repulsive Fermi-Hubbard model

We now examine the ideas from above for the Fermi-Hubbard model

$$\hat{\mathcal{H}}_0 = -\sum_{j,\sigma} \left(c_{j,\sigma}^\dagger c_{j+1,\sigma} + \text{H.c.} \right) + U \sum_j n_j^2, \tag{4.28}$$

where $c_{j,\sigma}$ annihilates a fermion at site j with the spin $\sigma = \{\uparrow, \downarrow\}$, and $n_j = \sum_\sigma c_{j,\sigma}^\dagger c_{j,\sigma}$ is the fermion density at the site. For OBC we study the CFS χ_J^o with respect to the total current, $\hat{\mathcal{H}} = \hat{\mathcal{H}}_0 + \lambda \hat{J}_{\text{tot}}$, with

$$\hat{J}_{\text{tot}} = -\mathrm{i} \sum_{j,\sigma} \left(c_{j,\sigma}^\dagger c_{j+1,\sigma} - c_{j+1,\sigma}^\dagger c_{j,\sigma} \right). \tag{4.29}$$

With the arguments above one obtains

$$\frac{\chi_J^o}{L^2} = \frac{7\zeta(3)}{\pi^4} K_c(\nu, M) + O(\frac{1}{L}), \tag{4.30}$$

Here ν denotes the lattice filling and M is the magnetization.

In Fig. 4.4 we show how expression (4.30) may be exploited to extract the Luttinger-liquid parameter K_ρ. Comparing both the theoretical values of Eq. (4.30) for different fillings and values of the interaction U in which we make use of the analytically known results for the values of K_ρ [224], with numerical results obtained by a DMRG calculation. Without extrapolation χ_J/L^2 for one system size $L = 128$ already reproduces very accurately the theoretical expectation.
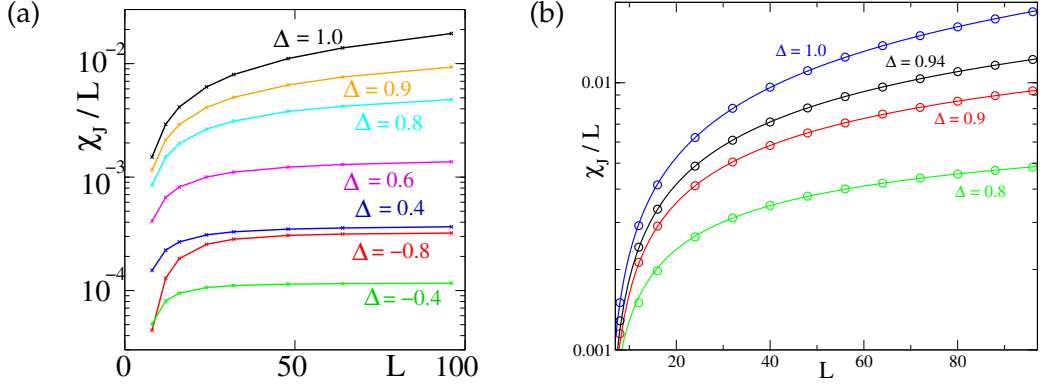
Fig. 4.5: (a) The finite-size scaling of the CFS χ_J in the spin-1/2 XXZ chain with PBC, for different values of Δ (taking $\delta d = 10^{-3}$). (b) Different fits to χ_J/L for $\Delta \geq 0.8$ including subleading corrections. At $\Delta = 0.8$ the data is fitted to Eq. (4.33), $10^3\chi_J/L = 1.57 \ln L - 2.33$. At $\Delta = 0.9$ and $\Delta = 0.94$ are fitted according to Eq. (4.34), with $10^3\chi_J/L = 2.46L^{0.33} + 0.84 \ln L - 5.55$ and $10^3\chi_J/L = 1.17L^{0.5} + 1.11 \ln L - 4.44$ resp. The $\Delta = 1$ results are fitted to Eq. (4.35), $10^3\chi_J/L = 4.91(\mathrm{li}(4L)/4 - L/\ln(4L)) - 3.86$.

4.4.3 Periodic boundary conditions

Since the Drude-part for PBC always is located at $\omega = 0$ we do not have to include it into the calculation of the CFS in Eq.(4.21). Thus the CFS here is determined by the regular part of the conductivity σ_1 enabling us to probe its properties.

A perturbative calculation [35] proposes the following weak coupling relation for regular conductivity of the XXZ-model

$$\sigma_1(\omega) \sim \Delta^2 \omega^{8K-5} . \tag{4.31}$$

We may now use the CFS in PBC to survey this conjecture only performing static ground-state simulations. From Eq. (4.21) and (4.31) we obtain the following scaling relations in different regimes. The CFS has a usual extensive dependence on the system size for $K > 5/8$, i.e. $\Delta \lesssim 0.8$,

$$\chi_J^{PBC} \propto L + \cdots, \quad K > \frac{5}{8}. \tag{4.32}$$

However, the situation becomes non-trivial for $K \leq 5/8$:

$$\chi_J^{PBC} \propto L(\ln L + const) + \cdots, \quad K = \frac{5}{8} \tag{4.33}$$

and

$$\chi_J^{PBC} \propto L^{6-8K} + \cdots, \quad \frac{1}{2} < K < \frac{5}{8} . \tag{4.34}$$

At the BKT-point $\Delta = 1$ the presence of logarithmic corrections yield the following scaling

$$\chi_J^p = L\left[\frac{\mathrm{li}(AL)}{A} - \frac{L}{\ln(AL)} + const\right] + \cdots \sim (L/\ln L)^2 + \cdots, \quad \Delta = 1 \tag{4.35}$$

where li is the logarithmic integral function. We perform DMRG calculations in PBC with up to $L = 100$ sites keeping about $m \sim 1000$ states to achieve good accuracy. As shown in Fig. 4.5 the CFS per site saturates quickly for $\Delta \lesssim 0.8$ in accordance of Eq.(4.32). For $\Delta < 0.5$ we observe small numerical prefactors of about
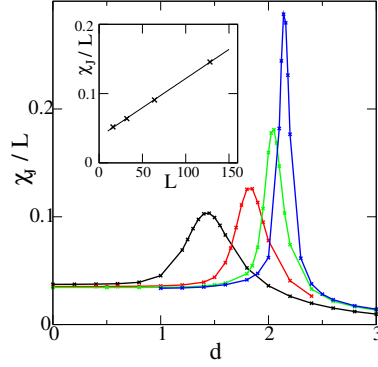
Fig. 4.6: The CFS of a spin-$\frac{1}{2}$ ladder defined by (4.36), with OBC, in the vicinity of the Ising phase transition from the Néel to the rung-singlet state as obtained by DMRG calculations (J_R = 3 and Δ = 1.5) for system sizes of L = 16, 32, 64 and 128 rungs. The inset again shows the scaling with the system-size for fixed parameters.

~ 10^{-4} to 10^{-3}, which can be related to the fact that the contribution from the regular part of the conductivity to the f-sum rule is small. Fig. 4.5 (b) presents fits of Eq. (4.33), (4.34) and (4.35) to the numerical data. Including subleading corrections the numerical data is in agreement with the scaling relations and thus nicely confirms the result of Eq. (4.31).

4.4.4 Gapped phases

In gapped phases the Drude weight disappears. Indeed the whole conductivity vanishes below an excitation gap ω_0. Thus we expect a typical L-scaling of the CFS as we illustrate for two gapped phases of the antiferromagnetic spin-1/2 spin ladder defined by the Hamiltonian

$$
\begin{aligned}
\hat{\mathcal{H}}_{\text{Lad}} \;=\; & \sum_{l,\alpha}\left[S^x_{l,\alpha} S^x_{l+1,\alpha} + S^y_{l,\alpha} S^y_{l+1,\alpha} + \Delta S^z_{l,\alpha} S^z_{l+1,\alpha} \right] \\
& + \; J_R \sum_l \mathbf{S}_{l,1}\cdot\mathbf{S}_{l,2} + d \sum_{l,\alpha}(\mathbf{S}_{l,\alpha}\times\mathbf{S}_{l+1,\alpha})^z .
\end{aligned}
\tag{4.36}
$$

Here $\alpha = 1,2$ denotes the two legs of the ladder. This model exhibits a Ising quantum phase transition between the gapped Néel and rung-singlet states. As shown in Fig. 4.6 the CFS at the phase transition exhibits quadratic scaling of the peak and in its wings an ordinary L scaling.

4.4.5 Conclusions

In summary we have shown how the fidelity susceptibility can be exploited as a powerful tool for the analysis of quantum phase transitions. The FS typically exhibits an extensive behavior with the system size L. However, for certain perturbations, in particular the current or polarization operators of a given model, these scaling relations may become unusual. For OBC we obtain a super-extensive scaling that bears the complication of a possible masking of quantum phase transitions. We have shown how the CFS in OBC may be exploited as a tool for a direct calculation of Luttinger-liquid parameters. For PBC we obtain a usual extensive behavior,

which for the case of the CFS may be exploited analyzing the real regular part of
the conductivity.

In this context interesting extensions are the study of the CFS in larger sys-
tems, or systems with infinite boundary conditions by means of iDMRG or iTEBD
simulations in order to further verify Eq. (4.31). For iDMRG the scaling with the
system size should be replaced by a scaling with the matrix-dimensions which can
be mapped to a correlation length [175]. Other extensions could include the study
of different models with disorder or systems in higher dimensions.

Chapter 5

Ultracold Bosons in Zig-Zag Optical Lattices

Recent experimental advance in controlling motional degrees of freedom of ultra-cold bosonic atoms in optical lattices has opened the possibility of simulation of classical frustrated quantum antiferromagnetism by Struck et al. [1]. Motivated by this experiment we study the rich physics of strongly correlated triangular (zig-zag) ladder systems with bosons. This so-called J_1-J_2-model is one of the simplest paradigms for frustrated quantum systems and presents a rich physics due to the interplay between frustrated lattice geometry and interaction.

In the context of quasi one-dimensional magnetic materials [225–227] the corresponding spin-model has been extensively studied during the last decades. In the seminal work of Majumdar and Gosh [167] of the late 60s the famous analytical solution for the isotropic spin-1/2 J_1-J_2-model could be given proving the presence of a dimerized (D) ground state without magnetic field (compare chapter 3). Later studies revealed the Ising type phase transition between the critical XY and the D phase [228, 229]. Detailed ground-state properties in different regimes and for higher spins $S > 1/2$ have been discussed both numerically and analytically [230–233], at vanishing magnetic field [234], and with magnetic fields in the ferromagnetic [235] as well as antiferromagnetic regime [187, 223].

In the following we will discuss the properties of ultracold one-component bosons in different regimes keeping in mind the strong links to tradition condensed matter physics. We will show a wealth of ground-state phases including chiral superfluid (CSF) or exotic chiral Mott-insulator (CMI) phases. Various extensions of the model are discussed, including 3-particle on- and off-site-interactions, and strongly interacting dipolar molecules and variations of the geometry.

5.1 Frustrated classical magnetism in triangular lattices

Let us briefly review some aspects of Ref. [1] in which classical frustrated magnetism was simulated with bosons prepared in 2D triangular optical lattices (see Fig. 5.1 (a)). This situation may be described by a usual Bose-Hubbard model (2.10) where we will denote the hopping in the zig-zag directions with J_1 and in the horizontal direction with J_2. Without additional steps this system is not frustrated since both $J_1, J_2 > 0$.

By means of an elliptical shaking scheme one is able to manipulate the inter-site hopping-amplitudes J_1 and J_2 independently. Extending the analysis of Eq. (2.41) the fast lattice modulation is given by [236]

$$\mathbf{r}(t) = \Delta x_c \cos(\omega t)\mathbf{e}_c + \Delta x_s \sin(\omega t)\mathbf{e}_s \,. \tag{5.1}$$
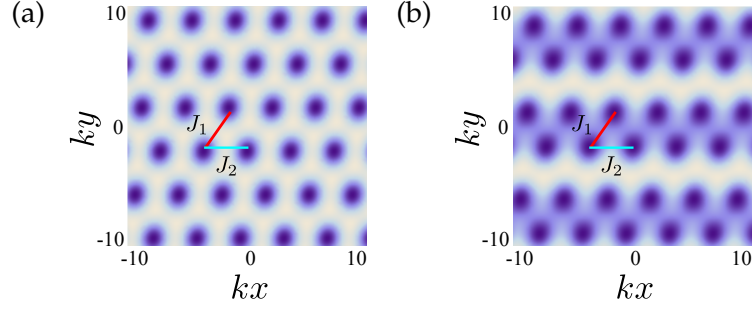
Fig. 5.1: (a) Triangular lattice (2.6) as described in Ref. [66]. (b) By incoherent superposition of an additional lattice $\sim \sin^2(\sqrt{3}ky/4 - \pi/4)$ stripes of zig-zag ladders are formed. Darker Regions mean lower potential.

The effective hopping now depends on the projection of the modulation direction on the vector connecting sites i and j, $\mathbf{x} = \mathbf{x}_i - \mathbf{x}_j$:

$$J_{ij} \rightarrow J_{ij}\mathcal{J}\left(\frac{K_{ij}}{\hbar\omega}\right) \tag{5.2}$$

with $K_{ij} = \sqrt{(F_c\mathbf{e}_c \cdot \mathbf{r}_{ij})^2 + (F_s\mathbf{e}_s \cdot \mathbf{r}_{ij})^2}$. Hence by appropriate modulation it is possible to change the sign of the hoppings. If a plaquette contains an odd number of antiferromagnetic bonds, hence, for $J_2 < 0$, the system is frustrated.

In Ref. [1] each lattice site represents an elongated tube of the optical lattice occupied by a large number of particles ($\rho \sim 250$ particles per tube). Hence, we assume that each lattice site may be described by a BEC with well defined local phase θ_i and particle density $\rho_i = \rho + \delta\rho_i$. The bosonic operators may be sufficiently well approximated by classical operators $\hat{b}_i^\dagger \approx \sqrt{\rho + \delta\rho_i}e^{i\theta_i}$. For weak interactions $U \ll J\rho$ we may neglect density fluctuations [1, 236]. Within this approximation we yield the following XY-model of classical spins $\mathbf{S}_i = [\cos\theta_i, \sin\theta_i]$

$$\hat{\mathcal{H}}_{class} \rightarrow 2\rho\sum_{ij} J_{ij}\cos(\theta_i - \theta_j) = 2\rho\sum_{ij} J_{ij}\mathbf{S_i} \cdot \mathbf{S_j} \tag{5.3}$$

Using TOF measurements Struck et al. are able to reproduce the classical phase diagram including phases with ferromagnetic and rhombic order for the non-frustrated case, and different types of spiral phases with a spontaneously broken symmetry for the frustrated part of the phase diagram.

The quantum phase diagram of ultracold bosons in triangular lattices for different values of U has been sketched in Ref. [236]. For small interactions one finds SF ground-states with spiral or staggered Néel-order. For large interactions in the
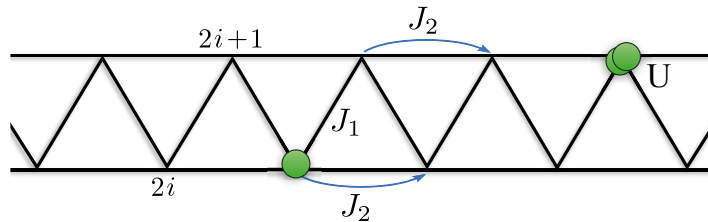

Fig. 5.2: Scheme of the BH model on a triangular ladder with hopping amplitudes J_1, J_2 and interaction U.
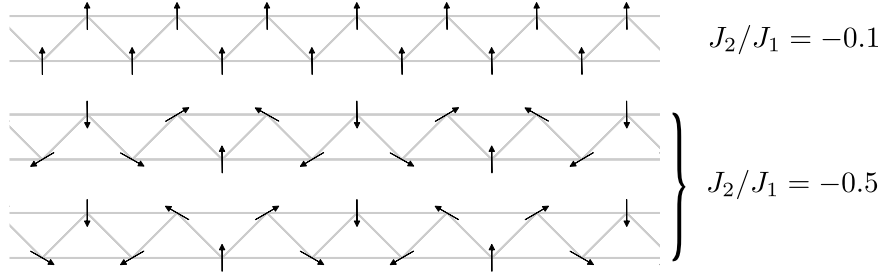
Fig. 5.3: Ground-state configuration of the system of classical spins Eq.(5.5) for $J_1 = 1$ and $J_2 = -0.1$ (top) and $J_2 = -0.5$ (middle and bottom).

spin-1/2 limit it is numerically hinted [237] that at half integer filling spin liquid phases with exponentially decaying spin-correlations may exist. For antiferromagnetic interaction Mott-lobes are enlarged due to frustration. Note that the precise form and properties of the strongly correlated quantum regime are very difficult to study theoretically, and a quantitative analysis such as Ref. [236] is often restricted to limiting or weakly interacting cases. In order to circumvent this difficulty we focus on quasi-one dimensional triangular ladders for which a detailed theoretical analysis is possible.

Experimentally triangular ladders may be engineered in a straight-forward way by employing super-lattice techniques. As illustrated in Fig. 5.1 (b) the stripes of zig-zag are separated from each other by a large potential barrier, which significantly suppresses the inter-chain tunneling. The total Hamiltonian is given by

$$\hat{\mathcal{H}}_{zz} = -J_1 \sum_i \hat{b}_i^\dagger \hat{b}_{i+1} + \text{H.c.} - J_2 \sum_i \hat{b}_i^\dagger \hat{b}_{i+2} + \text{H.c.} +$$

$$+ \frac{U}{2} \sum_i \hat{n}_i(\hat{n}_i - 1) - \mu \sum_i \hat{n}_i \, . \tag{5.4}$$

The elements of this model are sketched in Fig. 5.2. Within the large density weak coupling approximation $\rho \gg 1$, $U \ll J_1\rho$ we yield the following model of classical spins $S \to \infty$

$$\hat{\mathcal{H}}_{zz,class} \to 2\rho J_1 \sum_i \cos(\theta_i - \theta_{i+1}) + 2\rho J_2 \sum_i \cos(\theta_i - \theta_{i+2}) \tag{5.5}$$

For $J_1 > 0$ the system is ferromagnetic and all spins are aligned for $j = -J_2/|J_1| < 1/4$ (see Fig. 5.3). For $J_1 < 0$ the configuration is a Néel-like antiparallel alignment of the spins. For the classical spin system a continuous $U(1)$ symmetry is broken, spontaneously selecting a rotation angle. For $j > 1/4$ frustration leads to two degenerate ground states: The spins rotate clockwise or counterclockwise (as shown in Fig. 5.3). This helical or spiral phase with a broken $U(1) \times Z_2$ symmetry is characterized by a finite helicity

$$\kappa = \sqrt{1 - \frac{1}{16j^2}} \, . \tag{5.6}$$

5.2   The dilute two-component Bose gas regime

Main features of zig-zag model Eq. (5.4) may be understood from its single particle dispersion relevant for $U \to 0$ or $\rho \to 0$,

$$\epsilon(k) = -2J_1(\cos k + j \cos 2k) \tag{5.7}$$

with $j \equiv J_2/J_1$ (for convenience we choose $J_1 < 0$ in the following). For $j < 1/4$ the dispersion has a single minimum at $k = \pi = -\pi$. At the Lifshitz point, for $j > 1/4$, the dispersion $\epsilon(k)$ presents two non-equivalent minima at $k = \pm Q \equiv \pm \arccos[-1/4j]$ (see Fig. 5.4 (a)).

Due to the emergence of two degenerate minima in the single particle dispersion relation, the physics at finite U may become very non-trivial. In the following we will discuss an intuitive and also quantitative picture of the emergence of various quantum phases in the limit of vanishing particle density $\rho \to 0$: an (ordinary) superfluid phase (SF), a chiral superfluid phase (CSF) and a two component superfluid (2SF).

The ideas and methods have been developed in [37] in the context of frustrated spin-S $J_1 - J_2$-models, for which we will present some detailed numerical analysis below.

5.2.1   2SF and CSF phases

For a single non-degenerate dispersion minimum the system is a one-component phase quasi-condensing in this lowest minimum; a finite $U > 0$ will induce a true superfluid phase (SF).

In the presence of two non-equivalent minima at $\pm Q$ the ground state of a non-interacting boson system is highly degenerate and the effect of interactions becomes crucial, selecting a particular ground state. The particles at low energies mainly populate the two dispersion minima at Q and $-Q$. We can interpret them as two different bosonic flavors and map to an effective two component model with intraspecies-coupling between bosons of the same species and interspecies coupling between different flavors. Typically two different types of superfluid ground states may be stabilized: Either the bosons equally occupy both minima, i.e. both flavors are present, the 2SF phase, or one of them is spontaneously selected and a one component SF phase with a spontaneously broken symmetry is realized.

The latter is the case of the CSF, corresponding to the classical helical phase, which exhibits a non-zero average momentum. Hence, in the CSF-phase (quasi)-momentum distribution would show in TOF-measurements vanishing and appearing peaks at Q or $-Q$ from measurement to measurement [38]. In the thermodynamic limit it exhibits a non-vanishing local boson current or chirality

$$\kappa_i = \frac{i}{2}(b_i^\dagger b_{i+1} - \text{H.c.}) \tag{5.8}$$

In a finite system this locally defined chirality is always zero. However, the CSF is clearly characterized by the long-range ordered chirality-chirality correlations

$$\kappa^2 = \lim_{|i-j| \to \infty} \langle \kappa_i \kappa_j \rangle . \tag{5.9}$$

The 2SF phase does not exhibit a finite chirality. A TOF-measurement would always show two distinct peaks in each experiment realization. The two component
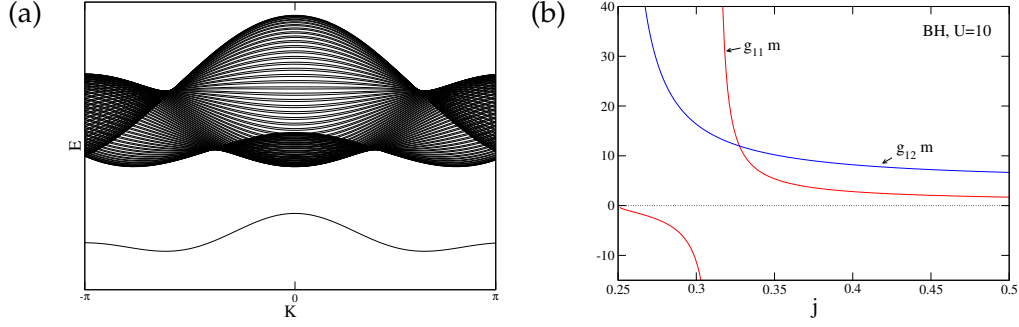
(a)

(b)

Fig. 5.4: (a) Single and two-particle spectrum of Bose-Hubbard model in the zigzag ladder with an frustration of $j = 0.7$. Both curves are shifted against each other due to a chemical potential. The single-particle dispersion exhibits two minima at $\pm Q$. Close to $K = 0$ the 2-particle spectrum is degenerate. (b) Bare coupling constants for the dilute BH model on a zig-zag ladder as function of j ($U/J = 10$).

phase is characterized by a central charge $c = 2$, counting the number of gapless modes (see chapter 4). In the CSF phase we find $c = 1$ (compare also Fig. 5.5).

5.2.2   Dilute limit

As shown in [37] one may gain quantitative insight in the competition between CSF and 2SF phases from the low energy scattering properties of two bosons on the triangular ladder. From the two particle problem we obtain different types of scattering solutions and extract two relevant scattering lengths: one for bosons belonging to the same single-particle minimum, $a_{1,1} = a_{2,2}$, and other one for bosons belonging to distinct minima $a_{1,2}$. One can relate the 1D scattering length to the amplitude of the contact interaction potential of the two-component Bose gas of mass m as

$$g_{i,j} = -2/a_{i,j}m. \tag{5.10}$$

Hence, one effectively interprets the systems as a continuum two-component Lieb-Liniger model [53]. If the intra-component interaction is stronger than the inter-component interaction $g_{1,1} = g_{2,2} > g_{1,2}$ in the limit of vanishing density $\rho \to 0$ the 2SF phase is favored. For a dominant inter-component interaction $g_{1,1} = g_{2,2} < g_{1,2}$ the particles preferably occupy only one of the two minima that is spontaneously chosen, and hence the system is in the CSF phase (see Fig. 5.4).

As shown in [37] in the dilute limit it is possible to obtain the renormalized intra- and inter-component interactions analytically as an exact solution to the corresponding Bethe-Salpeter equation. A detailed analytical treatment can be found in Ref. [37]. We will, however, present a more intuitive but completely equivalent approach to obtain $g_{1,1}$ and $g_{1,2}$ form the two-particle scattering problem.

5.2.3   The two particle scattering problem

A general 2 particle state my be described by

$$|\Psi_K\rangle = \sum_x c_{x,x}\left(\hat{b}^\dagger\right)^2|0\rangle + \sum_{x,y>x} c_{x,y}\hat{b}^\dagger_x\hat{b}^\dagger_y|0\rangle \tag{5.11}$$
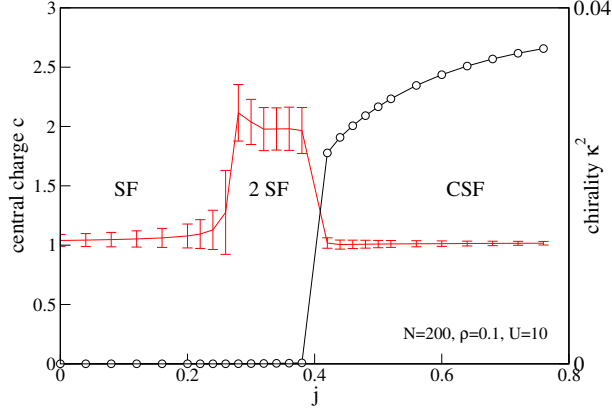
Fig. 5.5: Central charge (+) and chirality (◯) for $L = 200, \rho = 0.1, U = 10$. In spite of larger error-bars in the estimation of central-charge one clearly observes a finite 2-component SF region with central charge close to $c = 2$ separating one-component SF and CSF phases.

Due to the conservation of total momentum $K = k_1 + k_2$ in the scattering process one can express the amplitudes as $c_{x,x+r} = C_r e^{iK(x+\frac{r}{2})}$. The Schrödinger equation $\hat{\mathcal{H}}|\Psi\rangle = \Omega|\Psi\rangle$ for the two particle problem leads for the amplitudes C_r to the following system of coupled equations

$$(\Omega - 2U)C_0 = -2\sqrt{2}(J_1 \cos\left(\frac{K}{2}\right)C_1 + J_2 \cos(K)C_2)$$

$$(\Omega - V_1)C_1 = -2J_1 \cos\left(\frac{K}{2}\right)(\sqrt{2}C_0 + C_2) - 2J_2 \cos(K)(C_3 + C_1)$$

$$(\Omega - V_2)C_2 = -2J_1 \cos\left(\frac{K}{2}\right)(C_1 + C_3) - 2J_2 \cos(K)(\sqrt{2}C_0 + C_4)$$

$$\Omega C_r = -2J_1 \cos\left(\frac{K}{2}\right)(C_{r-1} + C_{r+1}) - 2J_2 \cos(K)(C_{r-2} + C_{r+2}), r \geq 3 \quad (5.12)$$

Here for the sake of completeness we have added nearest and next-nearest neighbor interaction terms $V_1 \sum_i n_i n_{i+1}$ and $V_2 \sum_i n_i n_{i+2}$. In the thermodynamic limit the energy is given by

$$\Omega = \epsilon(k_1) + \epsilon(k_2) = -4(J_1 \cos(k) \cos\left(\frac{K}{2}\right) + J_2 \cos(2k) \cos(K)) \quad (5.13)$$

with the half relative momentum $k = (k_1 - k_2)/2$. Both single particle and 2-particle spectra are shown in Fig. 5.4.

For the scattering of two particles in the vicinity the same minimum with momentum $k_1 = Q + k$ and $k_1 = Q - k$, i.e. total momentum $K = Q$, one may solve Eq. (5.12) with an Ansatz

$$C_r = \cos(kr + \delta_{11}) + v e^{-\kappa_0 r} \quad (5.14)$$

The coefficients C_0, δ_{11} and v are determined by the first three equations of (5.12) and, hence, depend on the interactions. The scattering lengths may be extracted from the scattering phase shift δ_{11}

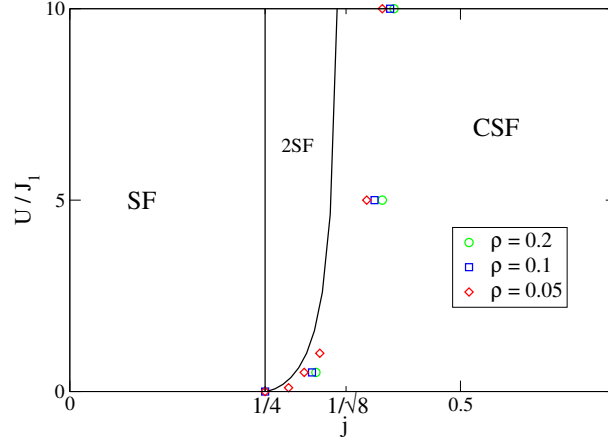$$a_{11} = \lim_{k \to 0} \cot(\delta_{11})/k. \quad (5.15)$$

Fig. 5.6: Phase diagram of bosons on the zig-zag-ladder in the dilute limit ($\rho \rightarrow 0$). The straight lines are analytical results, the points indicate numerical estimates of the 2-component-SF to CSF transition (cf. Fig. 5.5) for different finite densities.

For the case of scattering particles in the vicinity of two different dispersion minima, i.e. total momentum $K = 0$, the scattering states are twofold degenerate: One may find a p and $\tilde{p} = p + \mathcal{O}(p^2)$ such that the energies of the scattering states with $k_1 = Q + p, k_2 = -Q - p$ and $\tilde{k}_1 = Q - \tilde{p}, \tilde{k}_2 = -Q + \tilde{p}$ are the same. To solve the Schrödinger equation (5.12) we use the Ansatz

$$C_r = \cos(kr + \alpha(k)) + v(k)\sin(\tilde{k}r) \qquad (5.16)$$

where $k = Q + p$ and $\tilde{k} = Q - \tilde{p}$ are the half relative momenta. As shown in [37] one may define the interspecies scattering phase shift as

$$\delta_{12} = -\arccos \frac{\cos(\alpha)}{\sqrt{\cos^2 \alpha + (v + \sin \alpha)}} \; ,$$

which can be seen in the limit $p \rightarrow 0$ of Eq. (5.16).

The crossing of the scattering lengths indicates a phase transition between 2SF and CSF phases. For $|g_{\alpha\beta}|m \ll 1$ the interpretation as a continuum Lieb-Liniger model is valid. In this limit for a negative $g_{11} < 0$ the bosons form an attractively interacting model, which signals the presence of bound states. For $|g_{11}|m \gg 1$ the system may enter a super-Tonks regime with Luttinger-liquid parameter $K < 1$. Here the scattering lengths may be interpreted as excluded volume of the particles [37].

5.2.4 Dilute limit phase diagram

For the Bose-Hubbard model (5.4) we calculate the bare couplings mg_{11} and mg_{12} as function of U and j. An example is shown in Fig. 5.4 (b). The intersection of two curves signals the CSF-2SF transition, described by

$$U = \frac{\left((4j)^2 - 1\right)^{3/2}}{4j^2(1 - 8j^2)}.$$

The transition from the ordinary SF to the 2SF or CSF regions in the dilute limit takes place at $j = 1/4$ where dispersion gets a second minimum. The resulting phase diagram is shown in Fig. 5.6.
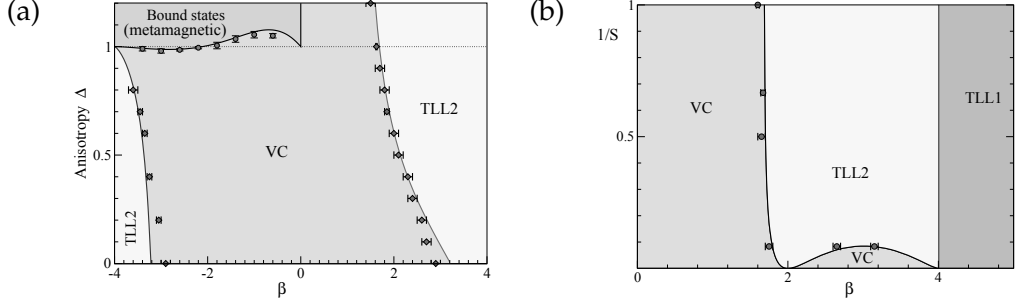
Fig. 5.7: (a) Phase diagram of anisotropic ($J_1^z/J_1 = J_2^z/J_2 = \Delta$) frustrated $S = 1$ chain below the saturation field. (b) Phase diagram of the isotropic frustrated Spin-S chain below the saturation field as function of S and β. Symbols correspond to the transition points extracted from DMRG calculations.

We use DMRG calculations for several small but finite fillings $\rho = 0.2 - 0.05$ to confirm this analytical result. Generally, there is a good agreement between numerical and analytical findings. The cut through the phase diagram in Fig. 5.5 for fixed ρ and U clearly shows a finite region where the momentum distribution shows two peaks, but no chirality is found. Furthermore we extract the central charge c which is consistent with this analysis. The obvious discrepancy between numerical and analytical results may be explained by the fact that DMRG calculations have to be performed at a finite density and proper extrapolation to $\rho \to 0$ remains difficult. Since the amplitude of order parameters such as κ vanishes with vanishing density $\rho \to 0$ this poses further restrictions to the numerical method.

5.2.5   The frustrated spin-S chain

The before-mentioned approach has been introduced and studied both analytically and numerically in Ref.[37] in collaboration with A. Kolezhuk, F. Heidrich-Meisner and T. Vekua in the context of the frustrated spin-S chain model

$$
\begin{aligned}
\mathcal{H} &= \sum_n \Big\{ \frac{J_1}{2}(S_n^+ S_{n+1}^- + S_n^- S_{n+1}^+) + J_1^z S_n^z S_{n+1}^z - H S_n^z \\
&+ \frac{J_2}{2}(S_n^+ S_{n+2}^- + S_n^- S_{n+2}^+) + J_2^z S_n^z S_{n+2}^z \Big\},
\end{aligned} \tag{5.17}
$$

where $S_n^\pm$ and S_n^z) are spin-S operators acting at site n. J_1, J_1^z and J_2, J_2^z are nearest-neighbor (NN) and next-nearest neighbor (NNN) interactions. The dilute limit corresponds to a large external magnetic field H close below saturation magnetization. For convenience we use the parameter $\beta = J_1/J_2 = 1/j$. The description and derivation of the two-component particle model is completely equivalent to the bosonic case as discussed above. The main difference is given by the spin-commutation relations which lead to distinct prefactors in the kinetic energy part. The 2-particle
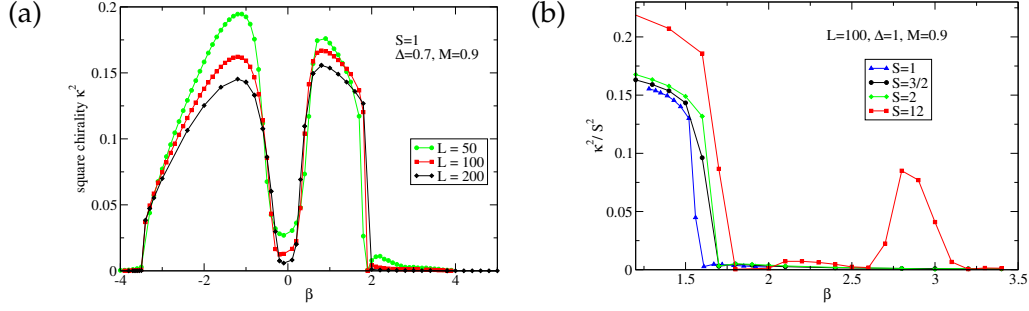
Fig. 5.8: (a) Chirality order parameter κ^2 for frustrated antiferromagnetic $S = 1$ chain for $\Delta = 0.7$, at fixed value of the magnetization $M = 9/10$, as a function of the frustration parameter $\beta = J_1/J_2$. (b) κ^2 for frustrated isotropic antiferromagnetic spin-S chains ($M = 9/10$, $L = 100$).

Schrödinger-equation is described by the following system of equations:

$$\Omega_0 C_0 = 2\sqrt{S(2S-1)}\left(J_1 C_1 \cos\left(\frac{K}{2}\right) + J_2 C_2 \cos(K)\right),$$

$$(\Omega_0 - J_1^z)C_1 = 2J_1\sqrt{S(2S-1)}C_0 \cos\left(\frac{K}{2}\right) + 2SJ_1 C_2 \cos\left(\frac{K}{2}\right) + 2SJ_2(C_1 + C_3)\cos(K),$$

$$(\Omega_0 - J_2^z)C_2 = 2J_2\sqrt{S(2S-1)}C_0 \cos(K) + 2SJ_2 C_4 \cos(K) + 2SJ_1(C_1 + C_3)\cos\left(\frac{K}{2}\right),$$

$$\Omega_0 C_r = 2SJ_1 \cos\left(\frac{K}{2}\right)(C_{r+1} + C_{r-1}) + 2SJ_2 \cos(K)(C_{r+2} + C_{r-2}) \quad (r \geq 3).$$

$$(5.18)$$

For the spin model we denote in the following the chiral Luttinger liquid phase (analog to the bosonic CSF phase) as vector-chiral (VC) phase, the two(one) component (Tomonaga-)Luttinger-liquid phase will be simply denoted TLL2 (TLL1) corresponding to the 2SF (SF) phase.

In Fig. 5.7 (a) we present the phase diagram for model (5.17) for the $S = 1$ case in both antiferromagnetic $\beta > 0$ and ferromagnetic $\beta < 0$ regimes as function of the frustration and the anisotropy $\Delta = J_1^z/J_1 = J_2^z/J_2$ including detailed numerical evidences for the applicability of the analytical approach. For this case the agreement of analytical (straight line) and numerical results (diamonds) is very good. Fig. 5.8 (a) shows the chirality κ^2 for a cut through the phase diagram of Fig. 5.7 (a). Interestingly the TLL2 phase strongly increases with increasing anisotropy. On the ferromagnetic side a region of a dilute magnon-gas with and effective attraction is found for $\Delta \gtrsim 1$. Numerically here we observe the emergence of macroscopically large magnon bound states. In the magnetization curve $M(H)$ this so called meta-magnetic behavior leads to a macroscopically large jump from saturation magnetization to a finite value of M (see section 5.5 for more details and examples on this method in a different context). The pink circles in Fig 5.7 (a) depict the onset of meta-magnetism as obtained from DMRG calculations.

While for small spin S for $\beta > 0$ one observes just one phase-transition from the VC to the TLL2 phase around $\beta \simeq 1.6$, remarkably, for $S \geq 12$ one encounters a revival of the VC phase as shown in Fig. 5.7 (a). We verified the possibility for three consecutive TLL2-VC transitions simulating a spin $S = 12$ model in the dilute limit (cf. the chirality data shown in Fig. 5.8 (b)).

5.3 Quantum phases of ultra-cold bosons in zig-zag optical lattices

In the following we will discuss the physics of commensurate fillings (ρ = 1/2, ρ = 1, ...) where one may observe additional gapped, Mott-insulators (MI) or dimer-phases (D). We will in detail examine the possibility of exotic gapped chiral phases, which present an excitation gap as well as non vanishing chiral currents. At unit filling we are able to confirm the presence of a chiral Mott insulator. Finally we present a full phase diagram for the grand canonical ensemble including a detailed picture of the interplay of SF, 2SF and CSF phases at finite fillings.

  Part of the following discussion is based on the publication [38] which was developed in collaboration with L. Santos and T. Vekua.

5.3.1 Unit filling

At the Lifshitz point the single particle dispersion relation becomes quartic close to the single minimum at $k = \pi$, i.e. $\epsilon(k) \sim (k - \pi)^4 + \cdots$. Due to the flatness of the dispersion-relation, the effective mass

$$m = (\partial^2 \epsilon(k)/\partial k^2)^{-1}_{k=\pi} = \frac{1}{-2J_1(1 - 4j)} \tag{5.19}$$

diverges. Hence, even vanishingly small interactions become relevant at commensurate fillings. The effect, that a constrained mobility may largely enhance the role of interactions, has been studied also for exactly flat bands in e.g. Kagome or saw-tooth lattices [238] (see also section 5.7).

  In Fig. 5.9 we present the phase diagram for unit filling as function of the frustration parameter j and interaction U/J_1 as obtained from DMRG and exact diagonalization simulations. The phase diagram exhibits a rich sequence of phase transitions driven by the frustration j including SF, MI, CMI and CSF phases. Below we will discuss in detail the presence of the tiny CMI phase. Consistent with the above discussion, at small interactions $U \sim J_1/2$ we numerically still observe a
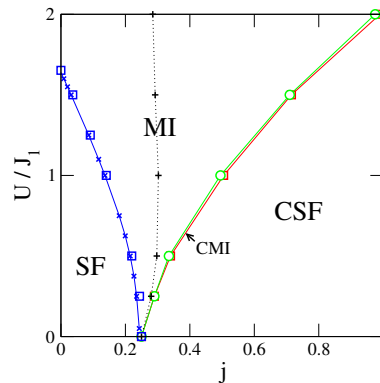

Fig. 5.9: Phase diagram of model (5.4) for unit-filling as function of the interaction strength U/J and the frustration j, with the boundary of the chiral phase (red □) and SF-phases indicated by critical Luttinger parameter K = 2 (green ○ and blue □). x denote the SF-MI phase transition as obtained by the level-crossings (see text). + denotes the Lifshitz-line.
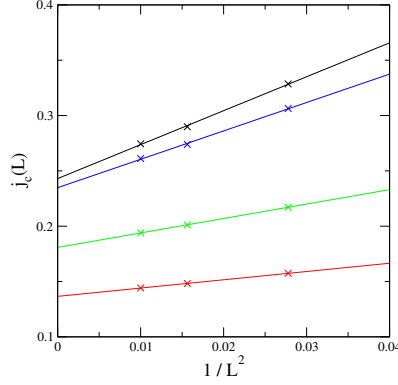
Fig. 5.10: Finite size scaling of the position of the crossing of the excitations ΔE_n and ΔE_4 and extrapolation with a linear function in $1/L^2$ to obtain the $L \to \infty$ limit for (from top to bottom) $U/J = 0.1, 0.5, 1.5$ and 2.

MI phase close to the Lifsitz-point $j = 1/4$. The MI phase splits into two regions of commensurate and incommensurate behavior. This Lifshitz line departs from the non-interacting value $j = 1/4$ and is indicated by the dotted line. Here the quasi momentum distribution acquires a double maximum. Examples will be shown below in Fig. 5.11 (b) and (c).

Within a bosonization treatment the commensurate region may be described by a usual sine-Gordon model (2.25). In weak coupling one finds [38] for the velocity and Luttinger-liquid parameter

$$v(j) \sim \sqrt{\bar{n}U/m\pi^2} = v(0)\sqrt{1-4j}\,, \quad K(j) \sim \sqrt{\bar{n}\pi^2/Um} = K(0)\sqrt{1-4j} \qquad (5.20)$$

where $v(0)$ and $K(0)$ are the values of the single chain. Remarkably, this approximation describes the SF-MI phase transition curve quite well, $U_c(j) \sim U_c(0)\sqrt{1-4j}$.

A bosonization description of the regime $j > 1/4$ may be done starting from the limit of two decoupled chains $J_2/J_1 \to \infty$ and perturbatively adding the zig-zag hopping for small J_1 [239]. For each subchain we introduce two pairs of bosonic fields (θ_1, ϕ_1) and (θ_2, ϕ_2). After forming symmetric and antisymmetric combinations $\theta_\pm = (\theta_1 \pm \theta_2)/\sqrt{2\pi}$, $\phi_\pm = \sqrt{\pi}(\phi_1 \pm \phi_2)/\sqrt{2}$ the effective low-energy model is given by [38]

$$\hat{\mathcal{H}} = \sum_{\alpha=\pm} \frac{v_\alpha}{2}\left[\frac{(\partial_x\phi_\alpha)^2}{K_\alpha} + K_\alpha(\partial_x\theta_\alpha)^2\right]$$
$$+ \lambda\partial_x\theta_+ \sin\sqrt{2\pi}\theta_- - 2\mathcal{M}\cos\sqrt{2\pi}\phi_+ \cos\sqrt{2\pi}\phi_- \,. \qquad (5.21)$$

$v_\pm$, $K_\pm$, and $\mathcal{M}$ are generally phenomenological parameters. In the CSF phase $\partial_x\theta_+ \sin\sqrt{2\pi}\theta_-$ becomes relevant introducing a gap in the anti-symmetric sector and resulting in a finite chirality $\kappa \sim \langle\sin\sqrt{2\pi}\theta_-\rangle$ [240].

Due to the incommensurability in the $j > 1/4$-region the numerical analysis of the phases and phase transitions requires the simulation of large systems. In the commensurate region $j < 1/4$, however, the SF-MI boundary may be analyzed from small system sizes in exact diagonalization calculations: Borrowing the procedure proposed by Refs. [101, 241] we calculate the crossings of the first neutral excitation ΔE_0^1 and four particle excitation ΔE_4^0 at a finite system with L sites and $N = L$ particles for periodic boundary condition in the momentum $k = \pi$ sector. Here we
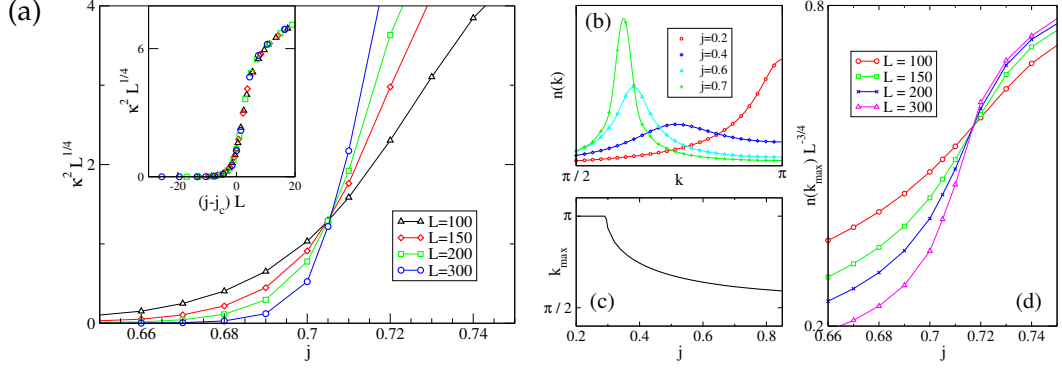
Fig. 5.11: (a) The scaling of chirality $\kappa^2 \cdot L^{1/4}$ close to MI-CMI-transition on the $U = 3$-line. The inset shows the collapse of all finite system size data to one curve. So for $U = 3$ one finds the MI-CMI Ising-phase-transition at $j_1 = 0.705 \pm 0.001$. (b) Momentum distribution $n(k)$ ($U = 3$, $L = 100$). The position of the maximum k_{max} shown in (c) is practically independent of L. At $j \approx 0.3$ the peak departs from π and n_k acquires two inequivalent maxima at $\pm k_{max}$. (d) Scaling of $n(k_{max})L^{-3/4}$ for different L. The crossing of the curves indicates the BKT-transition at $j \approx 0.717 \pm 0.001$.

define the excitation gaps

$$\Delta E_0^1(L, N) = E_0(L, N) - E_1(L, N) \tag{5.22}$$

and

$$\Delta E_M^0(L, N) = \frac{E_0(L, N + M) - 2E_0(L, N) + E_0(L, N - M)}{2} \tag{5.23}$$

with the ith energy-level $E_i(L, N)$ of a system of L-sites and N particles. Without any restriction of the local bosonic Hilbert space (i.e. keeping at most N particles on each site) we are able to calculate finite system size crossings for $L = 6, 8$ and 10 which may be extrapolated linearly with $1/L^2$ to the thermodynamic limit as shown in Fig. 5.10. The SF-MI phase boundary connects to the well known 1D BH-model result at $j = 0$, $U \simeq 3.3J_1$ as discussed in chapter 2.

The level crossing analysis is perfectly consistent with our DMRG calculations in which we may extract the Luttinger liquid parameter K from the behavior of single particle correlations functions, known to be $K = 2$ at the BKT transition point. In the following we will discuss this method more in detail for the second BKT-type transition in the region of incommensurate correlations.

5.3.2 The chiral Mott-insulator

Interestingly, bosonization analysis [38, 230] suggests the possible existence of a gapped chiral phase, the chiral Mott-insulator (CMI), at the boundary between MI and CSF phase. Due to symmetry considerations going from the MI to the CSF phase the system may first undergo an Ising-type phase-transition where chirality sets in but the excitation gap remains. The transition from the CMI and CSF phase is of BKT type, where the gap closes.

Typically, gapped chiral phases are very narrow and due to the sequence of Ising and BKT transitions very difficult to observe numerically. For spin systems
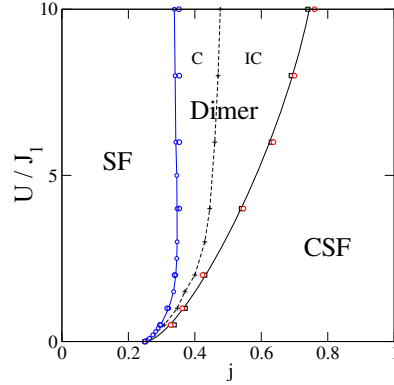
Fig. 5.12: Phase diagram for bosons as a function of the frustration parameter j and on-site interaction U at half filling. □: boundary of chiral phases characterized long-range ordered chirality-chirality correlations $\langle \kappa_i \kappa_j \rangle$, ○: SF-phases indicated by critical Luttinger parameter $K = 0.5$. + characterizes the transition between incommensurate and commensurate behavior.

the existence of a chiral-Haldane and a chiral-Large-D phase was indicated within an infinite DMRG approach by Hikihara et al. [232, 233] for zig-zag spin chains. Dhar et al. [242, 243] proved the emergence of an intermediate CMI-phase for the fully-frustrated Bose-Hubbard-model (see chapter 10). Here we will modify the procedure presented in the latter work, which allows for the study of the type of the phase transitions within open-boundary finite size DMRG-calculations.

In order to study the phase transitions to the chiral phases, we extract the chiral order parameter κ from the saturation behavior of the chirality-chirality correlation-functions at long distances $\kappa^2 = \lim_{|i-j| \to \infty} \langle \kappa_i \kappa_j \rangle$. In a plot of finite system size data $\kappa^2 \cdot L^{1/4}$ over $L(j - j_c)$ all curves collapse to one line (cf. inset of Fig. 5.11 (a)). Hence, the transition between chiral and non-chiral phases is unambiguously of Ising-type, showing the correct scaling relations. The transition can be located precisely by the intersection of $\kappa^2 \cdot L^{1/4}$ lines.

For the definition of the subsequent BKT-transition to the CSF phase, we calculate the Luttinger-Liquid-parameter K from single-particle-correlation function $G(i, j)$. We fit the correlations to $G(r)^{1/2K} \cos(\omega x + \phi)$ with $G(r)$ including conformal corrections for finite system sizes (2.26). To get a lower bound for the transition point a power law fit has been applied to shorter distances after dividing out incommensurate oscillations. Both fitting procedures suffer from finite size corrections.

A more accurate estimate of the BKT-transition point is provided by the analysis of the quasi-momentum distribution $n(k)$ [242, 243]. Since $G_{ij} \sim e^{-iQ(i-j)}|i - j|^{-c}$ with $c = 1/4$ at the BKT-transition, $n(k)$ has a maximum at Q and its height depends on system size as

$$n(Q) \approx \sum_{i,j} e^{iQ(i-j)} G_{ij} \sim \sum_i \zeta(c, i) \sim L^{1-c} . \qquad (5.24)$$

This behavior can be seen in Fig. 5.11 (d) showing a nice intersection of $n(k_{max}) \cdot L^{c-1}$.
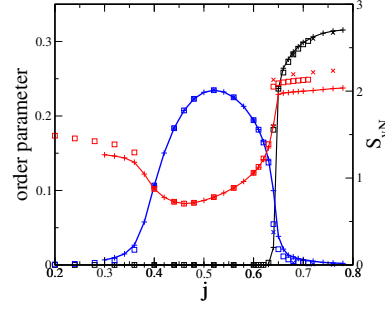
Fig. 5.13: Chirality, dimerization and entanglement entropy for half filled BH-model on a triangular ladder (U = 6). The values are taken from iDMRG calculation for $M = 100$ (+), $M = 200$ ($\square$) and $M = 300$ ($\times$)

5.3.3   Half filling

Model 5.4 reduces for the hardcore-boson limit ($U \to$ inf) at half filling to the frustrated spin-1/2 XY-model without external magnetic field

$$\hat{\mathcal{H}} \ = \ \sum_i J\left[(\mathbf{S}_i \mathbf{S}_{i+1})_{XY} + j(\mathbf{S}_i \mathbf{S}_{i+2})_{XY}\right] . \tag{5.25}$$

where $(\mathbf{S}_i \mathbf{S}_{i+1})_{XY} \equiv b_i^\dagger b_i + $ H.c. and b_i being hardcore bosons, $(b_i^\dagger)^2 = 0$. The ground-state phase-diagram of this model [229, 234] exhibits a SF(XY)-phase for $j \lesssim 0.33$, a gapped dimer-phase with non-vanishing dimerization, $\mathcal{O}_D = b_i(b_{i+1}^\dagger + b_{i-1}^\dagger)$, and for sufficiently large $j \gtrsim 1.32$ [234] a CSF phase. Numerical studies [234] apparently exclude the possibility of an intermediate gapped dimer-chiral phase. In the following we study the fate of these phases at finite values of U/J_1. The phase-diagram is shown in Fig. 5.12. Interestingly, due to the quartic behavior of the single-particle dispersion, as discussed above, all three phases survive in the limit of $U \to 0$.

The dimer and chiral order parameters can be calculated numerically by analyzing the long range behavior of dimer-dimer and chirality-chirality correlations. For open chains also the local dimerization is non zero. Fig. 5.13 shows a cut through the phase diagram 5.12 at $U/J_1 = 6$ as obtained by iDMRG calculations. Dimer and
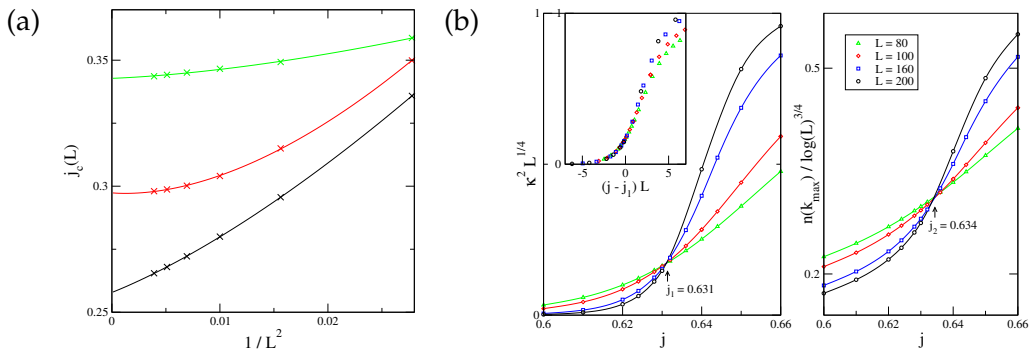

Fig. 5.14: (a) Finite-size-scaling of the position $j_c(L)$ of the crossings of neutral and charged excitations for the SF-D transition from exact-diagonalization and DMRG calculations (periodic boundary conditions) for (from bottom to top) $U = 0.1, 1, 12$. (b) Scaling of chirality κ (left) and momentum distribution (right) close to the D-CSF transition (U=6).
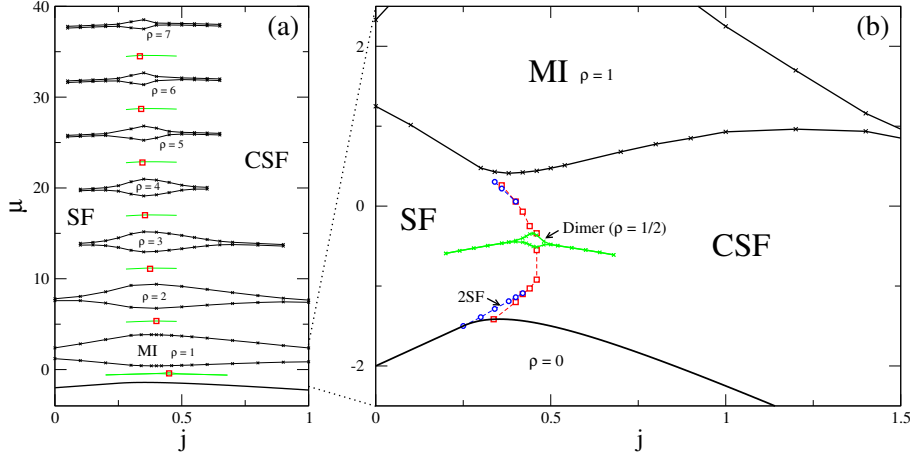
Fig. 5.15: Quantum phases of the bosonic zig-zag model within grand canonical ensemble for chemical potential μ and frustration j for $U = 6J$. (a) MI phases at high filling-factors (small systems up to $L = 40$ sites, high fillings above $\rho = 2$ are considered by restricting particle fluctuations to $\rho - 2, \rho - 1, \ldots \rho + 2$ particles). Green straight lines illustrated the line of half integer filling $\rho = n + 1/2$ with integer n. The red square depicts the onset of chirality. (b) Detailed results for the low filling region. MI and dimer boundaries are extrapolated results for finite size scaling from $L = 40 - 200$ sites. The points at $\rho = 0$ are taken from analytical results.

chiral phases can be identified clearly by the corresponding order parameter. Additionally we display the entanglement entropy which is constant with respect to system size or matrix dimension in the gapped Dimer phase.

The SF-D phase transition may be analyzed precisely by level-spectroscopy [229]. It is characterized by the crossing of the neutral excitation ΔE_0^1 and first charged excitation ΔE_1^0. In Fig. 5.14 we show the finite-size data with up to $L = 16$ sites. In order to obtain precise results even in the limit of low interactions we do not restrict local bosonic Hilbert space (i.e. $n_{max} = L/2$). As shown in Ref. [229] the transition point scales like $j_c + \alpha/L^2 + \beta log(L)/L^4 + \ldots$ and the data in Fig. 5.14 (a) fits well to this behavior.

In Fig. 5.14(b) the scaling behavior of chirality at the D-CSF is analyzed. Close to the phase transition the scaling may be consistent with a Ising phase transition. Assuming a scaling of the single particle correlations as $G(i,j) \sim \frac{log(|i-j|)^{1/2}}{x}$ [35] at the phase transition to the gapless chiral phase, we analyze in analogy to the previous section the scaling behavior of the peak of the quasi momentum distribution, for which follows $n(k_{max}) \sim log(L)^{3/4}$ as shown in Fig. 5.14 (b). The extracted transition points are, within the error bars, consistent with the onset of chirality. Hence our study does not indicate any hint of an intermediate dimer-chiral phase in this regime.

5.3.4 The grand-canonical phase diagram

While up to now we have focused on the physics at a fixed number of particles, it is in particular of experimental relevance to study the grand-canonical phase diagram. In Fig. 5.15 we display the phase diagram as function of j and chemical potential μ for $U = 6J_1$.

As shown in Fig. 5.15 (a) close to the Lifshitz point MI phases may be observed

even for relatively high filling-factors $\rho > 7$, as expected due to the quartic dispersion relation. Note, that for $j = 0$ only one Mott-lobe can be observed for this value of U (see chapter 2). We can only resolve the Dimer-gap at half integer filling for $\rho = 1/2$. The onset of chirality at half filling slowly approaches the classical result $\rho \to \infty$ at which the SF-CSF transition happens at $j = 1/4$.

In Fig. 5.15 (b) we display in detail the phase boundary between 2SF and CSF phases. The SF-2SF phase here can be identified by a cusp in the $\mu - \rho$–curve in general characterizing a change in the number of gapless modes (see also section 5.6 for further examples). The finite density results are consistent with the phase transition points obtained in the dilute limit $\rho \to 0$ (see section 5.2).

5.4 Bosons with a 3-body hardcore constraint

While in traditional many-body paradigms interactions are typically of two-body type, as discussed in chapter 2 three-particle interactions in the form of a three-body hard-core constraint due to large three-body-losses [106], or induced finite three- and even four-body on-site interactions [113, 114] have received a lot of attention recently. Here we discuss the effect of three-body on-site interactions

$$U_3 \sum_i \hat{n}_i(\hat{n}_i - 1)(\hat{n}_i - 2) \tag{5.26}$$

in model (5.4). The following results have been developed in collaboration with L. Santos and T. Vekua and published in Ref. [38].

5.4.1 Emergence of HI-phase for 3-body interactions

Bosonic models with a three-body constraint $(\hat{b}_i^\dagger)^3 = 0$ ($U_3 \to \infty$) may to a large extent be mapped to spin-1 systems. As shown in Ref. [244] the exact mapping may be given as

$$\hat{n}_i = 1 - S_i^z , \quad \hat{b}_i^\dagger = \frac{2 + \sqrt{2}}{4} S_i^- - \frac{2 - \sqrt{2}}{4}(S_i^z S_i^- + S_i^- S_i^z) . \tag{5.27}$$
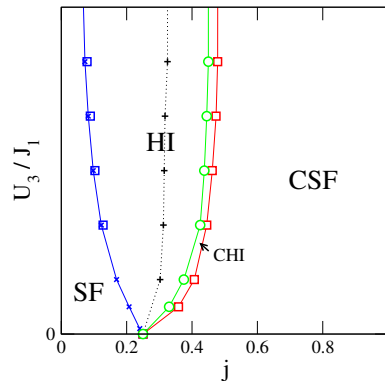

Fig. 5.16: Emergence of the HI phase for a finite three body repulsion U_3. □ depicts the SF-boundary as defined by critical exponents. The SF-HI boundary is consistent with the result obtained by level-spectroscopy (×). The onset of chirality is shown as ◯. + indicated the Lifshitz-line.
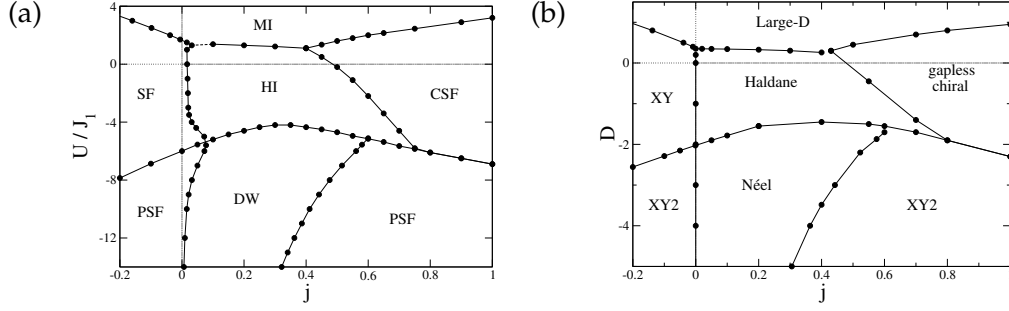
Fig. 5.17: (a) Phase diagram of constraint bosons $U_3 \to \infty$. (b) Phase diagram of the corresponding spin-1 system (5.28).

Neglecting particle-hole symmetry breaking terms for model (5.4) we arrive at the frustrated spin-1 model

$$\hat{\mathcal{H}}_S \sim \sum_i \left[(\mathbf{S}_i \cdot \mathbf{S}_{i+1})_{XY} + j(\mathbf{S}_i \cdot \mathbf{S}_{i+2})_{XY} + D(S_i^z)^2 \right] \tag{5.28}$$

where $(\mathbf{S}_i \cdot \mathbf{S}_j)_{XY} \equiv S_i^x \cdot S_j^x + S_i^y \cdot S_j^y$, the single-ion anisotropy D and the next-nearest neighbor frustrating exchange j. This model has been extensively studied in Refs. [232, 233, 245]. Hence, for constraint bosons on a zig-zag lattice we expect the possibility for a Haldane-insulating phase due to geometric frustration in the absence of long range interactions as known from the spin-1 case. As shown in Ref. [38] the HI phase can be described by a sine-Gordon model (5.21) with $K < 2$. Due to $\mathcal{M} < 0$ a hidden string order (2.38) is selected.

Our DMRG-results indicate that indeed at the Lifshitz-point, $j = 1/4$, a HI is stabilized at $U = 0$ for arbitrarily weak U_3 as presented in Fig. 5.16. As for the case of a 2-body interaction from section 5.3 we obtain a finite region with a coexistence of a gap, string order and chirality, the chiral Haldane-insulator (CHI). In the limit of $U_3 \to \infty$ the results are consistent with the observation of the chiral Haldane-phase in Ref. [233] for spin-1 case.

5.4.2   The phase diagram for 3-body constraint bosons

In the following we derive a detailed phase diagram for the limit $U_3 \to \infty$ presented in Fig. 5.17 (a). Given the correspondence to the spin-1 system this extends the work in [230, 232, 233, 239] to the case of vanishing nearest-neighbor interactions and negative single-ion anisotropies.

Starting from the HI phase as discussed above for $U = 0$, increasing $U > 0$ can induce a Gaussian HI-MI phase transition. This resembles the phase transition between Haldane and large-D phases induced by single-ion anisotropy in spin-1 chains [101]. This transition is well described by the onset of parity-order (2.19) $\mathcal{O}_P^2$ in the MI phase and a vanishing string order (2.38) $\mathcal{O}_S^2$ as can be seen in Fig. 5.18 (a). The energy gap vanishes at the Gaussian transition line. For twisted boundary conditions this transition is also characterized by ground state level crossing [246].

The SF phase which occupies a large part of the non-frustrated phase diagram for $j < 0$ is separated from the MI and HI by BKT transitions. The CSF to MI and HI boundary may host tiny CMI and CHI phases (Fig. 5.18 (b)) which are not resolved in Fig. 5.17. As described in section 5.3 the analysis of the energy level structure offers a precise estimate of BKT-transition lines in the commensurate regime.
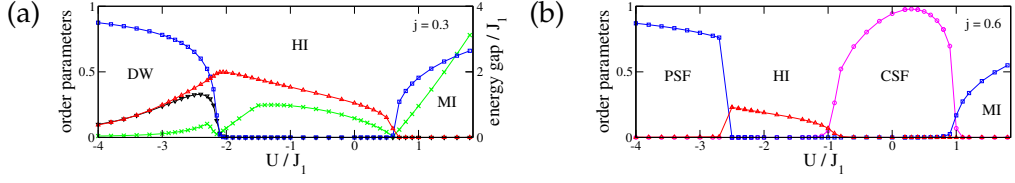
Fig. 5.18: Order parameters $\mathcal{O}_P^2$ (□), $\mathcal{O}_S^2$ (△), $\mathcal{O}_{DW}$ (▽), κ^2 (○) and energy gap (×) as function of U/J for constrained bosons on the (a) $j = 0.3$, (b) $j = 0.6$ line ($N = 160$). The parity, as defined in the Mott state, must get an additional oscillating factor in the DW phase $\mathcal{O}_P^2 \to (-1)^{i-j}\mathcal{O}_P^2$.

We again analyze the crossing between ΔE_4^0 and the neutral excitation ΔE_0^1; the positions of level crossings can be extrapolated to $L \to \infty$ with an $1/L^2$-law for constraint/spin-1 case from system sizes up to 16 sites (see Fig. 5.19) and agree well with the estimates from the calculation of Luttinger-liquid-parameters.

In Fig. 5.17 (b) we present as a comparison the phase diagram of the pure spin-1 system (5.28). The numerical-analysis suggests that the BKT-transition separating XY-Haldane and XY2-Néel-phases is located exactly at $j = 0$. In the constraint BH-model however this BKT-transition line is shifted to the positive j site. Similar behavior has been reported by Ref. [244] for the case of a BH with next-nearest neighbor interactions.

Pair superfluid phase

Interestingly due to 3-body constraint $U_3 \to \infty$ the bosonic model (5.4) remains stable even for attractive 2-body interactions $U < 0$. Analogously to the XY1 to XY2 transition studied in a spin-1 systems [246] for sufficiently large on-site attractions $-U$ the bosons may form a superfluid of bound pairs. This pair superfluid phase (PSF) is characterized by a non-vanishing parity order parameter $\mathcal{O}_P^2$, contrary to the MI phase with a staggered oscillation. For the non-frustrated BH model the PSF phase has been studied in Ref. [186].

The presence of the PSF phase may be understood from the large coupling limit $U \to -\infty$. Here, the ground-state manifold, given by the $\hat{\mathcal{H}}_{int}$ eigenstates $U_0 = \{\otimes_{i=1\ldots N} |n\rangle_i, n = 0, 2\}$, is 2^L-fold degenerate. We may introduce a pseudo-spin-1/2,
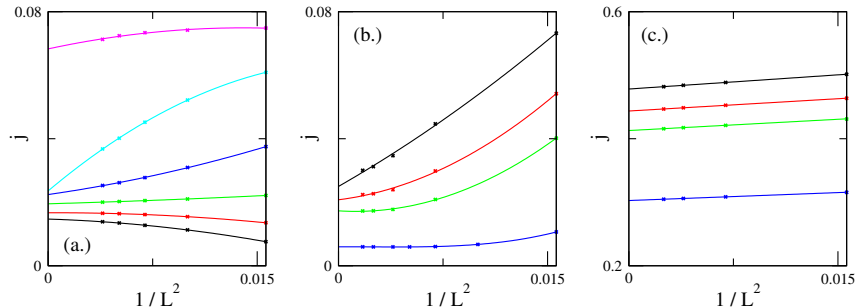

Fig. 5.19: Level-crossing analysis for constraint bosons for different BKT-transition-lines (see text). (a.) HI-SF transition for (from bottom to top) $U = 0, -1, -2, -3, -4, -5$. (b.) PSF-DW-transition for $U = -15, -10, -9, -8$. (c.) DW-PSF-transition for the same values as in (b.). Here the intersections accurately fit an $c_0 + c_1 L^{-2}$ behavior.
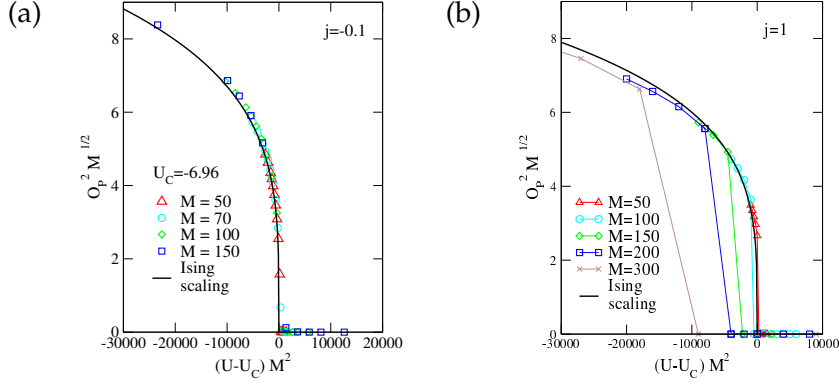
Fig. 5.20: (a) Scaling of Parity-Order-Parameter for PSF to SF transition with Matrix-dimension M accurately follows Ising transition laws. (b) PSF to CSF transition shows deviations from Ising-scaling exhibiting a steep jump in parity order.

identifying $|0\rangle \to |\downarrow\rangle, |2\rangle \to |\uparrow\rangle$ and define the pseudo-spin operators

$$\tau_i^- \to (-1)^i b_i^2/\sqrt{2} \,,$$
$$2\tau_i^z \to b_i^\dagger b_i - 1 \,. \qquad (5.29)$$

A standard second order degenerate perturbation theory [247] lifts the degeneracy and the system is described by an effective Hamiltonian

$$\hat{\mathcal{H}}_{eff}(E) = P_0 H_{tun} P_0 + P_0 \hat{\mathcal{H}}_{tun} P_1 \frac{1}{E - P_1(\hat{\mathcal{H}}_{tun} + \hat{\mathcal{H}}_{int})P_1} P_1 \hat{\mathcal{H}}_{tun} P_0 \qquad (5.30)$$

where P_0 is a projector to U_0 and $P_1 = 1 - P_0$. In terms of the spin-1/2 operators this may be written as

$$\hat{\mathcal{H}}_{\frac{1}{2}} = \frac{J_1^2}{|U|} \sum_i \left[\tau_i \tau_{i+1} + j^2 \left(\tau_i^z \tau_{i+2}^z - \tau_i^x \tau_{i+2}^x - \tau_i^y \tau_{i+2}^y \right) \right]. \qquad (5.31)$$

For $j = 0$ we are at the $SU(2)$-symmetric Heisenberg point. The ferromagnetic $j^2 J_1$ terms break the symmetry down to $U(1)$ and a gapless XY-phase of the spin-1/2 chain is expected (see Ref. [38]), which corresponds to the PSF phase.

The phase transition between the SF and the PSF at unit filling is of Ising type. Its position can be extrapolated very precisely from level-crossing between one-particle $\Delta E_1^0(L)$ and two-particle-excitation-gap $\Delta E_2^0(L)$. In Fig. 5.20 (a) we study the scaling of $\mathcal{O}_P^2$ at this phase transition using iDMRG calculations. As shown in [248] the correlation length for the quantum Ising model scales like $\xi_M = M^\kappa$ with $\kappa \approx 2$, where M denotes the Schmidt/Matrix-dimension. Using Ising critical-exponents $\beta = 1/8$, $\nu = 1$ the order parameter behaves like

$$\mathcal{O}_P^2 = M^{-2\beta\nu} f\left((U - U_c)M^{\frac{1}{\nu}}\right)$$

The collapse of the data to one curve confirms the Ising nature of the SF-PSF phase transition.

Also for large values of $j > 0$ we observe a PSF phase for sufficiently attractive values of $-U$. Our DMRG simulations show a narrow region where a direct, apparently first-order, HI-PSF transition occurs, characterized by discontinuous jumps of
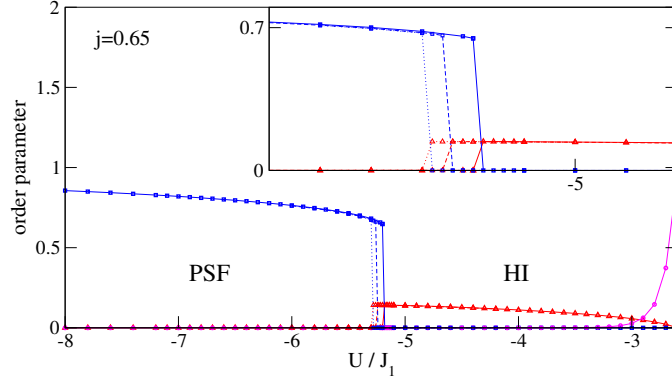
Fig. 5.21: Parity-order $\mathcal{O}_P^2$ ($\square$) and string-order $\mathcal{O}_S^2$ ($\triangle$) parameters for constrained bosons ($j = 0.65$) at to the HI - PSF transition of iDMRG calculations for different Matrix/Schmidt-dimensions: $M = 50$ (dotted line), $M = 100$ straight line, $M = 200$ (dashed line). The transition point shifts slightly with increasing M.

$\mathcal{O}_{S,P}^2$ (Fig. 5.21). Although one might guess an Ising character of the phase transition between the broken discrete parity symmetry CSF phase to the restored symmetry PSF phase, this nature cannot be confirmed from the behavior of the order parameters as illustrated in Fig. 5.20. An increasing discontinuity of $\mathcal{O}_P^2$ and κ hints to a weakly first-order nature of this phase transition.

Charge density wave phase

Increasing the density of doublons in a HI phase with a diluted charge density wave order one should naturally expect a transition to a fully (antiferromagnetically) ordered CDW phase. Indeed, for small $j > 0$ at attractive U we observe a CDW phase separating the two PSF regions (Fig. 5.17). Fig. 5.18 (a) shows for $U/t < -3$ a region with both $\mathcal{O}_S^2 > 0$ and $\mathcal{O}_{CDW} > 0$.

Interestingly, in the effective strong coupling model (5.31) the gapped CDW phase may be induced by third order terms corresponding to the ring exchange along the elementary triangle of the zig-zag chain, with amplitude jJ_1^3/U^2 [38]. Hence, the CDW extends all the way into the $U \to -\infty$ limit consistent with the numerical simulations. Its width decreases as $\sim J_1/|U|$.

As shown in Fig. 5.18 (a) the energy gap vanishes at this Ising type transition line between HI and DW phase. The PSF-DW transition is of BKT-type and can be characterized by energy level crossing between first neutral excited and two-particle-excitation (Fig. 5.19 (b) and (c)). At this point both density-density $\langle n_i n_j \rangle$ and two-particle $\langle (b_i^\dagger)^2 (b_j)^2 \rangle$ correlations coincide and decay as $\log^{1/2}(x)/x$.

5.5   Staggered fluxes and Dzyaloshinskii-Moriya interactions

Recently, lattice modulation experiments [137] have shown the possibility to generate effective complex hopping amplitudes by applying a modified shaking-scheme that explicitly breaks certain time reversal symmetries [249]. In Ref. [137] the fol-

lowing forcing (see also Fig. 5.22 (a)) was used

$$F(t) = \begin{cases} F_0 \sin(t/T_1) & \text{for } 0 < t < T_1 \\ 0 & \text{if } T_1 < t < T \end{cases} .$$ (5.32)

The effective complex hopping matrix element is

$$J_{eff} = \frac{T - T_1}{T} e^{iK\frac{T_1}{T}} + \frac{T_1}{T} \mathcal{J}_0(K) e^{iK\frac{T-T_1}{T}}$$ (5.33)

with $K = \frac{F_0 d}{\omega_1}$ in a one dimensional lattice with lattice constant d. The use of a tri-angular lattice, or any similar geometry without pairwise parallel edges, allows for the creation of finite, but staggered, fluxes. This technique was employed in Ref.[250] for the simulation of classical spin XY models in a triangular lattice with tunable gauge fields. A modification as proposed by Ref. [249] with different onsite potentials could be used to extend these schemes for uniform fluxes or non abelian gauge fields. In the following we will show how staggered fluxes in triangular ladders, which as well plays a role in traditional solid state models, have an important effect on the properties of the ground-state phase diagram.

In general the zig-zag ladder with staggered fluxes may now be written as

$$\hat{\mathcal{H}} = -J \sum_i e^{i\phi/2} \hat{b}_i^\dagger \hat{b}_{i+1} - J' \sum_i \hat{b}_i^\dagger \hat{b}_{i+2} + \frac{U}{2} \sum_i \hat{n}_i(\hat{n}_i - 1) - \mu \sum_i \hat{n}_i .$$ (5.34)

We may split the complex hopping part

$$-iD \sum_j \left[b_j^\dagger b_{j+1} - b_{j+1}^\dagger b_j \right]$$

with an amplitude $D = \Im J_{eff}$. For the case of hardcore bosons $U \to 0$ this may be rewritten as Dzyaloshinskii-Moriya[251, 252] (DM) like interaction

$$-D \sum_j \left(\mathbf{S}_j \times \mathbf{S}_{j+1} \right)^z .$$ (5.35)

A finite staggered flux $|D| > 0$ breaks parity symmetry such that the ground state acquires a finite chirality, as can be see from the single-particle dispersion

$$\epsilon(k) = J \cos k + J' \cos 2k + D \sin(k) .$$ (5.36)

For any finite $|D| > 0$ the position of the single minimum shifts to a finite momentum $Q \neq 0$ such that even for the non-frustrated chain $\kappa \neq 0$ (see Fig. 5.23 (a)). For $J_2 = 0$ one easily finds $\kappa = D/\sqrt{D^2 + J_1^2}$. For the case of $j > 1/4$ the degeneracy
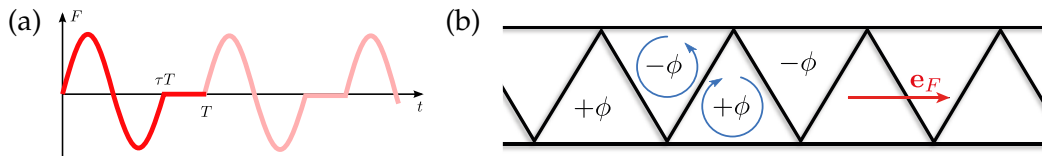

Fig. 5.22: (a) Shaking scheme for the creation of complex hoppings Eq.(5.32). (b) A driving parallel to the legs of the triangular ladder may be employed to create a staggered flux configuration.
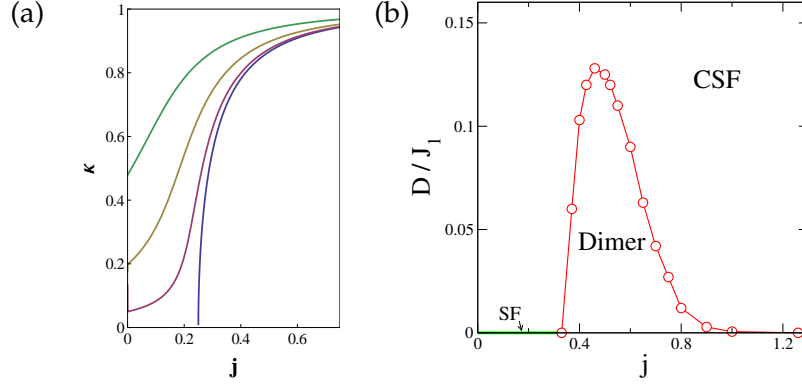
Fig. 5.23: (a) Chirality / helicity κ of model (5.4) for the limit $U \rightarrow 0$ and (bottom to top) $D/J \rightarrow 0$, $D/J = 0.05$, 0.2 and 0.2. (b) Phase diagram of half filled hard-core bosons ($U \rightarrow \infty$) for finite flux $D > 0$. The green line at $D = 0$ marks the non-chiral SF phase.

between the two minima is lifted and one one minimum of $\epsilon(k)$ is lowered (see Fig. 5.24 (a)).

Hence, SF and CSF phases are expected to be adiabatically connected. Fig. 5.23 (b) illustrates this for the case of a half filled strongly interacting bosons in the limit $U \rightarrow \infty$. As discussed in detail in section 5.3 for $D = 0$ SF and CSF phases are separated by a gapped Dimer-phase. For $D > 0$ this phase is destabilized and undergoes a transition to a (C)SF phase. For a finite $D > 0$ we also observe a finite current or chirality within the Dimer phase.

5.5.1 Isotropic ferromagnetic $J_1 - J_2$-model with Dzyaloshinskii-Moriya interaction

DM-interactions play an important role in solid state systems. In particular the isotropic $J_1 - J_2$-model spin-1/2 model with DM interactions has been considered a one-dimensional prototype of the magnetoelectric coupling between electric polarization and magnetization in multiferroic materials [253]. Multiferroics like $LiCu_2O_2$ exhibit simultaneously multiple spontaneous ferroic orderings such as ferromagnetism, ferroelectricity or ferroelasticity [254]. They allow for the steering of the polarization and magnetic-ordering with an external electric field [255, 256] and hence are considered as interesting candidate for possible spintronic and quantum

Fig. 5.24: (a) Single particle dispersion in the presence of a finite flux $D/J_1 = 0.14$, $J_1 = 1$, $J_2 = -1$ (b) Two particle scattering continuum and bound states for the same parameters. (c) Zoom into the $k \approx \pi$ region.
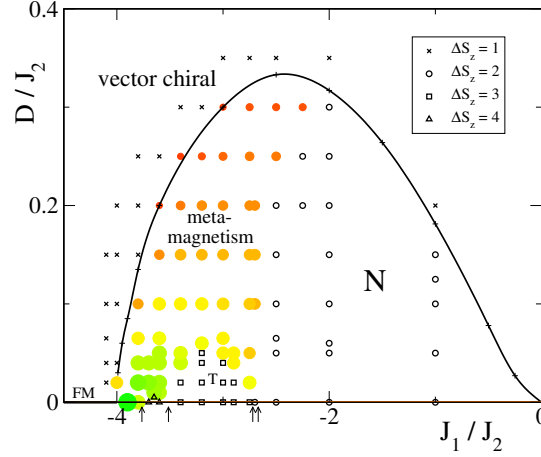
Fig. 5.25: Multi-magnon bound-states and meta-magnetism just below saturation magnetization. The filled circles indicate that for these parameters the system experiences a meta-magnetic ju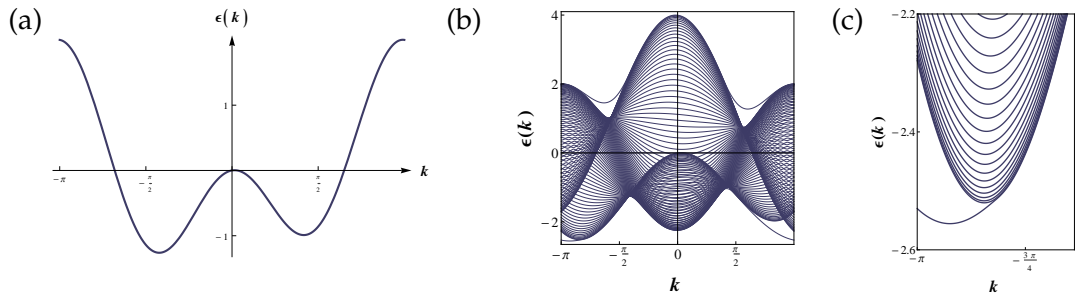mp in magnetization when lowering the magnetic field from saturation magnetization. The size of the circle encodes the height of the jump $\Delta S_z/L$ (big green points indicate jumps of $\Delta S_z/L \approx 0.4$ to ≈ 0.05 for small red points).

information devices.

The full model Hamiltonian is given by [39]

$$\hat{\mathcal{H}} = J_1 \sum_j \mathbf{S}_j \cdot \mathbf{S}_{j+1} + J_2 \sum_j \mathbf{S}_j \cdot \mathbf{S}_{j+2} - B \sum_j \mathbf{S}_j \cdot \mathbf{S}_{j+2} + \mathbf{E} \cdot \mathbf{P} \,. \tag{5.37}$$

J_1 is chosen to be ferromagnetic (< 0) and J_2 antiferromagnetic (> 0) and we study the effect of DM-coupling D for strong magnetic fields B. The coupling between the static electric field $\mathbf{E}$ and the polarization $\mathbf{P}$ may be expressed as

$$\mathbf{E} \cdot \mathbf{P} = D \sum_j \left(\mathbf{S}_j \times \mathbf{S}_{j+1} \right)^z \tag{5.38}$$

where the strength D of the DM like interaction $D \sim E$.

In the context of cold atom experiments a precise simulation of model (5.37) would require the engineering of attractive nearest and repulsive next-nearest neighbor interactions, which could be realized in the zig-zag lattice geometry as introduced in section 5.1 with dipolar atoms or molecules.

The following results have been published in Ref.[39] in collaboration with M. Azimi, L. Chotorlishvili, S. Mishra, T. Vekua, and J. Berakdar.

5.5.2 Multi-polar bound-states and meta-magnetism in large magnetic fields

Interestingly, for the case of ferromagnetic $J_1 > 0$ coupling a series of N-magnon bound states evolves as function of the frustration $\beta = J_1/J_2$. For $J_1/J_2 \to -4$ nematic (N), incommensurate nematic (IN), triadic (T) and quartic (Q) phases are realized for sufficiently high magnetic fields, which are Luttinger liquid phases of two-, three- and four-body bound states. In Fig. 5.25 the $D = 0$ phases at saturation magnetic field are indicated by small arrows

Fig. 5.26: Phase diagram for (a) $J_1/J_2 = -1.0$ and (b) $J_1/J_2 = -3.2$ with spin-density-wave/nematic (N), triadic (T), chiral (VC) and fully polarized phase (F). The big green line marks a macroscopic jump in magnetisation profile.
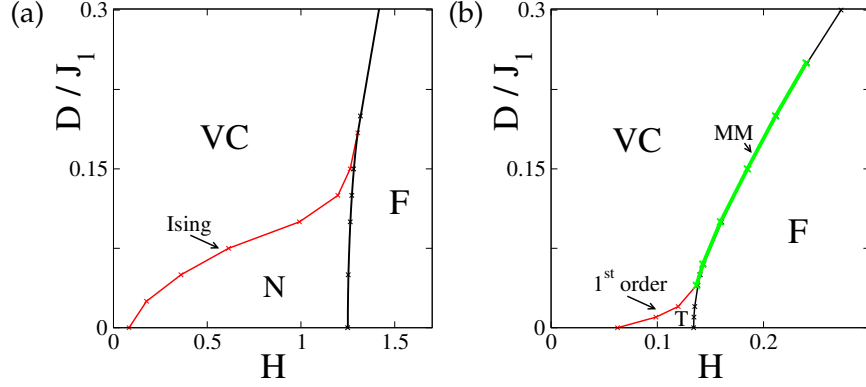
The nematic phase of 2-magnon bound pairs the pair correlation $\left\langle S_i^+ S_{i+1}^+ S_j^- S_{j+1}^- \right\rangle$ shows algebraic decay while single-particle correlation $\left\langle S_i^+ S_j^- \right\rangle$ decays exponentially. Lowering the magnetic field a crossover to a spin density wave (SDW) phase is observed in which density correlation $\left\langle S_i^z S_j^z \right\rangle$ become dominant and finally a phase transition to a CSF phase of single particles. This phase transition may be of first order showing a meta-magnetic behavior, i.e. a macroscopic jump in magnetization at the transition field. Close to J_1/J_2 the meta-magnetic region is expected to extend up to saturation magnetization [257]. The magnetization curves (see Fig. 5.27 (b)) exhibit steps of $\Delta S^z = 1, 2, 3$ or 4 for VC, N/IN, T or Q phases, resp.

For $D > 0$ all these phases acquire a finite chirality κ. This is illustrated in Fig. 5.24 (b) and (c) which shows the 2-magnon bound states below the two-magnon scattering continuum with the minimum shifted away from π. We also analyze multi-magnon bound-states, following the approach from Ref. [258], for $D > 0$. Also in the T and Q phases the lowest excitation shifts to an incommensurate value. Interestingly, the crossings between N, T, and Q bound-states are almost not affected by the presence of the DM-interaction. However, as our DMRG simulations show, these phases are suppressed already for a small $D > 0$. The phase diagram for the strong magnetic field limit is shown in Fig. 5.25.

For $j \lesssim -2$ we find macroscopic jumps below saturation magnetization in the magnetization-profile. The system prefers to form bound states of macroscopic numbers of magnons suppressing the T and Q phases. The transition between the molecular and meta-magnetic phases to the atomic (VC) fluid is for high magnetic fields well described by the boundary between an attractive and repulsive magnon-gas as obtained from 2-particle scattering calculations (see section 5.2). In Fig. 5.25 this boundary, shown as solid line, is consistent with the DMRG simulations.

We now analyze the DM-interaction induced phase transitions between the multi-polar bound-state phases and the atomic vector chiral (VC) phase more in detail. As shown in Fig. 5.25 the three- and four-body multi-polar-phases are extremely sensitive to DM anisotropy. In Fig. 5.26 we study the phase transitions in a finite magnetic field. The T or Q phases are connected to VC via a first order phase transition, possibly with an intermediate macroscopic jump of density (see Fig. 5.27 (a)).
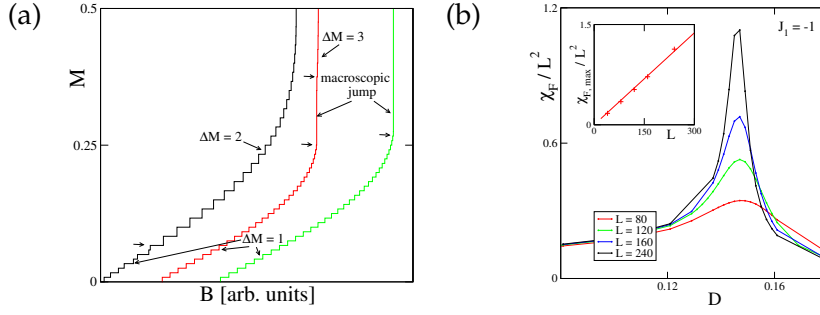
Fig. 5.27: (a) Magnetization curves $M = M(H)$ for $J_1 = -3.2$ and (from left to right) $D = 0, 0.04, 0.08$ ($L = 120$, $J_2 = 1$). (b) Scaling of the fidelity suszeptibility near the nematic to chiral phase transition for $J_1 = -1$ and $M = 0.4$.

Interestingly, the transition between atomic VC and nematic phase may be of Ising type. In Fig. 5.27 (c) the scaling of the fidelity susceptibility χ_D with respect to D reveals the Ising nature of the phase-transition between nematic and vector-chiral phase due a linear scaling of the peak with system size L with respect to the wings (see chapter 4).

5.6 Polar molecules in frustrated triangular ladders

In section 5.4 we have shown how the three-body on-site interactions in the form of a 3-body hard-core constraint may lead to interesting new physics. Recently, it has been proposed how finite three-body nearest-neighbor interactions may be achieved under realistic conditions for a system of polar molecules [103]. Several recent works have studied the effect of the role of inter-site three-body interactions in lattice gases. E.g. in 2D supersolid and Devil's staircase phases [259] or in 1D systems a gapped phase with simultaneous charge-density-wave (CDW) order and bond-order (BO) [260] have been found.

In the following we consider a system of polar molecules in a frustrated triangular ladder as depicted in Fig. 5.28, characterized by the following Hamiltonian

$$\hat{\mathcal{H}} = -J_1 \sum_i (b_i^\dagger b_{i+1} + \text{H.c.}) - J_2 \sum_i (b_i^\dagger b_{i+2} + \text{H.c.})$$
$$+ V \sum_i n_i n_{i+1} + W \sum_i n_i n_{i+1} n_{i+2} . \tag{5.39}$$

Here, we just consider the case of hard-core particles $\left(b_i^\dagger\right)^2 = 0$.

Fig. 5.28: Triangular ladder lattice with two- and three-body interactions, V and W, respectively. The hopping along the rungs and the legs are $J_1 > 0$ and $J_1' < 0$, respectively.
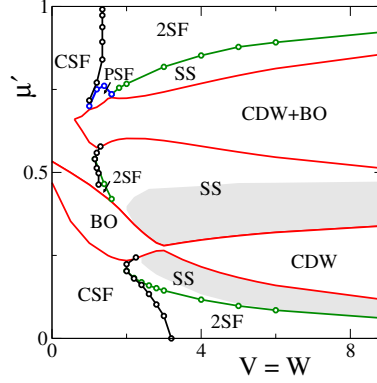
Fig. 5.29: Phase diagram of model (5.39) as a function of μ' and $V = W$, for $J_2 = -J_1 = -1$. Here $\mu' = \frac{9+4\mu}{20W+18}$ is the scaled chemical potential such that $\mu' = 0(1)$ corresponds to the vacuum (full) state. Solid red curves mark the boundaries of gapped phases. The shaded region corresponds to the cSS phase.

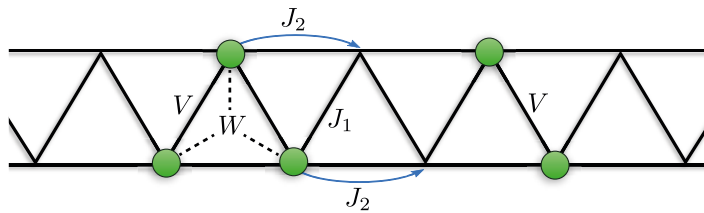In particular we are interested in the appearance of different kinds of supersolid phases in the presence of large two- and three-body interactions V and W. We observe phases with coexisting bond- and supersolid order characterized by the structure-factor

$$S_{BO}(k) = \frac{1}{L^2} \sum_{i,j} e^{ik(i-j)} \langle B_i B_j \rangle, \tag{5.40}$$

where $B_i = b_i^\dagger b_{i+1} + b_{i+1}^\dagger b_i$. The CDW presents a finite value of the density-density structure factor

$$S_{CDW}(k) = \frac{1}{L^2} \sum_{i,j} e^{ik(i-j)} (\langle n_i n_j \rangle - \langle n_i \rangle \langle n_j \rangle). \tag{5.41}$$

The following results and discussion have been published in Ref.[40] in collaboration with T. Mishra and L. Santos. A large part of the DMRG simulations have been performed by T. Mishra in the context of this work.

5.6.1   The ground-state phase diagram

In Fig. 5.29 we present the very rich quantum phases of model (5.39) as function of the chemical potential and the interaction strength for strong frustration $J_1 = -J_2$. The three-body interactions explicitly break particle-hole symmetry, which results in a strongly asymmetric phase diagram for $\rho < 1/2$ and $\rho > 1/2$.

The low filling part of the phase diagram is dominated by the effect of the two-particle interactions. At half filling at small $V \lesssim 3$ the system presents a gapped Dimer-phase , here denoted as bond ordered phase (BO) (see section 5.3). For large V the system favors a CDW phase. The phase transition is of first order as discussed in [261].

Due to the three body interaction for $\rho = 2/3$ we observe another gapped phase, BO+CDW, that possesses both BO and CDW orders simultaneously. The $S_{CDW}(k)$ has a peak at $k = 2\pi/3$. For a chain-lattice the (BO+CDW) phase has previously been observed in [260].

For incommensurate phases we observe the typical structure of subsequent CSF to SF transitions with a possible intermediate 2SF phase (see section 5.3). All these
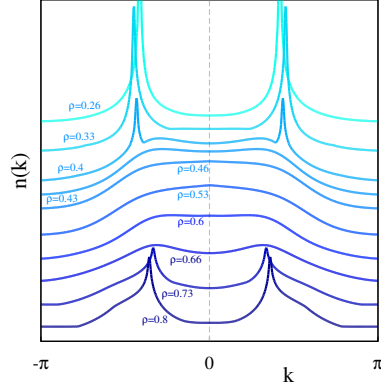
Fig. 5.30: Momentum distribution $n(k)$ for different densities ($V = W = 2.6$, $L = 180$). The single curves have been shifted for clarity. In the 2SF ($\rho = 0.33$, 0.4, 0.73, and 0.8) and the CSF phase ($\rho = 0.26$), $n(k)$ exhibits two peaks at incommensurate momenta $\pm k$. When approaching the SS phase the momentum distribution broadens but still shows two maxima (for $\rho = 0.4$, 0.43, 0.6, and 0.66), characterizing the icSS region. However, at intermediate fillings ($\rho = 0.53$) only one maximum is observed (cSS region).

phases exhibit a supersolid character, hence we denote the one component Luttinger liquid phase as a supersolid (SS). Remarkably, in addition to a finite CDW order we observe a finite coexisting bond order. Figure 5.32 and 5.33 depict the maximum of $S_{BO}(k)$ and $S_{CDW}(k)$ as a function of ρ showing that clearly the system exhibits simultaneous CDW and BO orders not only at the gapped BO+CDW at $\rho = 2/3$, but for incommensurate fillings within the superfluid region. In Fig. 5.32 apart from estimating c we have computed the gap in the entanglement spectrum, $\Delta_{es}(l)$.

Interestingly, the SS phase splits into two regions: In the commensurate supersolid (cSS) we observe a single maximum of the momentum distribution $n(k)$ at $k = 0$. The incommensurate supersolid (icSS) (shown as shaded region in Fig. 5.29) exhibits two maxima of $n(k)$ (see Fig. 5.30). The cSS region grows slowly with increasing $V = W$ (e.g. we do not observe a single maximum for $\rho > 2/3$ for $W = V \lesssim 20$). However, as we show below, in the limit of strong interactions only the cSS phase survives.

5.6.2   Dilute limit

We examine the limit of the dilute bosonic model, mapped into a spin-1/2 model $(0, 1 \rightarrow \uparrow, \downarrow)$, along the lines of the discussion in section 5.2. In the dilute limit the Hamiltonian becomes a J_1–J_2 model with NN and NNN $S^z S^z$-interactions:

$$\hat{\mathcal{H}}_{1/2}^{\text{dilute}} = J_1 \sum_i S_i^+ S_{i+1}^- + J_2 \sum_i S_i^+ S_{i+2}^- + \text{H.c.}$$
$$+ J_1^z \sum_i S_i^z S_{i+1}^z + J_2^z \sum_i S_i^z S_{i+2}^z \tag{5.42}$$

where $S_i^{x,y,z}$ denote the spin operators associated to the site i. For the low-filling limit, the spin couplings are given by $J_1^z = V = W$ and $J_2^z = 0$. The resulting phase diagram is shown in the main panel of Fig. 5.31 (a). By increasing J_1^z one observes the

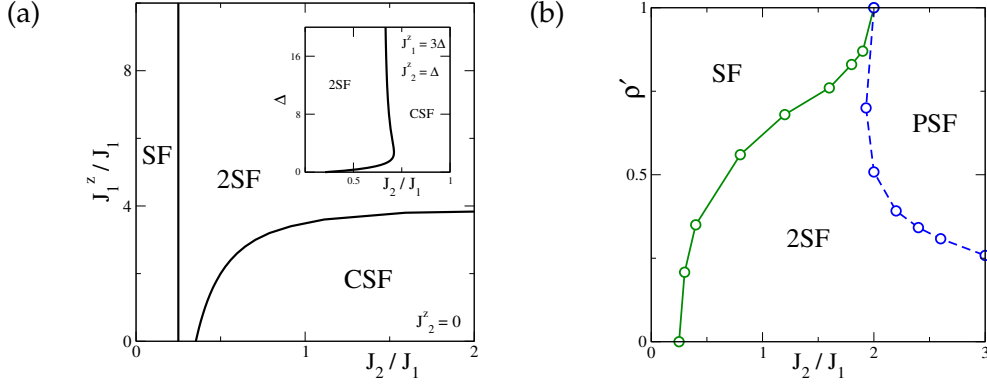Fig. 5.31: (a) Analytical prediction of the phase diagram for filling $\rho \to 0$ as function of the frustration J_2/J_1 and the interaction $J_1^z = V = W$ and $J_2^z = 0$. The inset shows the phase boundary for $J_1^z = 3\Delta$ and $J_2^z = \Delta$ which corresponds to the particular case of $\rho \to 1$ of model (5.39). (b) Phase diagram of model (5.43) as a function of J_2/J_1 and the effective density ρ'.

transition between the CSF and the 2SF phase for $J_2/J_1 > 1/\sqrt{8}$. The estimated value $J_{1,c}^z/J_1 \approx 3.6$ for $J_2 = J_1$ is consistent with our numerical estimates of the transition taken at finite density.

Note that at high fillings just below saturation, $\rho \to 1$, we may again describe the system with the model (5.42). However, due to the broken particle-hole symmetry of model (5.39), the effective spin model presents different spin couplings, $J_1^z = 3\Delta$ and $J_2^z = \Delta$ with $\Delta = V = W$. As shown in the inset of Fig. 5.31 (a), the CSF to 2SF transition at large fillings would be predicted for much lower values of J_2/J_1. However, in our numerical calculation we still find such a transition at $J_1 = J_2$ for high filling, which corresponds to the discrepancy already reported in Ref. [37] for spin-$\frac{1}{2}$-systems with large values of J_1^z and J_2^z.

5.6.3 Limit of strong interactions

Interesting insight in the properties of the system is provided by the analysis of the strongly-interacting regime $V = W \gg J_1, J_2$ (still assuming hardcore bosons). Let us first consider the case of low filling $\rho < 1/2$, where three-body-interactions play a negligible role. In that regime we may identify pairs of subsequent $|01\rangle$ particles as $|1\rangle_{eff}$ and the remaining empty sites $|0\rangle$ as $|0\rangle_{eff}$. In this mapping the number of sites of the effective hardcore bosons is reduced to $L' = L - N$ and the total density of the effective model ρ' fulfills $\rho = \frac{1}{1/\rho'+1}$. To first order in $(J_1, J_2)/V$ the effective quasi-particle model is given by an interaction-free $J_1 - J_2$ Hamiltonian (similar models have been studied on square lattices in Refs. [262, 263]):

$$\hat{\mathcal{H}}_{eff} = J_1 \sum_i c_i^\dagger c_{i+1} + J_2 \sum_i c_i^\dagger (1 - c_{i+1}^\dagger c_{i+1}) c_{i+2} + \text{H.c.,} \qquad (5.43)$$

where $c^\dagger$ (c) are creation (annihilation) operators for the effective quasi-particles. The correlated NNN tunnelling in Eq. (5.43) stems from the fact that a hopping to site $i+2$ is only allowed if there is no neighboring quasi-particle $|1\rangle_{eff}$ on site $i+1$. Model (5.43) also applies in the high-filling regime, $\rho > 2/3$. In that case, we may identify tuples of three sites $|011\rangle \to |1\rangle_{eff}$ and the remaining occupied sites $|1\rangle$ as $|0\rangle_{eff}$. The effective length reduces to $L' = L - 2N$, and the density is mapped as
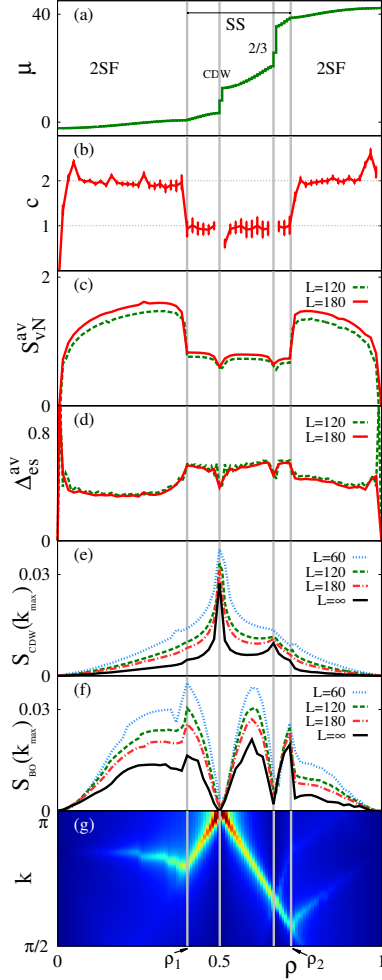
Fig. 5.32: Cut through the phase diagram of Fig. 5.29 at large interactions, $V = W = 8.0$, and $|J_1| = J_2 = 1$. We depict as a function of ρ: (a) Chemical potential μ ($L = 120$), (b) central charge c ($L = 180$), (c) averaged entanglement entropy, (d) averaged entanglement gap, (e) maximum of $S_{CDW}(k)$, and (f) maximum of $S_{BO}(k)$. In panel (g) we show the structure-factor $S_{CDW}(k)$ as a function of (quasi)momentum k and ρ ($L = 120$).
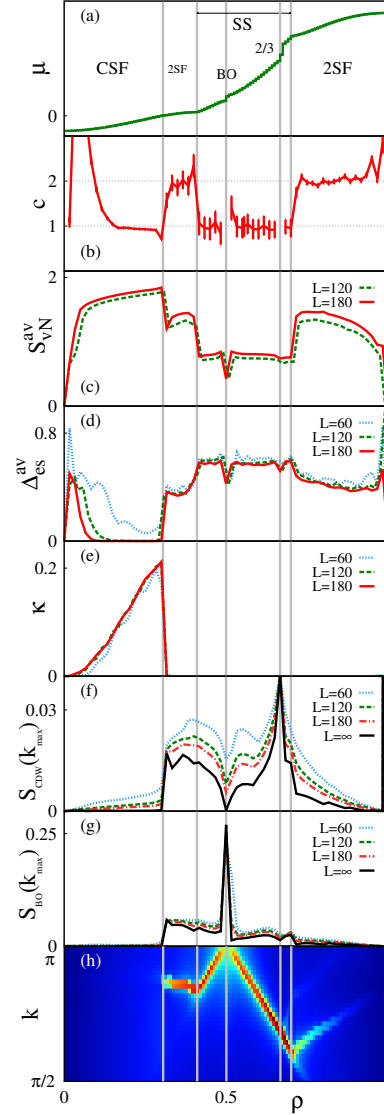
Fig. 5.33: Cut through the phase diagram of Fig. 5.29 for $V = W = 2.6$. We depict as a function of ρ: (a) Chemical potential μ ($L = 120$), (b) central charge c ($L = 180$), (c) averaged entanglement entropy, (d) averaged entanglement gap, (e) chirality κ, (f) maximum of $S_{CDW}(k)$, (g) maximum of $S_{BO}(k)$ (both (f) and (g) are obtained by means of a linear extrapolation to $L \to \infty$ using the two largest system sizes $L = 120$ and $L = 180$). The panel (h) depicts $S_{CDW}(k)$ as function of (quasi)momentum k and filling ρ ($L = 120$).

$\rho = 1 - \frac{1}{1/\rho'+2}$. The phase diagram of model (5.43), depicted in Fig. 5.31 (b), shows a SF-2SF transition for a critical $J_2/J_1 < 2$. We do not find any region with a finite chirality. The SF phase of model (5.43) may be identified with the SS phase of the original model due to the structure of the effective quasi-particles.

In Fig. 5.32 we depict our numerical results obtained for the original model (5.39) in the regime of large interactions ($V = W = 8$ and $|J_2| = J_1 = 1$). These numerical results agree well with those obtained from the strongly-interacting quasi-particle model (5.43). For low and large fillings ($\rho < 1/2$ and $\rho > 3/2$) we observe a 2SF to SF transition, clearly revealed by the central charge c and the entanglement properties. The critical density for the SF-2SF transition obtained from the effective model matches well with the numerical estimates resulting from model (5.39). Figures 5.32 show SF-2SF transitions at $\rho_1 \approx 0.4$ and $\rho_2 \approx 0.72$ which agrees perfectly with $\rho'_c \approx 0.64$. For all incommensurate densities $S_{CDW}(k)$ and $S_{BO}(k)$ exhibit a maximum at $k \neq 0$ which extrapolates to finite values in the thermodynamic limit (the extrapolation has been performed with polynomials of first and second order in $1/L$).

As shown in Fig. 5.31 (b), for large values of the NNN hopping J_2, it is energetically favorable at high densities to create pairs of holes (PSF phase), because the correlated NNN hopping of isolated quasi-holes is suppressed at high densities. This PSF phase at large NNN-hoppings is connected to the small PSF region shown in Fig. 5.29, and will occupy larger regions of the phase diagram with increasing J_2. A similar situation has been recently studied for the case of low fillings in strongly interacting dipolar lattice gases [264].

For the particular choice of interactions $V = W$ the region of intermediate fillings $1/2 < \rho < 2/3$ in the large interaction limit may be mapped to a simple model of non interacting hardcore particles. By adding single particles on top of the perfect $\rho = 1/2$ CDW phase one creates two domain-wall excitations that behave again as particle-pairs $|11\rangle$ of two sites. However, this pair may only move by single sites with some amplitude J_1. It is precisely the large three-body interaction W that creates an effective hard-core repulsion of these excitations. Analogously one can start the description on the background of the perfect 2/3-crystalline phase. Hence, the large interaction limit of the intermediate fillings is described by a simple non-interacting spinless fermion model on a chain, explaining why in the large interaction limit all SS regions map to a one-component standard SF phase. This phase exhibits a single maximum in the momentum distribution, broadened due to the size of the effective quasi-particles and thus at large interactions only the cSS phase is present.

5.7   The sawtooth ladder

A natural extension of the zig-zag ladder is to allow for difference in the tunneling amplitude between upper and lower leg. The resulting, so called railroad trestle models, are of the form:

$$\mathcal{H}_{rrt} = -t \sum_i (a_i^\dagger b_i + b_i^\dagger a_{i+1} + \text{H.c.})$$

$$- t' \sum_i (a_i^\dagger a_{i+1} + \text{H.c.}) - t'' \sum_i (b_i^\dagger b_{i+1} + \text{H.c.}) \qquad (5.44)$$

Here, a_i and b_i bosons operate on the upper (B) and lower (A) leg resp. We will consider the interesting case of $t'' = 0$, the so called sawtooth-ladder model (see

Fig. 5.34).

$$\mathcal{H}_{ST} = -t \sum_i (a_i^\dagger b_i + b_i^\dagger a_{i+1} + \text{H.c.}) - t' \sum_i (a_i^\dagger a_{i+1} + \text{H.c.})$$

$$+ \frac{U}{2} \sum_{\nu \in \{A,B\}, i} n_i^\nu (n_i^\nu - 1). \tag{5.45}$$

The following results and discussion have been published in Ref.[41] in collaboration with T. Mishra and L. Santos. A large part of the DMRG simulations have been performed by T. Mishra in the context of this work.

5.7.1   Non-interacting case

Again, it is convenient to study the non-interacting regime ($U = 0$) for which we find two energy bands α and β

$$\hat{\mathcal{H}}_{ST,U\to 0} = 2 \sum_k [\epsilon_\alpha(k)\alpha_k^\dagger \alpha_k + \epsilon_\beta(k)\beta_k^\dagger \beta_k] \tag{5.46}$$

with the dispersion

$$\epsilon_{\alpha,\beta}(k) = -t' \cos 2k \mp 2t[\cos^2 k + (t'/2t)^2 \cos^2 2k]^{1/2} . \tag{5.47}$$

Interestingly, the lowest band becomes flat at $|t'| = t/\sqrt{2}$. As shown in Ref. [238] in the flat-band case a gapped valence bond crystal phase my be found at $\rho = 1/4$ filling. For $|t'| < t/\sqrt{2}$ the dispersion of the lower band ϵ_α exhibits a single minimum in the lowest band at $k = 0$. For $|t'| > t/\sqrt{2}$ it has a single minimum at $k = \pi/2$ (which corresponds to $k = -\pi/2$ due to the doubled unit cell). As a result, for non-interacting bosons, a transition occurs from a superfluid phase at $k = 0$ (SF$_0$) to a superfluid phase at $k = \pi/2$ (SF$_{\pi/2}$). In the SF$_{\pi/2}$ the B leg is strongly depopulated.

5.7.2   The phase diagram

In Fig. 5.35 we present the phase diagram of model (5.45) for unit filling as function of t' and U. As discussed above in section 5.3 the flatness of the band at $|t'| = t/\sqrt{2}$ is expected to induce a MI-phase for arbitrary interaction-strength as an intermediate phase between the SF$_0$ and SF$_{\pi/2}$ phases. Interestingly, in our DMRG calculations we observe a third superfluid phase next to the SF$_{\pi/2}$ phase which, remarkably, exhibits a supersolid character, i.e. a density modulation on the A leg. Detailed calculations show [41] that this SS-phase remains stable away from unit-filling.
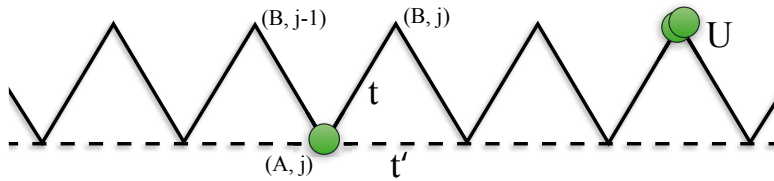

Fig. 5.34: Scheme of the sawtooth lattice. The V-shaped plaquettes are non-frustrated, whereas the △-shaped plaquettes are frustrated.
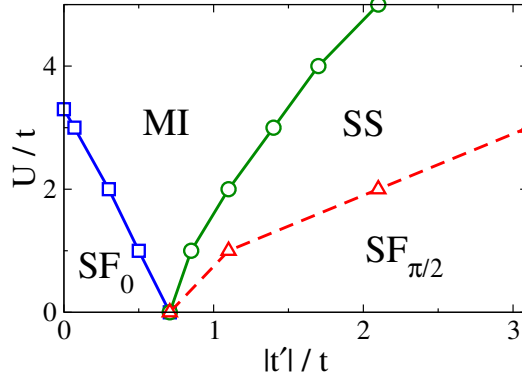
Fig. 5.35: Phase diagram of Model (5.45) for $\rho = 1$ as a function of $|t'|/t$ and U/t.

5.7.3   Classical limit

An intuitive insight on the emergence of the SS is obtained from the classical limit of model (5.45). We assume each site to be in a coherent state with a well defined density and phase, 0 or π, corresponding to the two possible minima of $E_\alpha(k)$. We consider a simplified model in which $b_j = \eta$, $a_{2j} = \xi$, and $a_{2j+1} = \chi$, such that we allow for both a possible density imbalance between the A and B legs, and for an even-odd asymmetry in the A leg. We may hence minimize the energy, which without loss of generality may be calculated for a four-site unit cell:

$$\langle \mathcal{H} \rangle = -4t(\xi\chi + \chi\eta) - 4t'\xi\eta +$$
$$+ U\left(\xi^4 + 2\chi^4 + \eta^4\right) - \mu\left(\xi^2 + 2\chi^2 + \eta^2\right) \qquad (5.48)$$

Within this approach the phase diagram splits into three regions (Fig. 5.36(d)). For $|t'|/t < 1/\sqrt{2}$ the three coefficients have the same sign, and the particles occupy both A and B sites corresponding to the SF$_0$-phase (Fig. 5.36(a)). For small U/t and $|t'|/t > 1/\sqrt{2}$, the B sites depopulate ($\eta = 0$), the density is homogeneous in the A sites ($|\chi| = |\xi|$), and $sign(\chi) \neq sign(\xi)$, corresponding to the SF$_{\pi/2}$ phase (Fig. 5.36(b)). A sufficiently strong repulsive interaction $U/t > (U/t)_c$ redistributes population to the B sites. However, how the particles re-distribute in the A leg is crucially determined by the existence of frustrated and un-frustrated plaquettes in the sawtooth lattice. In order to minimize kinetic energy particles favor the un-frustrated V-shaped plaquettes of the sawtooth forming V-shaped dimers. As a result particles break the translational symmetry spontaneously, preferably occupying every second V-plaquette (Fig. 5.36 (c)), which leads to a density modulation in the A sites, that characterizes, as mentioned above, the SS phase.

5.7.4   Roton instability

Insight on the nature of the SF$_{\pi/2}$-SS transition is obtained in the limit in which $U \ll E_\beta(k) - E_\alpha(k)$ for all k. In that case we may project model (5.45) onto the lowest energy band:

$$\hat{\mathcal{H}}_{ST} \simeq \sum_k E_\alpha(k)\alpha_k^\dagger \alpha_k + \frac{U}{2}\sum_{q,k,k'} f_{k,k'}^{k+q,k'-q} \alpha_{k+q}^\dagger \alpha_{k'-q}^\dagger \alpha_{k'}\alpha_k, \qquad (5.49)$$
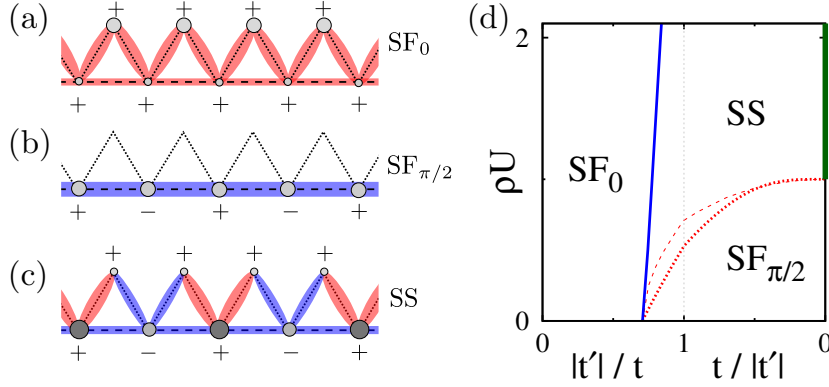
Fig. 5.36: (Color online) Sketch of the SF_0 (a), $SF_{\pi/2}$ (b) and SS (c). The circle size is proportional to the local density, whereas $\pm$ denote the sign. (d) Phase diagram in the weak-coupling limit as function $U\rho$ and $|t'|/t$ for a fixed (but arbitrary) filling. The SF_0 to the SS phase is shown as a solid line. The dotted and dashed lines depict, respectively, the $SF_{\pi/2}$-SS transition line obtained from the variational approach (5.48) and the roton instability. At $t = 0$ SS-order vanishes (thick solid line) resulting in an highly degenerate ground-state, since particles may occupy the uncoupled B sites in an arbitrary configuration.

with $f_{k_1,k_2}^{k_3,k_4} = \prod_{l=1}^{4} \cos(\theta_{k_l}) + \prod_{l=1}^{4} \sin(\theta_{k_l})$. Note that, although the on-site interactions are contact-like, the effective interactions are momentum dependent. Considering the $SF_{\pi/2}$ phase, we may assume condensation at $\pi/2$, and evaluate the corresponding Bogoliubov spectrum of excitations, $\epsilon(k)^2 = \left(\widetilde{E_A}(k) + 2U\rho(1 + \cos 2\theta_k)\right)\widetilde{E_A}(k)$ with $\widetilde{E_A}(k) = E_A(k) - 2t' + U\rho(\cos 2\theta_k - 1)$. As usual the spectrum exhibits a linear (phonon-like) dispersion for k close to $\pi/2$. Interestingly, for finite ρU it acquires a local minimum at $k = 0$, that resembles the roton dispersion minimum of superfluid helium [265], and that occurs, as for dipolar condensates [266], due to the momentum dependence of the interactions. For a critical value of ρU the roton-like minimum reaches zero energy, becoming unstable and marking the transition to the SS. As shown in Fig. 5.36 (d) the critical ρU for the roton instability agrees well with the $SF_{\pi/2}$-SS transition line obtained by the classical model. Hence, we can conclude that the $SF_{\pi/2}$ is destabilized through the roton instability that leads to the SS phase.

5.8   Conclusions

In summary we have obtained the full phase diagram of ultracold bosons in frustrated zig-zag optical lattices. The system exhibits very rich ground-state physics: Apart from CSF and 2SF phases different types of gapped phases including chiral MI phases have been found. We have introduced a analytical method for the analysis of dilute limit properties and presented detailed numerical support for its results. These arguments will be employed in the following chapter in a different context.

Three body on- or off-site interactions or long range repulsions give rise to topological Haldane insulator, super-solid phases or meta-magnetic behavior. Some of these quantum phases can be naturally identified with equivalent phases and find-

ings in corresponding spin-models. Hence, the results complement the various the-
oretical approaches to this and similar models as well as the experimental efforts in
the field of ultracold gases.

The different variations in the geometry of section 5.7 remain to be studied more
in detail. In particular the connection between chiral phases in the zig-zag ladder
and the super-solid phases discussed in the context of sawtooth models or gener-
ally rail-road-trestle models have to be understood.

Chapter 6

Artificial Magnetic Fields in Two-leg Ladder Systems

Some of the most interesting phenomena in modern physics emerge in strongly correlated quantum many body systems exposed to strong magnetic fields. So for example the quantum Hall[19] or fractional quantum Hall[158] effect, whose experimental discovery also had a huge impact on theoretical models and methods.

Another very early example is the effect discovered by Meissner and Ochsenfeld [267] that magnetic fields may be expelled from superconductors, screened by a thin layer of superconducting currents exponentially confined to the boundary. For type-II superconductors the magnetic field may penetrate the sample after a critical field strength forming vortices of quantized flux in the configuration of screening supercurrents [268].

Some theoretically proposed effects have remained elusive for a long time. So the fractional band structure of non-interacting lattice-fermions, the "butterfly" discovered by Hofstadter[269] (see Fig. 6.1), whose experimental observation in real materials would demand ridiculously high magnetic field strengths.

Already in his seminal work Douglas Hofstadter proposes the engineering of a "synthetic two-dimensional lattice of considerably greater spacing than that which characterizes real crystals" [269]. Cold atoms in optical lattices due to their large lattice constant (as compared to typical condensed matter systems) constitute a perfect testbed for the emulation of the Hofstadter-model. The possibility to study quantum Hall and fractional quantum Hall physics, topological phases and transitions
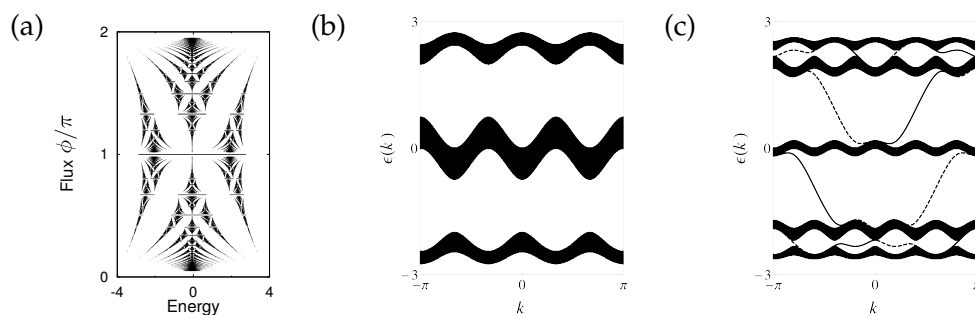
Fig. 6.1: Fractal bandstructure of a square flux-lattice - the "Hofstadter-butterfly" (a). Black lines denote the extend of bands for a given flux. (b) Examples of the band-structure for $\Phi/\Phi_0 = \frac{1}{3}$ on a torus. (c) The presence of open boundaries leads to chiral edge states as shown for $\Phi/\Phi_0 = 2/5$ on a cylinder-geometry. Solid (dashed) lines depict left (right) moving states. The edge-state have been calculated employing transfer matrix-techniques as introduced in [270].

as well as anyonic excitations in a strongly correlated, highly tunable, and clean cold atomic system attracts a huge interest in theory and experiment. An obvious drawback is, however, that the trapped atoms are neutral and, hence, magnetic fields have to be artificially induced.

In the following, after a brief review of some recent experimental attempts and breakthroughs for the simulation of synthetic quantum magnetism, we will discuss the properties of a very simple paradigm, the two leg ladder with a homogeneous flux, which exhibits, as we will show, a very rich physics.

6.1 Magnetic fields and lattice systems

External electric and magnetic fields enter in the quantum mechanical Hamiltonian as ($c = 1$)

$$\hat{\mathcal{H}} = \frac{(\hat{\mathbf{p}} - e\mathbf{A})^2}{2m} + e\Phi \, , \tag{6.1}$$

where the potentials Φ and $\mathbf{A}$ are defined up to a gauge transformation. In the presence of a lattice within the tight-binding approximation the dependence on the field may be absorbed into an additional phase factor of the usual hopping matrix element, the so called Peierls phase

$$J_{x,y} \rightarrow J_{x,y}\, \mathrm{e}^{-\mathrm{i}\frac{e}{\hbar}\int_{R_x}^{R_y} d\mathbf{r}\cdot\mathbf{A}(\mathbf{r},t)} \, . \tag{6.2}$$

For a homogeneous field perpendicular to our system we may choose the gauge $\mathbf{A} = (0, B\,x, 0)$, and the transition amplitude along y gains an x-dependence, $\mathrm{e}^{-\mathrm{i}(\pm a)\frac{e}{\hbar}B\,x}$. Figure 6.2 illustrates this situation for the case of a 2D square lattice. The total Hamiltonian of this Hofstadter-model is given by

$$\hat{\mathcal{H}}_H = -\, J_x \sum_{x,y} \mathrm{e}^{\mathrm{i}x\phi} a_{x,y}^\dagger a_{x,y+1} - J_y \sum_{x,y} a_{x,y}^\dagger a_{x+1,y} + h.c. \tag{6.3}$$

with $\phi = 2\pi B a^2 \frac{e}{\hbar} = 2\pi\Phi/\Phi_0$, and the magnetic flux quantum $\Phi_0 = \frac{h}{e}$. Hence, a particle hopping around a plaquette picks up an additional phase proportional to the magnetic field.

If $\Phi/\Phi_0 = \frac{p}{q}$ is a rational number the Hamiltonian (6.3) is periodic in space and we typically expect to find q distinct energy bands in the single particle spectrum. This leads to the astonishing fractal Hofstadter-butterfly band-structure. In Fig. 6.1 some examples are shown. It has been shown that the bands are characterized
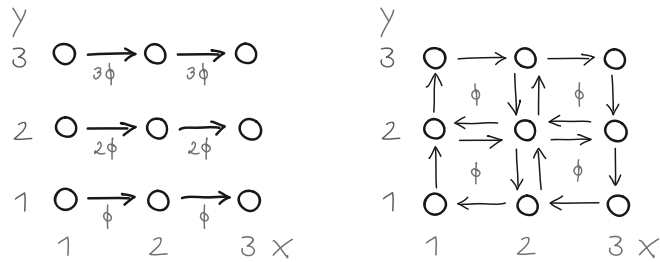
Fig. 6.2: Fluxes on a 2D square lattice as described by Eq. (6.3).
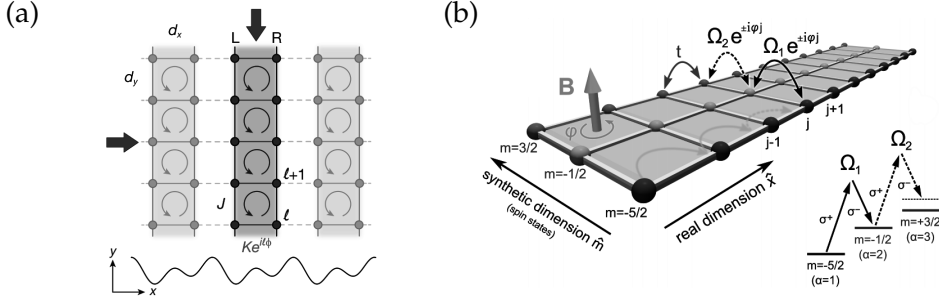
Fig. 6.3: (a) Experimental scheme for the generation of synthetic magnetic field in bosonic ladders. Figure adapted from Ref.[2]. (b) Synthetic gauge fields in synthetic dimensions. Three atomic hyperfine-states are laser coupled to form the rungs of a ladder system. Figure adapted from Ref.[273].

by nontrivial topological invariants, Chern numbers. These can be related to the number of conducting edge states in open boundary systems (see Fig. 6.1 (d)) and hence to a quantized conductance of each band[271].

As mentioned above a $\Phi/\Phi_0 \sim 1$ in traditional solid state systems would require fields of the order $10^5 T$ (assuming $a \sim \mathring{A}$). In order to realize larger fluxes of experimentally achievable magnetic fields the lattice constant has to be enlarged. Apart from ultracold quantum gas experiments, recently, the Hofstadter model has been realized in graphene [272].

6.2 Synthetic magnetic fields

6.2.1 Rapidly rotating BECs

Early attempts for the generation of synthetic gauge fields focused on fast rotating BECs [274]. Here the Coriolis force in the rotating system resembles the effects a the Lorentz force. In fact, in a co-moving frame the Hamiltonian of a system rotating with an angular frequency may be rewritten in the form [275]

$$\hat{\mathcal{H}}_{rot} = \frac{(\hat{\mathbf{p}} - \mathbf{A})^2}{2m} + V(\mathbf{r}) + W_{rot}(\mathbf{r}) \tag{6.4}$$

where $V(\mathbf{r})$ is an external potential and the artificial vector potential is given by $\mathbf{A} = m\mathbf{\Omega} \times \mathbf{r}$ with the rotation vector $\mathbf{\Omega}$. Note, that the additional centrifugal potential $W_{rot} = -A^2/2m$ repels particles form the center. Hence, fast rotations will require a compensating strong trapping of the particles in order not to cause an instability of the system. Experiments in rotating BECs or lattices systems have been conducted with great success [276, 277], observing large Abrikosov vortex-lattices [278] and occupation of the lowest Landau-level [279]. However, entering a strongly correlated regime with rotation techniques remains challenging due to technical difficulties for achieving sufficiently large angular momenta per particle [275].

6.2.2 Laser assisted hopping

The seminal proposal of Jaksch and Zoller [280] provided an alternative scheme based on laser assisted tunneling in optical lattices. The basic constituents are a

tilted optical lattice (in one direction), which will suppress tunneling in that direction and a set of Raman-lasers which effectively restore the tunneling and allow for the imprinting of a (spatially dependent) Peierls phase. One decade after the Jaksch-Zoller proposal staggered [281] and rectified [13, 14] effective magnetic fields have been realized in experiments with some simplifications [282] and modifications [283]. While the original proposal relies on the trapping of two hyperfine-states in spin-dependent shifted optical lattices the experiments in Munich and Boston with a ^{87}Rb gas [13, 14] just require a single component and two far detuned running-wave Raman lasers.

Basic scheme

In the experiment an optical lattice is tilted in, say, x-direction with an energy-shift Δ from site to site. Local eigenstates are described by Wannier-Stark states which may be approximated by the Wannier-functions of the original lattice [283]

$$\psi_j(x) \simeq w(x - jd) + \frac{J}{\Delta}\left[w(x - (j+1)d) - w(x - (j-1)d)\right] \tag{6.5}$$

The 3D on-site wavefunction at site j is $\Phi_j(\mathbf{r}) = \psi_j(x)\varphi(y,z)$ and for simplicity we use $\varphi(y,z) \simeq w(y)w(z)$.

We assume the tilting to be large enough $J \ll \Delta, U$ such that the hopping is suppressed. Raman-assisted hopping is realized by two lasers with Rabi frequencies $\Omega_{1,2}$, wave vectors $\mathbf{k}_{1,2}$, and frequencies $\omega_{1,2}$. Following Ref. [283], we evaluate the Raman-assisted hopping, J_x from site j to site $j + 1$:

$$J_x = \frac{V_R}{4} \int d^3\mathbf{r}\, \Phi_{j+1}(\mathbf{r})^* e^{i\delta\mathbf{k}\cdot\mathbf{r}} \Phi_j(\mathbf{r}), \tag{6.6}$$

where $\delta\mathbf{k} = \mathbf{k}_1 - \mathbf{k}_2$, and $V_R = \frac{\hbar|\Omega_n||\Omega_m|}{\delta}$, with δ the (large) detuning to the one-photon transitions. For $J_x \ll \Delta$ within the harmonic approximation we yield

$$J_x \simeq iJ_x \frac{V_R}{2\Delta} \sin\left(\frac{\delta k_x d}{2}\right) e^{i\delta k_x d(j+1/2)}. \tag{6.7}$$

Interestingly, a finite $\delta k_x \neq 0$ is necessary to establish a significant assisted hopping [13, 14, 283].

Floquet analysis

Following Ref.[147, 282] we may express the two running-wave beams in the form of a local optical potential with a spatially dependent force. In the tight-binding approximation we obtain

$$\hat{\mathcal{H}}(t) = -J_x \sum_{x,y} b_{x,y}^\dagger b_{x+1,y} - J_y \sum_{x,y} b_{x,y}^\dagger b_{x,y+1} + H.c. + \sum_{x,y}\left(x\Delta + V_{x,y}(t)\right)n_{x,y} \tag{6.8}$$

where $V_{x,y}(t) = V_R \sin(\omega t + \phi_{x,y})$ with $\phi_{x,y} = \delta\mathbf{k}\cdot\mathbf{r}$. As described in section 2.5 we may apply a unitary transformation

$$U(t) = e^{-i\sum_{x,y}\left(x\omega t + \tilde{V}_{x,y}(t)\right)n_{x,y}} \tag{6.9}$$

with $\tilde{V}_{x,y}(t) = \int_0^t V_{x,y}(t')dt'$ to move the time dependence in the hopping part of the Hamiltonian.

$$\hat{\mathcal{H}}(t) = -J_x \sum_{x,y} e^{i\left(\tilde{V}_{x,y}(t)-\tilde{V}_{x+1,y}(t)-\omega t+\tilde{\Theta}_{x,y}\right)} a^\dagger_{x,y} a_{x+1,y} + H.c.$$

$$-J_y \sum_{x,y} e^{i\left(\tilde{V}_{x,y}(t)-\tilde{V}_{x,y+1}(t)+\tilde{\Theta}'_{x,y}\right)} a^\dagger_{x,y} a_{x,y+1} + H.c. \tag{6.10}$$

After time-averaging we obtain, assuming the resonance condition $\Delta = \omega$, the Hofstadter-model (6.3)

$$\hat{\mathcal{H}}_{eff} = -\tilde{J}_x \sum_y e^{i\Phi_{x,y}} b^\dagger_{x,y} b_{x+1,y} - \tilde{J}_y \sum_{x,y} b^\dagger_{x,y} b_{x,y+1} + H.c. \tag{6.11}$$

with $\Phi_{x,y} = (\phi_{x,y} + \phi_{x+1,y})/2$ and

$$\tilde{J}_x = J_x \mathcal{J}_1 \left(\frac{V_R}{2\omega} \sin(\phi_{x,y} - \phi_{x+1,y}) \right)$$

$$\tilde{J}_y = J_y \mathcal{J}_0 \left(\frac{V_R}{2\omega} \sin(\phi_{x,y} - \phi_{x,y+1}) \right) . \tag{6.12}$$

Hence, also the hopping in the y-direction gets renormalized due to the laser assisted hopping. For a weak coupling $V_R \ll \omega$ we arrive at the result (6.7).

This scheme has been employed in 2D systems to study cyclotron orbits particles in the Hofstadter model [13, 14] and phases with non-trivial Chern-numbers [148]. By superlattice-techniques in Ref. [2] arrays of square-ladders have been created (see Fig. 6.3 (a)).

6.2.3   Synthetic gauge fields in synthetic dimensions

A different approach for the simulation of magnetic fields relies on the light assisted coupling of different hyperfine states. Breakthrough work in this field has been conducted in the group of Ian Spielman with the realization of synthetic unidirectional spin-orbit coupling [284]. Recent extensions of these ideas combine a one dimensional real-space lattice with a laser induced coupling of different hyperfine states constituting a so called synthetic dimension [285]. These experiments show the possibility to create artificial magnetic fields in multi-leg ladders with fermions [273] and bosons [286]. The coupling of internal spin states via two-photon Raman transition allows for a phase imprinting along the rungs (see Fig. 6.3 (b)). Due to the sharp edge of the system and direct observability of the leg (species) resolved occupation and momentum-distribution it was possible to observe chiral edge states and orbit skipping phenomena.

6.3   Ladders

Motivated by the recent experimental realizations by Atala et al.[2], in this chapter we will focus on the properties of interacting bosons in a simplified geometry, the two-leg square ladder system as sketched in Fig. 6.4. The system is described by the following Hamiltonian

$$\hat{\mathcal{H}} = -J \sum_r (b^\dagger_{1,r} b_{1,r+1} + b^\dagger_{2,r} b_{2,r+1}) - J_\perp \sum_r e^{ir\Phi} b^\dagger_{1,r} b_{2,r} + H.c. + \frac{U}{2} \sum_r n_r(n_r - 1) , \tag{6.13}$$

with the rung-coupling $J_\perp$ and the leg-hopping J. The model exhibits a gauge-freedom to choose different Peierls phases as long as the total flux per unit cell stays constant, e.g. a symmetric configuration

$$\hat{\mathcal{H}} = -J\sum_r (e^{i\frac{\Phi}{2}} b^\dagger_{1,r} b_{1,r+1} + e^{-i\frac{\Phi}{2}} b^\dagger_{2,r} b_{2,r+1}) - J_\perp \sum_r b^\dagger_{1,r} b_{2,r} + H.c. + \frac{U}{2}\sum_r n_r(n_r - 1) \,.$$

(6.14)

Such ladder models have also been realized with arrays of superconducting Josephson-junctions in a magnetic field almost two decades ago [287, 288] and still are subject to active research [289]. Here the bosonic particles are Cooper pairs of electrons.

Two-leg ladder models with magnetic field have been studied theoretically starting in the mid 80s in the context of Josephson junction arrays using field theoretical methods [290, 291] and with a mapping to classical frustrated XY-models[292, 293]. A detailed treatment of interacting bosons in two-leg ladders using bosonization was later also elaborated in Ref.[294].

Predictions from mean field arguments or field theoretical and bosonization analysis include very interesting phenomena such as vortex lattices [294], Mott insulators with Meissner Currents [295, 296], Laughlin-like-states [297] or phases with spontaneously broken leg imbalance [298, 299]. Also fermionic ladders have been studied theoretically [300–303]. The amount of both theoretical and recent experimental efforts in the study of the simple two-leg bosonic flux ladder model was for a long time contrasted by the lack of a detailed numerical analysis of the ground-state phases and properties. There have been few exact diagonalization [304] and DMRG studies focusing on the flux $\phi = \pi$ case [242, 243], or the study of the momentum distribution [305].

The following results close this gap and have been published in Ref.[42, 43] in collaboration with M. Piraud, F. Heidrich-Meisner, I. McCulloch, U. Schollwöck, and T. Vekua. An extensive part of the DMRG calculations has been performed by M. Piraud employing DMRG-codes supplied by I. McCulloch.

6.3.1   Currents

An important (experimentally measurable [2, 273, 286]) observable in ladder systems are local and boundary currents. From the continuity equation

$$\left\langle \frac{dn_\mathbf{r}}{dt} \right\rangle = i\,\langle [\mathcal{H}, n_\mathbf{r}]\rangle = -\sum_{\langle \mathbf{s}\rangle} j(\mathbf{r} \to \mathbf{s})$$

(6.15)

Fig. 6.4: Bosons on a two-leg ladder in the presence on a homogeneous flux ϕ per unit cell with a rung-hopping $J_\perp$ and the leg-hopping J (6.14).
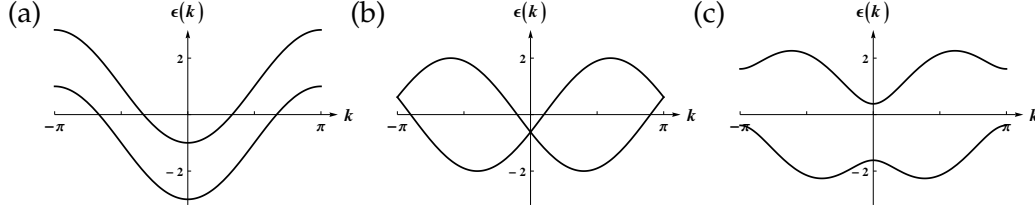
Fig. 6.5: Single particle energies $\epsilon(k)$ as defined by Eq. (6.19) for a two leg ladder for (a) $J_\perp = 1, \phi/\pi = 0.1$, (b) $J_\perp = 0, \phi/\pi = 0.8$ and (c) $J_\perp = 1, \phi/\pi = 0.8$.

we can define the current $j(\mathbf{r} \to \mathbf{s})$ from a site $\mathbf{r}$ to a neighboring site $\mathbf{s}$. In particular for model (6.14) we define

$$j_{\ell,r}^{\parallel} = iJa \left(b_{\ell,r+1}^\dagger b_{\ell,r} - b_{\ell,r}^\dagger b_{\ell,r+1} \right)$$
$$j_r^{\perp} = iJ_\perp a \left(e^{-ir\phi} b_{1,r}^\dagger b_{2,r} - e^{ir\phi} b_{2,r}^\dagger b_{1,r} \right) \tag{6.16}$$

Apart from the configuration of local currents the average current that circulates through the boundary of a system may reveal important properties of the quantum phase. This so called chiral current (also dubbed edge, screening or Meissner current) is defined as

$$j_c = \frac{1}{N} \sum_r \langle j_{1,r}^{\parallel} - j_{2,r}^{\parallel} \rangle \tag{6.17}$$

For a two leg ladder we may obtain it from the Hellmann-Feynman theorem as derivative of the ground state energy E^0 per particle

$$j_c = \partial_\phi E_0 / N . \tag{6.18}$$

6.4 Non-interacting particles

It is instructive to analyze the behavior of non-interacting particles in the flux-ladder [2]. In the symmetric gauge the Hamiltonian is easily diagonalized $\hat{\mathcal{H}} = \sum_k \epsilon_-(k) \alpha_k^\dagger \alpha_k + \sum_k \epsilon_+(k) \beta_k^\dagger \beta_k$ and the single particle energy is given by

$$\epsilon_\pm = -2J \cos(k) \cos \phi/2 \pm \sqrt{J^2 + K^2 - J^2(\cos \phi + 2 \cos 2k \sin^2 \phi/2)} \tag{6.19}$$

For a finite $J_\perp$ the energies split into two branches mixing particles on the lower and upper leg of the two ladders. The new creation and annihilation operators α_k and β_k are given by

$$b_k^1 = \cos \theta_k \alpha_k - \sin \theta_k \beta_k, \quad b_k^2 = \sin \theta_k \alpha_k + \cos \theta_k \beta_k$$

with the mixing angle given by $\cot \theta_k = -\frac{\epsilon_-(k) + 2\cos(k-\phi/2)}{K}$.

A prominent feature of the single particle dispersion relation is that it acquires a degenerate double minimum (see Fig. 6.5) for critical flux $\phi > \phi_c$, where

$$\phi_c = 2 \arccos \frac{-J_\perp + \sqrt{16 + J_\perp^2}}{4} \tag{6.20}$$

at $Q = -Q = \arcsin \pm \sqrt{(1 - \cos\phi)/2 - J_\perp^2 \cot^2 \phi/2}$. The line of this Lifshitz-transition to the frustrated regime is depicted in Fig. 6.8 (a).
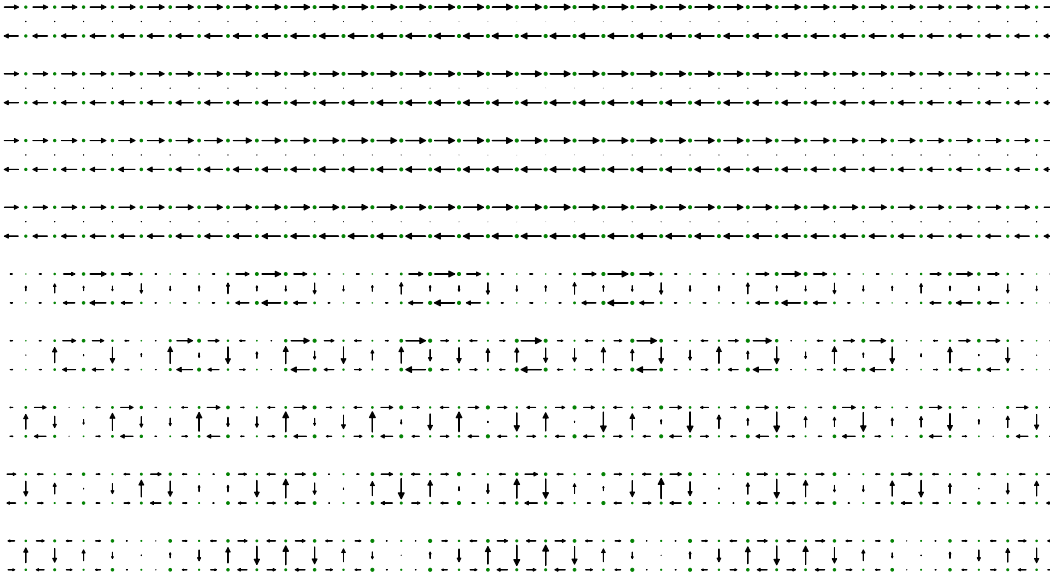
Fig. 6.6: Current configurations for non-interacting bosons on a ladder for $\phi/\pi =$ 0.1, 0.2, ...0.9. For $\phi/\pi \lesssim 0.42$ the ground state is non-degenerate and currents are mainly confined to the legs.

As intuitively clear from the $J_\perp \to 0$ limit the degenerate eigenstates $|Q\rangle$ and $|-Q\rangle$ correspond to particles preferably occupying the upper or the lower leg of the ladder. The particle-density on the upper or lower leg for $|Q\rangle$ (the lower or upper leg for $|-Q\rangle$) is given by $N_1 = N\cos^2\theta_k$ and $N_2 = N\sin^2\theta_k$ (shown in Fig. 6.7 (a)).

For non-interacting bosons the ground state for $\phi > \phi_c$ is highly degenerate in thermodynamic limit or for periodic boundary conditions: From the total number of N particles, M may occupy the minimum $|Q\rangle$, while $N - M$ particles remain in $|-Q\rangle$. Open boundary conditions on a finite system will result in a unique ground state, corresponding to an equal occupation of both minima since one does not observe any particle density imbalance. Remarkably, in spite of the highly degenerate
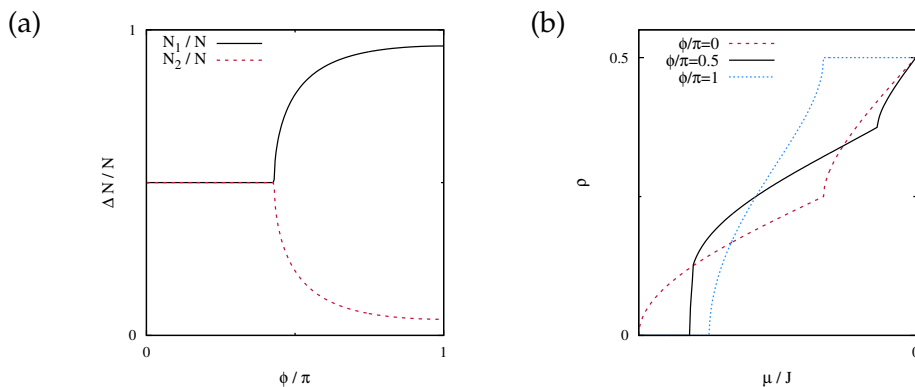
Fig. 6.7: (a) Particle-density on the upper or lower leg N_1/N and N_2/N as a function of the flux. (b) Equation of state $\rho(\mu) = \mu$ for non-interacting fermions on a ladder for $J_\perp = J$ and $\phi/\pi = 0, 0.5, 1$. The C-IC transition from the M to the V phase is characterized by a cusp signaling the change in number of Fermi-surfaces.
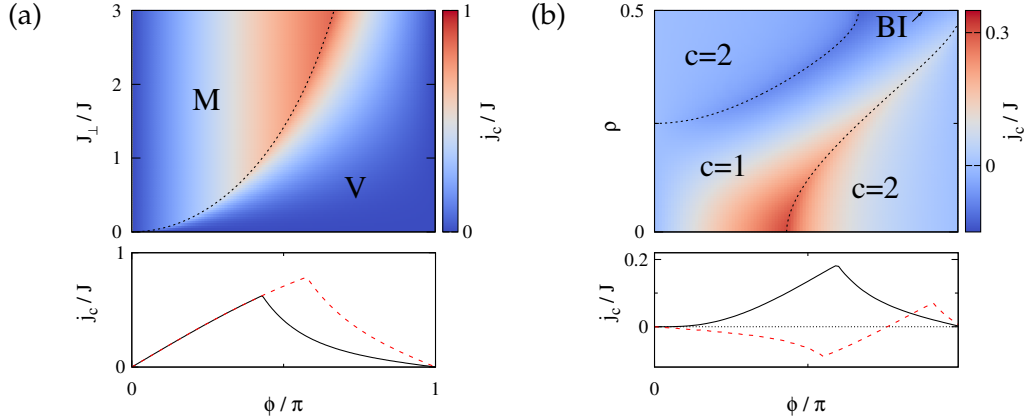
Fig. 6.8: Phase diagram for free particles. (a) The M and V-phases of non-interacting bosons on an two leg ladder. The lower panel depicts the chiral current for $J_\perp = 1$ and 2. (b) The phase diagram of free fermions as function of the filling ρ and flux ϕ. The lower panel shows the chiral-current j_c for $\rho = 0.1$ and 0.7.

ground state, the chiral current for all possible configurations is identical, since it is given by the ground-state energy derivative (6.18). For $\phi > \phi_c$ we find

$$ j_c = \frac{J_\perp^2 \sin\phi}{8J \sin^4 \frac{\phi}{2} \sqrt{1 + (J_\perp/2J \sin\frac{\phi}{2})^2}} \, . \tag{6.21}$$

while for the non-degenerate regime it saturates to $j_c = J \sin\frac{\phi}{2}$. This behavior of j_c, as shown in the lower panel of Fig. 6.8 (a), resembles the behavior of screening-currents of type-II superconductors. In fact this similarity is established by comparing typical current configurations as calculated for open systems in Fig. 6.6. In the non-degenerate regime $\phi < \phi_c$, which we will name Meissner (M) phase, the currents are preferably on the system-boundary, i.e. the legs, and strongly suppressed on the rungs. In the frustrated vortex (V) regime, $\phi > \phi_c$, vortices enter the system diminishing the chiral "screening" current. The density of vortices in the system ρ_V, describing the inverse average extent of single vortices, is zero in the M-phase, and a smooth monotonous function in the V-phase given by $\rho_V = Q/\pi$.

For further insight on the phase transitions we will discuss shortly the case of non-interacting spinless fermions, since here due to Pauli-principle the non-interacting problem has a well defined ground state for any filling. The V-phase exhibits two separate Fermi-seas. In a low energy description there a two gapless modes corresponding to excitations along the different Fermi-points. The V-phase is thus characterized by a central charge $c = 2$, while M-phase is a $c = 1$ Luttinger-liquid. Increasing the band-filling, as shown in Fig. 6.8 (b), distinct $c = 2$ regions may be explored. The phase boundaries for spinless fermions are given by

$$ n_c^{1,2} = \arccos\left(\pm J_\perp \cos(\phi/2) + \cos\phi\right)/(2\pi) \tag{6.22}$$

The change in the number of Fermi-points is reflected in a cusp in the equation of state $\rho(\mu) = \mu$ as shown in Fig. 6.7. This cusp-sigularity will be used as a precise signature of the commensurate-incommensurate transition from M- to V-phase. As shown in Fig. 6.8 (b) the chiral current for spinless fermions may be positive or negative. Negative currents result from the Pauli principle and the band structure.

For example the chiral current for a single band $J_\perp > 2$ in the vicinity of $\phi = 0$ is given by

$$j_c/\phi = -\frac{J^2 n\pi + J^2 \cos(n\pi)\sin(n\pi)}{J_\perp} + J\sin(n\pi) \tag{6.23}$$

For the filling $n \gtrsim 0.56$ this function becomes negative which may be related to the negative effective mass at the Fermi-point for $n > \frac{1}{2}$

6.5 Vortex and Meissner phases for hardcore bosons

From the DMRG-perspective the case of hardcore bosons $U \to \infty$ appears to be the easiest starting point due to local Hilbert-space restrictions. Also from the experimental perspective in typical setups the limit of low particle numbers per site demands a strong three dimensional confinement and thus would result in strong interactions. Hence, in the following section we concentrate on this case.

6.5.1 Results from bosonization

Ref.[42, 294] derive the low energy properties of model (6.14) starting from the limit of two weakly coupled chains hosting two independent bosonic modes. As in chapter 5 it is favorable to re-express the bosonic fields as symmetric and antisymmetric combinations. The low energy properties are then determined by the Hamiltonian density [42]

$$\mathcal{H}(x) = \frac{v_+}{2}\left[\frac{(\partial_x\phi_+)^2}{K_+} + K_+(\partial_x\theta_\alpha)^2\right] \tag{6.24}$$
$$+ \frac{v_-}{2}\left[\frac{(\partial_x\phi_-)^2}{K_-} + K_-(\partial_x\theta_- - \frac{\phi}{\sqrt{2\pi}})^2\right]$$
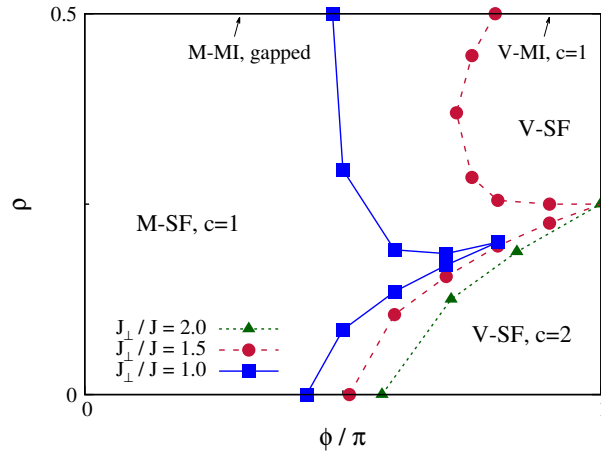$$- \cos\sqrt{2\pi}\theta_- \sum_{m=0,1}\lambda_m \cos\left[m\sqrt{8\pi}\phi_+ + 4m\pi nx\right]$$

Fig. 6.9: Phase diagram in the $\rho - \phi$ plane for different values of $J_\perp$. Part of the DMRG calculations have been performed by M. Piraud employing DMRG-codes supplied by I. McCulloch.
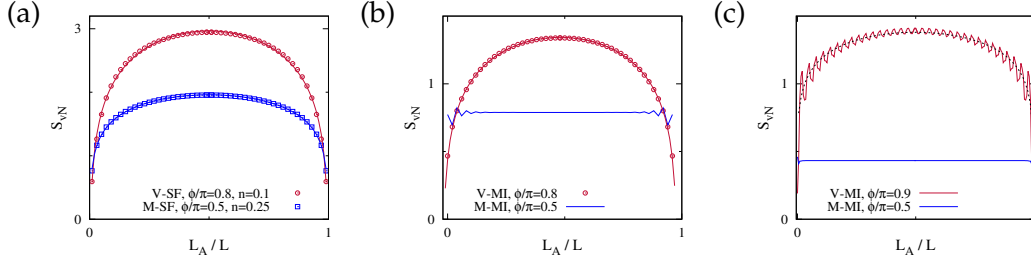
Fig. 6.10: Estimate of central charge from properties of the von-Neumann-entropy S_{vN} as function of partition size L_A/L. (a) The fit to Eq.(4.5) results in $c \approx 1.02$ and $c \approx 2.07$ for M-SF and V-SF phase. In the MI phases for V-MI we find $c \approx 0.96$ for periodic boundary conditions (b). Open boundaries (c) exhibit strong oscillations, however accurately yield a central charge $c \approx 1.03$ for V-MI phase. The completely gapped M-MI phase S_{vN} is flat.

where $\phi_\pm = \sqrt{\pi}(\phi_1 \pm \phi_2)/\sqrt{2}$, $\theta_+ = (\theta_1 + \theta_2)/\sqrt{2\pi}$, $\theta_- = (\theta_1 - \theta_2 + \phi x/\sqrt{\pi})/\sqrt{2\pi}$, and couplings constants $\lambda_m \sim J_\perp$. $K_\pm$ and $v_\pm$ are Luttinger-liquid parameters and sound velocities corresponding to the symmetric and antisymmetric sector.

As discussed in [294] the $\cos\sqrt{2\pi}\theta_-$ term opens a gap in the antisymmetric sector for any U and a $J_\perp$ in the M-phase. Assuming a decoupling of "spin" (antisymmetric) and "charge" (symmetric) degrees of freedom, on may describe the two sectors as two independent sine-Gordon models and introduce a vortex density defined as the number of solitons in the antisymmetric mode [42]. Interestingly the flux ϕ acts a a chemical potential in the antisymmetric sector. Fixing all other parameters and increasing the flux ϕ the system undergoes a commensurate-incommensurate transition at $\phi < \phi_c$ to a V-phase, gapless in the antisymmetric sector. The rung-current correlations decay algebraically as [294]

$$\langle j_R(x) j_R(x') \rangle \sim \frac{\cos 2\pi \rho_V(x - x')}{|x - x'|^{1/K_-}}. \tag{6.25}$$

Reference [294] shows how for certain commensurate vortex-densities $\rho_V = p/q$, with p vortices in q sites, the system may undergo a further C-IC transition to a so called Vortex-lattice (VL) phase, a phase of crystallized vortices, opening a gap in the antisymmetric sector. In this analysis, valid for $J_\perp \ll J$ each vortex lattice phase is realized close to its commensurate value of flux $\phi = \pi p/q + \delta\phi$ for weak interactions, as soon as the Luttinger-liquid parameter exceeds $K_- > \frac{q^2}{4}$. We will discuss this aspect in more detail in the following section.

6.5.2   The ground-state phase diagram

In Fig. 6.9 we present an overview of the ground-state phases as function of the free parameters density n and flux ϕ for different values of $J_\perp/J$. Interestingly, as for the case of free bosons or fermions the phase diagram basically splits into different regions of a Meissner superfluid (M-SF) and a vortex superfluid (V-SF) phase. The V-SF phase for larger fillings $\rho > 1/4$ is strongly suppressed with increasing $J_\perp/J$; for $J_\perp \gtrsim 1.3J$ we just observe a M-SF phase for $\rho > 1/4$.
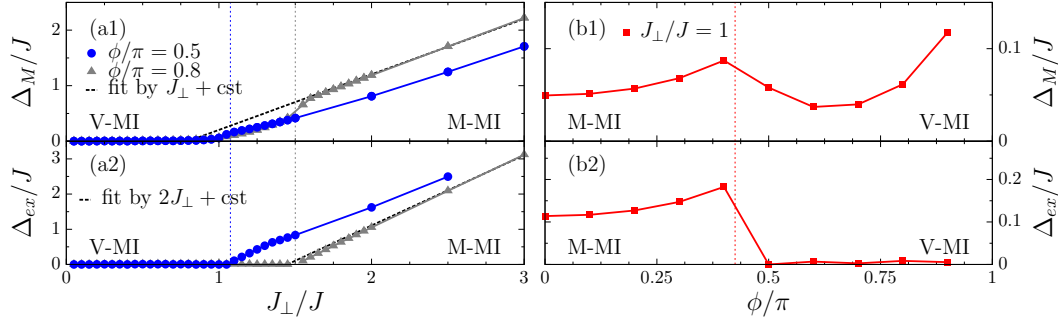
Fig. 6.11: Mass and neutral excitation gap in the V-MI and M-MI phases for $n = 1/2$ as function of $J_\perp$ and flux ϕ ($L = 201$ rungs). The DMRG calculations have been performed by M. Piraud employing DMRG-codes supplied by I. McCulloch.

Dilute limit

The lower V-SF lobe just vanishes for $J_\perp/J \to \infty$. The presence of the 2-component V-SF phase for $\phi > \phi_c$ is best understood from the limit $\rho \to 0$, in which ϕ_c coincides with the free boson case (6.20). Here, given a two fold-degenerate dispersion minimum for $\phi > \phi_c$, we may develop an effective 2-component boson theory as introduced in chapter 5. We will come back to this point in section 6.7. The hardcore interactions will always favor an equal population of both dispersion minima, which corresponds to the V-SF phase, resulting in an equal population of both legs.

Numerical results

As discussed for the case of free particles, the M-SF and V-SF phases can be discriminated by their local current configurations. An accurate identification is given by the calculation of the central charge, which is $c = 1$ for the M-SF and $c = 2$ for the V-SF phase. We extract the central charge c from scaling properties of the von-Neumann entropy as shown in Fig. 6.10.

The C-I phase boundary of the V-SF to the M-SF phase can be determined accurately from the equation of state $\rho = \rho(\mu)$, which exhibits a cusp-like behavior at this point. In Fig. 6.12 (a) we present the $\rho(\mu)$-curve for several cuts through the phase diagram 6.9.

As expected we do not observe VL phases for the hardcore boson case, since these states are most stable for the weakly interacting case

Commensurate densities

Contrary to spinless fermions [300] at half filling hardcore bosons $\rho = 1/2$ on a ladder always exhibit a Mott-insulating state with a finite mass gap $\Delta_M = (2E^0_{N=L/2} - E^0_{N=L/2-1} - E^0_{N=L/2+1})/2$, with E^m_n being the energy of the mth state in the sector of n particles. For a finite flux the MI-phase as the SF phases may split into two different regimes of a M-MI and a V-MI. While the M-MI phase is completely gaped, the V-MI phase exhibits still one gapless mode in the antisymmetric sector, i.e. the neutral excitation $\Delta_{ex} = E^0_{N=L/2} - E^1_{N=L/2}$ vanishes while $\Delta_M > 0$. In Fig. 6.11 we show the energy gap for the V-MI and M-MI phases as a function of $J_\perp$ and ϕ. This property is reflected by the central charge, which is $c = 1$ for the V-MI phase, as depicted in Fig. 6.10 (b) and (c). The totally gapped M-MI phase exhibits a flat $S_{vN}(x)$ curve.

(a)

(b)
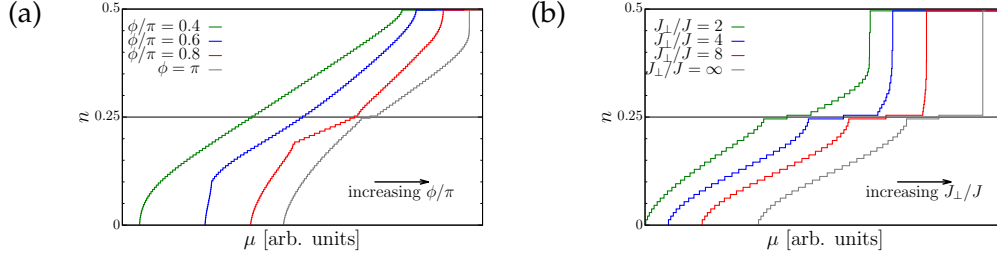
Fig. 6.12: (a) $\mu - \rho$-profiles at $J_\perp = 1.5J$ ($L = 100$) for different values of ϕ. The MI-VSF transition can be identified by the kink in the curve. (b) $\mu - \rho$-profiles at $\Phi = \pi$ flux for large values $J_\perp/J$ and the effective model (6.27). The widths of the extended plateau at quarter filling increases with $J_\perp/J$. For high fillings the system exhibits a macroscopic - meta-magnetic - jump to the half filled state. The chemical potential μ has been rescaled and shifted such that all curves fit in one figure.

The M-SF to V-SF boundary exhibits an unusual shape with a cusp around $\rho = 1/4$. This property can be related to the proximity of a gapped CDW phase at density $\rho = 1/4$ for $J_\perp > 1.7J$. A detailed picture of this phase can be obtained from large rung-coupling limit in the following subsection.

6.5.3 The strong-rung coupling limit $J_\perp \gg J$

An interesting limit amenable to analytical treatment is the case of strong interchain tunneling $J_\perp \to \infty$. In that regime we may introduce a pseudo-spin-1/2, identifying on rung j, $(|1,0\rangle_j + |0,1\rangle_j)/\sqrt{2} \to |\downarrow\rangle_j, |0,0\rangle_j \to |\uparrow\rangle_j$. Then the effective spin-$\frac{1}{2}$ model to the first order in $1/|J_\perp|$ is $\hat{\mathcal{H}}_{\frac{1}{2}} = J\hat{\mathcal{H}}_{\frac{1}{2}}^0 + J^2/|J_\perp|\hat{\mathcal{H}}_{\frac{1}{2}}^1$:

$$\hat{\mathcal{H}}_{\frac{1}{2}}^0 = \cos\left(\frac{\Phi}{2}\right)\sum_x S_x^+ S_{x+1}^- + h.c.$$

$$\hat{\mathcal{H}}_{\frac{1}{2}}^1 = -\cos\left(\frac{\Phi}{2}\right)^2 \sum_x S_x^+(1/2 + S_{x+1}^z)S_{x+2}^- + h.c.$$

$$-\frac{1}{2}\sin\left(\frac{\Phi}{2}\right)^2 \sum_x S_x^+(1/2 - S_{x+1}^z)S_{x+2}^- + h.c.$$

$$-\frac{1 + 3\cos(\Phi)}{2}\sum_x S_x^z S_{x+1}^z \tag{6.26}$$

In this effective model zero magnetization corresponds to quarter filling $\rho = 1/4$ in the original ladder-model, the fully polarized states correspond to zero or half filling. For small fluxes the first order term $\hat{\mathcal{H}}_{\frac{1}{2}}^0$ clearly dominates and the system behaves as a one component $c = 1$ Luttinger-liquid. Close to $\Phi = \pi$ the higher order terms become relevant. At $\Phi = \pi$ one remains with the correlated hopping term and nearest-neighbor Ising-type interactions:

$$\hat{\mathcal{H}}_{\frac{1}{2}} = -\frac{J^2}{2|J_\perp|}\sum_x S_x^+(\frac{1}{2} - S_{x+1}^z)S_{x+2}^- + h.c. - 2S_x^z S_{x+1}^z \tag{6.27}$$

Hence, for low fillings the system behaves as two single chains coupled only by the repulsive $S^z - S^z$ interaction. For large fillings due to the correlated hopping basically all tunneling processes are strongly suppressed and only the Ising term

$S_x^z S_{x+1}^z$ remains. That is why in the vicinity of $\phi = \pi$ the ground state at quarter filling ($\rho = 1/4$) in effective spins is a doubly degenerate Néel state, that in bosons translates into the charge density wave state. When changing flux from π the system at $\phi = \phi_c < \pi$ undergoes a transition from a Néel state ($\phi_c < \phi \leq \pi$) into a gapless XY phase ($\phi \leq \phi_c$) that is characterized by $c = 1$ (e.g. for $J_\perp = 4J$ we find $\phi_c \approx 0.9\pi$). The existence of a fully gapped state at $\rho = 1/4$ for strong $J_\perp$ in the vicinity of $\phi = \pi$ and a direct transition from fully gapped state to $c = 1$ phase with diminishing ϕ explains the tendency of the $c = 1$ M-SF region piercing the $c = 2$ phase displayed on Figs. 6.9.

The effective spin-$\frac{1}{2}$ model (6.27) reveals an interesting feature, namely metamagnetic behavior just under the saturation magnetization, that corresponds to $n = 0.5$ filling for bosons. The magnetization curve exhibits a macroscopic jump to the saturation magnetization whose size increases with $J_\perp/J$. As one can see from Eq. (6.27), for $J_\perp/J \to \infty$ and $\rho > 1/4$, the ground-state energy is a linear function of ρ, and thus in the equation of state $n = n(\mu)$ (Fig. 6.12 (b)) the whole range of densities $1/4 < \rho < 1/2$ is unstable.

6.6 The Josephson junction limit

As a limit complementary to the previously discussed hardcore bosons, we will now revise the physics of weakly interacting bosonic particles on a two leg ladder. This regime has been extensively studied in the context of Josephson junctions ladder [290–293]. Interestingly, this description of superconducting islands proximity-coupled to its neighbors can be also applied to the more recent experimental realizations [2, 286] in the context of ultracold bosonic atoms: The experiments are realized in the regime of large fillings $\rho \gg 1$ and weak but finite interactions. Since the interactions are small $U \ll J\rho$ we neglect charging effects of the superconducting islands [293], however, the interactions and densities are assumed to be large enough to suppress density fluctuations. Within the weak coupling approximation (see chapter 5) we yield the following frustrated XY-model of classical spins

$$\mathcal{H} \to -2J\rho \sum_{\ell=1,2;r=1}^{L} \cos(\theta_{\ell,r+1} - \theta_{\ell,r}) - 2J_\perp\rho \sum_{r=1}^{L} \cos(\theta_{1,r} - \theta_{2,r} - r\phi). \qquad (6.28)$$

This model has been studied using the effective potentials method [292, 306], which will allow for a description of ground-state properties, or a transfer matrix approach [293] at finite temperatures $\beta = 1/k_B T$. Assuming periodic boundary conditions, model (6.28) may be mapped to a one dimensional chain

$$\mathcal{H} = -4J\rho \sum_{r=1}^{L} \cos((\alpha_{r-1} - \alpha_r)/2 + \phi) - 2J_\perp\rho \sum_{r=1}^{L} \cos(\alpha_r), \qquad (6.29)$$

with $\alpha_i = \theta_{1,r} - \theta_{2,r} - r\phi$ and without loss of generality $\theta_{1,r+1} - \theta_{1,r} = \theta_{2,r} - \theta_{2,r+1}$. We may evaluate the partition function $Z = \text{tr } \hat{P}^L$ in the thermodynamic limit by means of the transfer matrix [293]

$$\hat{P}(\alpha, \alpha') = 4\pi e^{\beta 2J_\perp(\cos(\alpha)+\cos(\alpha'))/2} \mathcal{J}_0\left(4\beta J \cos\left((\alpha - \alpha')/2 + \phi\right)\right) \qquad (6.30)$$

We calculate its eigenvalues λ_n, $n = 0, 1, 2, \ldots$ and $|\lambda_n| > |\lambda_{n+1}|$ by numerical diagonalization of P which determine the spacial decay and periodicity of typical
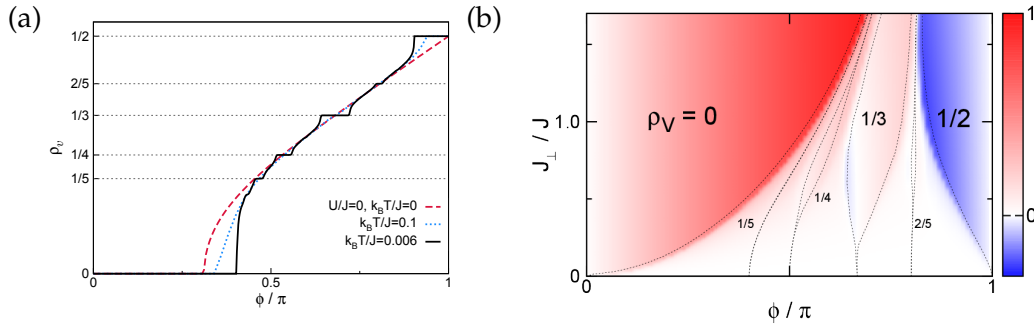
Fig. 6.13: (a) Vortex-density of the bosonic ladder in the weak coupling limit for $k_BT = 0.006J$ (solid black line) and $k_BT = 0.1J$ (dotted blue line) for $J_\perp = J/2$. As a comparison we also depict the free boson case (dashed red line). (b) Phase diagram in the ϕ, $J_\perp$ plane. The dotted lines depict the largest vortex-plateaus which remain stable for $k_BT = 0.01$. The shading encodes the chiral-current j_c for $k_BT = 0.01J$. In the limit of $J_\perp/J \to 0$ the extent of the vortex-lattice phases shrinks and each vortex-lattice is realized at a "commensurate" flux $\phi = p\pi/q$.

correlation functions. The phase of the second largest eigenvalue can be related to the spacial periodicity of the phase fluctuations which is equal to the vortex density

$$\rho_v(\phi) = \mathrm{Arg}[\lambda_1(\phi)]/2\pi . \qquad (6.31)$$

Surprisingly, the ground state of model (6.28) is entirely different from the non-interacting model studied in section 6.4. While in the latter situation we just observe two regimes, of a Meissner and a vortex-SF-like phase, in the high filling weak interaction regime vortex-lattice phases are stabilized [290]: It can be shown that for each commensurate vortex-density $\rho_V = p/q$, with p and q being coprime integers, the vortices form regular crystals of p vortices every q plaquettes. A cut through the phase diagram, as shown in Fig. 6.13 (a), thus resembles a complete fractal devil's staircase structure, while the vortex-density for the non-interacting case (red dashed line) is a smooth curve, except for the Meissner phase. The width of the plateaus depends on the rung-coupling $J_\perp$ as shown in the phase diagram Fig. 6.13 (b). In one dimension finite temperature effects immediately destroy the vortex-crystal introducing a finite number of defects. Thus, with increasing temperature the plateaus of constant vortex-density are gradually washed out. In Fig. 6.13 (a) for $k_BT/J \sim 0.006$ many plateaus for small values of q plateaus are visible (solid black line) and the vortex lattice $VL_{1/2}$ may be observed even for k_BT of a few tenths of J.

References [292, 293] focused on the calculation of vortex-density and ground-state energies. However, the experimentally relevant chiral-current was not discussed. We evaluate the chiral-current for finite temperatures k_BT using the transfer matrix approach through the generalization of Hellman-Feynman-theorem (6.18), by the derivative of the free energy with respect to the flux,

$$j_c(\phi) = -\frac{k_BT}{N}\frac{\partial \ln Z}{\partial \phi} . \qquad (6.32)$$

The shadings of the phase diagram Fig. 6.13 (b) encode the chiral current. A detailed discussion is postponed to section 6.8.

6.7 The ground-state phase diagram for moderate interactions

Starting from the limit of weakly interacting bosons in the literature the effect of quantum fluctuations has been discussed in Ref.[290, 294] showing the stability of the vortex-lattices and vortex-liquids in the presence of finite interactions. However, bosonization is typically restricted to weak rung-coupling limits $J_\perp \ll J$ and small fluxes. Other approaches such as mean-field treatments [298] remain questionable in one dimensional systems. In the following we present the first observation of several vortex-lattice phases in the microscopic BH model using DMRG. The special case $\phi = \pi$ has been studied before using DMRG [242, 243]. The described CSF-phase corresponds to the $VL_{1/2}$ phase, however, this connection has not been made.

We use large scale DMRG simulations in order to study the ground-state properties of model (6.14) in the limit of moderate interactions $U \sim J$ and fillings $0 < \rho \lesssim 2$. The results are summarized in the representative phase diagrams Fig. 6.14 (a) and (b), which show the wealth of quantum phases of the model. Apart from the V-SF and M-SF phases we observe extended regions of vortex-lattice phases $VL_{1/2}$ and $VL_{1/3}$ in Fig. 6.14 (a). Furthermore, interestingly, for large values of $J_\perp/J$ a phase occurs with a spontaneously broken particle density imbalance between the legs, the biased ladder phase (BLP), as conjectured before from mean field approach [298]. In Fig. 6.14 (b) we study the stability of the $VL_{1/2}$ phase as a function of interactions, U, and the density, ρ. As we expect from the weak-coupling analysis for smaller interactions and larger fillings the extent of the VL region increases. This is consistent with the bosonization analysis of Ref. [294], which also indicates that VL-phases are a weak-coupling property.

We perform DMRG calculations for open boundary conditions and systems with up to $L = 160$ rungs, using 1000 DMRG states. Since the local Hilbert space of bosons is generally unconstrained we employ a cutoff of the maximal occupation. We typically keep up to four bosons per site, which is justified due to the repulsive nature of the onsite interactions $U > J$. By comparison with larger and smaller cutoffs we have verified the numerical accuracy of the quantities shown here. Fig. 6.15 illustrates the dependence of the chiral current on the bosonic cutoff. For $U \gtrsim J$ the results, obtained by keeping $n_{max} = 4$ particles per site, are already well converged.
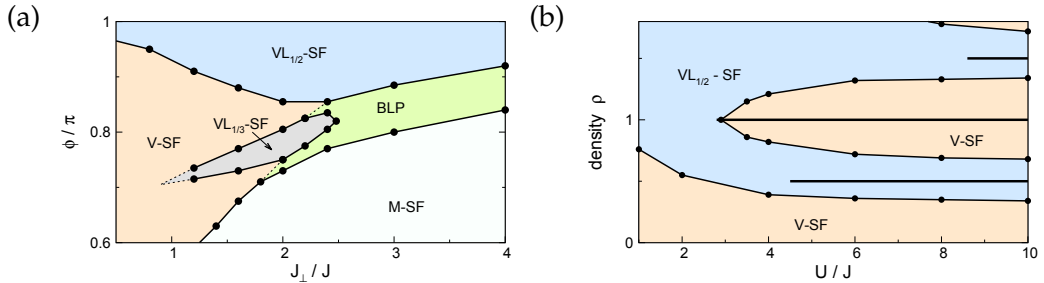
Fig. 6.14: Representative phase diagrams of interacting bosons in a two leg ladder subject to a magnetic field. (a) Phase diagram in the ϕ $J_\perp$ plane for $U = 2$. (b) Phase diagram in the U-ρ plane for $\phi = 0.9\pi$ and $J_\perp/J = 1.6$. The solid horizontal lines correspond to phases at commensurate particle density $\rho = 0.5, 1, 1.5, 2$ with a MI-gap.
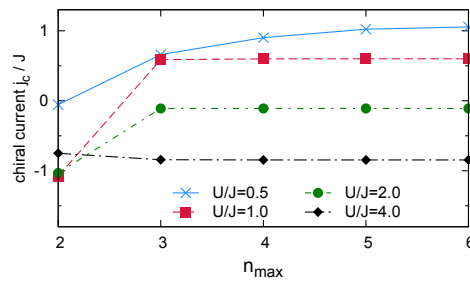
Fig. 6.15: Dependence of the chiral current on the bosonic cutoff n_{max}. DMRG calculation for the parameters of Fig. 3, $\rho = 0.5$, $\phi = 0.9\pi$ and $L = 40$ rungs.

For $0 < U \lesssim J$ we observe and verify, increasing n_{max} further, the tendency of a revival of the V-SF phase with positive chiral current for some $U < U_c < J$.

Close to the V-SF to VL_{ρ_v}-SF boundaries, the DMRG simulations tend to converge to metastable excited states with larger or smaller vortex density. Here, we have performed several calculations starting from different randomly chosen initial states. We select the lowest energy states of the ensemble to obtain the ground-state properties.

Vortex lattice phases

As an important part of our analysis we study the local current configurations of the model. In Fig. 6.17 we show the local current and density structure for a cut through the phase diagram 6.14 (a) for $J_\perp = 1.6$. One may directly observe certain plateaus of vortex-densities 0, 1/3 and 1/2. In these vortex-lattice phases while increasing the flux, the current-configuration remains stable.

Apart from identifying the vortex-lattice and Meissner phases by their characteristic local current configurations, they may be clearly discriminated from the vortex-liquid phase by calculating the central charge c extracted from entanglement-scaling properties as shown in the previous section. In Fig. 6.16 (a) we depict the extracted central charge for the data shown in Fig. 6.17 which is well consistent with $c = 1$ in the VL and M SF phases and $c = 2$ in the V-SF phase. Interestingly, as shown
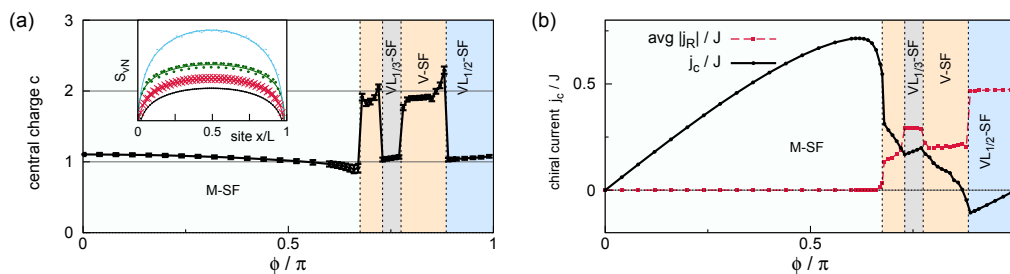
Fig. 6.16: Characteristic observvles and order parameters in the Vortex-lattice phases. (a) The extracted central charge for the same cut. (b) Example of the Block-entanglement entropy for the different phases for (from top to bottom) $\phi/\pi = 0.8$ (V-SF), 0.74 (VL13), 0.62 (M), 0.96 (VL12) (c) Chiral current and average rung-current for the same paramters as in Fig. 6.17.
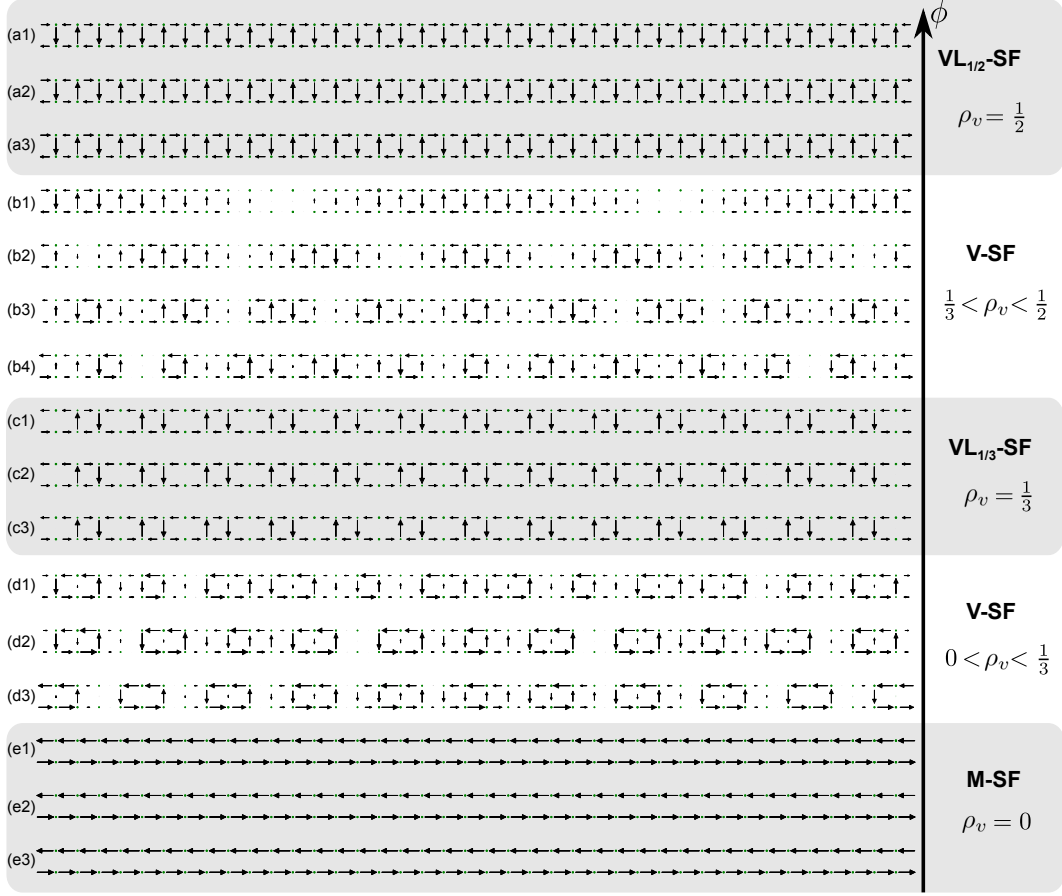
Fig. 6.17: Local current configurations for a cut through the phase diagram Fig. 6.14 (a) for $J_\perp = 1.6J$ ($U = 2J$ and $\rho = 0.8$)and (in descending order) (a1) $\phi = 0.95\pi$, (a1) 0.93π, (a3) 0.9π, (b1) 0.88π, (b2) 0.86π, (b3) 0.82π, (b4) 0.79π, (c1) 0.77π, (c2) 0.75π, (c3) 0.73π, (d1) 0.71π, (d2) 0.69π, (d3) 0.68π, (e1) 0.64π, (e2) 0.6π, and (e3) 0.56π ($L = 120$ rungs). We only depict the behavior for the middle rungs of the ladder ($40 \leq r \leq 80$) in the bulk of the system. The length of the arrows encodes the absolute value of the local currents and the size of the circles encodes the onsite density.

in Fig. 6.16 (b), the entanglement entropy in open boundary systems exhibits small oscillations that follow the lattice structure of the VL phases.

As for the M-SF phase the chiral-current but also the averaged rung-current may be used as indicator for in the VL-phases. The j_c exhibits a characteristic linear increase with the flux ϕ as presented in Fig. 6.17 (c), which we will discuss more in detail in the section 6.8. The average rung current $\mathrm{avg}|j_R|$ exhibits a stable large plateau in the VL-phases. The transition to the V-SF phases is indicated by a marked drop of $\mathrm{avg}|j_R|$.

In Fig. 6.18 we present selected examples for the microscopic structures of the vortex-lattice configurations of M-SF, $VL_{1/3}$ and $VL_{1/2}$. The VL phases are characterized by an intermediate Meissner-like region (indicated by the dashed line in Fig. 6.18) in which the current circulates in a counter-clockwise direction, and the vortices with a reversed current.
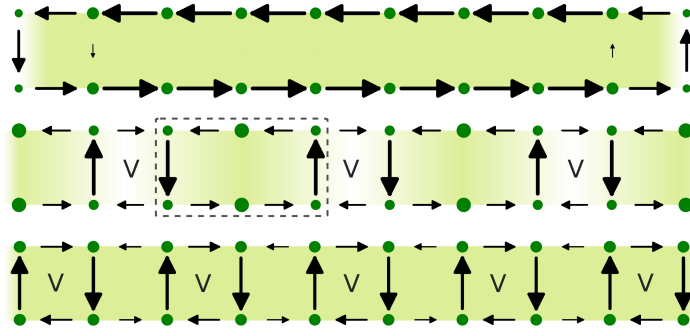
Fig. 6.18: Examples for local current (arrow-lengths) and density configurations (shading and size of the circles) (obtained from actual DMRG calculations for $U = 2J$, $J_\perp = 1.6J$, $\rho = 0.8$) of the M-SF (top, $\phi = 0.6\pi$, $L = 10$) and VL$_{1/3}$ (middle, $\phi = 0.8\pi$, $L = 120$) and VL$_{1/2}$ ($\phi = 0.9\pi$, $L = 120$).

The biased leg phase

Our DMRG simulations provide the first direct observation of the BLP phase and prove its stability even for moderate interactions and small fillings (see Fig. 6.14). The current configuration of the BLP phase is very similar to the M-phase. As shown in Fig. 6.19, the current flows through the boundary of the ladder while the rung currents are suppressed. The particle density, however, exhibits a marked imbalance between the legs, which we quantify by calculating

$$\Delta n = \sum_r \left(n_{1,r} - n_{2,r} \right) / N . \tag{6.33}$$

In the thermodynamic limit the ground state is thus two fold degenerate, spontaneously breaking the Z_2 mirror symmetry between the legs.

In order to numerically stabilize the simulation of the BLP phase, we add small potentials at the boundary of the ladder explicitly breaking the symmetry of the system. We verify by comparing to simulations with smaller or larger edge potentials, that their effect does not influence the order-parameters. Interestingly, also an unbiased not fully converged DMRG simulation will typically exhibit a finite Δn selecting one of the two degenerate ground states depending on the initial random configuration. The presence of explicit symmetry breaking terms, however, significantly improves the speed of convergence of the simulation.

We identify the phase transition by a sharply increasing particle density imbalance between the legs Δn, as presented in Fig. 6.20. The data is consistent with a second order Ising type transition between the M-SF and the BLP phase, as one might expect from to the spontaneous symmetry breaking. However, since we cannot exclude a weak first-order nature of the transition this aspect should be subject to further research.
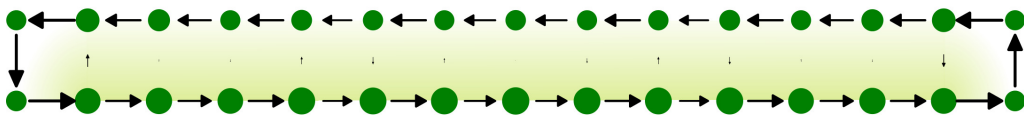
Fig. 6.19: Typical current and density configuration of the BLP phase.
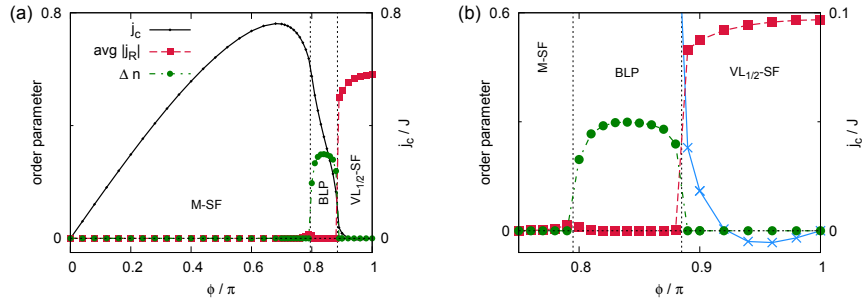
Fig. 6.20: (a) and (b) present order parameters for the BLP phase, the chiral current j_c, the averaged rung-current $\mathrm{avg}|j_R|$ and the density imbalance $|\Delta n|$ for a cut through the phase diagram 6.14 for $J_\perp/J = 3$. (b) shows a zoom of the BLP-VL$_{1/2}$ transition.

The dilute limit

We may derive an effective description of the BLP phase valid in the limit of vanishing particle densities from two-particle scattering properties closely following the scheme described in chapter 5. In the V-SF phase the intra-species interaction $g_{11} > g_{12}$ is dominant. Both dispersion minima are equally populated. Dominant inter-species scattering $g_{11} < g_{12}$ results a spontaneously broken state with a dominant occupation of the dispersion minimum at $k = Q$ or $k = -Q$. Interestingly, the occupation of only one minimum results in a preferential population of the particles on one leg (see Fig. 6.7 (a)). Hence, the phase realized for $g_{11} < g_{12}$ corresponds to the BLP phase.

In order to obtain a quantitative description we will follow the path discussed in Refs. [37, 307]. For the cases were the single particle dispersion develops a two particle minimum, one may derive an effective two component boson model for the lowest occupied particle species, each corresponding to one minimum of the dispersion relation of the lowest band. Neglecting scattering to the excited band, one may obtain g_{11} and g_{12} by solving the Bethe-Salpeter equation for the renormalized two-body interaction vertex, which in general may be done by numerical integration techniques. Figure 6.21 depicts g_{11} and g_{12} for a flux $\phi = 0.8\pi$ and $J_\perp = 3.5J$. Interestingly, for a finite range of U the interspecies coupling g_{12} is dominant and thus the BLP phase is realized. As expected for larger values of U/J the systems enters the V-SF phase, with a homogeneous density distribution. Unfortunately the numerical approach suffers strongly from convergence problems close to the M-SF boundary.

Mott phases

The previous discussion was focused on incommensurate particle densities. At commensurate fillings $\rho = 1/2, 1, 3/2, \dots$ we observe Mott phases with a finite mass gap Δ_M at sufficiently large U/J. These phases are depicted in Fig. 6.14 (b) as solid horizontal lines for a large flux $\phi = 0.9\pi$. A detailed picture may be found in Fig. 6.26 anticipating the discussion of the following section.

The MI-region exhibits a rich structure. At half filling, surprisingly, we find a largely extended fully gapped VL$_{1/2}$-MI phase. The BKT transitions between VL$_{1/2}$-SF and VL$_{1/2}$-MI at fillings $\rho = 0.5$ and $\rho = 1.5$ shown in Fig. 6.14 are determined by numerically analyzing correlation functions. At the transition from
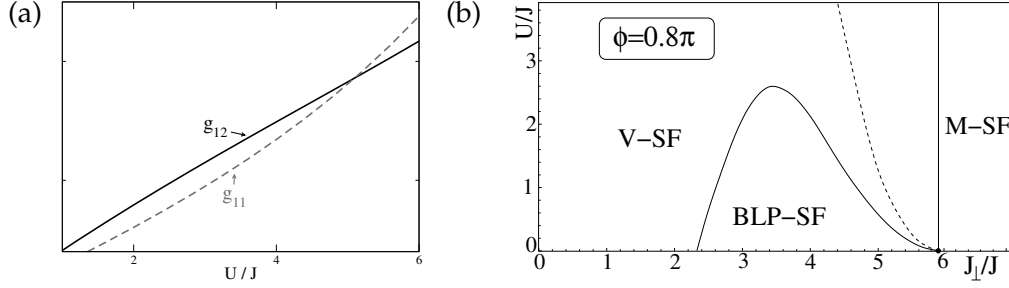
Fig. 6.21: (a) Typical effective coupling parameters for the dilute limit calculations, here for $J_\perp = 3.5$, $\phi = 0.8\pi$. (b) Phase diagram for the dilute limit. The dashed line depicts the values where a super-Tonks regime is reached. Results are obtained by Temo Vekua using a the 2-particle scattering approach.

the $VL_{1/2}$-SF to the $VL_{1/2}$-MI, bosonization predicts that the single-particle correlation function decays as $\langle a_{l,r}^\dagger a_{l,r+x} \rangle \sim x^{-\frac{1}{4}}$ (up to logarithmic corrections). The transition point can be extracted accurately from the finite-size scaling behavior of peaks in the quasi-momentum distribution function (see chapter 5). Surprisingly, in the hardcore limit, $U/J \to \infty$, we expect a transition to a gapless V-MI phase from the analysis of section 6.5.2. The position and character of this transition could not be yet determined.

The Mott-insulating region at unit filling $\rho = 1$ is even richer. Besides a narrow $VL_{1/2}$-MI region, a Meissner Mott-insulator state (M-MI) state is realized with increasing U/J. For the BKT transition inside the vortex lattice at $\rho_v = 1/2$ the single-particle correlation function decays as $\langle a_{l,r}^\dagger a_{l,r+x} \rangle \sim x^{-\frac{1}{8}}$ (up to logarithmic corrections) [43]. Other phase transitions are estimated from the behavior of the chiral current as well as from the local-current structure. Our simulations cannot exclude the possibility of an intermediate V-MI phase between the $VL_{1/2}$-MI and M-MI phases at unit filling. For the special case $\phi = \pi$, however, Dhar et al. [242, 243] showed that a direct transition between the $VL_{1/2}$-MI and M-MI phases is realized.

6.8   Chiral-current reversal: Swimming against the tide

6.8.1   The chiral current

In all recent experimental realizations in the context of ultra-cold gases [2, 273, 286] a detailed focus has been laid on the observation of the chiral current. Apart from its experimental accessibility the chiral-current is a useful tool for the characterizations and study of the different quantum phases and phase transitions in the two leg ladder. As already shown in section 6.4 for the non-interacting case the M-SF to V-SF transition can be identified by a cusp in the j_c curve. In the following we study properties of the chiral current as function of the rung coupling $J_\perp/J$.

As discussed in Ref. [42] for weakly coupled chains $J_\perp \ll J$ and for small ϕ field theoretical arguments show a general quadratic increase of j_c with $J_\perp$,

$$j_c \sim \frac{J_\perp^2}{J\phi^{3-1/K_0}} + O(J_\perp^4) \,, \tag{6.34}$$

where K_0 is the LL parameter for the Bose-Hubbard model of decoupled chains $J_\perp = 0$. Note that K_0 ranges from $K_0 = \infty$, for $U = 0$, to $K_0 = 1$, for hardcore bosons.

In Fig. 6.22 we depict this $J_\perp^2$ dependence for $\rho = 0.5$ and different values of U and a flux $\phi = \pi/2$. In the M phase for small U the numerical data resembles the non-interacting boson $U = 0$ result in which the j_c-curve becomes flat and independent of $J_\perp$. For large U we observe, however, a $1/J_\perp$ decay similar to the case of free fermions.

We can reproduce this result in the $J_\perp \gg J$ limit, by using second order perturbation theory at $\rho = 0.5$. We obtain

$$ j_c = \frac{J^2(4J_\perp + U)^2}{2J_\perp U(2J_\perp + U)} \sin(\phi). \tag{6.35} $$

The asymptotic value of is plotted in the inset of Fig. 6.22. Interestingly only for the hard-core limit the chiral current vanishes for $J_\perp \to \infty$.

In Fig. 6.23 we calculate the chiral-current from the transfer matrix approach in the weak coupling regime. As expected the results obtained for high temperatures, $k_B T \sim J$, and fluxes $\phi \sim \pi/2$ compare well to the results presented in [2] in a similar regime. For small $J_\perp$ the j_c increases quadratically and saturates for large values of the rung coupling. Around $\phi = \pi/2$ the largest values of the flux may be obtained. This situation is as well described by the physics of non-interacting bosons.

We may now examine the chiral current for lower temperatures. Already for $k_B T \sim J/10$ (cf. Fig. 6.23 (b)) the picture is surprisingly different. j_c apparently is no longer a monotonous function of ϕ for $\phi > \pi/2$. Even more surprisingly, for large fluxes $\phi \sim 0.9\pi$ the chiral current reverses its direction.

6.8.2 Flux increase in enlarged unit-cell systems

A reversed chiral current generally is a very exotic and non classical situation. The path of particles of electric charge q subject to a magnetic field is bended by the Lorentz force, $F_L = q\mathbf{v} \times \mathbf{B}$. The current of classical particles on a one dimensional path thus acquires a definite handedness or chirality (depending on q, B). Counter-clockwise rotating particles will produce a positive chiral current. Also non interacting bosons on a single plaquette always rotate counterclockwise with respect to
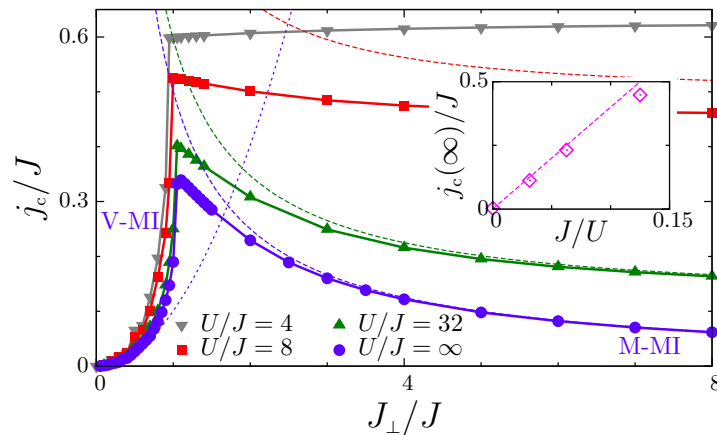
Fig. 6.22: at $\phi/\pi = 0.5$ for HCBs as well as $U/J = 4, 8, 16$ and 32 (see legend). Dashed lines: Theoretical predictions for HCBs and $J_\perp \ll J$ and $J_\perp \gg J$ [see Eqs. (6.34) and (6.35)]. Inset: Asymptotic value $j_c(J_\perp/J \to \infty)$ as a function of $1/U$, together with the fit $j_c(\infty) \propto 1/U$. ($U/J < \infty$: $L = 60$, $L = 201$ for $U/J = \infty$).

(a)

(b)

$\phi / \pi = 0.5$ ......
$\phi / \pi = 0.7$ – – –
$\phi / \pi = 0.9$ ——
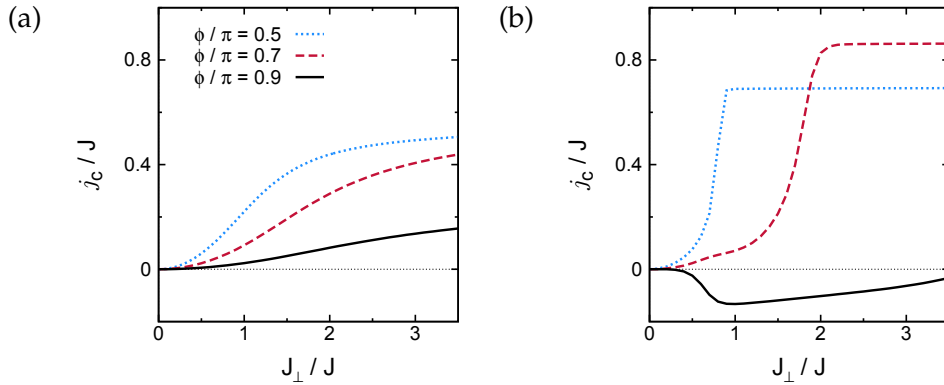
Fig. 6.23: Chiral current as obtained by the weak coupling limit for (a) $k_B T = J$ and (b) $k_B T = J/10$.

the synthetic magnetic field. The chiral-current goes like $j_c = \sin(\phi/4)$, $\phi \in (-\pi, \pi)$ modulo 2π. If we now assemble the single plaquettes to an extensive lattice, the current circulates counterclockwise along the boundary. All physical observables $\mathcal{A}$ on a lattice are periodic with respect to the flux $\mathcal{A}(\phi) = \mathcal{A}(\phi + 2\pi)$. Since the chiral current is an antisymmetric function $j_c(\phi) = -j_c(\phi + \pi)$, an inversed magnetic field causes an inversed circulation direction of the particles.

While, as discussed for non-interacting fermions, a current reversal may be related to a band-effect and the effective mass of the particles, here we discuss a different mechanism for the creation of negative j_c, which is inherently related to (interaction-driven) spontaneous symmetry breaking and the wave like nature of quantum particles. The basic idea of the mechanism is sketched in Fig. 6.24. The relevant unit-cell of the ground state does not necessarily coincide with the elementary unit-cell of the lattice. If in a ground state with spontaneously broken translational symmetry the effective unit-cell is doubled, due to their wave-like nature quantum particles may experience a doubled flux $\phi_{eff} = 2\phi$ piercing the new effective unit-cell. As a consequence, the effective flux may fall into a regime corresponding to an effectively inverted magnetic field, i.e. for $\pi/2 < \phi < \pi$ the effective flux falls in the domain $\phi_{eff} \in (-\pi, 0)$ modulo 2π. Hence chiral current may be reversed. Analogously the same argument may be extended to tripled, quadrupled, ... unit-cells. A state with a M-fold enlarged unit-cell gives rise to an effective flux $\phi_{eff} = M\phi$. Hence the chiral current may be reversed for $M\phi \in (-\pi, 0)$ modulo 2π.

For the two-leg ladder model states with a broken translational symmetry are vortex-lattices. In the following we will show how the effectively doubled, tripled,... unit-cell may lead to current-reversal effects.
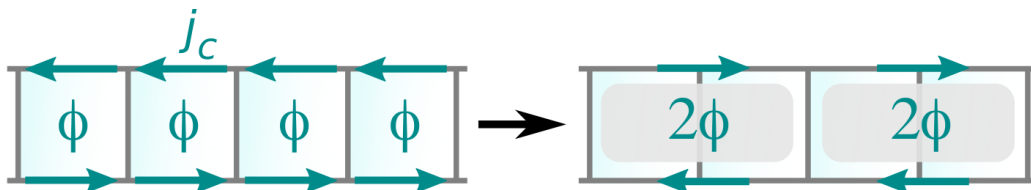
Fig. 6.24: Scheme of the effective flux doubling mechanism.
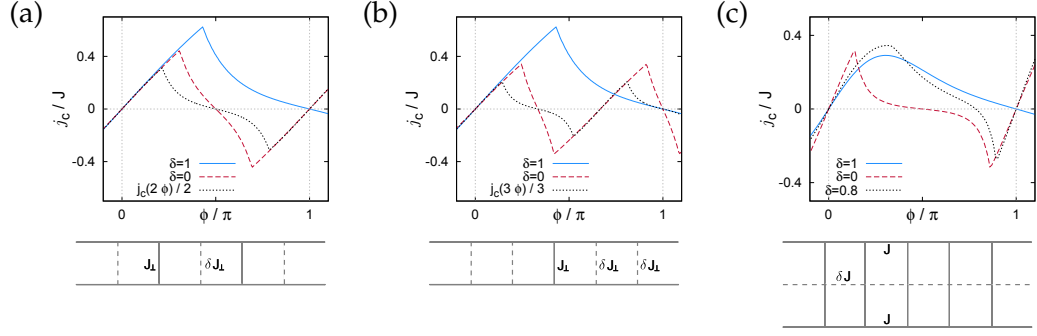
Fig. 6.25: j_c in externally distorted lattices. The unit-cell is explicitly doubled (a) and tripled (b). Removing the middle leg in a three-leg ladder (c) explicitly doubles the unit-cell.

6.8.3 Externally distorted lattice

Before discussing states with a spontaneously broken translational symmetry we will consider the very intuitive case of an externally distorted lattice. For simplicity we consider model 6.4 with $U = 0$ and certain rung-couplings being removed

$$\hat{\mathcal{H}}_\delta = -\tilde{J} \sum_{i,j} e^{i\phi} b_{i,j}^\dagger b_{i,j+1} - \tilde{J}_\perp \sum_j \delta_j b_{1,j}^\dagger b_{2,j} + H.c. \tag{6.36}$$

In Fig. 6.25 (a) we show the case of every second rung being removed ($\delta_{2j} = 0$ and $\delta_{2j+1} = 1$). The unit-cell is doubled and so is the effective flux; for $\pi/2 < \phi = \pi$ the chiral current becomes negative. Note, that due to the additional site the current of the system may differ from the case of a explicitly doubled flux $j_c(2\phi)/2$. We also explore this property for tripled unit-cells ($\delta_j = 1$ for j modulo 3 = 0 else $\delta_j = \delta$) as shown in Fig. 6.25 (b). Removing every third bond ($\delta_j = \delta$ for j modulo 3 = 0 else $\delta_j = 1$) will also result in a tripled unit-cell and a comparable behavior of the chiral current (not shown). For the sake of completeness in Fig. 6.25 (c) we depict the case of a three-leg ladder

$$\hat{\mathcal{H}}_\delta^3 = -\tilde{J} \sum_{i,j} e^{i\phi} b_{i,j}^\dagger b_{i,j+1} - \tilde{J}_\perp \sum_j \delta_{i,j} b_{i,j}^\dagger b_{i+1,j} + H.c. \tag{6.37}$$

The middle leg has been perturbed ($\delta_{i,j} = \delta$ for $i = 2$ else $\delta_{i,j} = 1$). Again, here the flux is effectively doubled and the current reversed, which shows the generality of the mechanism. Interestingly, in this case a phase transition from a M to a V-phase is induced by the perturbation - the unperturbed three-leg ladder for non-interacting bosons $U = 0$ just realizes a M-phase.

In fact, the idea of generating an effectively enlarged flux by applying an external perturbation to the system has been successfully exploited for example for the realization of the Hofstadter-model in graphene [272].

6.8.4 Moderate interactions

The main result of Ref.[43] is, however, the presence of the effective flux increase mechanism in the absence of external perturbations. While Hamiltonian (6.14) is translational invariant, its VL ground states in the presence of interaction break the translational symmetry. Our DMRG results present detailed evidence for the interaction driven current-reversal effect. In Fig. 6.26 we present the chiral-current j_c
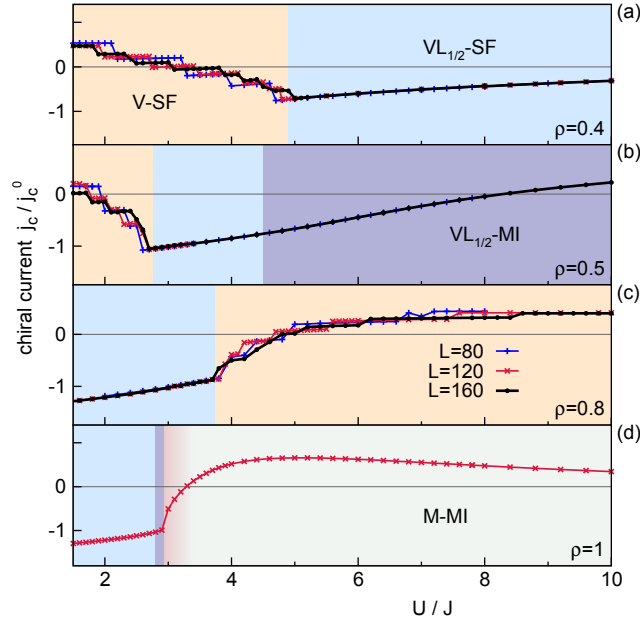
Fig. 6.26: Chiral current j_c as function of the interaction strength U/J in the proximity of the vortex-lattice phase $VL_{1/2}$ at $\phi = 0.9\pi$, $J_\perp = 1.6J$ for densities (a) $\rho = 0.4$, (b) $\rho = 0.5$, (c) $\rho = 0.8$, (d) $\rho = 1$. The figure shows results for three system sizes [$L = 80$ (blue symbols), $L = 120$ (red symbols) and $L = 160$ (black symbols)]. For $\rho = 1$ we just show points for $L = 120$, which agree with the data for $L = 80$ on the scale of the figure.

as functions of the interactions strength U/J for several densities close to the $VL_{1/2}$ phase. The exact value for $U = 0$ is $j_c^0 \simeq 0.08J > 0$, independently of ρ and consistent with our numerical simulations. With increasing interactions U/J the current-reversal effect may be suppressed for both commensurate and incommensurate fillings. It is always maximal for the smallest U/J within the VL-phase. This behavior can be explained by an decrease of the effective de-Broglie wavelength due to a gradual localization of the particles with increasing interaction strength. Only particles with a large wavelength may experience the effective flux of the enlarged unit-cell. The chiral-current reversal is robust against the presence or absence of a mass gap as shown in Fig. 6.26. Interestingly the absolute value $|j_c|$ may exceed the $U = 0$ value.

In Fig. 6.26 due to the incommensurate vortex density a significant system-size dependence is present in vortex-liquid superfluid states (V-SF) showing small steps [308]. In vortex-lattice phases the finite size dependence is reduced. Generally in the thermodynamic limit $L \to \infty$ in the V-SF phases $|j_c|$ is expected to continuously decrease when approaching a VL phase and show a cusp-like behavior at the phase boundary.

In the parameter regime studied in the work we do not observe the current reversal effect in the $VL_{1/3}$ phase, since it is realized for $\phi > 2/3\pi$ such that $3\phi \in (0, \pi)$ modulo 2π. However, as shown in Fig. 6.16 (b) the effective flux tripling is still evident from the linear increase of j_c with the flux resembling a copy of a mini-Meissner phase. This idea is elaborated more in detail in the following section.

Interestingly also the bosonization analysis of [294], valid for $J_\perp \ll J$, obtains the
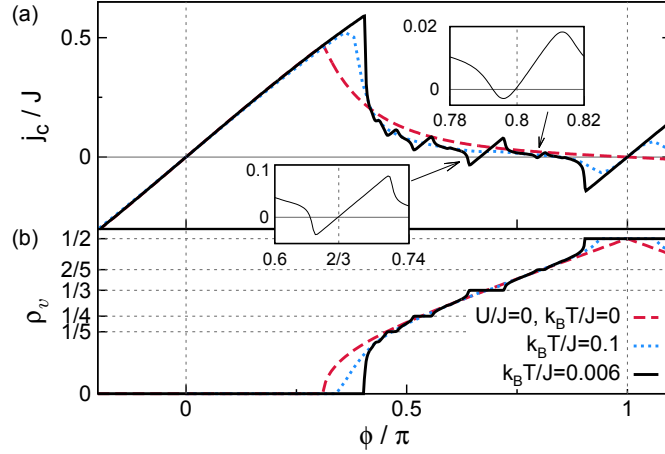
Fig. 6.27: Weak-coupling regime $\rho \gg 1$, $U \ll J\rho$. (a) Chiral current j_c/J and (b) vortex density as a function of flux for $J_\perp = J/2$. In vortex-lattice states with $\rho_v = 1/3, 2/5, 1/2$ at low temperatures we observe a reversal of the chiral current. The temperature is $k_BT = 0.006J$ (continuous lines) and $k_BT = 0.1J$ (dotted lines).

sign change of the chiral current. However, Ref. [294] does not discuss this effect or its physical background.

6.8.5 Weak interactions and finite temperatures

Further evidence for the conjectured flux increase mechanism is provided in the weak coupling regime, where the VL-phases are more stable. In fact here, at sufficiently low temperatures, we observe the chiral current reversal due to an effective flux increase in the proximity of several vortex lattice phases (for vortex-densities $\rho_v = 1/3, 2/5, 1/2$ in Fig. 6.27 (a)). The chiral-current vanishes at the commensurate flux $\phi/\pi = p/q$, since here $\phi_{eff} = 0$ modulo 2π.

The self-similar structure of the j_c curve may be understood as a result of the effective flux increase mechanism. The chiral current of the vortex-lattices corresponds to the chiral current of a copy of the Meissner phase at an increased effective flux. We verify this property by reconstructing the chiral current curve in Fig. 6.28 (a) by replacing the chiral current within the region of stability of the VL phase by the chiral current of free bosons with a M times enlarged unit cell

$$j_c = \frac{J}{M}\sin\frac{M\phi}{2}. \tag{6.38}$$

Thus for the Meissner state ($M = 1$) which is stable for $0 < \phi/\pi < 0.406 \ldots$ the current is given by $j_c = J\sin\frac{\phi}{2}$. For the the $VL_{1/2}$ phase, stable for $0.906\cdots < \phi/\pi <= 1$, ($M = 2$) it is $j_c = \frac{J}{2}\sin\phi$, etc.

Although for finite temperatures $k_BT/J > 0$ (in Ł $\to \infty$ limit) the crystalline order of the VL phases is immediately destroyed, the chiral-current reversal may still survive in the presence of a finite number of defects as also observed in the previous section for the neighboring V-SF phases. In particular for the $VL_{1/2}$ phase the current reversal can survive up to temperatures $T \simeq J/2$ (cf. Fig. 6.28 (b)) for $J_\perp \simeq J$ and $\phi \simeq 0.9\pi$. With such temperatures being within experimental reach the VL phases might actually be characterized by the spontaneous chiral current reversal.
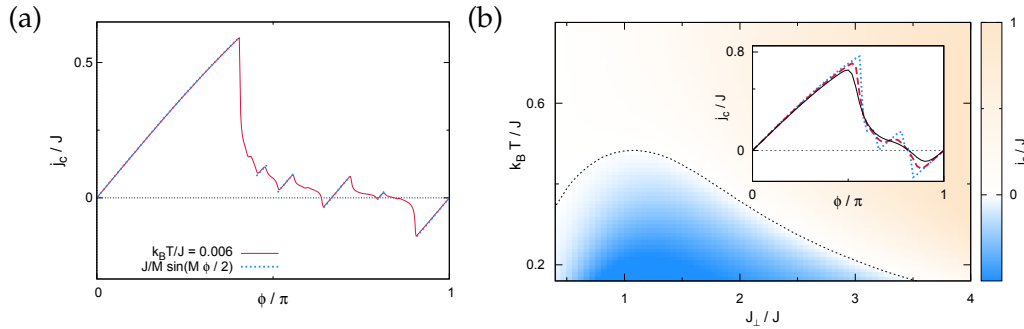
Fig. 6.28: (a) Construction of the self-similar structure of the j_c curve via effective flux increase mechanism. (b) Temperature dependence of the chiral current in the weak-coupling limit. The coloring in the main panel encodes the strength of the chiral current j_c/J as a function of temperature $k_B T/J$ and rung-coupling $J_\perp/J$ for $\phi = 0.92\pi$. The curve defined as $j_c/J = 0$ is highlighted with a dotted line. The inset shows j_c/J for $J_\perp/J = 1$ as a function of the flux ϕ for several temperatures $k_B T/J = 0.01$ (dotted blue line), 0.1 (dashed red line) and 0.2 (solid black line).

6.9   Conclusions

In the previous sections we have presented a detailed and extensive study of the ground-state physics of model (6.14). Besides the observation of the vortex and Meissner-SF and MI phases, vortex-lattice phases and their microscopic structure as well as the BLP phase have been found in an extended area. These findings could inspire further experimental approaches in the field. We furthermore studied the properties of the chiral current in different regimes. In the proximity of vortex-lattice phases with a spontaneously broken translational symmetry the chiral current may reverse it circulation direction. We explain this exotic feature by the effective flux of the enlarged unit-cell.

Recently, quantum phases of hardcore bosons on a three leg ladder geometry [309] have been studied. Interestingly, on a three leg ladder even for hard core particles different types of VL-phases and a staggered-current phase can be found. For the latter a current-reversal due to spontaneous flux increase has been observed.

The microscopic model (6.14) is relevant for the experiments realized by [2, 14]. An important experimental realization are the experiments in synthetic dimensions as discussed above [273, 286] where the presence of interactions on the rungs may play an important role and should be included in further studies. A question naturally rising from the discussion of vortex-lattices, is also the connection to the physics studied extensively in 2D such as the connection to fractional quantum Hall effect. Recently the presence of a Laughlin-like phase for commensurate particle and vortex densities was conjectured [297] for a two leg ladder in the presence of strong nearest-neighbor interactions. The existence and properties of such phases and connections should be explored further.

Chapter 7

Modulated Interactions

As elaborated in the previous chapters fast periodic modulations have been established as a powerful element of the cold atoms toolbox for the engineering of effective lattice models [1, 13, 14, 133–138, 144]. Inspired by these experimental advances the periodic modulation of interparticle interactions has been proposed as a method for the engineering of an effective non-linear hopping that depends on the occupation differences at neighboring sites [44, 45, 139, 310]. After a brief review of the underlying idea of periodically modulated interactions and properties of certain schemes and effective models, we show that a combined modulation of lattice and interactions [46] allows for the engineering of a broad class of models with correlated hopping. We will show how bosonic models with exotic MI phases that exhibit both parity and string order as well as Fermi-Hubbard models in unconventional parameter regimes relevant for cuprate superconductors can be simulated.

7.1 Periodically modulated interactions

The fast periodic modulation of an externally applied magnetic field, e.g. $B(t) = B_0 + B_1 \cos \omega t$, in the vicinity of magnetic Feshbach resonance (2.3) will induce a fast modulation of the scattering-length,

$$a(t) = a_{bg} \left(1 - \frac{\Delta B}{B(t) - B_r}\right) \approx a_0 + a_1 \cos \omega t \,. \tag{7.1}$$

Here ΔB and B_r are the width and the position of the Feshbach resonance and the latter approximation is valid for small $B_1/(B_0 - B_r) \ll 1$. Such a fast modulation of the scattering length and the resulting modulation of the interparticle interactions induce a non-linear or correlated hopping term which depends on the density difference of the different lattice sites [44].

7.1.1 The effective model

In the single band approximation the resulting Bose-Hubbard Hamiltonian is given by

$$\hat{\mathcal{H}}(t) = -J \sum_{\langle ij \rangle} \hat{b}_i^\dagger \hat{b}_j + \frac{U_0 + U_1(t)}{2} \sum_i \hat{n}_i (\hat{n}_i - 1) \,. \tag{7.2}$$

Here the modulated interactions are given by a periodic $U_1(t) = U_1(t + T)$, which we assume to be unbiased $\int_t^{t+T} dt' \, U_1(t') = 0$. We employ a unitary transformation $\hat{U}(t)$, with

$$\hat{U}(t) = e^{\mathrm{i} \frac{V(t)}{2} \sum_j \hat{n}_j (\hat{n}_j - 1)} \,, \tag{7.3}$$

in order to transform Hamiltonian (7.2) into the comoving frame. Choosing $\frac{d}{dt}V(t) = U_1(t)$, which is periodic $V(t) = V(t+T)$ since $U_1(t)$ is unbiased, moves the time dependence into the hopping term. Integrating out the fast modulation ($\omega = 2\pi/T \gg J/\hbar, U_0/\hbar$) we obtain

$$\hat{\mathcal{H}}_{\text{eff}} = -\sum_{\langle ij \rangle} \hat{b}_i^\dagger J_{\text{eff}}(\hat{n}_i - \hat{n}_j)\hat{b}_j + \frac{U_0}{2}\sum_i \hat{n}_i(\hat{n}_i - 1),\qquad(7.4)$$

with an effective density-dependent hopping

$$J_{\text{eff}}(\Delta\hat{n}) = \frac{J}{T}\int_0^T dt\, e^{iV(t)\Delta\hat{n}}.\qquad(7.5)$$

For a cosine-modulation $U_1(t) = \cos\omega t$ this results in an effective hopping depending on the Bessel-function

$$J_{\text{eff}}(\Delta\hat{n}) = \mathcal{J}_0\left(\frac{U_1}{\omega}\Delta\hat{n}\right).\qquad(7.6)$$

7.1.2 Complex tunneling amplitudes

In the construction of the unitary transformation (7.3) the choice of the function $V(t)$ is apparently well defined up to a time-independent constant which may result in a complex part of th effective hopping term. In the following we will show how the apparent gauge freedom is be fixed and discuss properties of complex density dependent tunneling amplitudes. These results have been published in Ref.[47] in collaboration with G. Sun, D. Poletti and L. Santos.

The momentum distribution

$$\rho_L(k,t) = \frac{1}{NL}\sum_{l,j} e^{-ik(l-j)}\langle\psi(t)|\hat{b}_l^\dagger\hat{b}_j|\psi(t)\rangle,\qquad(7.7)$$

as accessed in TOF measurements, is an important experimental observable which is not gauge invariant but depends on the presence and form of complex Peierls phases in the model. In Ref. [137] TOF experiments have been employed to prove the engineering of complex Peierls phases in an one dimensional system using lattice shaking techniques. Only a lattice modulation scheme explicitly breaking certain time reversal symmetries [137, 249] may realize complex hopping terms (see section 5.5). In a one dimensional model a shift of the quasi momentum distribution due to the complex phase can be prepared and measured.

The quasi-momentum distribution for modulated interactions is affected drastically. In general the single-particle correlation function for a state $|\psi(t)\rangle$ in the laboratory frame is given by

$$\langle\psi(t)|\hat{b}_i^\dagger\hat{b}_j|\psi(t)\rangle = \langle\psi'(t)|\hat{b}_i^\dagger e^{iV(t)(\hat{n}_i-\hat{n}_j)}\hat{b}_j|\psi'(t)\rangle.\qquad(7.8)$$

where $|\psi'(t)\rangle$ denotes the state in the comoving frame. Hence, the quasi-momentum distribution measured in the laboratory $\rho_L(k,t)$ only coincides with the one determined by the effective model

$$\rho_E(k) = \frac{1}{NL}\sum_{l,j} e^{-ik(l-j)}\langle\psi'|\hat{b}_l^\dagger\hat{b}_j|\psi'\rangle\qquad(7.9)$$
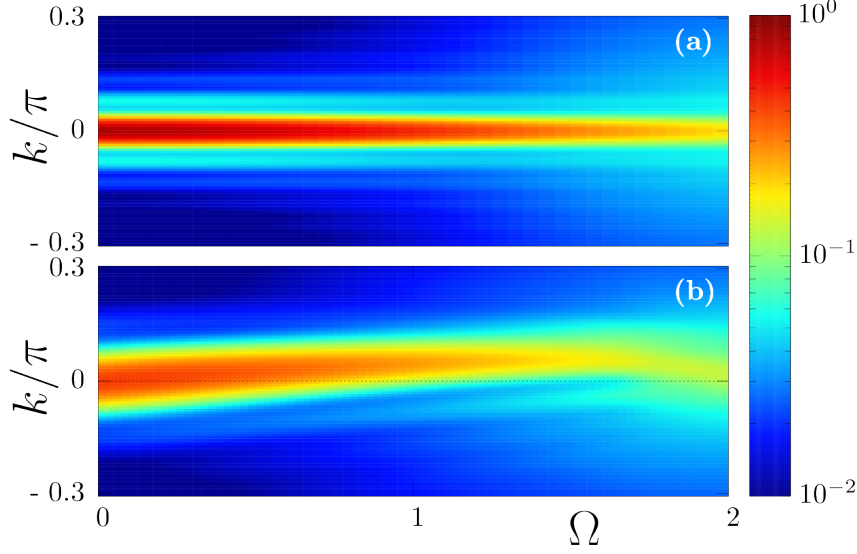
Fig. 7.1: (a) Quasi-momentum distribution of the ground-state of (7.4) with the effective hopping (7.10) as a function of Ω for $n = 1$ and $U_0 = J$. In order to exclude possible superfluid-to-insulator transitions we keep $J/J_0(\Omega)$ constant. (b) Same as (a) but with an on-site energy gradient, $\epsilon \sum_j j n_j$ with $\epsilon = 0.2J$. DMRG calculations were performed in $L = 36$ sites, with a maximal site occupation of 6 bosons.

for a stroboscopic set of measurements $t = nT$, with $n = 0, 1, \ldots$ at which the effective model acquires a complex density dependent phase determined by $V(0)$. Performing the stroboscopic measurements at different discrete times $nT + T_{initial}$ one may evaluate a different effective model with a different complex phase. However, the time evolution between $t = 0$ and $t = T_{initial}$ must be explicitly considered as initial condition $|\psi'(0)\rangle = \mathcal{T} e^{-i \int_{-t_0}^0 \hat{H}'(t') dt'} |\psi(-t_0)\rangle$, where $\mathcal{T}$ denotes time ordering.

For the particular case of a sinusoidal modulation $U_1(t) = \tilde{U}_1 \sin(\omega t)$ one yields $V(t) = \frac{\tilde{U}_1}{\omega} [1 - \cos(\omega t)]$ and, thus,

$$J_{\text{eff}}(\Delta \hat{n}) = |J \mathcal{J}_0(\hat{n}_i - \hat{n}_j)| e^{i\Omega(\hat{n}_i - \hat{n}_j)} \tag{7.10}$$

with $\Omega = \tilde{U}_1 / \hbar \omega$ [47].

It is important to note, that a complex phase, which depends on the density difference of adjacent sites $(\hat{n}_i - \hat{n}_j)$ may be gauged out by defining new bosonic operators

$$\hat{b}_j \rightarrow e^{-i\Omega \hat{n}_j} \hat{b}_j \tag{7.11}$$

and, hence, does not affect the spectrum of the Hamiltonian, determining ground-state phases or dynamics. However, as for the lattice shaking it has an effect on the momentum distribution. Since $J_{\text{eff}}(-\Delta \hat{n}) = J_{\text{eff}}(\Delta \hat{n})^*$ and, hence, $\phi(-\Delta \hat{n}) = -\phi(\Delta \hat{n})$. In a homogeneous system where quantum fluctuations of the occupation of adjacent sites do not have any preferred direction, there will not be a net effective Peierls phase and, hence, no shift of the momentum distribution. However, the quantum fluctuations lead to a stochastic character of Peierls phase and result in an effective coherence of the momentum distribution. This blurring of the quasi-momentum

distribution as function of Ω for a sinusoidal shaking is shown in Fig. 7.1 (a). A potential gradient in the model that results in a density gradient $\langle \hat{n}_j - \hat{n}_{j+1} \rangle \neq 0$ leads to a non-zero average effective Peierls phase. This results in a net shift and a broadening of the momentum distribution as shown in Fig. 7.1 (b).

In the next chapter we will show how density dependent modulations and Raman assisted tunneling schemes may be employed in order to realize non-gaugeable density dependent Peierls phases resulting in a fascinating novel regime of physics. In the subsequent part of this chapter we will focus on real effective hopping amplitudes $J_{\text{eff}} = J_{\text{eff}}^*$.

7.1.3   Fermions

Analog to the case of a one component bosonic gas the interaction term of a two component fermions described by a Fermi-Hubbard model may be modulated

$$\hat{\mathcal{H}}^F = \sum_{\langle i,j \rangle, \sigma = \uparrow, \downarrow} \left(\hat{c}_{i\sigma}^\dagger \hat{c}_{j\sigma} + \text{H.c.} \right) \quad + \quad [U_0 + U_1 \cos(\omega t)] \sum_j \hat{n}_{j\uparrow} \hat{n}_{j\downarrow}. \tag{7.12}$$

For the case of a spin-independent lattice, we reach for sufficiently fast modulations the effective Hamiltonian:

$$\hat{\mathcal{H}}_{eff}^F = U_0 \sum_j \hat{n}_{j\uparrow} \hat{n}_{j\downarrow} - \sum_{\langle i,j \rangle, \sigma = \uparrow, \downarrow} \left(\hat{c}_{i\bar{\sigma}}^\dagger J_{\text{eff}}(\hat{n}_i - \hat{n}_j) \hat{c}_{j\bar{\sigma}} + \text{H.c.} \right) \tag{7.13}$$

with $\bar{\sigma} = -\sigma$. We may reformulate (7.13) in a more general way

$$\hat{\mathcal{H}}_{eff}^F = U_0 \sum_j \hat{n}_{j\uparrow} \hat{n}_{j\downarrow} - \sum_{\langle i,j \rangle, \sigma = \uparrow, \downarrow} (\hat{c}_{i\bar{\sigma}}^\dagger \hat{c}_{j\bar{\sigma}} + \text{H.c.}) \mathcal{P}(\hat{n}_{i\sigma}, \hat{n}_{j\sigma}). \tag{7.14}$$

Here

$$\mathcal{P}(\hat{n}_{i\sigma}, \hat{n}_{j\sigma}) \equiv t_{AA}(1 - \hat{n}_{i\sigma})(1 - \hat{n}_{j\sigma}) + t_{BB} \hat{n}_{i\sigma} \hat{n}_{j\sigma} + t_{AB} \left[\hat{n}_{i\sigma}(1 - \hat{n}_{j\sigma}) + \hat{n}_{j\sigma}(1 - \hat{n}_{i\sigma}) \right] . \tag{7.15}$$

This corresponds to model (7.13) for $t_{AA} = t_{BB} = J_{eff}(0)$, and $t_{AB} = J_{eff}(1)$ and, hence, $|t_{AB}/t_{AA}| < 1$. The correlated hopping Fermi-Hubbard models (7.14) have been studied extensively during the last decades as a model for cuprate superconductors [311–315]. A detailed revision of the physics in the context of ultracold fermions in optical lattices with modulated interactions has been published recently [45].

7.1.4   The Kohn-metal

Modulated interactions and the resulting effective correlated hopping models lead to a rich physics. For both fermions and bosons in the effective correlated hopping Hamiltonian for any modulation the decay rate of doublons into single particles $|20\rangle \leftrightarrow |11\rangle$ (for fermions $|1\rangle$ may be $|\uparrow\rangle$ or $|\downarrow\rangle$) is reduced since $|J_{eff}(1)| \leq J$. The tunneling of single particles is fixed $|J_{eff}(0)| = J$. Most interesting physics in this regime may be observed at the particular point $J_{eff}(1) = 0$. For a sinusoidal modulation roots of Bessel-function have to be hit $\mathcal{J}_0(\Omega) = 0$, e.g. $\Omega \simeq 2.4048\ldots$. In this limit the decay of doublons $|02\rangle \leftrightarrow |11\rangle$ is forbidden. We will in the following revise the special physics in this limit for the case of fermions

$$\hat{\mathcal{H}}_{J_{eff}(1)=0}^F = U_0 \sum_j \hat{n}_{j\uparrow} \hat{n}_{j\downarrow} - \sum_{\langle i,j \rangle, \sigma = \uparrow, \downarrow} (\hat{c}_{i\bar{\sigma}}^\dagger \hat{c}_{j\bar{\sigma}} + \text{H.c.}) \left(1 - \hat{n}_{i\sigma} - \hat{n}_{j\sigma} + 2\hat{n}_{i\sigma} \hat{n}_{j\sigma} \right) , \tag{7.16}$$

for which an analytical solution may be found in one dimension.

As also shown in Refs [45] model (7.16) exhibits a high symmetry due to its both exact conservation of doublons and single particles. A MI state, which purely consist of singly occupied sites (of a random configuration of up or down spins), e.g.

$$|MI\rangle = \cdots |1\rangle_i |1\rangle_{i+1} |1\rangle_{i+2} \cdots = \cdots |\uparrow\rangle_i |\uparrow\rangle_{i+1} |\downarrow\rangle_{i+2} \cdots \qquad (7.17)$$

is obviously a zero-energy eigenstate of the Hamiltonian (7.16) since no further hopping may occur. It is favorable to consider an arbitrary MI state out of this highly degenerate ensemble as a quasi-vacuum in the following. Both the number of doublons D and holons $H = N - 2D$ on top of $|MI\rangle$, for at most N particles on the lattice, are conserved quantities. They may be treated as two types of impenetrable hardcore particles. Due to the hardcore constraint the total kinetic energy of both holon and doublon fluids equals, again fixing a given order of holons and doublons along the chain, a single component gas of hardcore particles. Thus for a chain of L sites, N particles and D doublons we obtain en energy

$$E(N, D) = -tE_{sf}(N - 2D, L) + U \cdot D \qquad (7.18)$$

with $E_{sf}(N, L) = -2 \sum_{k=1}^{N-2D} \cos \frac{k\pi}{L+1}$ the energy of a single component gas of hardcore particles. A minimization of $E(N, D)$ with respect to D for a given filling N/L yields the canonical ground-state phase diagram shown in Fig. 7.2 (a). Apart from the MI-phase at unit-filling, for sufficiently large interactions for $n < 1$ a SF phase of pure holons (HSF) or for $n > 1$ a pure doublon metal (DSF) phase is realized [311]. For attractive interactions $U < -4J$ the system enters an insulating completely paired phase I2. No single particles remain unpaired and the ground states constitute of an, again highly degenerate, configuration of doublons and holons.

For $-4 < U < -4 \cos \rho \pi$ the system enters the exotic Kohn-metal phase [311, 312, 316]. Here doublons, holons as well as single particles are present. Thus, although all particles may move locally and the phase exhibits a metallic character due to the vanishing excitation gap, the phase is globally insulating. Holons and doublons may not penetrate each other which leads to a vanishing Drude weight [311, 312, 316]. In a grand canonical ensemble as shown in Fig. 7.2 (b) the Kohn-metal phase, however, occupies a single line at $\mu = 0$. This will severely impede any experimental study, in cold atom experiments, which typically have to deal with a finite trapping
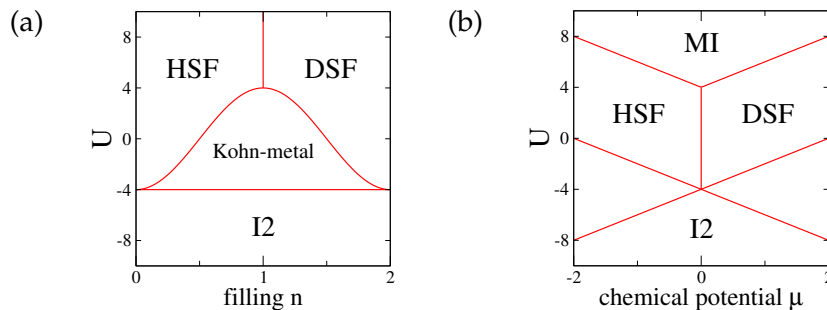

Fig. 7.2: Phase diagram of model (7.13) for the solvable point $J_{eff}(1) \to 0$. While in a canonical phase diagram (a) the Kohn-metal phase occupies an extended region of the phase diagram, in a grand-canonical picture (b) it is just realized for the line $\mu = 0$.

potential. In a local density approximation (2.28) one may expect a marked jump in the density separating sharply the DSF and HSF phases.

The complete phase diagram (see e.g. left part of Fig. 7.10) accessible with a pure modulation of interactions will be discussed more in detail in the following section.

For the case of softcore bosons still some decay channels exist due to the formation of triplons, which, however, may be energetically unfavorable. As shown in Ref.[44] indeed the ground-state physics for small fillings $n < 2$ and $J_{eff}(1) = 0$ is given by phases with a quasi-conserved number of doublons $|2\rangle$ and single particles $|1\rangle$. A pure holon and a pure doublon SF phase may be realized, as well as a defect free MI phase $|\dots 1111 \dots\rangle$. In a trap the HSF and DSF phases are separated by a sharp jump in density.

As shown in Ref. [44] the negative sign $J_{eff}(1) < 0$ (which may be gauged out as discussed above) of the tunneling may lead to a crossover from a SF-phase with dominant single particle correlations $G_1(i,j) = \langle b_i^\dagger b_j \rangle$ to a region with dominant two particle correlations $G_2(i,j) = \langle (b_i^\dagger)^2 (b_j)^2 \rangle$. Note that in 1D both G_1 and G_2 decay algebraically and thus this region is no PSF-phase.

7.2   Doubly Modulated Lattice Gases

As we have argued so far modulated interactions allow for the creation of certain effective correlated hopping Hubbard models with a decreased doublon decay or creation rate. In the following we will consider the combined coherent modulation of interactions and lattice (shaking), which happens to present a much richer physics than just the sum of its both parts, realizing a much broader class of correlated hopping Hubbard models and asymmetric tunneling rates.

The following section is based on the publication [46] which was developed in collaboration with L. Santos and D. Poletti.

For the case of a one component Bose gas the lattice Hamiltonian is given by

$$\hat{\mathcal{H}} = -J \sum_{\langle i,j \rangle} \hat{b}_i^\dagger \hat{b}_j + \frac{U(t)}{2} \sum_j \hat{n}_j (\hat{n}_j - 1) + F(t) \sum_j j \hat{n}_j \,. \tag{7.19}$$

The interaction and the tilting term are unbiased and periodically modulated, $U(t) = U_0 + U_1 f_U(t) = U_0 + U_1 f_U(t+T)$ and $F(t) = F_1 f_F(t) = F_1 f_F(t+T)$. Analog to the previous discussions for the case of a sufficiently fast modulation we arrive at the time independent effective description

$$\hat{\mathcal{H}}_{eff} = -J \sum_{\langle i,j \rangle} \hat{b}_i^\dagger \mathcal{F} \left(i - j, \hat{n}_i - \hat{n}_j \right) \hat{b}_j + \frac{U_0}{2} \sum_j \hat{n}_j (\hat{n}_j - 1) \tag{7.20}$$
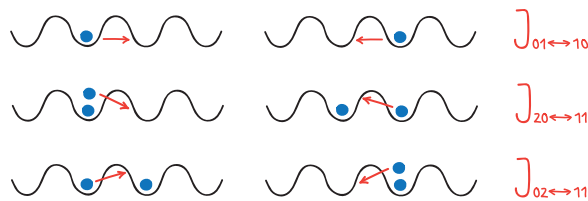
Fig. 7.3: Scheme of the hopping processes and effective rates.

For the case of a sinusoidal modulation $f_U(t) = f_F(t) = \cos(\omega t)$ we yield

$$\mathcal{F} = \mathcal{J}_0 \left[\frac{F_1}{\hbar\omega}(i-j) + \frac{U_1}{\hbar\omega}\left(\hat{n}_i - \hat{n}_j\right) \right] . \tag{7.21}$$

An important consequence of the double modulation is that tunneling may now be direction dependent. A hopping process to the left is given by

$$\frac{J_{(n_j,n_{j+1}) \leftrightarrow (n_j+1, n_{j+1}-1)}}{J} = \mathcal{J}_0 \left(\frac{U_1}{\hbar\omega}(n_j - n_{j+1} + 1) - \frac{F_1}{\hbar\omega} \right), \tag{7.22}$$

with $J_{(n_i,n_j) \leftrightarrow (n_i+1,n_j-1)}$ denoting the hopping rate from site j with n_j particles before the hop to site i with initially n_i particles. A hop to the right has the amplitude

$$\frac{J_{(n_j,n_{j+1}) \leftrightarrow (n_j-1, n_{j+1}+1)}}{J} = \mathcal{J}_0 \left(\frac{U_1}{\hbar\omega}(n_{j+1} - n_j + 1) + \frac{F_1}{\hbar\omega} \right). \tag{7.23}$$

The effective hopping rates and processes are sketched in Fig. 7.3.

7.2.1 Asymmetric tunneling.

An important feature of such doubly modulated (DM) Hamiltonians is that in general $J_{(1,1)\leftrightarrow(2,0)} \neq J_{(1,1)\leftrightarrow(0,2)}$ different to the standard Hubbard models. This breaking of mirror symmetry of DM results in unusual insulating phases.

CDW phases

A limit, quite typically encountered for doubly shaken Hamiltonians, which allows for an quasi-analytical treatment is given for the case in which there is one dominant tunneling process. Interestingly, one might explicitly engineer the situation in which all tunneling processes except for one exactly vanish by employing a a rectangular modulation function such that $F(x) = \mathrm{sinc}(x)$ and setting $U_1 = \pi$ and $F_1 = (\nu - 1)\pi$.

Generally for a dominant hopping $J_{(0,\nu+1)\leftrightarrow(1,\nu)}$ (or equivalently $J_{(\nu+1,0)\leftrightarrow(\nu,1)}$) for $\nu \in 2,3,\ldots$ a gapped CDW phase at filling $\rho = n + (\nu+1)/2, n = 0,1,\ldots$ for $\nu \neq 1$
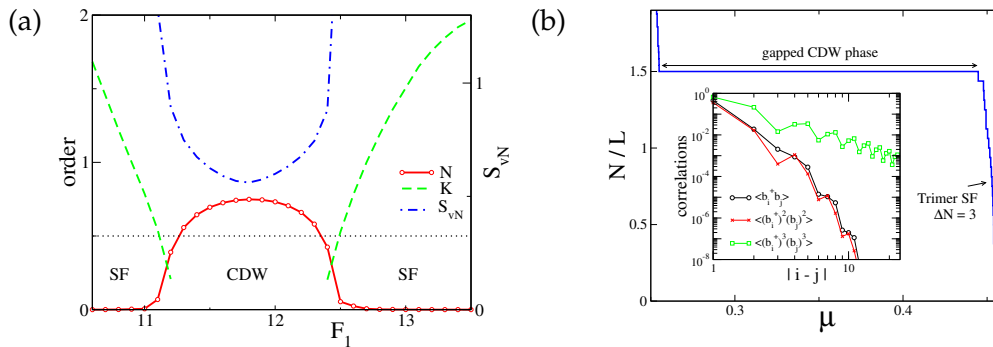
Fig. 7.4: (a) Néel order and entanglement entropy S_{vN} at $n = 3/2$ filling for sinusoidal modulation with $U_1 = 6$ ($U = 1$, iDMRG simulation with $M = 100$).The Luttinger-liquid parameter K is extracted from the algebraically decaying correlation-functions. (b) Equation of state for sinusoidally double modulated BH-model with $U_1 = 9, F_1 = 18$ and $U = 0.2$ ($L = 48$ sites). The inset shows single, two and three particle correlation functions for the trimer SF phase.
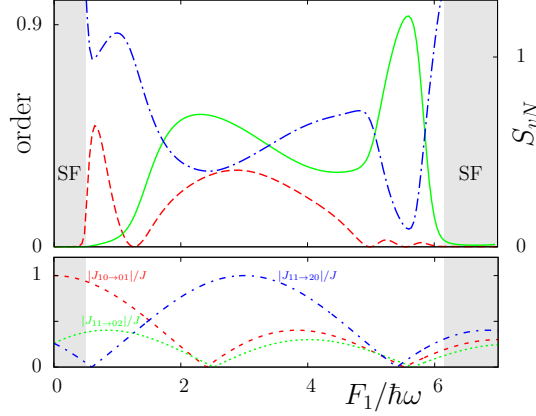
Fig. 7.5: iDMRG results for the effective model (7.20) (with 4 bosons per site, keeping up to $M = 200$ states) for $\mathcal{O}_P^2$ (solid), $4\mathcal{O}_S^2$ (dashed), and S_{vN} (dot-dashed) as a function of $F_1/\hbar\omega$ for $U_0/J = 1.2$, unit filling, and $U_1/\hbar\omega = 3$. In the shaded SF-regions we find a logarithmic divergence of S_{vN} with the number of kept matrix-states M. (bottom) Relevant hopping rates.

may be stabilized. It is formed by the Ising-Néel like product state build of the local dimers

$$\cos\phi \, |n, n+\nu+1\rangle_{x,x+1} - \sin\phi \, |n+1, n+\nu\rangle_{x,x+1} \qquad (7.24)$$

with $\phi = \arctan(z - \sqrt{z^2+1})$ and $z = U\nu/(2J_{(0,\nu+1)\leftrightarrow(1,\nu)}\sqrt{n+1}\sqrt{n+\nu+1})$.

In Fig. 7.4 (a) we present numerical data proving the stability of a CDW-phase $n = 3/2$ filling (i.e. $\nu = 2$, $n = 0$) for a sinusoidal shaking with $U_1 = 6$ as function of F_1. Around $F_1 = 12$ one observes a region with finite Néel order and a non-diverging entanglement entropy S_{vN} indicating a gapped phase. At the boundary to the surrounding the SF-phases the Luttinger-liquid parameter K exceeds $K > 1/2$ as suggested for a BKT type phase transition from the SF to the CDW phase.

For low incommensurate fillings a superfluid of ν locally bound bosons can be established: a pair superfluid for dominant $J_{(1,1)\leftrightarrow(0,2)}$, trimer superfluid for dominant $J_{(1,2)\leftrightarrow(0,3)}$, etc. Fig. 7.4 (b) shows the occurrence of a trimer-superfluid for a dominant $J_{(1,2)\leftrightarrow(0,3)}$ for a thin region in grand-canonical ensemble characterized by steps of $\Delta N = 3$ in the $\mu - \rho$ curve and algebraically decaying three-particle correlations $\langle (b_i^\dagger)^3(b_j)^3 \rangle$ while one- and two particle correlations vanish exponentially fast.

MI phases with both string and parity order

The case of unit filling is different since here for a dominant tunneling $J_{(1,1)\leftrightarrow(0,2)}$ (i.e. $\nu = 1$, equivalently $J_{(1,1)\leftrightarrow(2,0)}$) no local CDW order is initially preferred. However, we still observe a gapped MI phase at unit filling as shown in Fig. 7.5 for $U_1/\hbar\omega = 3$ and a broad region of F_1 (at $0.5 \lesssim F_1/\hbar\omega \lesssim 6.2$).

Conventional MI phases exhibit parity order $\mathcal{O}_P^2$ (2.19) due to the pairwise appearance of holons and doublons. String order $\mathcal{O}_S^2$ (2.38) is a characteristic feature of the (diluted) CDW order. For a direction dependent tunneling a Mott-insulating phase may exhibit a finite string order $\mathcal{O}_S^2 > 0$ due to the formation of quasi bound holon doublon pairs in one preferred direction. This is consistent with [173] showing that the absence of certain symmetries such a mirror symmetry allows for a crossover of HI and MI phases. Fig. 7.5 presents data for this

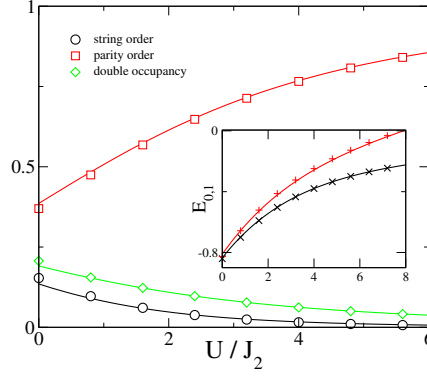Fig. 7.6: Double-occupancy, string, and parity-order for model 7.25. The straight-lines show the analytical results, the symbols denote DMRG-results ($L = 72$ sites). The inset shows the energies E_0 and E_1 of ground- and first excited state. The symbols depict DMRG-data ($L = 36$ sites) while straight lines corresponds to the analytical results (7.28) and (7.29).

exotic property of the MI phase with both $\mathcal{O}_P^2 > 0$ and $\mathcal{O}_S^2 > 0$ due to the hopping asymmetry. Typically we find $\mathcal{O}_P^2 > \mathcal{O}_S^2$. At the symmetric points for which $J_{(1,1)\leftrightarrow(2,0)} = J_{(1,1)\leftrightarrow(0,2)}$ the string order vanishes (at $F_1/\hbar\omega \simeq 1.2, 5.2$ and 5.5). Interestingly, for $J_{(1,1)\leftrightarrow(2,0)}, J_{(1,1)\leftrightarrow(0,2)} \ll J_{(1,0)\leftrightarrow(0,1)}$, we even obtain $\mathcal{O}_P^2 \ll \mathcal{O}_S^2$. Here doublon-holon pairs are broken to a large extent but still present diluted "antiferromagnetic" defect order, i.e. in this region the insulator rather behaves as a HI.

Dominant $J_{(1,1)\leftrightarrow(2,0)}$

An exemplification of above described unconventional MI phases will now be discussed for the case $J_{(1,1)\leftrightarrow(0,2)}, J_{(1,0)\leftrightarrow(0,1)} \ll J_{(1,1)\leftrightarrow(2,0)}$. In Fig. 7.5 we find this situation e.g. in the vicinity of $F_1/\hbar\omega \approx 2.4$. In this limit neglecting all hoppings except for $J_2 \equiv J_{(1,1)\leftrightarrow(2,0)}$ we may express Hamiltonian (7.20) as

$$\hat{\mathcal{H}}_2 = \sum_i J_2 P_i^1 \hat{b}_i^\dagger P_{i+1}^1 \hat{b}_{i+1} + H.c. + \frac{U}{2} \sum_i n_i(n_i - 1) \qquad (7.25)$$

where P_i^1 is a projector to the subspace of 1 particle on site i. At unit-filling only the configurations $|02\rangle_{x,x+1}$ and $|11\rangle_{x,x+1}$ on adjacent sites x and $x + 1$ are favorable. We will introduce the mapping to a spin model by $|02\rangle_{x,x+1} \to |\uparrow\downarrow\rangle_x$ and $|11\rangle_{x,x+1} \to |\downarrow\downarrow\rangle_x$. The configuration $|\uparrow\uparrow\rangle_{x,x+1}$ is forbidden. Note that in this treatment we just consider the sub-manifold without any configuration $|20\rangle_{x,x+1}$ or any isolated doublons or holons surrounded by single particles since this space is completely disconnected from the rest. With these assumptions we may rewrite Eq. (7.25) as a transverse-field Ising model

$$\hat{\mathcal{H}}_2^{\text{eff}} = \sum_i J_{(1,1)\leftrightarrow(2,0)} \left(S_i^+ + S_i^-\right) + U\left(\frac{1}{2} + S_i^z\right) + V\left(\frac{1}{2} + S_i^z\right)\left(\frac{1}{2} + S_{i+1}^z\right) \quad , V \to \infty \quad (7.26)$$

We take $V \to \infty$ in order to project out $|\uparrow\uparrow\rangle_{x,x+1}$-components. This is the Ising model with transverse and longitudinal magnetic fields in the vicinity of its tri-critical point between ferro-, antiferro- and paramagnetic phases [317]. Since both longitudinal and transverse components are present there is no simple solution of this
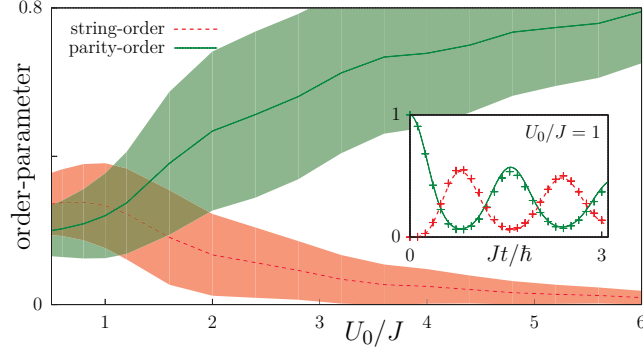
Fig. 7.7: Parity-order $\mathcal{O}_P^2$ (solid) and string-order $\mathcal{O}_S^2$ (dashed) in a sudden-quench situation for $F_1/\hbar\omega = 2.4$, $U_1/\hbar\omega = 3$ for a system initially prepared as deep Mott-insulator. The inset shows the dynamics for $U_0/J = 1$. The curves are obtained from iTEBD-simulations using the effective model (7.20), whereas the crosses indicate the results directly obtained from TEBD-simulations ($L = 60$ sites and $N = 60$ particles, $\hbar\omega = 20\pi J$) of Eq. (7.19). In the main figure we depict the time average of the orders for $2 < Jt/\hbar < 6$ as a function of U_0 for the same F_1 and U_1. The shaded regions indicate the variances of the orders, associated to the dynamics after the quench. The TEBD-simulations of model (7.19) as shown in the inset have been performed by Dario Poletti employing the ALPS libraries [319, 320] and the code IVAN.

model in terms of a Jordan-Wigner-transformation. Following Ref. [317], we may still provide a quasi-analytical solution for the bosonic model. A similar model has been studied recently in experiments [318].

Assuming periodic boundary conditions the ground state of Eq. (7.26) lies in the momentum $k = 0$ sector within the manifold $\{|m\rangle, m \in (0, L/2)\}$ with

$$|0\rangle = |\downarrow\downarrow \ldots\rangle \triangleq |111\ldots\rangle$$

$$|m\rangle = \frac{1}{\sqrt{w(L,n)}}(PS^+)^m |0\rangle \tag{7.27}$$

and P the projector which removes $|\uparrow\uparrow\rangle_{x,x+1}$. Hence, m describes the number of double-occupations. The normalization factor is given by $w(L,m) = \frac{L(-1+L-m)!}{(L-2m)!m!}$. For open boundaries we may take the variational ansatz using the same manifold - but here the normalization factor has to be changed to $w_o(L,m) = \frac{(L-m)!}{(L-2m)!m!}$.

In the thermodynamic limit the ground state is described by a Gaussian-shaped wavefunction in m-space sharply centered around a certain number of doublons $m_0(U)$. After mapping to a harmonic oscillator the ground-state energy per site is given as solution of the equation

$$64 + 16E_0U + U^2 - 44E_0^2 + (10E_0 - U)\sqrt{20E_0^2 - 12E_0U + U^2} = 0$$

and $m_0(U) = \frac{6E_0 - U + \sqrt{20E_0^2 - 12E_0U + U^2}}{8E_0}$. So for $U = 0$ one finds $m_0(0) = (3 - \sqrt{5})/4 \approx 0.19$.

The average number of double-occupations are given by $N_2 = \langle m \rangle = m_0$. N_2 is small for positive interactions and in this case string and parity-order can be

described by the following simple expression

$$\mathcal{O}_P^2 \approx \left\langle (2m-1)^2 \right\rangle \quad \text{and} \tag{7.28}$$

$$\mathcal{O}_S^2 \approx \left\langle 2m^2(m-2) \right\rangle. \tag{7.29}$$

In Fig. 7.6 we show that the analytical expressions (7.28) and (7.29) compare well to results of a DMRG calculation of model (7.25). Both string as well as parity order are non-zero, the string-order, however, vanishes with increasing U as shown in Fig. 7.6.

The Ising-model (7.26) (i.e. n_{max} = 2 bosons) exhibits a gap (even at U = 0) as shown in [317] which opens linearly with $J_{(1,1)\leftrightarrow(2,0)}$ to the momentum $k = \pi$ sector. In the bosonic model (7.25) the lowest excitation is a single impurity $|20\rangle$ which cannot decay and disconnects two parts of the chain. Hence, the gap is given by $\Delta E \propto e_L - e_{L-1} \propto E_0/L \propto J_{(1,1)\leftrightarrow(2,0)}$ for U = 0. So, interestingly, also this MI phase may persist for vanishing residual interaction strengths $U \to 0$. DMRG-calculations show a gap of $\Delta E = 0.51...J_{(1,1)\leftrightarrow(2,0)}$ for U = 0. The inset of Fig. 7.6 shows the ground- and excited-state-energy for different values of U from the DMRG-calculation and the variational ansatz (7.27).

7.2.2 Time-dependent simulation.

Ground-state properties analyzed so far may be prepared experimentally in a slow quasi-adiabatic ramping process after having prepared the system in the ground state in the absence of any modulation. It is, however, interesting to consider the properties of a fast switching of the double modulations. For simplicity we focus here on the situation that a defect free MI state at large U_0/J and unit filling is initially prepared. At time t = 0 DM is abruptly switched on. Figure 7.7 shows this sudden quench situation for a switching on of a sinusoidal DM to values $U_1/\hbar\omega = 3$ and $F_1/\hbar\omega = 2.4$ and different values U_0/J. We monitor the evolution of string and parity order after the quench, as shown in the inset of Fig. 7.7 for a residual final interaction $U_0 = J$. Initially the defect free MI state exhibits a perfect parity-order $\mathcal{O}_P^2 = 1$ and no string order $\mathcal{O}_S^2 = 0$. Due to the creation of defects after the abrupt quench $\mathcal{O}_P^2$ decreases and $\mathcal{O}_S^2$ increases. Interestingly, for the parameters chosen both time averaged $\mathcal{O}_S^2$ and $\mathcal{O}_P^2$ remain finite after the quench. The average values of the orders for $2 < Jt/\hbar < 6$ are shown in the main panel of Fig. 7.7 as a function of U_0. They present a similar qualitative dependence on U_0/J as the ground state shown in Fig. 7.6.

The inset of Fig. 7.7 as well presents a comparison between the dynamics of the effective model (7.20) and the full dynamical time evolution of the double modulation Eq. (7.19), showing the validity of the effective model for describing the dynamic evolution.

7.2.3 Symmetric tunneling

In the following we will explore the case of a mirror symmetric tunneling $J_{(1,1)\leftrightarrow(2,0)} = J_{(1,1)\leftrightarrow(0,2)}$. Figure 7.8 illustrates the possibility of realizing a broad range of values of $J_{(1,1)\leftrightarrow(2,0)}/J_{(0,1)\leftrightarrow(1,0)}$ for a sinusoidal modulation with appropriately chosen U_1 and F_1 such that $\mathcal{J}_0\left[(F_1 + U_1)/\hbar\omega\right] = \mathcal{J}_0\left[(F_1 - U_1)/\hbar\omega\right]$.
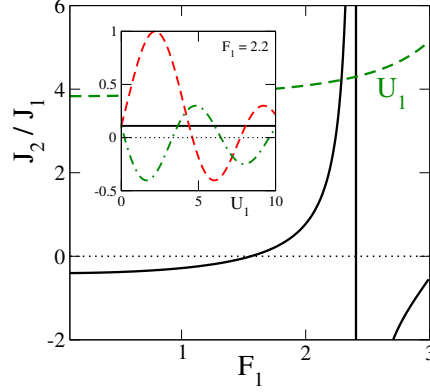
Fig. 7.8: For appropriately chosen parameters F_1 and U_1 one can get almost arbitrary $J_2 \in [0, \infty]$ (solid line). Shown here is an example of $1.5 < F_1 < 2.4$ and U_1 (dashed line) accordingly between 3.8 and 4.3. The inset depicts $J_{(1,1)\leftrightarrow(2,0)}$ (red line), $J_{(1,1)\leftrightarrow(0,2)}$ (green line) and $J_{(0,1)\leftrightarrow(1,0)}$ (solid black line) for as function of U_1 for $F_1 = 2.2$.

The correlated-hopping Fermi-Hubbard model

The DM-scheme allows for the simulation of the full parameter space of the correlated-hopping Fermi-Hubbard model (7.14) relevant for for cuprate superconductors, while pure modulation of interactions only permits $0 \leq |t_{AB}/t_{AA}| \leq 1$ [45]. In Fig. 7.9 we present the grand-canonical phase diagram for $U_0 = 0$. The lines $t_{AB} = t_{AA}$ correspond to the usual Fermi-Hubbard model. The case $t_{AB} = 0$ has been discussed in detail in section 7.1.4.

As shown in [314] for $t_{AB} < t_{AA}$ the spin-sector is gapless. From calculating the Luttinger-liquid parameter $K_\rho = 1$, extracted from the long wavelength behavior of the static charge structure factor [321], we may define the boundary between a gapless phase with dominant triplet superconducting (TS) correlations $\langle \mathcal{Q}_{0+}^\dagger \mathcal{Q}_{j+} \rangle$, with $\mathcal{Q}_{j\pm} \equiv c_{j+1\downarrow}c_{j\uparrow} \pm c_{j+1\uparrow}c_\downarrow$ and another phase with dominant spin-density wave (SDW) correlations, $(-1)^j \langle \hat{n}_{0-}\hat{n}_{j-} \rangle$, with $\hat{n}_{j\pm} \equiv \hat{n}_{j\uparrow} \pm \hat{n}_{j\downarrow}$. For $t_{AB} < 1$ along the line of unit filling ($\mu/t_{AB} = 0$) the TS-correlation functions become degenerate with the spin-bond-ordering wave (SBOW) correlations, $\langle \mathcal{S}_0^\dagger \mathcal{S}_j \rangle$ with $\mathcal{S}_j \equiv \sum_\sigma \sigma(\hat{c}_{j+1\sigma}^\dagger \hat{c}_{j\sigma} + \text{H.c.})$, as discussed in [314].

For $t_{AB}/t_{AA} > 1$ the spin sector becomes massive and for $U = 0$ three different phases may occur [314]. At unit filling $n = 1$ we find a totally gapped phase with bond-ordering wave (BOW) order, $\langle \mathcal{B}_0^\dagger \mathcal{B}_j \rangle$ with $\mathcal{B}_j \equiv \sum_\sigma (\hat{c}_{j+1\sigma}^\dagger \hat{c}_{j\sigma} + \text{H.c.})$. In Fig. 7.9 the size for the BOW-phase corresponds to the charge gap at unit filling.

At incommensurate fillings we observe a gapless phase with dominant density wave (CDW) correlations, $(-1)^j \langle \hat{n}_{0+}\hat{n}_{j+} \rangle$, and a gapless phase with dominant singlet-superconducting (SS) correlations, $\langle \mathcal{Q}_{0-}^\dagger \mathcal{Q}_{j-} \rangle$.

From the perturbative analysis in Ref. [314] one may see that for fixed t_{AB}, t_{AA} and $U_0 > 0$, the spin gap opens at a critical μ_{cr}. Hence, for an overall confinement one may observe a spatial boundary between spin-gapped and spin-gapless phases, which may be revealed experimentally. In particular the BOW phase in experiments will show a characteristic plateau in an external confining potential.
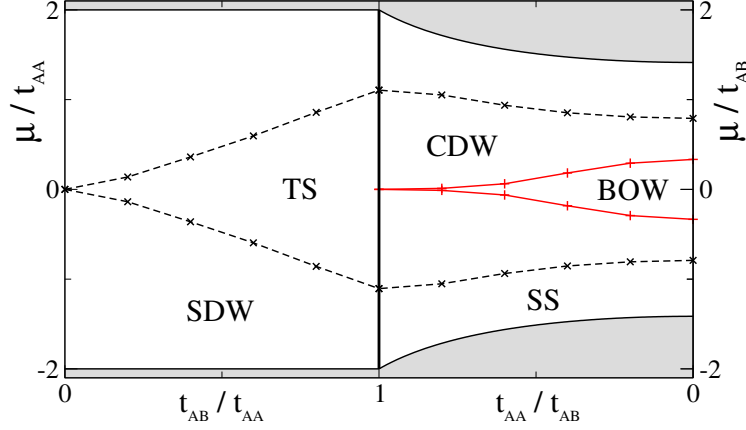
Fig. 7.9: Phase diagram for the Fermi-Hubbard-model as a function of μ/t_{AA} and t_{AB}/t_{AA} for $U_0 = 0$. This is consistent with the perturbative result from [314] for $t_{AA} = t_{AB}$. The shaded regions denote the vacuum or the fully occupied state. All results are extrapolated to the thermodynamic limit from open boundary DMRG-calculations with up to $L = 144$ sites.

Bosons

Finally we may study the phase diagram of the Bose Hubbard model with DM (7.20) and symmetric doublon creation rates $J_2 \equiv J_{(1,1)\leftrightarrow(2,0)} = J_{(1,1)\leftrightarrow(0,2)}$ (for simplicity we introduce the short hand $J_1 \equiv J_{(1,1)\leftrightarrow(2,0)}$). Again the case $J_2 < J_1$ has been studied in the context of a sole modulation of interactions [44]. So here we focus on the interesting case $J_1 < J_2$. Since the higher tunneling processes typically will remain asymmetric, we will study small fillings and moderate residual interactions U.

In Fig. 7.10 (a) we present the grand-canonical phase diagram for model (7.20). Similar to the correlated hopping FH model (7.14) for the bosonic case a large $J_2 > J_1$ will favor a gapped MI phase. The residual interaction $U_0 = 3$ for the simulation of Fig. 7.10 (a) is chosen to be slightly below SF-MI transition for $J_2 = 1$. Increasing J_2 drives the system into the gapped MI-phase. A second important feature of the regime $J_2 > J_1$ is the emergence of a PSF phase at low fillings. The single particle correlations $\langle b_x^\dagger b_y \rangle$ decay exponentially in PSF region, while density-density and pair-correlations $\langle (b_x^\dagger)^2 (b_y)^2 \rangle$ remain algebraically (not shown). In the $\mu - \rho$ curve we observe jumps of two particles as shown in Fig. 7.10 (b). For $1 < J_2 \lesssim 3$ we observe an interesting meta-magnetic transition (cf. section 5.5) to the SF-phase. Here the $\mu - \rho$ curve exhibits a macroscopic jump as illustrated in Fig. 7.10 (b).

We may analyze the emergence of the PSF from the dilute limit examining the two-particle problem as introduced in section 5.2. The Schrödinger equation for two particles may be reduced to the following system of coupled equations for the amplitudes C_r

$$(\Omega - U)C_0 = -2\sqrt{2}tJ_2 \cos \frac{K}{2} C_1$$

$$\Omega C_1 = -2t \cos \frac{K}{2} (\sqrt{2}J_2 C_0 + J_1 C_2)$$

$$\Omega C_r = -2tJ_1 \cos \frac{K}{2} (C_{r-1} + C_{r+1}), r \geq 2. \tag{7.30}$$
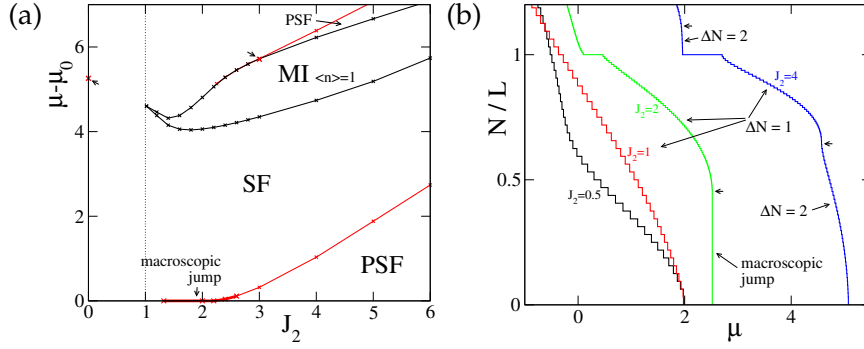
Fig. 7.10: (a) Phase diagram for doubly-shaken bosons as function of chemical potential μ and pair production rate J_2 ($U_0 = 3$) with μ_0 the chemical potential of the vacuum. The small arrows show positions of macroscopic jumps in filling. (b) Filling $\langle n \rangle / L$ as function of the chemical potential for different values of J_2 for the parameters of (a). Note that $J_2 = 0.5$ and 1 curves are for system-size of $L = 32$, while $J_2 = 2, 4$ curves are for $L = 128$. In the PSF-regime one observes steps of $\Delta N = 2$ and a macroscopic jump close to the transition to the SF regime.

In the thermodynamic limit the scattering energy continuum is given by $\Omega = \epsilon(k_1) + \epsilon(k_2) = -4tJ_1 \cos k \cos \frac{K}{2}$. For $J_2 > \sqrt{1 + U_0/4}$ the two-particle bound state becomes the ground state of the 2-particle problem. Note that this derivation essentially holds as well for Fermi-Hubbard model.

7.3   Conclusions

In this chapter we have analyzed in detail the physics emerging from fast modulated interactions. They allow for the realization of "stochastic" density dependent Peierls phases and a certain class of correlated hopping Hubbard models, including an interesting insulating metallic phase (Kohn-metal). The double modulation of interactions and lattice position may be used a tool for the precise control of selected hopping processes. A mirror-asymmetric hopping will lead to exotic insulating phases with both parity and string order. Furthermore an even broader class of correlated hopping Hubbard models may be realized.

While here we focused on the effect of double modulations in one dimensional systems, a natural extension of this work would be the application of DM to 2D- and 3D-systems. Here, the combination of elliptical lattice shaking [137] and periodically modulated interactions may lead to an even richer physics due to different select hopping processes in different directions.

Modulated interactions are subject to current experimental research [322]. However, as all large amplitude modulation techniques, in general may suffer from a large heating due to multi-photon transitions to higher bands [323]. Similar models may, however, be realized driving resonant transitions between different Floquet-sectors [144] with weak modulations, which may lead to less heating and simplified experimental schemes.

Chapter 8

Density Dependent Artificial Magnetic Fields

In the previous chapters we have seen how artificial gauge fields and synthetic electromagnetism in cold neutral gases may be engineered and studied [275, 324] using laser-assisted hopping or shaking techniques. While the gauge fields studied so far are static and do not provide a dynamical feedback between matter and gauge fields, in many areas of physics ranging from condensed-matter [325] to quantum chromodynamics [326] dynamical gauge field theories have been shown to play an important role. Hence, during the recent years there have been various attempts and a growing interest in studying such dynamical quantum field theories in cold atom experiments [27, 28, 327–333].

In this chapter we will present different schemes how a certain class of dynamical gauge fields may be engineered, in which there is no discrimination between particle and gauge fields degrees of freedom. The particle-density provides a back-action on the synthetic gauge fields of the system. Such density dependent gauge fields have been studied in the context of fractional quantum Hall effect [334], generalized statistics in one dimension [335], quantum magnetism [336], chiral solitons [337] or one-dimensional anyons [338]. Recently, experimental schemes for the realization of density dependent synthetic magnetism (DDSM) have been proposed for Bose-Einstein condensates [339] and optical lattices [338]. The ideas presented in this chapter extend the proposal and analysis of Ref. [338]. In particular we will study hopping terms with density dependent Peierls phases of the form

$$\hat{\mathcal{H}}_{i,j}^{ddsm} = \hat{b}_i^\dagger e^{i\phi\hat{n}_i}\hat{b}_j^\dagger + H.c. \, . \tag{8.1}$$

We will investigate feasible experimental set-ups and the physical effects of DDSM in 1D and 2D lattices. We show that DDSM results in a very rich physics including novel quantum phases or density and statistically induced quantum phase transitions in anyon Hubbard models. Moreover, we will show how effective fluxes in 2D lattices are induced by quantum and density fluctuations and crucially affect the quasi-momentum distribution or the expansions-dynamics of holons and doublons on top of a Mott-insulator.

8.1   DDSM using periodically modulated interactions

Periodically modulated interactions and the corresponding effective Hamiltonians, as studied in chapter 7, provide a method for the engineering of density dependent complex phases. In section 7.1.2 we discussed that these phases, however, may be eliminated by a simple gauge transformation. In the following section we demonstrate, how modulated interactions in combination with Raman-assisted hopping

may be employed for the creation of a density-dependent Peierls phase that cannot be gauged out and, hence, result in non-trivial ground-state physics. Although the resulting effective model is different from the anyonic Hubbard model [48, 338] (see discussion in sections 8.2) we show that it shares its fundamental properties: A density-dependent (drift of the) momentum distribution, gauge-induced SF to MI transitions and a stabilization of the Hubbard model for vanishing interactions.

The following section is based on the publication [47] which was developed in collaboration with G. Sun, D. Poletti and L. Santos. Part of the DMRG calculations has been performed by G. Sun.

8.1.1   The AB model

The main scheme for the creation of a density dependent Peierls phase of the form (8.1) is sketched in Fig. 8.1. It basically resembles the seminal experimental proposal by Jaksch and Zoller [280].

Two-components of bosonic particles $|A\rangle$ and $|B\rangle$ are trapped in a tilted 1D spin-dependent lattice. Due to the tilting the natural hopping is strongly suppressed and four Raman-beams between A and B sites as well as B and A sites are employed to restore a laser-assisted hopping (see Fig. 8.1 (a)). In this way the lattice is split into two sublattices A and B. The main idea of our proposal is to use the AB and BA lasers in a pulsed way: for a time period $0 < t < T/2$ Raman assisted hopping couples an A site with the B site at their right, and for $T/2 < t < T$ it couples an A site with the B site at their left. We further assume that the interactions of the A component $U_A(t) = U_{A0} + U_{A1}(t)$ are modulated in time with a period T as (see 8.1 (b))

$$
U_{A1}(t) = \begin{cases} \tilde{U}_{A1}\sin(\omega_{AB}t) & \text{for } 0 < t < T/2 \\ -\tilde{U}_{A1}\sin(\omega_{AB}t) & \text{for } T/2 < t < T \end{cases} \tag{8.2}
$$

where $\omega_{AB} = 4\pi/T$. The total time-dependent Hamiltonian is given by

$$
\hat{\mathcal{H}}^{AB} = -\sum_j \left[J_{AB}(t)\hat{b}_{2j}^\dagger \hat{b}_{2j+1} + J_{BA}(t)\hat{b}_{2j}^\dagger \hat{b}_{2j-1} + \text{h.c.} \right]
$$
$$
+ \frac{U_A(t)}{2}\sum_j \hat{n}_{2j}(\hat{n}_{2j}-1) + \frac{U_B}{2}\sum_j \hat{n}_{2j+1}(\hat{n}_{2j+1}-1). \tag{8.3}
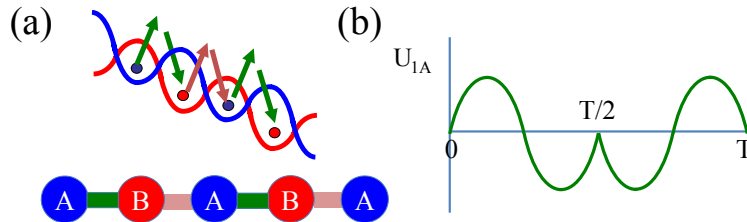$$

Fig. 8.1: Scheme of the AB-model. (a) For $0 < t < T/2$ Raman assisted hopping couples an A site with the B site at their right; for $T/2 < t < T$ it couples an A site with the B site at their left. (b) Sketch of the modulation function $U_{A1}(t)$.

where

$$J_{AB}(t) = \begin{cases} J & \text{for } 0 < t < T/2 \\ 0 & \text{for } T/2 < t < T \end{cases} \quad \text{and} \quad J_{BA}(t) = \begin{cases} 0 & \text{for } 0 < t < T/2 \\ J & \text{for } T/2 < t < T \end{cases} \tag{8.4}$$

Even (odd) sites index the A (B) sublattice. The interactions of the B component U_B are kept constant. For simplicity we choose $U_{A0} = U_B \equiv U$. Contrary to the schemes discussed by [338] and in section 8.2, here, for an experimental realization we assume that interaction shifts are smaller than the laser linewidth. Furthermore the tilting has to be chosen larger than the Raman-induced hopping rate and the interaction energy in order to avoid photon-assisted resonances.

Assuming a fast modulation (see section 2.5) we yield the following time independent effective model

$$\hat{\mathcal{H}}_{\text{eff}}^{AB} = -\sum_j \left[\hat{b}_{2j}^\dagger \tilde{J}_{AB}(\hat{n}_{2j}) \hat{b}_{2j+1} + \hat{b}_{2j}^\dagger \tilde{J}_{BA}(\hat{n}_{2j}) \hat{b}_{2j-1} + \text{h.c.} \right]$$

$$+ \frac{U}{2} \sum_j \hat{n}_{2j}(\hat{n}_{2j}-1) + \frac{U}{2} \sum_j \hat{n}_{2j+1}(\hat{n}_{2j+1}-1), \tag{8.5}$$

with $\tilde{J}_{AB}(\hat{n}_{2j}) = \frac{J}{T}\int_0^{T/2} dt\, e^{iV(t)\hat{n}_{2j}/\hbar}$, $\tilde{J}_{BA}(\hat{n}_{2j}) = \frac{J}{T}\int_0^{T/2} dt\, e^{iV(t+T/2)\hat{n}_{2j}/\hbar}$, and $V(t) = \int_0^t U_{A1}(t')dt'$. Hence, for the above mentioned case of a piecewise sinusoidal shaking Eq. (8.2) we obtain a density dependent hopping amplitude and phase

$$\tilde{J}_{AB}(\hat{n}_{2j}) = \frac{J}{2}J_0(\Omega_{AB}\hat{n}_{2j})e^{i\Omega_{AB}\hat{n}_{2j}} = \tilde{J}_{BA}(\hat{n}_{2j})^* \tag{8.6}$$

So here the phase is always strictly coupled to the modulus of the hopping. One may choose more generally

$$U_{A1}(t) = \begin{cases} \tilde{U}_{A1}\sin(\omega_{AB}t + \phi_1) & \text{for } 0 < t < T/2 \\ -\tilde{U}_{A1}\sin(\omega_{AB}t + \phi_2) & \text{for } T/2 < t < T \end{cases} \tag{8.7}$$

Note that $\phi_1 = 0$, $\phi_2 = \pi$ reproduces the case shown in Fig. 8.1 (b). The effective tunneling is given by

$$\tilde{J}_{AB}(\hat{n}_{2j}) = \frac{J}{2}J_0(\Omega_{AB}\hat{n}_{2j})e^{i\Omega_{AB}\cos(\phi_1)\hat{n}_{2j}} \quad \text{and}$$

$$\tilde{J}_{BA}(\hat{n}_{2j}) = \frac{J}{2}J_0(\Omega_{AB}\hat{n}_{2j})e^{i\Omega_{AB}\cos(\phi_2)\hat{n}_{2j}}.$$

A unitary gauge transformation $b_{2j}^\dagger \to b_{2j}^\dagger e^{-i(\Phi_{AB}+\Phi_{BA})/2\hat{n}_{2j}}$ may be used to obtain

$$\tilde{J}_{AB}(\hat{n}_{2j}) = \frac{J}{2}J_0(\Omega_{AB}\hat{n}_{2j})e^{i\Phi/2\hat{n}_{2j}} = \tilde{J}_{BA}(\hat{n}_{2j})^*$$

Hence, $\Phi = \Phi_{AB} - \Phi_{BA} = \Omega_{AB}[\cos(\phi_1) - \cos(\phi_2)]$ may be changed keeping the hopping modulus unaffected.

The AB-model shows a striking similarity to the Anyon-Hubbard model (AHM) introduced in Ref. [338] (see section 8.2 for a detailed discussion). We may recast it as an anyon-like model without Peierls phases by defining $\hat{a}_{2j} = e^{i\Omega_{AB}\sum_{l<j}\hat{n}_{2l}}\hat{b}_{2j}$, and $\hat{a}_{2j+1} = e^{i\Omega_{AB}\sum_{l\leq j}\hat{n}_{2l}}\hat{b}_{2j+1}$. Even site operators a_{2j} fulfill anyonic commutation relations

$$e^{i\Omega_{AB}}\hat{a}_{2j}^\dagger\hat{a}_{2j'} = \hat{a}_{2j'}\hat{a}_{2j}^\dagger. \tag{8.8}$$

Odd site operators a_{2j+1} act like bosons under exchange. In the following we will show, that the AB-model and the AHM indeed share important properties.
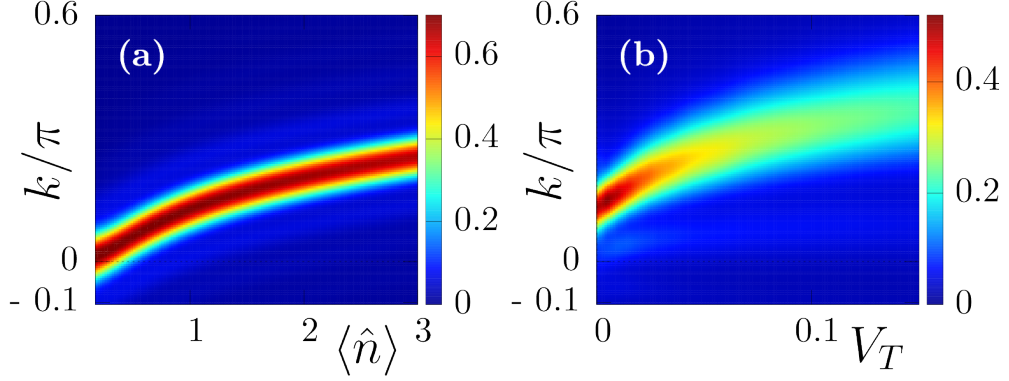
Fig. 8.2: (a) Ground-state quasi-momentum distribution for model (8.5) for an homogeneous distribution in 24 sites with $\Omega_{AB} = \pi/4$, $U = 0.2J$, and a density $\langle \hat{n} \rangle$; (b) harmonically trapped gas V_T for $\Omega_{AB} = \pi/4$, $U = J$ and 24 particles in 24 sites ($n_{max} = 10$). DMRG-simulations have been performed by G. Sun.

8.1.2 Quasi-momentum distribution

An important feature of a one-dimensional anyonic model is the effect on the quasi-momentum distribution as may be probed easily in TOF experiments. It has been studied to a large extent in Refs. [338, 340, 341]. Note, that for a synthetic static gauge field the drift of the quasi-momentum distribution in a 1D lattice gas was experimentally studied in detail [137].

We illustrate the properties of the quasi-momentum distribution of the AB-model in Fig. 8.2. A change in the average density $\langle \hat{n} \rangle$ will induce a drift of the momentum distribution shown in Fig. 8.2 (a) for an homogeneous system with $\Omega_{AB} = \pi/4$ and $U = 0.2J$. In an harmonic trap $V_T \sum_j (j - L/2)^2 \hat{n}_j$ this effect can be steered by compressing the gas by a larger V_T. As shown in Fig. 8.2 (b) the quasi-momentum distribution shifts with increasing V_T because the central density grows. Due to the inhomogeneity of the density distribution the TOF-pictures blurs.

8.1.3 Correlation functions in the superfluid regime

In order to obtain an understanding of the effect of the density-dependent phase on the ground-state phase diagram, we start with an analysis valid in the in the weakly-interacting regime. As introduced in section 2.2.4 the bosonic operators may be expressed as $\hat{b}_j^\dagger \rightarrow \sqrt{\rho(x_j)} e^{-i(\theta(x_j) - \eta x_j)}$, with

$$\rho(x) = \rho_0 - \frac{1}{\pi} \nabla \phi(x) + \rho_0 \sum_{p \neq 0} e^{i2p(\pi \rho_0 + \phi(x))} , \qquad (8.9)$$

with the average density ρ_0, and x_j the position of site j. We introduce η to account for a global gaugeable phase shift. An expansion of Hamiltonian (8.5) yields the following form of the Hamiltonian in terms of phase and density fluctuations ϕ and θ

$$\hat{\mathcal{H}} = \frac{u}{2\pi} \int dx \left[K^{-1}(\partial_x \phi)^2 + K(\partial_x \theta)^2 + 2\gamma(\partial_x \phi)(\partial_x \theta) \right], \qquad (8.10)$$

where u is a velocity, K is the Luttinger parameter which can be introduced phenomenologically. Interestingly a mixing term γ has to be added due to the density-
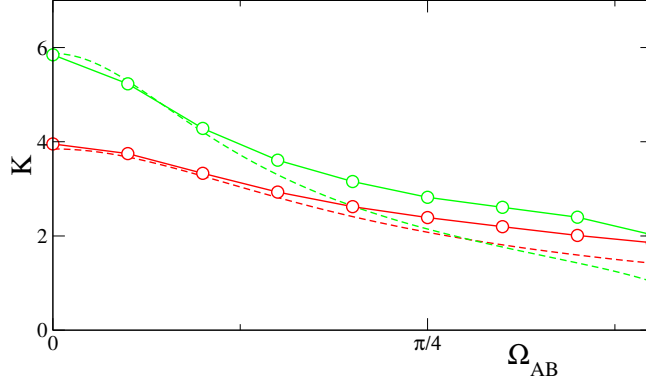
Fig. 8.3: Behavior of the Luttinger parameter K as a function of Ω_{AB} for $U = J/2$ for $\rho_0 = 1.75$ (upper curves) and $\rho_0 = 0.75$ (lower curves). Dashed lines indicate the analytical estimation (8.11) in the weak-interaction regime, whereas the circles denote our results obtained from DMRG calculations of the single-particle correlation function.

dependent Peierls phase. This term does not lead to any effect on the correlation functions [47], which exhibit the usual power law decay as $\langle \hat{b}_i^\dagger \hat{b}_j \rangle \propto |i - j|^{-1/2K}$.

In the weak-coupling regime the Luttinger parameter K is given by

$$K^2 = \frac{\pi^2 \rho_0 \tilde{F}(\rho_0)}{\frac{2U}{J} - \mathcal{R}\left(\rho_0 \frac{d^2 \tilde{F}}{d\rho^2}(\rho_0) + 2 \frac{d\tilde{F}}{d\rho}(\rho_0) \right)} \tag{8.11}$$

with $\mathcal{R}$ the real part, $\tilde{F}(\rho) = F(\rho)e^{-i\arg(F(\rho_0))}$, and $F(\rho) = J_0(\Omega_{AB}\rho)e^{i\Omega_{AB}\rho}$ for the AB model. In Fig. 8.3 we illustrate the validity of the approach in the SF regime and for small Ω.

Eq. (8.11) shows that for the correlated hopping, both density dependent amplitude and phase, play the role of an effective repulsive interaction. The derived expression is also valid for the AHM (see Eq. (8.21)).

8.1.4   Statistically-induced phase transitions

The effective repulsion induced by the density dependent Peierls phase has important consequences on the ground-state phase diagram. A changing of the statistical angle Φ may induce SF to MI transitions as observed in Ref. [338]. In Fig. 8.4 we show how several MI phases are induced by varying Φ. The MI phases survive for a broad range of U/J as can be seen in Fig. 8.4 (a) (note that at $\Omega_{AB} = 0$ the MI phase at unit filling closes around $J/U \approx 0.3$). Interestingly, due to the broken AB-symmetry also gapped phases at fractional fillings $1/2, 3/2, \ldots$ are stabilized.

The emergence of fractional filling MI phases at $\rho = 1/2$ can be best understood from the limit of hardcore particles $J/U \ll 1$. In this limit one can reduce the description to the manifold of 0 and 1 particles per site and introduce an effective spin-$\frac{1}{2}$ Hamiltonian $\hat{\mathcal{H}}_{1/2}$ in perturbation theory up to second order J/U with near-
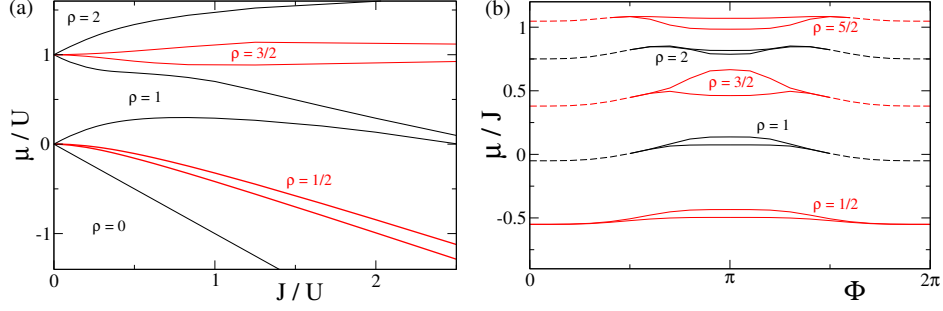
Fig. 8.4: Mott phases at half-integer and integer fillings (a) MI-lobes for $\Omega_{AB} = \pi/2$, $\Phi = \pi$. (b) Varying the relative phase Φ may induce phase transitions in the ground state. Here we choose $\Omega_{AB} = \pi/2$ and change Φ for $J/U = 2$ (dashed lines indicate a closing gap)

est neighbor interactions and staggered correlated hopping:

$$\hat{\mathcal{H}}_{1/2} = -J \sum_j [\hat{S}_j^+ \hat{S}_{j+1}^- + \text{h.c.}]$$

$$+ J_c \sum_j [\hat{S}_j^+ \left(\frac{1}{2} + \hat{S}_{j+1}^z\right) \hat{S}_{j+2}^- + \text{h.c.}] +$$

$$+ J_s \sum_j (-1)^j [\hat{S}_j^+ \left(\frac{1}{2} + \hat{S}_{j+1}^z\right) \hat{S}_{j+2}^- + \text{h.c.}] +$$

$$+ \Delta \sum_j \hat{S}_j^z \hat{S}_{j+1}^z \tag{8.12}$$

with coefficients $J_c = \frac{J^2}{U} \frac{1+\Gamma^2}{2}$, $J_s = \frac{J^2}{U} \frac{1-\Gamma^2}{2}$ and $\Delta = -\frac{J^2}{U}(1+|\Gamma|^2)$ and $\Gamma \equiv \frac{1}{2}\mathcal{J}_0(\Omega_{AB})e^{i\Phi/2}$. Using the standard bosonization dictionary [35] the continuum limit of this Hamiltonian may be expressed as a sine-Gordon Hamiltonian of the density and phase fluctuations $\theta(x)$ and $\phi(x)$. It is precisely the staggered (next-nearest-neighbor) hopping that introduces at half filling a spin-Peierls like term $\sim \sin 2\phi(x)$ which becomes relevant for Luttinger-liquid parameters $K < 2$. That is why at half filling we observe the immediate opening of band insulator gap for arbitrarily small tunneling J/U which is consistent with our numerical simulations. The $S^z - S^z$-interaction contributes with $\sim \cos 4\phi(x)$ terms, which are irrelevant for $K > 1/2$.

The opening of a gap may be also understood in an easier way if we just consider the correlated hopping parts $S_j^+ \hat{S}_{j+1}^z \hat{S}_{j+2}^-$ of the second order perturbation, since this part may be analytically solved by mapping to free fermions:

$$\hat{\mathcal{H}}_{1/2}^{\text{sf}} = -J \sum_j \hat{c}_j^\dagger \hat{c}_{j+1} + J_c \sum_j \hat{c}_j^\dagger \hat{c}_{j+2} +$$

$$+ J_s \sum_j (-1)^j \hat{c}_j^\dagger \hat{c}_{j+2} + \text{h.c.}$$

Here one finds the spin-Peierls like band-gap opening $\sim |J_s|$ at half filling.

8.1.5 Vanishing on-site interaction

While the appearance of the gap at half fillings can be described nicely in large interaction limit, it is remarkable that the gap survives also for very small interactions
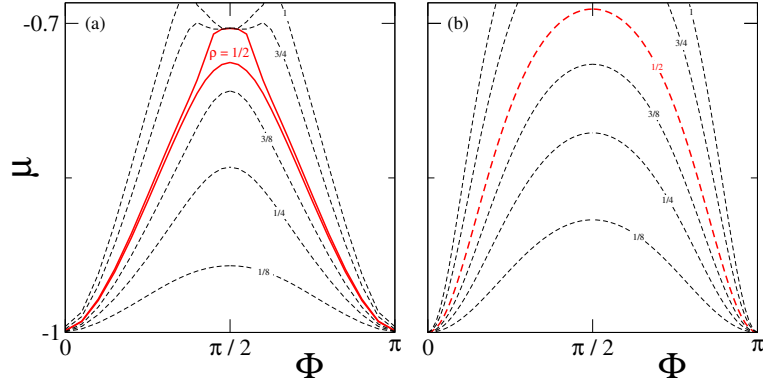
Fig. 8.5: Behavior of the AB-model for vanishing on-site interactions $U = 0$. Lines of constant density and MI phase at $n = 1/2$ from DMRG (a) and a coherent state variational approach (b). In the DMRG-calculation system size L and maximal occupation number of bosons per site n_{max} have been scaled carefully (up to $n_max = 12$ and $L = 144$ sites). For fillings $n \leq 1/2$ the calculation already shows almost perfect convergence for $n_{max} = 2$.

U as can be seen in Fig. 8.4 (a), without any apparent tendency to close. Indeed the gapped phase may even survive to the limit $U \to 0$ as shown in Fig. 8.5 as function of Φ. While the usual Bose Hubbard model becomes unstable in the limit $U \to 0$ in a grand canonical ensemble (bunching of curves of constant filling for $\Phi = 0$), the density dependent hopping stabilizes the system such that the system effectively behaves as a repulsively interacting Bose gas.

The stability of the AB-model (however, not the gaped phases at fractional fillings) for vanishing interactions can be seen from a simple variational ansatz using coherent states $|\alpha\rangle |\beta\rangle$. Minimizing the ground-state energy

$$|\alpha|^2 \left(\left(1 + e^{-2|\alpha|^2}\right)^2 - 4\mu^2 \right)/4\mu \tag{8.13}$$

as function of the chemical potential reproduces the qualitative behavior: a small difference in occupation of A and B sites and stability for $U = 0$ at small fillings (here for $\mu < -1/2$ the filling factor ρ remains finite). The DMRG-calculation indicates lower boundaries for the instability for certain values of Φ.

An analytical understanding away from the weak coupling regime of the behavior for $U \to 0$ may be obtained by the analysis of the two particle problem. Due to the conservation of total momentum in the scattering process one can express the amplitudes of a 2-particle scattering state (5.11) as $c_{x,x+r} = C_r e^{iQ(x+\frac{r}{2})}$ for x in one of the A sites and $c_{x,x+r} = D_r e^{iQ(x+\frac{r}{2})}$ for $x \in B$. Here $Q = q_1 + q_2$, the total momentum (below we employ $q = (q_1 - q_2)/2$ as the half relative momentum). The Schrödinger equation $\hat{\mathcal{H}}_{\text{eff}}^{AB} |\Psi\rangle = \epsilon |\Psi\rangle$ for the two particle problem leads to the
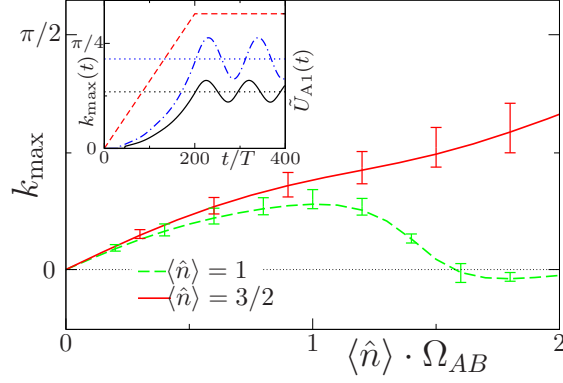
Fig. 8.6: Quasi-momentum k_{max} at which the quasi-momentum distribution of the B sublattice is maximal as a function of $\Omega_{AB}\langle\hat{n}\rangle$ for $\omega = 20J$ and $U = J$. Solid (dashed) lines denote the results obtained from the effective model (8.5) with $\langle\hat{n}\rangle = 3/2$ (1). The error bars denote the uncertainty (time average and standard deviation for $200 < t/T < 400$) of $k_{max}(t)$ for the case of a linear ramp of $\tilde{U}_{A1}$ with a ramp time of $\tau = 200T$. (inset) Solid and dash-dotted lines show $k_{max}(t)$ for $\langle\hat{n}\rangle = 3/2$ with $\Omega_{AB} = 0.4$ and 0.8, whereas the dotted line indicates the value of k_{max} for the effective model (8.5). We depict with a dashed line the ramp $\tilde{U}_{A1}(t)$.

following system of coupled equations for the amplitudes C_r and D_r

$$(\epsilon - U)C_0 = -\sqrt{2}J\,|\Gamma|\left(D_1\,e^{i(Q-\Phi)/2} + C_1\,e^{-i(Q-\Phi)/2}\right)$$

$$(\epsilon - U)D_0 = -\sqrt{2}J\,|\Gamma|\left(C_1\,e^{iQ/2} + D_1\,e^{-iQ/2}\right)$$

$$\epsilon C_1 = -\sqrt{2}J\,|\Gamma|\left(C_0\,e^{i(Q-\Phi)/2} + D_0\,e^{-iQ/2}\right) - J/2\left(C_2\,e^{-iQ/2} + D_2\,e^{iQ/2}\right)$$

$$\epsilon D_1 = -\sqrt{2}J\,|\Gamma|\left(C_0\,e^{-i(Q-\Phi)/2} + D_0\,e^{iQ/2}\right) - J/2\left(C_2\,e^{iQ/2} + D_2\,e^{-iQ/2}\right)$$

$$\epsilon C_{r\geq 2} = -J/2\left(C_{r-1}\,e^{iQ/2} + C_{r+1}\,e^{-iQ/2} + D_{r-1}\,e^{-iQ/2} + D_{r+1}\,e^{iQ/2}\right)$$

$$\epsilon D_{r\geq 2} = -J/2\left(D_{r-1}\,e^{iQ/2} + D_{r+1}\,e^{-iQ/2} + C_{r-1}\,e^{-iQ/2} + C_{r+1}\,e^{iQ/2}\right)$$

The energy of the two scattered particles is given by $\epsilon = -2J\cos(q)\cos(Q/2)$. In order to extract scattering properties we solve this set of equations with the ansatz $C_r = e^{-iqr} + v e^{iqr} + \beta\alpha^r$ and $D_r = e^{-iqr} + v e^{iqr} - \beta\alpha^r$ for $r > 1$. The equations for $r > 2$ can be solved by this ansatz if $2i\alpha\cos(q)\cos(Q/2) = (-1+\alpha^2)\sin(Q/2)$. We choose $|\alpha| < 1$ and solve the remaining four equations for C_0, D_0, v and β. Since the α part decays exponentially fast, we can extract the scattering length $a = -\lim_{q\to 0}\partial_q\delta$ with $v = e^{2i\delta}$, which after some algebra results in

$$a(U \to 0) = \frac{[3 + 5\cos(\Phi)]\,|\Gamma|^2 + 2}{[5 + 3\cos(\Phi)]\,|\Gamma|^2 - 2}, \tag{8.14}$$

By comparison to a 1D Bose gas of particles with mass m and contact-interaction one may extract an effective interaction strength $g = -2/(am)$ [37]. The scattering length diverges for $|\Gamma| \to 1/2, \Phi \to 0, 2\pi$ but remains finite and negative for any other phase Φ, which coincides with the observation that the AB-correlated hopping Hubbard model behaves as a repulsively interacting system for small filling even in the limit of $U \to 0$.
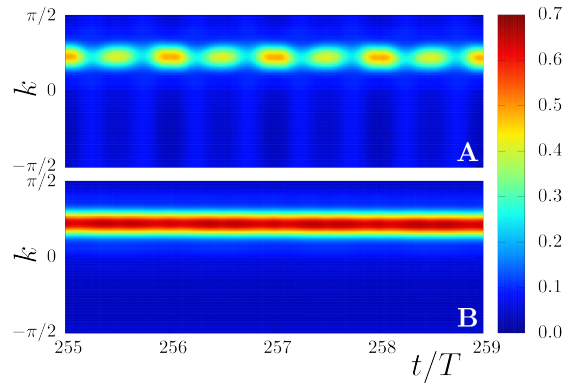
Fig. 8.7: Quasi-momentum distribution of the A and the B components in the laboratory frame as a function of time for $\langle \hat{n} \rangle = 3/2$ and $\Omega_{AB} = 0.8$, and same parameters as those of Fig. 8.6.

8.1.6   Adiabatic preparation

A typical experimental scenario as studied in the context of shaken lattices [151] might start with the preparation of a (ground)state of the non-modulated setup and then (quasi)adiabatically increase the modulation amplitude $\tilde{U}_{A1}$. We prepare the system at $t = 0$ in the ground state of the non-modulated Bose-Hubbard model at $U = 1$ and then as illustrated in the inset of Fig. 8.6 we slowly linearly ramp the modulation amplitude $\tilde{U}_{A1}(t) = \frac{t}{\tau}\tilde{U}_{A1}$ and the pulsed tunneling for $t < \tau$ of Eq.(8.3) in order to stay close to the ground state. For $t > \tau$ we keep the modulations constant and monitor the evolution of the momentum distribution. An example is shown in Fig. 8.7.

For the dynamical calculations we have used TEBD calculations for 16 sites with up to 300 states, and a maximal site occupation of 4 bosons. As in Ref. [151], we may simulate rather long evolution times ($t \sim 400T$) due to the quasi-adiabatic character of the dynamics. We have carried out our TEBD simulations for time steps $dt = T/400$ and $m = 300$ matrix states, which compare well to simulations with $dt = T/600$ and $m = 400$, showing the convergence of the results. Smaller system sizes, with a correspondingly decreased ramping and evolution time, display very similar behavior.

The evolution of the momentum k_{max} at which the momentum distribution is maximal is shown in the inset of Fig. 8.6 (black and blue curves). The non-adiabaticity of the finite ramping time leads to oscillations in the expectation value of k_{max} after the ramping procedure. The time-average and standard deviation are shown as points and error-bars in the main panel of Fig. 8.6 of the main text and compare very well to the ground-state expectation. Note that the drift k_{max} is only linear with $\Omega_{AB}\langle \hat{n} \rangle$ for a sufficiently small value of $\Omega_{AB}\langle \hat{n} \rangle$ and exhibits a non-trivial density dependence.

Since atoms at sites A and B belong to different species in Stern-Gerlach like TOF experiments it is possible to monitor the quasi-momentum distribution of atoms in state $|A\rangle$ and $|B\rangle$ separately. The TOF picture of the B sublattice at any time corresponds to that of the effective model (see Fig. 8.7). On the A sublattice

the single particle correlations are defined by

$$\langle \psi(t)|\hat{b}_{2i}^{\dagger}\hat{b}_{2j}|\psi(t)\rangle = \langle \psi'|\hat{b}_{2i}^{\dagger}e^{iV(t)(\hat{n}_{2i}-\hat{n}_{2j})/\hbar}\hat{b}_{2j}|\psi'\rangle \tag{8.15}$$

with $V(t)$ defined in the context of Eq. (8.5). Hence the momentum distribution of A coincides with that of the effective model at stroboscopic measurement times $t = nT$, for which $V(t) = 0$. At intermediate times we observe a blurring of the TOF picture due to the characteristic stochastic character of the density dependent phases (see chapter 7).

8.2 The 1D anyon Hubbard model

In this section we propose a possible experimental scheme for the realization of a density-dependent Peierls phase Eq.(8.1) in 1D using Raman assisted tunnelings extending the scheme of Keilmann et al. [338]. We will analyze in detail the physics emerging due to the interplay of the anyonic quantum statistics and the inherent 3-body hardcore constraint, which is due to the experimental scheme, including MI phases stable at attractive interactions and dimerized phases. Furthermore, at certain fillings we observe an exotic 2-component partially paired phase (PP) with a multi-peak momentum distribution.

The results presented in this section have been published in Ref. [48] which was developed in collaboration with L. Santos.

8.2.1 Density dependent Peierls phases

The original scheme of Keilmann et al. [338] suffers from a serious technical issue, which would basically render the idea unfeasible in experiments. With our extended proposal we may solve this drawback.

The original proposal of Keilmann et al.

The basic scheme of Ref. [338] for the realization of the AHM and a density dependent Peierls phase is, ignoring the discrimination between A and B particles, sketched in Fig. 8.8: A (one-component) bosonic gas is loaded in a tilted one dimensional optical lattice. Due to the strong tilting $U, \Delta \gg J$ the hopping J is strongly
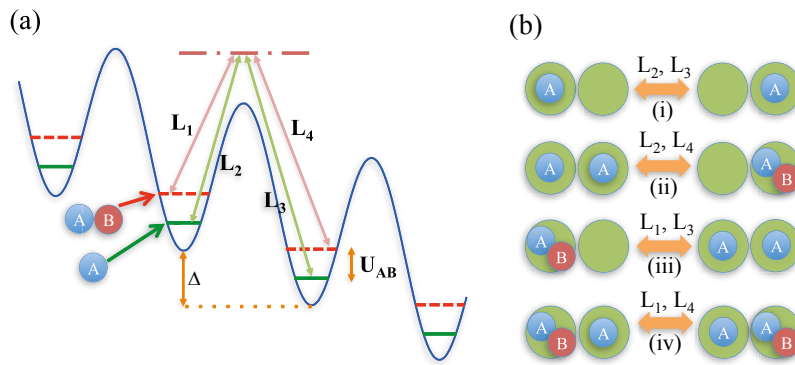

Fig. 8.8: (a) Sketch of the tilted optical lattice including the Raman-lasers $L_{1...4}$. (b) The four hopping processes relevant for the AHM.

suppressed. We decompose the desired hopping-process of the form (8.1) to the following events ((n, m) denote the occupation of n and m particles on adjacent sites):

(i) $(1, 0) \rightarrow (0, 1)$ has an energy difference $\Delta E_{\mathrm{i}} = -\Delta$. The hopping matrix element is $\langle 0, 1 | \hat{\mathcal{H}}_{i,i+1}^{ddsm} | 1, 0 \rangle = 1$

(ii) $(1, 1) \rightarrow (0, 2)$ with $\Delta E_{\mathrm{ii}} = -\Delta + U$ and $\langle 0, 2 | \hat{\mathcal{H}}_{i,i+1}^{ddsm} | 1, 1 \rangle = \sqrt{2}$

(iii) $(2, 0) \rightarrow (1, 1)$ is characterized by $\Delta E_{\mathrm{iii}} = -\Delta - U$ and $\langle 1, 1 | \hat{\mathcal{H}}_{i,i+1}^{ddsm} | 2, 0 \rangle = \sqrt{2} e^{i\phi}$

(iv) $(2, 1) \rightarrow (1, 2)$ with $\Delta E_{\mathrm{iv}} = -\Delta$ and $\langle 0, 2 | \hat{\mathcal{H}}_{i,i+1}^{ddsm} | 1, 1 \rangle = 2\sqrt{2} e^{-i\phi}$

For higher fillings further processes could be included. The key idea is that these hopping-events have to be resolved and assisted by a set Raman-lasers L_i, with Rabi frequencies $\Omega_j = |\Omega_j| e^{i\phi_j}$, wave vectors $\mathbf{k}_j$, and frequencies ω_j.

Always two lasers may induce one hopping process virtually coupling the particles in the atomic ground state to an excited state. Typically the frequencies ω_i of the Raman lasers are chosen to by far detuned (detuning in the order of $\delta \sim$ GHz) from the atomic transition in order to avoid large spontaneous emission losses. Hence, it is the resonance condition of the Raman-lasers that determines which states are coupled by the lasers. In Ref. [338] 4 lasers are proposed to build the transition between the processes (i)-(iv), hence, $\omega_2 - \omega_3 = \Delta E_{\mathrm{i}}$, $\omega_2 - \omega_4 = \Delta E_{\mathrm{ii}}$, $\omega_1 - \omega_3 = \Delta E_{\mathrm{iii}}$, and $\omega_1 - \omega_4 = \Delta E_{\mathrm{iv}}$. The two photon-Rabi-frequencies are engineered in such a way that the correct phases ϕ are imprinted in the tunneling processes (i)-(iv).

The crucial issue of this idea is that processes (i) and (iv) are energetically degenerated and, hence, may not be addressed with different lasers. As a result both the combination of L_2 and L_3, and of L_1 and L_4 induce both (i) and (iv), preventing the realization of the desired density-dependent Peierls phase.

Two-component system

In order to solve this issue we consider a bosonic species with two internal states, $|A\rangle$ and $|B\rangle$ confined to a tilted 1D optical lattice. For the specific case of ^{87}Rb, we may choose $|A\rangle \equiv |F = 1, m_F = -1\rangle$ and $|B\rangle \equiv |F = 2, m_F = -2\rangle$. The Hilbert-space of a single lattice site thus constitutes of empty sites (0), single occupied sites (A) or (B), doubly occupied sites (AA), (BB) or (AB), etc. We will consider an inter- and intraspecies interaction $U_{\alpha,\beta}$. Other atomic species and even fermionic atoms are possible (see Ref. [48]).

Raman-assisted hopping

No direct hopping occurs since $J \ll \Delta, U_{\alpha,\beta}$. Raman-assisted hopping is realized with the set-up of Fig. 8.8 (a) formed by four lasers $L_{j=1,...,4}$, with Rabi frequencies $\Omega_j = |\Omega_j| e^{i\phi_j}$, wave vectors $\mathbf{k}_j$, and frequencies ω_j. $L_{1,4}$ have linear polarization and $L_{2,3}$ circular σ_- polarization and couple states $|A\rangle$ and $|B\rangle$ far from resonance. $|B\rangle$ is just affected by lasers $L_{1,4}$ due to selection rules. Although again both $L_{2,3}$ and $L_{1,4}$ couple to $|A\rangle$, the coupling with $L_{1,4}$ can be made much smaller than that of $L_{2,3}$ due to different coupling strengths [48]. Hence we may assume below that $|A\rangle$ is just affected by $L_{2,3}$.

As discussed in section 6.2.2 we evaluate the Raman-assisted hopping, J_{nm}, given by lasers $L_{n=1,2}$ and $L_{m=3,4}$, from site j to site $j+1$ as

$$J_{nm} \simeq \mathrm{i}\left(\frac{V_{nm}}{2\Delta}\right) J \sin\left(\frac{\delta k_x^{nm} d}{2}\right) e^{\mathrm{i}\delta k_x^{nm} d(j+1/2)} e^{\mathrm{i}\phi_{nm}}. \qquad (8.16)$$

where $\phi_{nm} = \phi_n - \phi_m$, $\delta \mathbf{k}^{nm} = \mathbf{k}_n - \mathbf{k}_m$, and $V_{nm} = \frac{\hbar |\Omega_n||\Omega_m|}{\delta}$ and δ the (large) detuning to the one-photon transitions.

Each laser pair couples a different Raman transition (see Fig. 8.8):

(i) J_{23} characterizes the hopping (A,0)→(0,A), which is accompanied by an energy shift $\Delta E = -\Delta$. We hence demand $\omega_2 - \omega_3 = -\Delta$ and the transition amplitude is given by $V_{23} \simeq \frac{1}{2}\frac{\Omega_2 \Omega_3^*}{\delta}$ including the appropriate Clebsch-Gordan coefficients for the specific case of ^{87}Rb.

(ii) (A,A)→(0,AB) is given by J_{24}, being characterized by $\Delta E = -\Delta + U_{AB}$; we impose $\omega_2 - \omega_4 = -\Delta + U_{AB} + U$, with $U \ll U_{AB}, \Delta$ and the amplitude $V_{24} = \frac{1}{\sqrt{6}}\frac{\Omega_2 \Omega_4^*}{\delta}$

(iii) J_{13} is linked to the hop (AB,0)→(A,A); the energy shift is $\Delta E = -\Delta - U_{AB}$; we demand $\omega_1 - \omega_3 \simeq -\delta - U_{AB} - U$. $V_{13} = \frac{1}{\sqrt{6}}\frac{\Omega_1 \Omega_3^*}{\delta}$.

(iv) (AB,A)→(A,AB) is given by J_{14}; the energy shift is $\Delta E = -\Delta$; we impose $\omega_1 - \omega_4 = -\Delta$. The transition amplitude is given by $V_{14} = \frac{1}{3}\frac{\Omega_1 \Omega_4^*}{\delta}$.

In this frame U may be understood as an effective on-site interaction energy.

Spurious processes

Undesired spurious processes are in principle possible:

(v) (A,0) → (0,B); $\Delta E = -\Delta$

(vi) (A,A) → (0,AA): $\Delta E = -\Delta + U_{AA}$

(vii) (AA,0) → (A,A): $\Delta E = -\Delta - U_{AA}$

(viii) (AB,A) → (B,AA): $\Delta E = -\Delta + \delta U$, with $\delta U = (U_{AA} - U_{AB})$

(ix) (AA,B) → (A,AB); $\Delta E = -\Delta - \delta U$

Process (v) is just possible with J_{24} or J_{13}. But these laser combinations are (quasi) resonant with $-\Delta \pm U_{AB}$. For $U_{AB} \gg W$, with W the width of the Raman resonance (typically of the order of 50 Hz [283]), process (v) is far from resonance with either J_{24} or J_{13}. To neglect the (vi) and (vii) processes one needs $U_{AA} \gg W$. In contrast, to avoid (viii) and (ix) one must demand $\delta U \gg W$. The latter condition is certainly more strict, but may be attained with typical experiments parameters [48]. Interestingly, choosing a fermionic species only process (v) has to be handled.
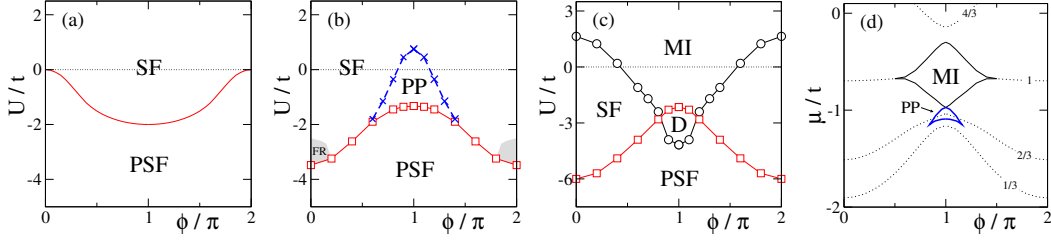
Fig. 8.9: Phase diagram of the AHM for fixed fillings: (a) dilute limit ($n \to 0$), (b) incommensurate intermediate fillings (here $\rho = 1/2$) and (c) unit filling ($\rho = 1$). The PSF-SF transition line (boxes or solid line in (a)), extracted from the crossing of two and one particle excitations coincides with the onset of parity order. At incommensurate fillings for small ϕ the system exhibits a first order transition from SF to PSF phase through a forbidden region (shaded area). (d) Phase diagram and lines of constant density for the AHM ($U = 0$) as function of chemical potential μ and statistical angle ϕ. Solid lines denote the MI and PP phase, the rest of the phase diagram is SF. Vacuum ($\rho = 0$) is below $\mu < -2$; for $\mu > 4$ the fully occupied phase ($\rho = 2$) is realized.

8.2.2 Effective 1D Hamiltonian

We assume $\frac{|\Omega_1||\Omega_4|}{4} = \frac{|\Omega_2||\Omega_3|}{3} = \frac{|\Omega_1||\Omega_3|}{2\sqrt{3}} = \frac{|\Omega_2||\Omega_4|}{2\sqrt{3}} = \Omega^2$, $\Omega_1 = |\Omega_1|e^{-i\phi}$, and $\Omega_{j=2,3,4} = |\Omega_j|$ and obtain the transition amplitudes $V_{23} \simeq \frac{\Omega^2}{\delta}$, $V_{24} = \sqrt{2}\frac{\Omega^2}{\delta}$, $V_{13} = \sqrt{2}\frac{\Omega^2}{\delta}e^{-i\phi}$, and $V_{14} = 2\frac{\Omega^2}{\delta}e^{-i\phi}$. Note that an additional factor $\sqrt{2}$ is used to mimic bosonic enhancement. We denote as c_j the bosonic operator corresponding to the Fock-state manifold $\{|0\rangle, |1\rangle \equiv |A\rangle, |2\rangle \equiv |AB\rangle\}$. Assuming $\mathbf{k}_{1,2} = k\mathbf{e}_y$, and $\mathbf{k}_{3,4} = k\mathbf{e}_x$, and $kd = \pi$, then

$$\mathcal{H} = -t\sum_j (-1)^j \left[c_j^\dagger e^{i\phi n_j} c_{j+1} + \text{H.c.} \right] + \frac{U}{2}\sum_j n_j(n_j - 1) \qquad (8.17)$$

with $n_j = c_j^\dagger c_j$, and $t = \left(\frac{\Omega^2/\delta}{2\Delta}\right) J$.

Note that the factor $(-1)^j$, which results from the x projection of $\delta\mathbf{k}$, may be easily eliminated by redefining the bosonic operators in the form: $b_{4l} = c_{4l}$, $b_{4l+1} = c_{4l+1}$, $b_{4l+2} = -c_{4l+2}$, $b_{4l+3} = -c_{4l+3}$, with l an integer. In this way we obtain the 1D model:

$$\mathcal{H} = -t\sum_j \left[b_j^\dagger e^{i\phi n_j} b_{j+1} + \text{H.c.} \right] + \frac{U}{2}\sum_j n_j(n_j - 1) \qquad (8.18)$$

After identification of $\alpha_j = e^{i\phi \sum_{1 \leq l \leq j-1} n_l} b_j$ this model may be mapped to the form of

$$\hat{\mathcal{H}} = -t\sum_j (\alpha_j^\dagger \alpha_{j+1} + \text{H.c.}) + \frac{U}{2}\sum_j n_j(n_j - 1) \qquad (8.19)$$

α_j and $\alpha_j^\dagger$ satisfy anyonic commutation relations $\alpha_j \alpha_k^\dagger - e^{-i\phi \,\text{sgn}(j-k)} \alpha_k^\dagger \alpha_j = \delta_{jk}$ and $\alpha_j \alpha_k - e^{-i\phi \,\text{sgn}(j-k)} \alpha_k \alpha_j = 0$. It must be stressed that with this definition on-site the particles behave as bosons as $\text{sgn}(0) = 0$.

Due to the effective implementation of the AHM in a cold atom scenario, the bosonic particles satisfy an additional three body hardcore constraint $b_i^\dagger b_i^\dagger b_i^\dagger = 0$. In the effective model the two-body interaction U may thus also be negative. Note

that important features of the ground-state physics presented here, the D and PP phases (although the latter also realized for repulsive interactions), are properties of the combination of the AHM and the three body hard-core constraint. That is why they were not observed in earlier studies of the AHM [338] of similar models [47].

8.2.3 Two body physics and weak coupling

As already discussed for the AB-model in section 8.1 the AHM behaves as a repulsively interacting system even in the limit of $U \to 0$ as can again be seen from the two-particle scattering length is given by

$$a = \frac{t(1 + \cos \phi)}{-2(2t + U) + 4t \cos \phi} \, . \tag{8.20}$$

The scattering length diverges for $\Phi \to 0, 2\pi$ but remains finite and negative for any other phase Φ. The Luttinger liquid parameter K in the weak coupling limit (see Eq.(8.11)) which for this case is given by

$$K^2 = \frac{\pi^2}{\phi^2 + \frac{U}{2\rho t}} \, . \tag{8.21}$$

K decreases with increasing ϕ which qualitatively has the same effect as U creating an effective on-site repulsion. In Figure 8.9 (a) we show the phase diagram of the AHM in the dilute limit which exhibits an atomic SF phase and a PSF phase of bound particle pairs. Consistent with the idea of an effective repulsion the SF-phase expands in the negative U region as $\phi > 0$.

8.2.4 Intermediate incommensurate fillings

In Fig. 8.9 (b) a representative phase diagram is shown for an incommensurate intermediate filling. The case of $\phi \to 0$ of a BH-model with a three-body hardcore constraint has been mentioned already in chapter 5. The system exhibits a superfluid (SF) to Mott-insulator (MI) transition and unit filling and sufficiently strong interactions U. For negative U a transition to a pair-superfluid phase (PSF) is realized. At incommensurate fillings this transition may become first order. As discussed in Ref. [342] for spin-1 models with negative single-ion anisotropies the transition between so called XY and XY2 phases (i.e. SF and PSF phase in boson language) is first-order, passing a region of macroscopic jumps in magnetization as function of magnetic field (i.e. in the density as function of chemical potential) for small magnetizations (i.e. close to unit filling). For other fillings the phase transition may become second order. This forbidden region (FR) is depicted as shaded area in phase diagram 8.9 (b). At fixed ρ the ground state is characterized by the formation of a macroscopically bound state with a phase separation of doublons and holes. The FR shrinks, however, fast with increasing ϕ.

Around $0.6 \gtrsim \phi/\pi$ another gapless region, which we will call partially paired (PP), may be observed between PSF and SF phases. The transition is indicated by a sharp kink in the $\mu - \rho$ curve (see Fig. 8.10 (a)) signaling a C-IC transition between a two- and a one-component phase as discussed in chapters 5 and 10. As depicted in Fig. 8.10 (a) the PP-phase exhibits an complex sequence of steps of 2 and 1 particles as a function of μ. Contrary to that, the SF and PSF-phases are characterized by a
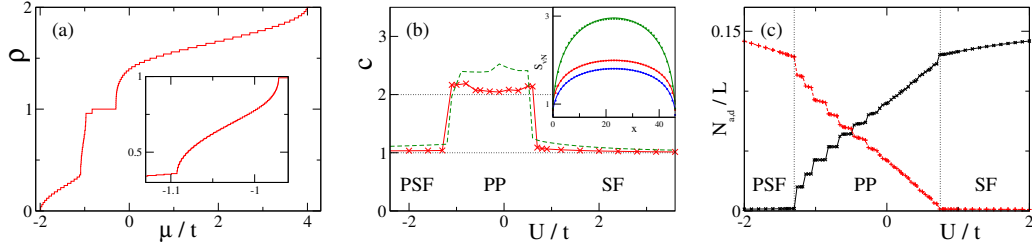
Fig. 8.10: Phase transitions of the AHM at incommensurate fillings for $\phi = \pi$. (Right) Equation of state, density n as function of chemical potential ($L = 48$). The inset shows a detailed view on the PP-region for $L = 240$ sites. (Middle) Estimation of the central charge ($L = 48$ and periodic boundary conditions). The inset shows fit to the block-entanglement-entropy S_{vN} for (from bottom to top) $U = 2, -2, -1.0$. (Right) Sum of local single- N_a and two-particle-correlations N_d ($L = 60$) as defined in the main text.
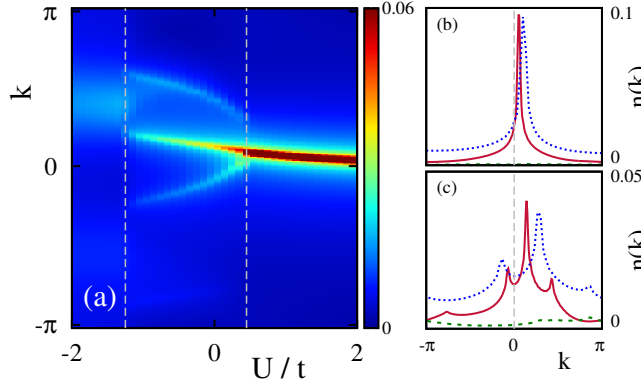
Fig. 8.11: Quasi-momentum distribution $n(k)$ for $\rho = 1/2$ as function of U/t for (a) $\phi = 0.9\pi$ and (b) $\phi = \pi$. The dashed lines denote the phase transitions between PSF, PP and SF phases.

pure sequence of steps of 1 and 2 in the $\mu - \rho$ curve respectively. The best character-istic of a two component PP phase and corresponding phase transition is the direct measurement of central charge, which is clearly $c = 2$ as shown in Fig. 8.10 (b).

Fig. 8.11 illustrates the momentum distribution for a cut through the phase di-agram of Fig. 8.9. In the PP phase, interestingly, the peak in the momentum distri-bution splits to a complicated multi-peak structure. The SF and PSF phases only exhibit a single (in the PSF blurred) maximum.

8.2.5   The nature of the PP phase

The nature of the PP phase may be understood by the following simplified pic-ture. While for larger statistical angles $\phi \to \pi$ the two particle physics is domi-nated by an effective strong repulsion as discussed above, for higher densities it may be energetically favorable to form doublons or more precisely dimers $|d\rangle_x = \alpha |11\rangle_{x,x+1} + \beta |20\rangle_{x,x+1}$ as may be understood from recasting the hopping term of the Hamiltonian in the following form

$$b_j^\dagger e^{i\phi n_j} b_{j+1} = J_1 b_j^\dagger b_{j+1} + J_2 b_j^\dagger n_j b_{j+1} \qquad (8.22)$$

with $J_1 = 1$ and $J_2 = -1 + e^{i\phi}$. For $\phi \approx \pi$ the second correlated hopping term becomes dominant, $J_2 = -2J_1$, and $|d\rangle_x$ will gain a large binding energy $-\sqrt{2}J_2$. However, the hopping of the dimers is reduced compared to single particles. In first order degenerate perturbation theory in the manifold of bound dimers it is given by $J_1/\sqrt{2}$. For a certain range of small on-site interactions and fillings it will be energetically favorable to occupy the ground state with both strongly bound doublon dimers $|d\rangle_x$ and remaining atomic dimers $|a\rangle_x = \alpha |01\rangle_{x,x+1} + \beta |10\rangle_{x,x+1}$. Neglecting interactions between these two quasi-particles, which may be reasonable for small doublon and atom densities ρ_a and ρ_d with $\rho_a + \rho_d \ll 1$, and also neglecting decay of the doublon dimers, which is suppressed by the effective hardcore constraint, one arrives at the following model describing two independent hardcore bosons species with different hopping rates (for $U = 0$)

$$\hat{\mathcal{H}}_{a,d} = J_1 \sum_x a_x^\dagger a_{x+1} + \text{H.c.} - J_1/\sqrt{2}e^{\arg J_2} \sum_x d_x^\dagger d_{x+1} + \text{H.c.} - J_1 \sum_x a_x^\dagger a_x - \sqrt{2}J_2 \sum_x d_x^\dagger d_x$$

$$(8.23)$$

where a_x $(a_x^\dagger)$ and d_x $(d_x^\dagger)$ are annihilation (creation) operators of hardcore atom and doublon dimers on sites $x, x+1$. The Hamiltonian has to be minimized under the constraint $\rho_a + 2\rho_d = \rho$. Although being certainly a very crude oversimplification, model (8.23) captures the main physical aspects of the PP phase. For $U \approx 0$ at low densities the ground state only contains species a; for higher fillings ($\rho \gtrsim 0.3$ for $U = 0$) both species are present. Here the $\mu - n$ curve shows an irregular pattern of steps of two or one particles. This mixed phase extends for values around $U = 0$, for $U \gg J_1$ only species a is present, for $U \ll -J_1$ one arrives at a pure d-phase. The a and d hopping terms contain a different phase-factor such that measuring an $a + d$-momentum distribution function one will observe several peaks.

We may test the assumptions made for the justification of model (8.23) by calculating the atom and doublon-dimerizations,

$$N_a = \sum_i \langle b_i^\dagger b_{i+1} \rangle, \quad N_d = \sum_i \langle (b_i^\dagger)^2 (b_{i+1})^2 \rangle, \quad (8.24)$$

shown in Fig. 8.10 (c), which approximately measure the densities ρ_a and ρ_d. While the SF and PSF phase are LL-phases of almost hardcore single particles or pairs (for $\phi = \pi$) in the PP phase both "species" are present. Although doublon dimer density is not a conserved quantity here the system exhibits many jumps to states with approximately finite doublon density.

We may compare the PP-phase with the Kohn-metal discussed in section 7.1.4. It is, however, important to note that as shown in Fig. 8.9 (d) the PP phase has a finite extent in both ϕ and μ-space (here shown for vanishing on-site interactions $U = 0$).

8.2.6 Unit filling

As studied in Refs. [47, 338], at commensurate filling, tuning of the statistical angle ϕ may induce phase transitions between SF and MI phases. This property may be understood on the basis of a weak coupling analysis, as presented above. Increasing ϕ induces an effective on-site repulsion that drives the system into the MI-phase, even for vanishingly small or negative residual interactions U as can be seen in Fig. 8.9 (c) and 8.9 (d). At fixed fillings this transition is of BKT-type and
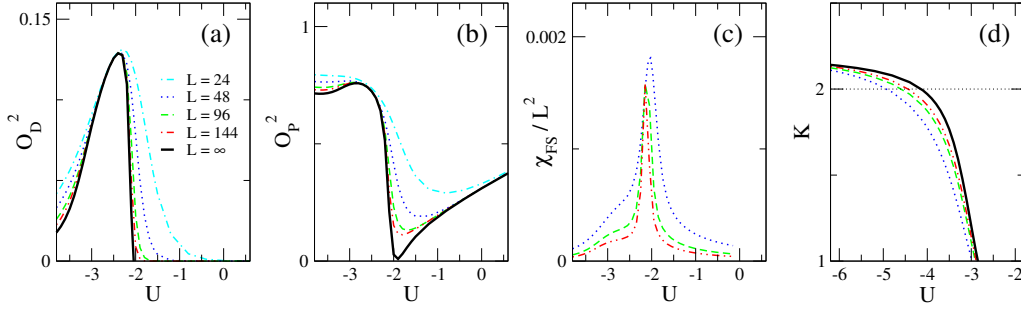
Fig. 8.12: Order parameters and phase transitions for unit filling ($\rho = 1$) and $\phi = \pi$ showing the PSF,D,MI phases: (a) Dimerization O_D, (b) parity order O_P, (c) fidelity susceptibility $\chi_F S/L^2$, and (d) Luttinger-liquid parameter K as extracted from the long wavelength limit of the structure factor [321].
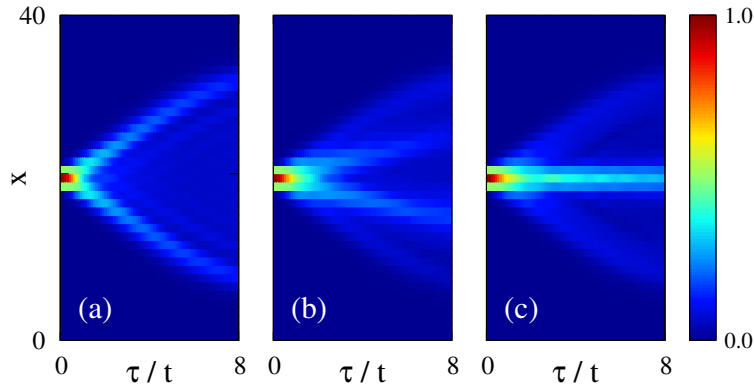
Fig. 8.13: Expansion dynamics of the density of the AHM with (a) $\phi = 0$, (b) $\phi/\pi = 0.6$ and (c) $\phi = \pi$ in a harmonic trap ($V = 0.02$, $U = 0$, $L = 40$ sites) initially prepared as fully localized state (2 particles) in the center of the trap.

may be numerically resolved by extracting Luttinger-liquid parameter $K = 2$, as shown in Fig. 8.12 (d), which is consistent with the opening of the energy gap.

For negative $U < 0$ one observes an Ising-type transition to the PSF as described above or, for $\phi \approx \pi$, a dimerized phase D. The Ising transition line is characterized by a crossing of single and two particle excitations and a sharp peak in the fidelity susceptibility diverging with L^2 (cf. Fig. 8.12 (c)). The D phase exhibits finite dimer-order parameter $O_D = \langle T_{L/2} - T_{L/2+1} \rangle$ with $T_i = b_i^\dagger b_{i+1} + H.c.$ as shown in Fig. 8.12 (a). A finite size scaling of the dimer order parameter results in the correct scaling relations and a collapse of data points (not shown). In all D, PSF and MI phases the parity order O_P^2 (2.19) remains finite and vanishes only at the Ising-critical line separating D and MI phase, as illustrated in Fig. 8.12 (b).

8.2.7   Dynamically probing the AHM

Quantum dynamics and quantum walks provide a possible scenario for studying properties of the anyonic statistics of the AHM in experiment. On a two body level this has been discussed extensively in Refs. [343–345]. In Fig. 8.13 we show the expansion dynamics of the real space density distribution of a cloud of two particles initially prepared on subsequent sited in the center of an harmonic trap. While the usual BH model shows a symmetric expansion Fig. 8.13 (a), for $\phi \neq 0, \pi$

one observes a strong asymmetry in the expansion dynamics due to the trapping potential and the fractional statistics. For $\phi = \pi$ the two anyons form a bound dimer state $|d\rangle_x$ that decays slowly and hence the expansion is strongly inhibited.

8.3 DDSM in ladders and 2D systems

After having studied purely one dimensional realizations of density dependent gauge fields in the previous sections we will now explore the effect of density-dependent synthetic magnetism (DDSM) in two dimensions. In particular, we are interested in a system described by the following Hamiltonian

$$
\begin{aligned}
\mathcal{H} \;=\; &-\sum_{\mathbf{r}}\left[t_x b^{\dagger}_{\mathbf{r}+\mathbf{e}_x} e^{i\phi_{\mathbf{r}} n_{\mathbf{r}}} b_{\mathbf{r}} + t_y b^{\dagger}_{\mathbf{r}+\mathbf{e}_y} b_{\mathbf{r}} + \text{H.c.}\right] \\
&+\frac{U}{2}\sum_{\mathbf{r}} n_{\mathbf{r}}(n_{\mathbf{r}}-1) - \mu \sum_{\mathbf{r}} n_{\mathbf{r}},
\end{aligned}
\tag{8.25}
$$

The first term of (8.25) accounts for the hopping of bosons along the two directions of the lattice, defined by lattice vectors $\mathbf{e}_x = (1,0)$ and $\mathbf{e}_y = (0,1)$ (see Fig. 8.14 (a) and (b)). The density dependent Peierls phase of the hopping amplitude ($e^{i\phi_{\mathbf{r}} n_{\mathbf{r}}}$) can be chosen in such a way that an effective net-magnetic flux per unit-cell is created.

Model (8.25) may be engineered by inducing both the tunneling in x as well as in y direction by Raman-lasers. We will hence consider a tilting of the optical lattice in both directions with $\Delta_x \neq \Delta_y$. Then using 6 Raman-lasers one may extend the scheme of section 8.3 to two dimensions [49]. Interestingly, already 4 lasers are sufficient to induce a rectified effective flux in the system, the resulting effective Hamiltonian will, however, generally exhibit a density dependent hopping amplitude [49]. For the sake of simplicity we will restrict our analysis to model (8.25).

Furthermore, we will concentrate on the case where the phases depend only on the position in the y-direction, i.e. $\phi_{\mathbf{r}} = \phi_j$. Due to the operator nature of this phase, quantum fluctuations of the density will crucially affect the effective magnetic flux. We demonstrate that DDSM has important consequences for bosons in two-leg ladders and 2D square lattices, leading to a non-trivial interplay between chirality and density modulations.

The following section is based on the publication [49] which was developed in collaboration with D. Huerga, G. Sun, D. Poletti and L. Santos. The cluster-meanfield results are contributed by D. Huerga. Main part of the time dependent calculations have been performed by G. Sun.
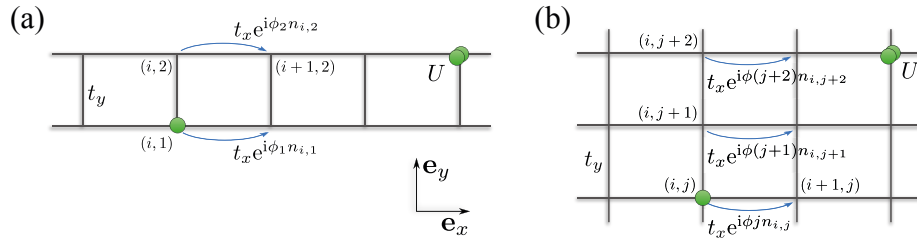

Fig. 8.14: Sketch of the density-dependent Peierls phases of the model (8.25) (a) on a ladder (see also Eq. (8.26)) and (b) of the 2D-square lattice.
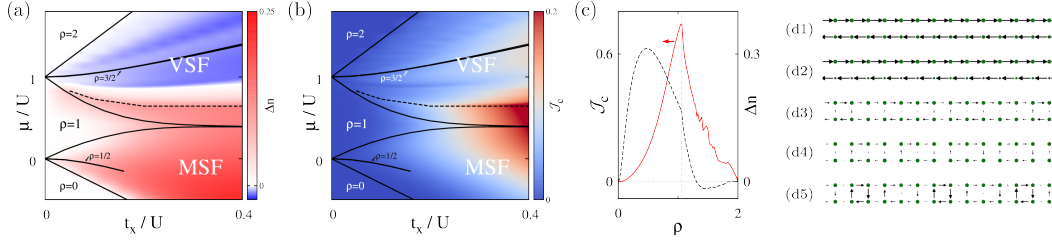
Fig. 8.15: (a) and (b) Phase diagram for a ladder with $t_y = t_x$, $\phi_1 = 0.8\pi$, and $\phi_2 = 0$ as function of t_x/U and chemical potential μ computed with the density matrix renormalization group (DMRG). The color code indicates (a) the particle density imbalance between the legs Δn and (b) the chiral current j_c (obtained from simulations with $L = 24$ rungs). Solid lines mark the MI with $\rho = 1$, and (very narrow) with $\rho = 1/2$ and $3/2$ (extrapolated to the thermodynamic limit from systems with up to $L = 96$ rungs). The dashed line denotes the MSF-VSF transition. (c) Δn (dashed) and j_c (solid) for the same parameters as in (a) and (b) but $U = 0$ and $L = 48$. (d1-5) Typical particle density and current configurations for $U = 0$ and (d1) $\rho = 0.1$, (d2) $\rho = 0.63$, (d3) $\rho = 1.25$, (d4) $\rho = 1.46$, (d5) $\rho = 1.77$. The size of the circles is proportional to the onsite-density, he arrows encode the strength of the local currents.

8.3.1 Density-dependent magnetism in ladders

Again the ladder geometry (cf. chapter 10) amenable to exact DMRG treatment constitutes a good starting point for a detailed analysis of 2D effects. In this situation the Hamiltonian is given by (see Fig. 8.14 (a))

$$
\begin{aligned}
\hat{\mathcal{H}}_{\text{ladder}} = &-t_x \sum_i \left[b_{i+1,1}^\dagger e^{i\phi_1 n_{i,1}} b_{i,1} + \text{H.c.} \right] \\
&- t_x \sum_j \left[b_{i+1,2}^\dagger e^{i\phi_2 n_{i,2}} b_{i,2} + \text{H.c.} \right] \\
&- t_y \sum_i \left[b_{i,2}^\dagger b_{i,1} + \text{H.c.} \right] \\
&+ \frac{U}{2} \sum_{i,j} n_{i,j}(n_{i,j} - 1),
\end{aligned}
\tag{8.26}
$$

MSF and VSF phases with imbalanced density

In the limit of strong on site repulsion $U \gg J$ model (8.26) with density dependent phases may readily be mapped onto a system of hardcore bosons without a flux for fillings $0 < \rho < 1$. For $1 < \rho < 2$ we may consider doublons $|2\rangle_{i,j}$ on top of a uniform MI-background $\prod_{i,j} |1\rangle_{i,j}$ as hardcore particles, which, however, now experience a finite flux $\phi = \phi_1 - \phi_2$, such that the effective Hamiltonian in this limit may be written as

$$
\hat{\mathcal{H}}_{\text{hardcore}}^{\rho>1} = -2t_x \sum_{i,j} \left[c_{i+1,j}^\dagger e^{i\phi j} c_{i,j} + \text{H.c.} \right] - 2t_y \sum_i \left[c_{i,2}^\dagger c_{i,1} + \text{H.c.} \right],
\tag{8.27}
$$

with $c_{i,j}$ ($c_{i,j}^\dagger$) being the creation (annihilation) operator of a doublon on site (i,j). Thus in the strongly interacting regime $U \gg J$, model (8.26) is expected to reproduce the physics of hardcore bosons in a magnetic static field exhibiting MSF and VSF phases as discussed in detail in section 6.5.2.

We may obtain a qualitative insight in the physics beyond this hardcore-limit by a simple mean-field decoupling. Due to the effective three-body hardcore constraint $(b_{\mathbf{r}}^\dagger)^3 = 0$ we may write the hopping term as $b_{\mathbf{r'}}^\dagger e^{i\phi n_{\mathbf{r}}} b_{\mathbf{r}} = b_{\mathbf{r'}}^\dagger (1 + (e^{i\phi} - 1)n_{\mathbf{r}})b_{\mathbf{r}}$. Using the decoupling $b_{\mathbf{r'}}^\dagger n_{\mathbf{r}} b_{\mathbf{r}} \simeq 2\kappa(\mathbf{r'}, \mathbf{r})(n_{\mathbf{r}} - \bar{n}_{\mathbf{r}}) + 2\bar{n}_{\mathbf{r}} b_{\mathbf{r'}}^\dagger b_{\mathbf{r}}$ we obtain the following expression

$$
\begin{aligned}
b_{\mathbf{r'}}^\dagger e^{i\phi n_{\mathbf{r}}} b_{\mathbf{r}} + \text{H.c.} \quad \simeq \quad & [(1 + 2\bar{n}_{\mathbf{r}}(e^{i\phi} - 1)b_{\mathbf{r'}}^\dagger b_{\mathbf{r}} + \text{H.c.}] \\
+ \quad & [2\kappa(\mathbf{r'}, \mathbf{r})(e^{i\phi} - 1) + \text{c.c.}](n_{\mathbf{r}} - \bar{n}_{\mathbf{r}}),
\end{aligned}
\tag{8.28}
$$

with the mean fields $\bar{n}_{\mathbf{r}} \equiv \langle n_{\mathbf{r}} \rangle$, and $\kappa(\mathbf{r'}, \mathbf{r}) \equiv \langle b_{\mathbf{r'}}^\dagger b_{\mathbf{r}} \rangle$. The first term of Eq. (8.28) gives rise to an effective Peierls phase coupled to the average density. Hence, particles encircling a plaquette of model Eq.(8.26) in the presence of a homogeneous average density will pick up an effective flux. Interestingly, the second term of Eq. (8.28) induces a local chemical potential which in a ladder (8.26) would result in a potential gradient between the two legs for $\phi_1 \neq \phi_2$. In the following we will test these findings by means of exact numerical DMRG calculations.

As for the case of a static flux the chiral current constitutes a useful observable, $j_c = j_1 - j_2$, where the leg currents are now defined by Eq. (6.15) including the density dependent Peierls phases as

$$
j_i = \frac{i}{L} \sum_j \langle b_{i,j}^\dagger e^{-i\phi_i n_{i,j}} b_{i+1,j} - \text{H.c.} \rangle
\tag{8.29}
$$

in units of $t_x/\hbar$. The dependence of j_c on the effective flux induced by the chemical potential μ or density ρ is illustrated in Fig. 8.15 (b) and (c) for the case for $\phi_1 = 0.8\pi$, and $\phi_2 = 0$. The superfluid regime splits into a MSF and a VSF phase as studied for the case of a static homogeneous flux in chapter 10. At the critical filling ρ_c the chiral current j_c presents a cusp, characteristic for the MSF-VSF transition. This transition is as well characterized by a kink in the equation of state $\rho(\mu)$. We also verify that the MSF and VSF phases exhibit central charge $c = 1$ and $c = 2$, respectively.

Fig. 8.15(a) and (c) presents evidence that the occupation-dependent Peierls phase leads to density imbalance between the legs,

$$
\Delta n = 2(\bar{n}_2 - \bar{n}_1)/(\bar{n}_2 + \bar{n}_1) \, .
\tag{8.30}
$$

In general $\Delta n \neq 0$ for both MSF as well as VSF phases. However, as can be seen in Fig. 8.15 (c) the MSF-VSF transition is characterized by a kink and a sharp drop of the imbalance Δn. Although, compared to the case of the BLP phase discussed in chapter 10 this imbalance corresponds to an explicitly broken symmetry between the legs, Δn depends non-trivially on μ or ρ. It may even change it sign going through a balanced point, $\Delta n = 0$.

Strong rung-coupling limit.

As for the case of static magnetic fields where the MSF-VSF transition has been explored for a fixed flux in Ref. [2] as function of t_y/t_x, also for the DDSM the rung hopping strength constitutes an important degree of freedom. In Fig. 8.16 (a) we study the phase diagram, in particular the commensurate-to-incommensurate MSF-VSF transition, on t_y for $U = 0$, $\phi_1 = \pi$, and $\phi_2 = 0$. Interestingly we basically observe two different regimes: for small interchain couplings $t_y/t_x \lesssim 1$ the MSF-VSF boundary (dashed line) is located close to unit filling, however, as $t_y/t_x \gtrsim 1$ it shifts quickly to larger densities $\rho \sim 3/2$.
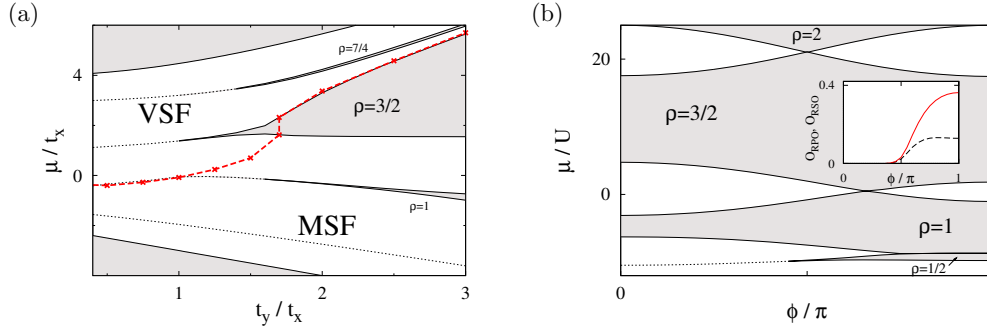
Fig. 8.16: (a) Phase diagram for a ladder with $U = 0$, $\phi_1 = \pi$, and $\phi_2 = 0$ as function of t_y and μ (in units of $t_x = 1$). As discussed in the main text for large densities a VSF is realized, while for low densities the system is in a MSF phase, separated by a commensurate-to-incommensurate (with respect to the vortex density ρ_V) phase transition (dashed line). Dotted lines denote lines of constant particle density $\rho = 1/2, 1, 3/2$ and $7/4$, while solid lines indicate the gapped phases. (b) Phase diagram as function of μ/U and $\phi_1 = -\phi_2 = \phi$ for $U = t_x$ and $t_y = 10t_x$ computed with DMRG. The shaded areas denote gapped phases of $\rho = 1/2, 1, 3/2$ and 2 filling - the white area correspond to MSF phases. As a characteristic feature of the density-dependent fields one observes a sequence of direct transitions between the gapped phases resulting in a macroscopic jump of density around $\phi = \pi$, $2\pi/3$ and $\pi/2$. All gapped phases exhibit finite rung-string order O_{RSO} and rung-parity order O_{RPO} as defined in the main text. The inset shows O_{RPO} (solid line) and O_{RSO} (dashed line) for $\rho = 1/2$.

For $\phi_1 - \phi_2 \neq \pi$ above a critical value of t_y/t_x the VSF phase may vanish. In the strong rung-coupling limit $t_y/t_x \gg 1$ several gapped band insulating phases at commensurate fillings $\rho = 1$ and $3/2$ are stabilized. The extent of the MI-phases strongly increases with t_y/t_x as discussed below. For the parameters of Fig. 8.16 (a) a MI-phase at $\rho = 1/2$ is suppressed. Additionally one may observe a gapped charge density wave phase at filling $\rho = 7/4$ (see chapter 10 for a detailed discussion of similar phases at 1/4 filling for density-independent synthetic magnetism). Apart from the SF-phases also the MI-phases may be of Meissner-MI (in Fig. 8.15(a) for $\rho = 1/2$ and $\rho = 1$) and of vortex-MI (for $\rho = 3/2$) types.

Again, the strong rung-coupling limit of $t_x, U \ll t_y$ is an interesting limit amenable to analytical treatment. Here we may project (8.26) to the basis of rung-singlet-states containing $N_j = 0, 1, 2, 3$ and 4 particles per rung j:

$$
\begin{aligned}
|\tilde{0}\rangle &= |0,0\rangle \\
|\tilde{1}\rangle &= (|0,1\rangle + |0,1\rangle)\sqrt{2} \\
|\tilde{2}\rangle &= (e^{i\frac{\phi_1+\phi_2}{2}}|2,0\rangle + \sqrt{2}|1,1\rangle + |0,2\rangle)/2 \\
|\tilde{3}\rangle &= (e^{i\frac{\phi_1+\phi_2}{2}}|2,1\rangle + |1,2\rangle)/\sqrt{2} \\
|\tilde{4}\rangle &= |2,2\rangle
\end{aligned}
\tag{8.31}
$$

with energies $\epsilon_0 = 0$, $\epsilon_1 = -t_y$, $\epsilon_2 = -2t_y + U/2$, $\epsilon_3 = -2t_y + U$ and $\epsilon_4 = 2U$.

At filling factors $\rho = 1$ and $\rho = 3/2$ one observes Mott-insulating phases with a gap of the order t_y and $2J_y$ resp. (see Fig. 8.16 (b)). The emergence of a Mott phase

at $\rho = 1/2$ is determined by the interplay of t_y and U: At fillings $\rho < 1$ the system is well described by a correlated hopping Bose-Hubbard model retaining $|\tilde{0}\rangle, |\tilde{1}\rangle$ and $|\tilde{2}\rangle$ states as, we will show in the following. For higher fillings it is sufficient to restrict the description to the manifold of $\{|\tilde{2}\rangle, |\tilde{3}\rangle\}$ or $\{|\tilde{3}\rangle, |\tilde{4}\rangle\}$ states recovering an effective hardcore boson model.

The effective hopping between rung singlets depends on the particular choice of ϕ_1 and ϕ_2 employed. For the symmetric configuration $\phi_1 = -\phi_2 = \phi$ the first order hopping matrix elements are given by

$$\langle \tilde{0}\tilde{1}| \hat{\mathcal{H}}_x |\tilde{1}\tilde{0}\rangle = -t_x \,,$$
$$\langle \tilde{2}\tilde{1}| \hat{\mathcal{H}}_x |\tilde{1}\tilde{2}\rangle = -t_x \left(1 + \cos(\phi)\right) \,,$$
$$\langle \tilde{3}\tilde{2}| \hat{\mathcal{H}}_x |\tilde{2}\tilde{3}\rangle = -t_x \left(1 + 2\cos(\phi)\right) \,,$$
$$\langle \tilde{3}\tilde{4}| \hat{\mathcal{H}}_x |\tilde{4}\tilde{3}\rangle = -2t_x \cos(\phi) \,. \tag{8.32}$$

Due to the broken space-inversion symmetry the doublon formation is direction dependent, $\langle \tilde{0}\tilde{2}| \hat{\mathcal{H}}_x |\tilde{1}\tilde{1}\rangle = -\sqrt{2}t_x$ and $\langle \tilde{2}\tilde{0}| \hat{\mathcal{H}}_x |\tilde{1}\tilde{1}\rangle - t_x \left(1 + \cos\phi\right)/\sqrt{2}$. For the symmetric configuration we may write the 0,1,2-particle Bose-Hubbard model in the following simplified form

$$\hat{\mathcal{H}} = -t_x \sum_j \left[B_j^\dagger (1 - \sin^2(\phi/2)N_j) B_{j+1} + \text{H.c.} \right]$$
$$+ \frac{U}{4} \sum_j N_j(N_j - 1) - (\mu + t_y) \sum_j N_j, \tag{8.33}$$

with $F[N_j] = (1 - N_j) + N_j(1 + \cos\phi)$ where B_j are bosonic operators in the space $\{|\tilde{0}\rangle, |\tilde{1}\rangle, |\tilde{2}\rangle\}$, and $N_j = B_j^\dagger B_j$.

The hopping terms vanish for $\phi = \pi$, $2\pi/3$ and $\pi/2$. Remarkably also second order corrections (including higher excitations, not shown) vanish (just the contrary than for a simple non density-dependent flux, see chapter 10) and thus one observes a series of direct transitions between gapped phases 1/2, 1, 3/2 and 2 with and infinite compressibility and a macroscopic jump of density (see Fig. 8.16 (b)).

For a general configuration of the phases we arrive at complex hopping terms and, hence, departing from the symmetric phase configuration $\Phi_1 = -\Phi_2$ the first order transitions (except for the one from $n = 3/2$ to $n = 2$) smoothen.

Due to the broken space-inversion symmetry all Mott insulating phases exhibit both a finite rung-string-order $O_{RSO} = (\langle N \rangle - N_j)(-)^{\sum_{j<k<l}\langle N \rangle - N_l}(\langle N \rangle - N_k)$ as well as rung-parity-order $O_{RPO} = (-)^{\sum_{j<k<l}(\langle N \rangle - N_k)}$, as may be seen in the inset of Fig. 8.16 (b) (compare chapter 7).

Symmetries and vortex-lattice phases

Density-independent static magnetic fields are up to a gauge transformation completely defined by the net flux per unit-cell of the lattice. Due to its operator-nature this is not true for the case of density-dependent Peierls phases. Indeed, as may be seen in Fig. 8.17, the phase diagram may significantly depend on the values of both phases ϕ_1 and ϕ_2 of model (8.26). While the MSF-VSF phase boundary mainly just depends on the total effective flux $\phi_1 - \phi_2$, only in the vicinity of $\phi_1 \simeq -\phi_2 \simeq \pi/2$, where also density imbalance Δn vanishes, we observe a vortex-lattice phase at
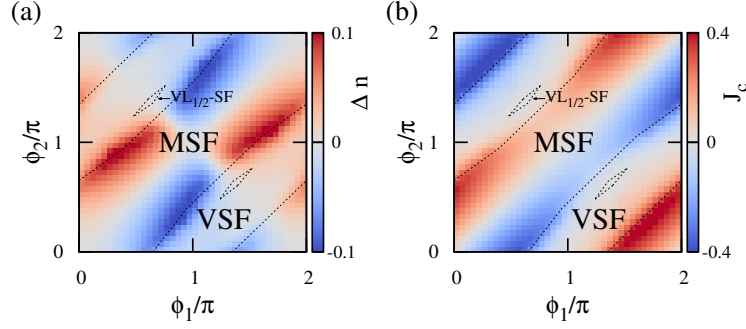
Fig. 8.17: (a) Density imbalance Δn and (b) chiral current j_c function of ϕ_1 and ϕ_2 for $t_x = t_y$, $U = t_x$ and $\rho = 1.25$ as obtained by DMRG calculations. In addition to the MSF and VSF phases a small vortex lattice phase at vortex-density $\rho_V = 1/2$, $VL_{1/2}$-SF may be observed. Dashed lines indicate the phase boundaries from the VSF to the MSF and $VL_{1/2}$-SF phases.

vortex-density $\rho_V = 1/2$ ($VL_{1/2}$ phase). Apart from the characteristic staggered pattern of the currents as shown for the case of static magnetic fields e.g. in Ref. [43], the $VL_{1/2}$ phase may be discriminated from the VSF phases by the calculation of the central-charge, which is $c = 1$ in vortex-lattice phases. For strong phase-imbalances $\phi_1 = 0, \phi_2 = \phi$ as in Fig. 8.15 no vortex-lattice phases are observed.

Note that the phase diagram is symmetric with respect to inversion of the phases $I_1 : (\phi_1, \phi_2) \rightarrow (-\phi_1, -\phi_2)$ and exchange of the two legs of the ladder $I_2 : (\phi_1, \phi_2) \rightarrow (\phi_2, \phi_1)$ for $\phi_1, \phi_2 \in [0, 2\pi)$. The density imbalance Δn (Fig. 8.17 (a)) is (anti)symmetric with respect to $I_1(I_2)$. The chiral current(Fig. 8.17 (b)) is an antisymmetric quantity under both I_1 and I_2.

8.3.2 Two-dimensional lattices.

We now extend the discussion of DDSM to two dimensional square lattices. Again, we should expect a non trivial interplay between the density-dependent phases and density modulations and the creation of an effective flux per plaquette. For simplicity we consider the limiting case of π-phases, i.e. $\phi_{\mathbf{r}} = j\pi$, for which the Peierls phase in Hamiltonian (8.25) takes the simpler form,

$$e^{i\phi_{\mathbf{r}} n_{\mathbf{r}}} = (-1)^{jn_{\mathbf{r}}} . \tag{8.34}$$

We numerically treat this problem by means of cluster mean-field theory as introduced in chapter 3. Here we use clusters of size $L_x \times L_y = 2 \times 2$ and 4×2 as well as 2×4. The results shown Fig. 8.18 remain basically stable under increasing of the cluster size. We define different order parameters for the characterization of different quantum phases, such as a $(0, \pi)$ charge density wave (CDW) order parameter

$$\rho_{CDW} = \sum_{\mathbf{r}} e^{-i\pi j} \langle n_{\mathbf{r}} \rangle / N \tag{8.35}$$

and the bond-chiral order parameter,

$$\eta = \frac{1}{N_b} \sum_{\langle \mathbf{r}, \mathbf{r}' \rangle} |\langle j(\mathbf{r} \rightarrow \mathbf{r}') \rangle| . \tag{8.36}$$
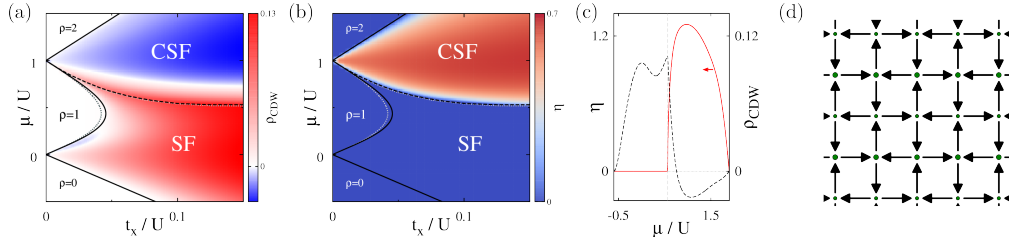
Fig. 8.18: (a) and (b): Ground state phase diagram of model (8.25) in 2D with π-phases $\phi_{\mathbf{r}} = j\pi$ and $t_x = 2t_y$ computed with CBMFT with clusters of size $L_x \times L_y = 2 \times 2$ (black lines) and 4×2 (dotted grey lines). Solid lines mark the boundaries of the MI, while the the onset of a finite chiral bond order parameter, η, signaling the CSF-SF transition, is marked with dashed lines and the dashed curve marks. The color code indicates (a) the charge density wave order parameter ρ_{CDW} and (b) the chiral bond order parameter η.(c) Chiral bond order parameter η (solid line) and charge density wave order parameter ρ_{CDW} (dashed line) for a cut in the phase diagram along $t_x/U = 0.1$. (d) Typical current and density configuration of the CSF phase. The size of the circles is proportional to the onsite-density, the lengths and widths of the arrows encode the strength of the local currents. Simulations have been performed by D. Huerga.

Note, that since calculations are performed in the thermodynamic limit the local current may be non zero for Peierls phases of (8.34). MI lobes and superfluid order are discriminated by the (non vanishing) condensate density,

$$\rho_0 = \langle b^{\dagger}_{\mathbf{k=0}} b_{\mathbf{k=0}} \rangle / N \qquad (8.37)$$

Fig. 8.18 (a) and (b) illustrate the phase diagram for the case $t_x = 2t_y$. Besides the MI phase at unit filling two different SF phases may be found. Both of them exhibit a modulated density as shown in Fig. 8.18 (c). For a critical $\mu > \mu_c$ a chiral SF phase with a modulated density and vanishing bond-chiral order emerges. The typical configuration of local densities and currents, which forms a fully stacked checkerboard pattern of vortices and anti-vortices, can be seen in Fig. 8.18 (d). The phase transitions are in all cases found to be of second order, signaled by discontinuities in the second order derivative of the energy with respect to the chemical potential.

8.3.3   Dynamically probing the density-dependent field.

Experimentally DDSM may be probed in particular by its intriguing dynamics. As an exemplification we study the dynamics of a defect on top of a MI with $\rho = 1$ in a two-leg ladder configuration, such as model (8.26) with $\phi_1 = -\phi_2 = \phi$ and $t_x = t_y$. The defect, a hole or a doublon, is initially prepared in the center of the ladder at site $(1, j = 0)$ and we monitor the light-cone like expansion of the density-perturbation. Similar dynamics has been studied recently in the context of Bose Hubbard models without gauge fields [346] and may be observed in experiments with single site resolution [82].

For the limit $U \gg t_x$ the defect expansion corresponds to a single particle with a hopping t_x for a holon on top of the MI background or $2t_x e^{\pm i\phi}$ for a doublon. In
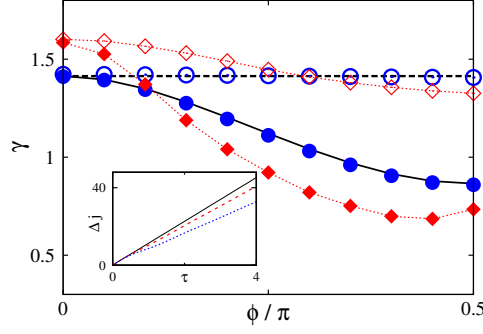
Fig. 8.19: Expansion coefficient γ of a defect along the ladder as a function of the effective flux ϕ for $t_x = t_y$, and $U/t_x = 50$ (circles) and $U/t_x = 10$ (diamonds). Hollow (filled) symbols denote the t-DMRG results for the holon (doublon) expansion. Dashed (solid) curves denote single-particle (exact diagonalization) results for holons (doublons), which match well with the t-DMRG results for large U/t_x. The inset depicts typical linear expansions of $\Delta j(\tau)$ for a doublon at $U \to \infty$ and $\phi/\pi = 0$ (solid line), 0.5 (dashed line) and 1 (dotted line). The TEBD-simulations have been performed by G. Sun.

both cases the excitation expands ballistically along the ladder, i.e.

$$\Delta j(\tau) = \sqrt{\langle j^2 \rangle (\tau)} \sim \gamma \tau \qquad (8.38)$$

In the following we considering the time τ in units of $\hbar/t_x$ for holons and $\hbar/2t_x$ for doublons. From the opening angle of the light cone we may define the expansion coefficient γ. The inset of Fig. 8.19 depicts examples of $\Delta j(\tau)$ for different ϕ for the hardcore limit. The black lines in Fig. 8.19 present the corresponding values of γ. In the hardcore limit holons do not experience any flux and hence the the expansion is ϕ-independent $\gamma = \sqrt{2}$. Doublons, however, are subject to an effective flux 2ϕ and their trajectories are diverted by cyclotron motion. Hence, their expansion is slowed down significantly and γ decreases with ϕ. This situation has to be contrasted with the case of density-independent magnetic fields. Here holons and doublons will both experience the same magnetic flux 2ϕ and propagate - up to a factor 2 due to bosonic enhancement - in the same way.

For lower U/t_x quantum fluctuations become relevant altering the defect expansion in an intriguing way. A perturbative treatment of the role of particle-hole fluctuations offers an instructive starting point of the study. Up to second-order one virtual doublon-holon pair may be created and annihilated which mediate new hoppings of the initial holon (doublon) of the form:

$$
\begin{aligned}
\hat{\mathcal{H}}^{(2)} &= \frac{-2t_x^2}{U} \sum_{i,j} \left[\alpha_i |j+2, i\rangle \langle j, i| + \text{H.c.} \right] \\
&\quad - \frac{2t_x t_y}{U} \sum_{i,j} \left[\beta_i |j+1, k \neq i\rangle \langle j, i| + \text{H.c.} \right],
\end{aligned} \qquad (8.39)
$$

where $|i, j\rangle$ denotes a defect at site (i, j), $\alpha_i \equiv e^{i\phi_i} (e^{-i\phi_i})$, $\beta_i = 1 + e^{i\phi_i} (1 + e^{-i\phi_{k \neq i}})$ for doublons (holons). In Fig. 8.20 we illustrate the validity of this simple perturbative approach, which is, however, limited to small time-scales. In order to study the influence of quantum fluctuations beyond perturbation theory we perform TEBD calculations, with system sizes up to 100 rungs keeping up to 1000 matrix states.
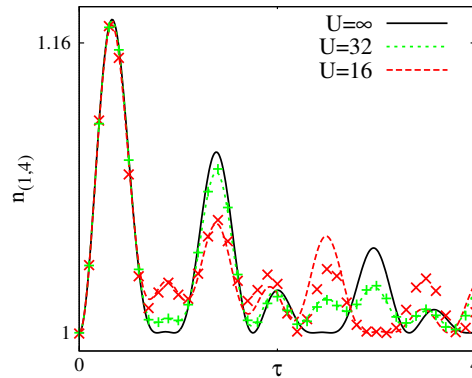
Fig. 8.20: Test of the perturbation theory for the dynamics of the particle density at site $(1,4)$ of a ladder of $L = 40$ rungs with an initially prepared doublon. Symbols correspond to TEBD data points, the continuous lines depict the results of the second order perturbation theory (8.39).

The symbols of Fig. 8.19 depict the expansion coefficients γ as obtained from TEBD calculations. For sufficiently large $U \gg t_x, t_y$ the results basically overlap with the hardcore limit calculations. Lowering the interactions (but staying clearly in the initial MI regime) we observe that for $\phi \approx 0$ fluctuations speed up the defect expansion both for holons and doublons in the same way. This becomes intuitively clear on the basis of Eq.(8.39) since due to the quantum fluctuations more expansion processes have to be considered. The interplay between quantum fluctuations and DDSM significantly affects this dynamics. As can be seen in Fig. 8.19 for large ϕ, surprisingly, fluctuations may even slow down the doublon expansion. Eq.(8.39) suggests that the effective magnetic flux seen by the doublons is modified and, hence, the cyclotron motion is strengthened. For smaller U/t_x also holons experience an effective flux induced by the virtual doublons created in top of the MI substrate. Thus also their expansion is slowed down as shown in Fig. 8.19.

8.4 Conclusions

In this chapter we have analyzed several experimentally feasible scenarios for the engineering of a certain kind of dynamical gauge fields which experience a direct feedback from the particle density. This density dependent synthetic magnetic fields may be created by fast modulated interactions or Raman-laser assisted hoppings in a two component atomic gas. The latter idea significantly extends the proposal of Ref.[338] which turns out to suffer from serious experimental issues. Different possibilities for the creation of DDSM have been studied recently in Ref.[347].

In one dimensional systems DDSM results in the interesting possibility of studying the anyon Hubbard model, which exhibits a density-dependent drift of the momentum distribution, statistically induced MI phases, as well as dimer and exotic two-component phases due to the interplay with an effective 3-body hard core constraint. For ladders and 2D square lattices we have shown that these fields lead to a rich ground-state physics characterized by the non-trivial interplay between density modulations and chirality. In two-leg ladders we observe a density-driven

Meissner- to vortex-superfluid transition. Moreover, DDSM significantly affects the dynamics of particles in the lattice. It leads in particular to an intriguing expansion dynamics for doublons and holons in a MI, which presents a remarkable dependence on quantum fluctuations and may be employed as an experimental probe of DDSM.

In the previous section we have investigated the properties of bosonic particles in the presence of DDSM. From the discussion in section 8.2 is is clear that in particular fermionic species may be a useful candidate for the realization of DDSM in cold atom experiments, since here a part of possible spurious processes mentioned in section 8.2 identically vanishes. While in one dimensional systems this could be exploited to study the anyon Hubbard model, in two and higher dimension a significantly different model would be realized.

Chapter 9

Alkali-Metal Spinor Systems

Ultracold spinor gases in optical lattices provide a very versatile element of the cold atom toolbox [30] for the study of quantum magnetism [348]. Due to the their spin dependent interactions and spin changing collisions (see section 2.3.1) multi-component fermionic or bosonic quantum lattice gases are expected to show interesting ground-state properties, ranging from magnetic Néel ordering in 2-component Mott insulators [10, 11] to spin liquids [349] or topological states in 1D [350, 351]. But also time dependent properties have attracted a lot of interest [25, 352]. In this chapter, inspired by recent experimental advance in the study of spin mixing dynamics [25] in ultracold fermionic ^{40}K-gases in optical lattices, we will study ground state and dynamical properties of 1D four-component alkali-metal fermions at half-filling in strong magnetic fields.

The ground-state properties of low dimensional properties of fermionic spinor gases have been studied extensively. For spin 3/2 fermions by means of bosonization techniques and large scale numerical DMRG calculations detailed phase diagrams have been derived for different fillings and different regimes of interactions [350, 351, 353–355].

Recently, the influence of magnetic fields and in particular the effect of the quadratic Zeeman splitting has been discussed [356] as an additional externally tunable degree of freedom of the manipulation of many-body dynamics. Due to their unpaired electron in the outer s-shell alkali atoms possess a hyperfine-structure composed of two manifolds of states with total spin $I \pm 1/2$. The hyperfine splitting may be controlled experimentally by external magnetic fields. In strong magnetic fields as described by the Paschen-Back effect[357] the electronic spin de-
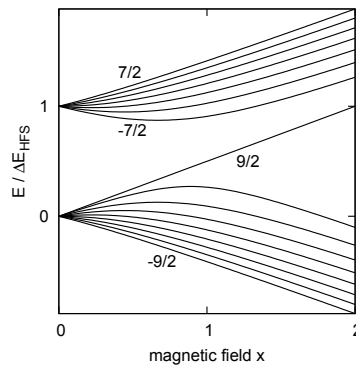

Fig. 9.1: Zeeman-splitting of hyperfine energy levels $E/\Delta E_{HFS}$ in the in magnetic field for ^{40}K. The magnetic field x is given in units of $x/B = (g_J - g_I)\mu_B/\Delta E_{HFS}$, where g_J and g_I denote the orbital and nuclear Landeé factors and μ_B is the Bohr-magneton.

couples from the nuclear spin leading to a twofold splitting of states as $\sim Bg_s m_s$. Thus energy levels have to bend down giving an intuitive picture for the nonlinear contributions to the energy level splitting, described as quadratic Zeeman-effect (QZE). The full dependence of the magnetic field is described by the Breit-Rabi formula [358] as shown in Fig. 9.1 for the case of fermionic Potassium ^{40}K. In Ref.[356] the quadratic Zeeman-effect was investigated for spin 3/2 fermions at quarter filling, where dimerized and Néel-ordered as well as gapless spin liquid phases have been observed.

9.1   Melting of the band-insulator

We will start with a brief review of the findings of Ref. [25]. Here, Krauser *et al.* show the realization of a fermionic spinor gas in an optical lattice with coherent spin oscillations due to spin changing-collision. In this experiment different hyperfine components of the 9/2-manifold of ^{40}K are trapped in an optical lattice. The system is prepared as an equal mixture of two different spin states, e.g. as $|9/2, 1/2\rangle$, at very large magnetic fields B such that the quadratic Zeeman-energy is minimized. Due to Pauli-blocking the system here is in a band-insulating state. For times $t > 0$ the magnetic field B is quenched to smaller values, which initializes spin oscillation due to spin-changing collisions. On a single lattice site an initially prepared $|9/2, 1/2\rangle$-state can be converted due to spin-changing collisions only to $|7/2, 3/2\rangle$, due to the conservation of total spin and Pauli-blocking. From Eq.(2.32) we obtain the general interaction Hamiltonian for this situation

$$\hat{\mathcal{H}}_I = \sum_{\alpha,\beta} U_{\alpha\beta} n_\alpha n_\beta + \gamma \left(\Psi^\dagger_{\frac{1}{2}} \Psi^\dagger_{\frac{9}{2}} \Psi_{\frac{7}{2}} \Psi_{\frac{3}{2}} + \Psi^\dagger_{\frac{3}{2}} \Psi^\dagger_{\frac{7}{2}} \Psi_{\frac{9}{2}} \Psi_{\frac{1}{2}} \right) . \tag{9.1}$$

For the moment we just take into account spin-changing collisions γ and the spin dependent interactions $U_{\frac{1}{2},\frac{9}{2}}$ and $U_{\frac{7}{2},\frac{3}{2}}$.

Hence, for the case of an infinitely deep optical lattice, i.e. tunneling $J = 0$, we rewrite the quench situation, following Ref. [25], in terms of a two body problem

$$\hat{\mathcal{H}} = \begin{pmatrix} 2q + U_{\frac{1}{2},\frac{9}{2}} & \gamma \\ \gamma & -2q + U_{\frac{7}{2},\frac{3}{2}} \end{pmatrix} \tag{9.2}$$

including the quadratic Zeeman-energy $q \propto B^2$. One observes typical Rabi-oscillations in the chirality

$$\tau(t) = \left(1 - \frac{\gamma^2}{2\gamma^2 + 8\tilde{q}^2} \right) + \frac{\gamma^2}{\gamma^2 + 8\tilde{q}^2} \cos \left(2\sqrt{\gamma^2 + 4\tilde{q}^2} \cdot t \right) \tag{9.3}$$

with $\tilde{q} = q + \frac{U_{\frac{1}{2},\frac{9}{2}} - U_{\frac{7}{2},\frac{3}{2}}}{4}$. Both frequency and amplitude of the oscillation depend on the value of the final magnetic field.

A finite tunneling $|J| > 0$ allows for the occupation of different states of the manifold through second-order processes. As shown in the experiment of Ref. [25] the dynamics of the quench situation, however, is dominated by the states of the on-site manifold manifold $\{9/2, 1/2, 3/2, 7/2\}$ even for a relatively large tunneling $J > U$. For very long time scales (of several tens of ms) the occupation of the spin states 5/2 or $-1/2$ is negligible.
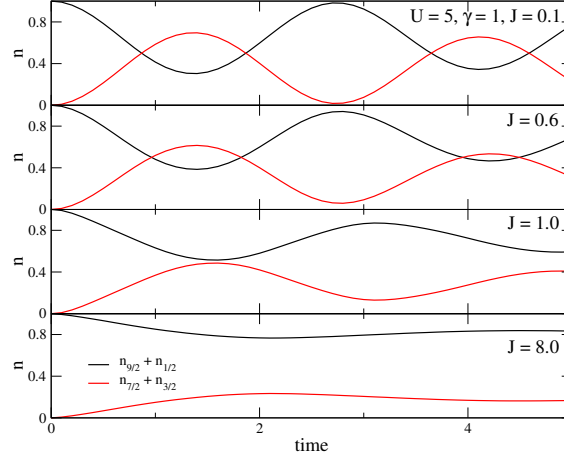
Fig. 9.2: Quantum quench from band-insulator ($q \to \infty$) with only $\pm 3/2$ sites popu-
lated to lower values of quadratic Zeeman energy $q = 0.3$ for different lattice depths,
tunneling amplitudes J/U resp.

In Fig. 9.2 we illustrate the evolution of the different particle occupations for dif-
ferent values of the tunneling J as obtained from iTEBD simulations of model (9.1).
For simplicity we assume $U_{\frac{1}{2},\frac{9}{2}} = U_{\frac{7}{2},\frac{3}{2}}$ and vary the hopping strength J. The system
is initially prepared in the $|9/2, 1/2\rangle$ manifold. At $t > 0$ both magnetic field and J
are quenched to the final values. The deep-lattice situation is accurately described
by Eq. (9.3). A finite tunneling leads to a strong damping of the oscillations as
well as to a shift in the frequencies that qualitatively compares to the experimental
results [25].

Inspired by this sudden quench experiments, we will explore in the follow-
ing the quantum phases that could be explored by (quasi) adiabatically lowering
the magnetic field for a system initially prepared in the practically zero entropy
band-insulating state. We will start with spin $F = 3/2$ fermions as could be exactly
realized for e.g. ^{132}Cs, ^{9}Be, ^{138}Ba or ^{201}Hg. In the second part we treat the case
of ^{40}K restricting the analysis to the manifold of $M \in \{9/2, 1/2, 7/2, 3/2\}$ and ne-
glecting transitions to other spin states, which may be reasonable within the above
mentioned scenario.

The following sections are based on the publication [50] which was developed
in collaboration with J. Jaramillo and T. Vekua.

9.2   Spin 3/2 fermions

For spin-3/2 fermions the interaction part of the Hamiltonian is given by (see sec-
tion 2.3.1)

$$\hat{\mathcal{H}}_I = - g_2 \left(n_{\frac{1}{2}} n_{\frac{3}{2}} + n_{-\frac{3}{2}} n_{-\frac{1}{2}} + n_{-\frac{1}{2}} n_{\frac{3}{2}} + n_{-\frac{3}{2}} n_{\frac{1}{2}} \right) - \frac{g_0 + g_2}{2} \left(n_{-\frac{1}{2}} n_{\frac{1}{2}} + n_{-\frac{3}{2}} n_{\frac{3}{2}} \right)$$
$$+ \gamma \left(c_{-\frac{3}{2}}^{\dagger} c_{\frac{3}{2}}^{\dagger} c_{\frac{1}{2}} c_{-\frac{1}{2}} + c_{-\frac{1}{2}}^{\dagger} c_{\frac{1}{2}}^{\dagger} c_{\frac{3}{2}} c_{-\frac{3}{2}} \right) \tag{9.4}$$

We denote again the spin changing collisions $\gamma = \frac{g_0 - g_2}{2}$. Since there are no unpaired
creation or annihilation terms as usual the total number of particles $N = N_{1/2} +
N_{-1/2} + N_{3/2} + N_{-3/2}$ is a good quantum number. Furthermore two spin-quantum

numbers are conserved $Q_S = N_{1/2} - N_{-1/2} + N_{3/2} - N_{-3/2}$ and $T = N_{1/2} - N_{-1/2} - N_{3/2} + N_{-3/2}$. Due to the spin-changing collision term the chirality $Q_B = N_{1/2} + N_{-1/2} - N_{3/2} - N_{-3/2}$ is not conserved in general. Generally this situation exhibits a high $SO(5)$ symmetry [353]. For the fine tuning $\gamma = 0$ the system is $SU(4)$ symmetric, and (among others) the chirality Q_B is conserved as well.

For large QZE $q \gg J, U$ the system approaches a band insulator (BI) state as discussed above. For a finite q and $\gamma > 0$ the formation of on-site singlets becomes favorable $|-1/2, 1/2\rangle + \alpha |-3/2, 3/2\rangle$. Without magnetic field, for repulsive interactions the half-filled ground-state phase diagram exhibits, additionally to the (site) singlet phase, a dimerized or spin-Peierls phase with a broken translational symmetry [353]. The phase diagram of the spin 3/2 fermions in the presence of a magnetic field is depicted in Fig. 9.3. At sufficiently large q the dimer phase, realized for $\gamma \lesssim 0.1$ at $q = 0$, is destabilized and an Ising phase transition to the singlet phase is induced. The singlet and BI phase are adiabatically connected.

In Fig. 9.4 we present the chirality τ for the parameters of Fig. 9.3 for different values of γ. τ is a monotonously increasing function of q that (quasi) saturates in the BI phase $\tau \simeq 1$. For the precise $SU(4)$ point of $\gamma = 0$ the system enters a gapless Luttinger liquid phase [50] for $q > q_c$ depicted in Fig. 9.3 as a straight line.

We calculate the local dimerization

$$D = |\sum_{\alpha,j} (-1)^j \langle \psi_{\alpha,j}^\dagger \psi_{\alpha,j+1} \rangle| / (L-1)$$

shown for $\gamma = -0.4$ in Fig. 9.4 (b). At the transition to the singlet phase this order parameter fulfills perfect Ising scaling relations shown by the collapse of different system-size data-points to one curve. For $q = 0$ this phase transition was predicted before in Ref. [353] as a function of γ. In Fig. 9.4 (c) we also present the fidelity susceptibility χ_F/L for the same parameters. It exhibits a pronounced peak diverging with the system size L at the Ising phase transition (cf. chapter 4). The crossover (indicated as dotted line in Fig. 9.3) from the singlet to the BI phase is characterized by a well defined local non-divergent maximum of χ_F.

In Ref. [356] a mapping to spin-models, established for the manifold of a fixed particle number per site, has been shown to be successful in the limit of large interaction U. For this case, however, we calculate the unrestricted problem. In numerical calculations it turns out to be favorable [351] to study the system as a two
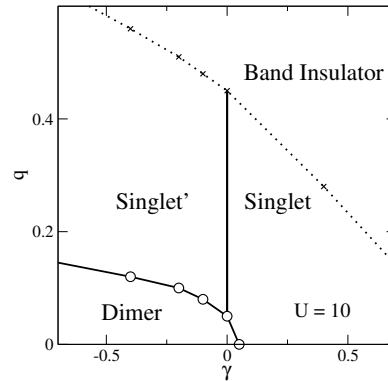

Fig. 9.3: Ground state phase diagram for $S = 3/2$ alkali fermions at half filling, as function of the quadratic zeeman energy q (in units of t) and $\gamma = (g_2 - g_0)/2J$ for the case of large interactions $(g_2 + g_0)/2 = 10J$.
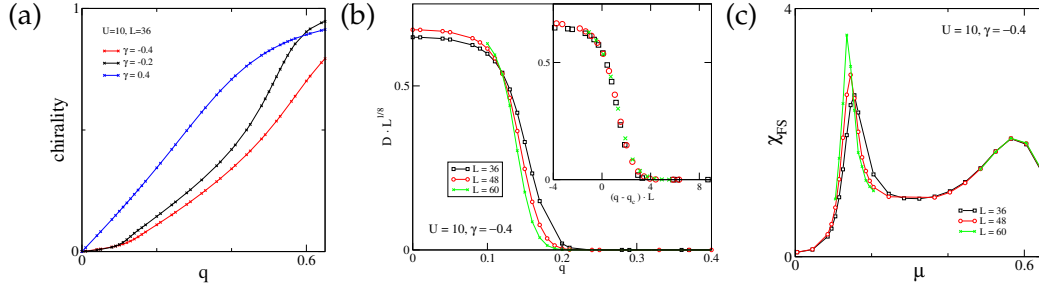
Fig. 9.4: (a) Chirality for several cuts through phase diagram Fig. 9.3 at $\gamma = (g_2 - g_0)/2t = -0.4, -0.2$ and 0.4. (b) Scaling of the local dimerization order parameter D. The inset shows the collapse of the data close to the Ising type phase transition. (c) Scaling of the fidelity susceptibility χ_{FS} for $\gamma = -0.4$ ($L = 36, 48, 60$).

component Fermi-Hubbard model on a ladder with appropriate rung interactions and pair tunneling terms. Although we may here just fix two $U(1)$-symmetries, due to the smaller local Hilbert-space [359] numerical DMRG calculations may be carried out faster. We keep in average up to 800 states and $L = 60$ sites.

9.3 Relevant model for ^{40}K atoms

In the following we study the ground-state phase diagram for the experimentally relevant situation of the multiplet $\{9/2, 1/2, 3/2, 7/2\}$ out of the 9/2 hyperfine manifold of ^{40}K. Associating $9/2 \rightarrow 1/2$, $1/2 \rightarrow -1/2$, $7/2 \rightarrow 3/2$ and $3/2 \rightarrow -3/2$ all quantities discussed above may be translated to the new situation. The Hamiltonian is given by Eq.(9.1). Contrary to the case of the spin 3/2 multiplet discussed above here interactions are strongly asymmetric being different combinations of the scattering lengths a_2^K, a_4^K, a_6^K, and a_8^K.

$$\gamma = \frac{\sqrt{6}}{5}(g_6 - g_8)$$

$$U_{\frac{7}{2},\frac{9}{2}} \sim g_8$$

$$U_{\frac{3}{2},\frac{7}{2}} \sim \frac{2}{5}g_6 + \frac{3}{5}g_8$$

$$U_{\frac{1}{2},\frac{9}{2}} \sim \frac{3}{5}g_6 + \frac{2}{5}g_8$$

$$U_{\frac{3}{2},\frac{9}{2}} \sim \frac{3}{10}g_6 + \frac{7}{10}g_8$$

$$U_{\frac{1}{2},\frac{3}{2}} \sim \frac{25}{66}g_2 + \frac{75}{286}g_4 + \frac{7}{33}g_6 + \frac{21}{143}g_8$$

$$U_{\frac{1}{2},\frac{7}{2}} \sim \frac{50}{143}g_4 + \frac{3}{110}g_6 + \frac{81}{130}g_8 \tag{9.5}$$

Explicit values for the scattering amplitudes a_F can be found in Ref.[25]. The high symmetry is broken and the system generally just retains a $U(1) \times U(1) \times U(1)$ symmetry corresponding to the particle number N and spins, as discussed above. We study again the ground-state phase diagram for $N = 2L$ particles and $Q_S = Q_T = 0$, i.e. keeping $N_{9/2} = N_{1/2}$ and $N_{3/2} = N_{7/2}$. The asymmetric situation now gives rise to a wealth of quantum phases as depicted in the ground-state phase diagram of Fig. 9.5.
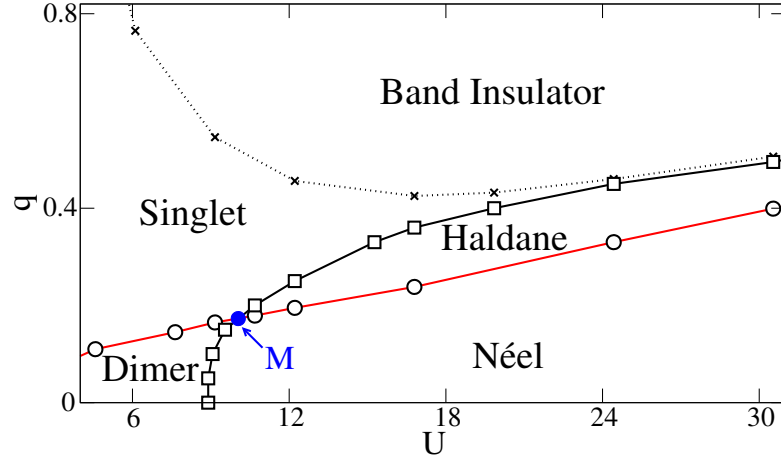
Fig. 9.5: Ground state phase diagram for a 4-component mixture of ^{40}K atoms at half-filling with the average interaction energy $U \sim \frac{4\pi\hbar^2}{m}(a_0^K + a_2^K + a_4^K + a_6^K + a_8^K)/5$ and the quadratic Zeeman coupling q. Dotted line indicates sharp cross-over and continuous lines are quantum phase transition lines, crossing at multi-critical point.

9.3.1 Large U regime

In the limit of large repulsive interactions U the ground-state properties may be described by the behavior of a few lowest on-site eigenstates with a fixed number of two particles per site. We perform a second-order quasi-degenerate perturbation theory to map the full 4-component fermion model to an effective spin-5/2-model of these states and project out states with higher or lower occupations which are separated by a large energy scale U. The effective Hamiltonian is given by[85]

$$\langle n|\hat{\mathcal{H}}_{eff}^{(2)}|n'\rangle = \frac{1}{2}\sum_{\nu}\langle n|\hat{\mathcal{H}}|\nu\rangle\langle\nu|\hat{\mathcal{H}}|n'\rangle\left[\frac{1}{E_n - E_\nu} + \frac{1}{E_{n'} - E_\nu}\right] \qquad (9.6)$$

with on-site energies E_n and the summation being performed over all intermediate states $|\nu\rangle$ with a triply and a singly occupied site. The effective Hamiltonian has generally a very complicated form for the considered alkali-models with doubly-occupation. However, the 6-dimensional on-site Hilbert-space significantly reduces computational complexity compared to the 36-dimensional full model and it may be efficiently analyzed numerically. We perform iTEBD calculations of the effective model (9.6). For the regime of moderate $U/J \lesssim 10$ we complement this analysis with DMRG calculations of the unconstrained model.

For vanishing magnetic fields $q = 0$ the on-site energy for $J \to 0$ is minimized by the pair $|1/2, 3/2\rangle$. Due to the constraint $Q_T, Q_S = 0$ and $N = 2L$ the degenerate ground state manifold for $J \to 0$ will contain as well L pairs of $|9/2, 7/2\rangle$. A finite hopping J will lift the degeneracy and stabilize a classical Neél-state formed by pairs of $|1/2, 3/2\rangle$ alternating with $|9/2, 7/2\rangle$ pairs as the ground state. For a dominating QZE $q \gg J, U$ the system enters again the BI phase formed by the on-site singlets $|9/2, 1/2\rangle$. Interestingly, an intermediate Haldane-phase with a non-local topological string order emerges as shown in Fig. 9.5.

This sequence of phases becomes clear intuitively as we map the $U \gg J$ limit with to an effective spin-1 model, associating $|1/2, 3/2\rangle$ and $|9/2, 7/2\rangle$ with $S^z = +1$ and $S^z = -1$ states, the on-site singlets $|9/2, 1/2\rangle + |7/2, 3/2\rangle$ form the $S^z = 0$ states.
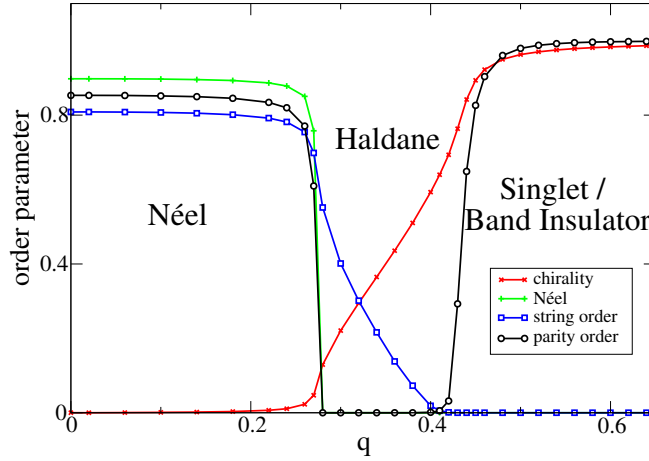
Fig. 9.6: Quadratic Zeeman coupling (measured in units of J) dependence of different order parameters along a cut of Fig. 9.5 for $U/J = 20$.

Hence, with

$$S_j^z = (n_{9/2,j} + n_{7/2,j} - n_{3/2,j} - n_{1/2,j})/2$$

we may calculate several order parameters borrowed from the typical spin-1 models: Néel order $\lim_{n\gg1}(-1)^n \langle S_j^z S_{j+n}^z \rangle$, parity order $\lim_{n\gg1}\langle e^{i\pi \sum_{j<k<j+n} S_k^z} \rangle$ and string order $\lim_{n\gg1}\langle S_j^z e^{i\pi \sum_{j<k<j+n} S_k^z} S_{j+n}^z \rangle$, are shown in Fig. 9.6 for a cut through the phase diagram at large U/J. The Haldane phase exhibits a antiferromagnetic-order diluted by defects that represent on-site singlets of the BI state that is characterized by a finite string order. We verify the topological character of the Haldane phase by monitoring the doubly degenerate entanglement spectrum [173].

As known from spin-1 models with a single-ion anisotropy [360] Néel- and Haldane phases are separated by an Ising-type phase transition. The Haldane to singlet transition is a Gaussian-type phase transition. At moderate U a Dimer-phase is realized, as discussed for the case of the $S = 3/2$-multiplet. It is separated from the Neel and singlet phases by an Gaussian and Ising-type phase transitions, respectively. Interestingly the 4-phases are expected to form a multi-critical point [50] as depicted in Fig. 9.5.

9.4   Conclusion

In summary we have shown, how a very rich phase ground-state phase diagram can be prepared as the spin-changing processes are allowed by adiabatically lowering the magnetic field and different MI states may be reached starting from a low entropy BI state. Due to interplay of spin-changing collisions and quadratic Zeeman coupling, the ground-state physics includes dimer and singlet phases for the symmetric $S = 3/2$ alkali fermion manifold and phases with antiferromagnetic and topological order for the asymmetric manifold of ^{40}K hyperfine states. The different quantum phases and phase transition may be studied without the need to change scattering lengths, just by means of controlling magnetic field and optical lattice depths.

Interestingly, Néel ordering may be revealed in Stern-Gerlach TOF experiments. After ramping up the lattice depth and decreasing the magnetic field, those sites

occupied with $|9/2, 7/2\rangle$ are immune to spin-changing collisions and, hence, in a state prepared as a Néel phase their occupation should stay maximally constant. Further studies may include the possibilities for a finite production of $M = 5/2$ and $M = -1/2$ components and examine possible timescales of the adiabatic preparation scheme.

Chapter 10

Conclusion and Outlook

In this thesis we have discussed various aspects and scenarios of strongly correlated ultracold quantum gases in low-dimensional optical lattices. A main focus was laid on recent developments in the quantum simulation of frustrated quantum magnetism and synthetic static and dynamical gauge fields. We have considered feasible setups for the experimental study of novel phenomena and analyzed the observable properties of the underlying physical models. Chapters 2-4 were devoted to an introduction to the different experimental and theoretical concepts and methods. We have first briefly introduced the main conceptual background and developments of ultracold quantum gases in chapter 2. Here we have also presented properties of the fundamental Bose-Hubbard model in low dimensions as well as details of the so called Floquet-engineering and the derivation of effective model Hamiltonians. Since the main findings of this thesis rely on large scale numerical calculations, in chapter 3 we have briefly introduced the main ideas behind exact-diagonalization and DMRG techniques and pointed out some recent developments and extensions. The power of DMRG is deeply connected to fundamental properties of quantum mechanical systems. Simultaneously such ideas from quantum information theory allow for a better understanding of the physical properties of the considered quantum states and the characterization of quantum phase transitions. We have summarized a few methods and properties, entanglement spectrum and entropy as well as the fidelity susceptibility in chapter 4. We have also studied unusual finite size scaling properties of the fidelity susceptibility for certain perturbations.

In chapter 5 we have investigated the properties of quantum emulators of frustrated quantum magnetism exemplified by the case of ultracold bosons in zig-zag optical lattices. This model, also of high relevancy for solid state physics, exhibits a very rich ground-state physics, including chiral and dimerized phases, known from corresponding spin models that we could extend to the bosonic model. In this context we have introduced an analytical method for the study of properties of frustrated quantum lattice gases at low densities. In different regimes and scenarios our findings furthermore include topological Haldane insulators for three body constraint gases or supersolid and metamagnetic phases for dipolar long-range interactions. Finally we have analyzed variations in the geometry - for the so called sawtooth ladder we found an unusual supersolid phase in the absence of long-range interactions.

In chapter 10 focused on the study of synthetic gauge fields. We have carefully analyzed interacting ultracold bosons in a two-leg square ladder geometry in the presence a homogeneous (synthetic) magnetic field. We would like to stress that for the first time we have been able to prove some previously conjectured properties of this microscopic model by an unbiased numerical approach, such as the stability

of several vortex-lattice phases or a biased ladder phase. We have illustrated the wealth of quantum phases, including also Meissner and vortex phases in both the SF and MI regime, in several representative phase diagrams for different ranges of interactions. Finally we have found an exotic quantum phenomenon connected to the vortex-lattice phases. For certain conditions, surprisingly, the boundary current may revert its circulation direction due to the spontaneously broken symmetry of the underlying quantum state.

The realization of the effective models studied in the previous chapters relies on the integration of fast degrees of freedom employed in the quantum lattice gas experiments. In chapter 7 we have reviewed the effective models, that could be generated by means of a fast modulation of on-site interactions. We have shown how the effectively generated nonlinear density dependent hopping terms allow for the study of certain correlated hopping Hubbard models relevant for cuprate superconductors. Furthermore, we presented a detailed analysis of the emergence of string an parity order in unconventional MI phases due to the simultaneous modulation of lattices and interactions.

While the gauge fields considered in chapter 5 and 10 are static, in chapter 8 we have pointed out several settings for the emulation of certain dynamical gauge fields. We have shown how density-dependent synthetic magnetic fields studied in this chapter could be engineered using modulated interactions or Raman assisted hoppings. Interestingly in one dimensional lattices DDSM allows for the study of anyon Hubbard models. In ladders and 2D square lattices DDSM leads to a non-trivial interplay between density modulations and effective magnetic fluxes in ground state and dynamical properties. We would like to note, that our first experimental proposal based on modulated interactions allows for the generation of anyon-like models without any restriction of the local particle density, while the Raman-laser setup would impose a three body hardcore constraint.

Finally, we have studied fermionic alkali spinor gases inspired by recent experimental advances. We have shown how the interplay between spin dependent interactions, spin changing collisions and a quadratic Zeeman coupling leads to a very rich ground-state physics at half filling that could be explored by means of slowly driven band- to Mott-insulator transitions. Besides of Néel and dimerized phases we have found a topological Haldane phase available for experimentally relevant parameters.

Let us now outline some possible further applications and extensions of the models and setups studied in this thesis. An important class of extensions can be summarized as variations of geometry or dimensionality. But also experimentally relevant aspects such as different interaction regimes, temperature or dynamical properties will provide important and non-trivial subjects of further work.

Most of the models studied in this thesis are bound to one dimensional chains or quasi one dimensional two-leg ladder geometries. Typically a study of a full two dimensional extensions of the models of frustrated quantum magnetism or artificial gauge fields with classical methods will remain elusive and, hence, be a task of the upcoming quantum simulation experiments. But already the study of three- or four- leg ladder geometries, feasible with DMRG and bosonization methods, may involve interesting phenomena and be of high experimental relevancy as can be seen in [273, 286]. As recently investigated in Ref.[309] bosonic atoms in three leg-ladders exhibit already in the hardcore regime a a very rich ground-state physics.

Generally, the possible ground-state phases of N-leg ladder bosonic systems remain to be explored, in particular the generalization of vortex-lattice phases and their connection to (fractional) quantum Hall physics. An interesting starting point could be already the weak coupling regime, which we have shown to provide an important insight for the two-leg ladder case.

Also the fate of the BLP phase in multi-leg ladder remains unclear. It would be useful to transfer the dilute limit analysis to N-leg ladder systems, which allowed for a prediction of the BLP phase in the two-leg ladder. In some cases multiply degenerate dispersion minima could result in a more complex ground-state diagram in the dilute limit. Furthermore, the connection of the BLP phase in the weak coupling regime should be analyzed. Including classical density fluctuations in the weak-coupling analysis of chapter 10 could be useful to analyze the experimental observability of the BLP phase, extending the study of Ref.[298].

Since synthetic dimension experiments constitute a very promising realization of synthetic gauge fields in N-leg ladder systems, the role of inter-particle interactions in strongly-correlated gases, both for bosons and fermions, has to be explored. Both rung-interactions, or for alkali-species also the exotic spin-changing collisions, should be considered. For the case of fermions recently interesting magnetic crystal phases with a relationship to the quantum Hall effect have been studied[302, 303].

Inter-ladder coupling offers the interesting possibility to perform a controlled cross-dimensional transition from a 1D to a 2D scenario. Within N-leg ladder calculations or a cluster mean-field approaches (such as shown in chapter 3) the residual 2D couplings between chains and ladders could be explored. In particular the stability with respect to residual 2D couplings of the interesting vortex-lattice phases, but also CSF and 2SF-phases in triangular ladders, could be examined.

Geometric variations may lead to the emergence of completely new phenomena. In chapter 5 we have studied this for sawtooth or generally railroad-trestle models. The connection between the observed supersolid and chiral phases should be analyzed in detail in this context. First numerical simulations indicate that, weakening the $t'' > 0$-bond of Eq.(5.44) the CSF phase survives almost to the sawtooth limit $t'' \to 0$, where a transition to the supersolid phase is observed. Interestingly the SS phase remains stable for a large regime of an ferromagnetic upper leg coupling $t'' < 0$. In this regime also a dilute limit picture of supersolid phases might be obtained for certain conditions.

Extensions of the study of DDSM could as well involve the analysis of generalized lattices, including zig-zag lattices. As a result, we expect that as a function of density and interactions the system will develop geometric frustration, as indicated by recent results [361]. The detailed investigation of 2D systems will be very interesting and could involve density induced topological phases, such a recently studied in Ref.[362].

Further possible scenarios for DDSM include density-dependent non-Abelian gauge fields, or dynamical gauge field realizations for for binary gases, e.g. two Fermi components or even Bose-Fermi mixtures. The simulation of situations in which e.g. the Peierls phase for the fermions depends on the density of bosons will allow for the study of the connection between the resulting models and lattice gauge theories relevant for high energy physics or condensed matter theory.

Bibliography

[1] J. Struck et al. "Quantum Simulation of Frustrated Classical Magnetism in Triangular Optical Lattices". In: *Science* 333.6045 (2011), pp. 996–999.

[2] M. Atala et al. "Observation of chiral currents with ultracold atoms in bosonic ladders". In: *Nature Phys.* 10 (2014), p. 588.

[3] P. Anderson. "More is different". In: *Science* 393 (1972), p. 4047.

[4] C. C. Bradley et al. "Evidence of Bose-Einstein condensation in an atomic gas with attractive interactions". In: *Physical Review Letters* 75.9 (1995), p. 1687.

[5] K. B. Davis et al. "Bose-Einstein condensation in a gas of sodium atoms". In: *Physical Review Letters* 75.22 (1995), p. 3969.

[6] M. H. Anderson et al. "Observation of Bose-Einstein condensation in a dilute atomic vapor". In: *science* 269.5221 (1995), pp. 198–201.

[7] D. Jaksch et al. "Cold bosonic atoms in optical lattices". In: *Physical Review Letters* 81.15 (1998), pp. 3108–3111.

[8] M. Greiner et al. "Quantum phase transition from a superfluid to a Mott insulator in a gas of ultracold atoms". In: *nature* 415.6867 (2002), pp. 39–44.

[9] B. Paredes et al. "Tonks–Girardeau gas of ultracold atoms in an optical lattice". In: *Nature* 429.6989 (2004), pp. 277–281.

[10] R. Jördens et al. "A Mott insulator of fermionic atoms in an optical lattice". In: *Nature* 455.7210 (2008), pp. 204–207.

[11] U. Schneider et al. "Metallic and insulating phases of repulsively interacting fermions in a 3D optical lattice". In: *Science* 322.5907 (2008), pp. 1520–1525.

[12] F. Jendrzejewski et al. "Three-dimensional localization of ultracold atoms in an optical disordered potential". In: *Nature Physics* 8.5 (2012), pp. 398–403.

[13] M. Aidelsburger et al. "Realization of the Hofstadter hamiltonian with ultracold atoms in optical lattices". In: *Physical Review Letters* 111 (2013), p. 185301.

[14] H. Miyake et al. "Realizing the Harper Hamiltonian with Laser-Assisted Tunneling in Optical Lattices". In: *Physical Review Letters* 111 (2013), p. 185302.

[15] B. Yan et al. "Observation of dipolar spin-exchange interactions with lattice-confined polar molecules". In: *Nature* 501.7468 (2013), pp. 521–525.

[16] S. Baier et al. "Extended Bose-Hubbard Models with Ultracold Magnetic Atoms". In: *arXiv preprint arXiv:1507.03500* (2015).

[17] M. Schreiber et al. "Observation of many-body localization of interacting fermions in a quasirandom optical lattice". In: *Science* 349.6250 (2015), pp. 842–845.

[18] J. G. Bednorz and K. A. Müller. "Possible highT c superconductivity in the Ba- La- Cu- O system". In: *Zeitschrift für Physik B Condensed Matter* 64.2 (1986), pp. 189–193.

[19] K. v. Klitzing, G. Dorda, and M. Pepper. "New method for high-accuracy determination of the fine-structure constant based on quantized Hall resistance". In: *Physical Review Letters* 45.6 (1980), p. 494.

[20] B. Lücke et al. "Twin matter waves for interferometry beyond the classical limit". In: *Science* 334.6057 (2011), pp. 773–776.

[21] A. Y. Kitaev. "Fault-tolerant quantum computation by anyons". In: *Annals of Physics* 303.1 (2003), pp. 2–30.

[22] M. Troyer and U.-J. Wiese. "Computational complexity and fundamental limitations to fermionic quantum Monte Carlo simulations". In: *Physical Review Letters* 94.17 (2005), p. 170201.

[23] U. Schollwöck. "The density-matrix renormalization group in the age of matrix product states". In: *Annals of Physics* 326.1 (2011), pp. 96–192.

[24] R. P. Feynman. "Simulating physics with computers". In: *International journal of theoretical physics* 21.6/7 (1982), pp. 467–488.

[25] J. S. Krauser et al. "Coherent multi-flavour spin dynamics in a fermionic quantum gas". In: *Nature Physics* 8.11 (2012), pp. 813–818.

[26] O. Boada et al. "Quantum simulation of an extra dimension". In: *Physical Review Letters* 108.13 (2012), p. 133001.

[27] J. I. Cirac, P. Maraner, and J. K. Pachos. "Cold atom simulation of interacting relativistic quantum field theories". In: *Physical Review Letters* 105.19 (2010), p. 190403.

[28] L. Tagliacozzo et al. "Simulation of non-Abelian gauge theories with optical lattices". In: *Nature communications* 4 (2013).

[29] I. Bloch, J. Dalibard, and W. Zwerger. "Many-body physics with ultracold gases". In: *Reviews of Modern Physics* 80 (2008), pp. 885–964.

[30] D. Jaksch and P. Zoller. "The cold atom Hubbard toolbox". In: *Annals of physics* 315.1 (2005), pp. 52–79.

[31] J. I. Cirac and P. Zoller. "Quantum computations with cold trapped ions". In: *Physical Review Letters* 74.20 (1995), p. 4091.

[32] R. Blatt and C. Roos. "Quantum simulations with trapped ions". In: *Nature Physics* 8.4 (2012), pp. 277–284.

[33] P. Schindler et al. "A quantum information processor with trapped ions". In: *New Journal of Physics* 15.12 (2013), p. 123012.

[34] S. Murmann et al. "Two Fermions in a double well: Exploring a fundamental building block of the Hubbard model". In: *Physical Review Letters* 114.8 (2015), p. 080402.

[35] T. Giamarchi. *Quantum physics in one dimension*. Internat. Ser. Mono. Phys. Oxford: Clarendon Press, 2004.

[36] S. Greschner, A. Kolezhuk, and T. Vekua. "Fidelity susceptibility and conductivity of the current in one-dimensional lattice models with open or periodic boundary conditions". In: *Physical Review B* 88.19 (2013), p. 195101.

[37] A. Kolezhuk et al. "Frustrated spin chains in strong magnetic field: Dilute two-component Bose gas regime". In: *Physical Review B* 85.6 (2012), p. 064420.

[38] S. Greschner, L. Santos, and T. Vekua. "Ultracold bosons in zig-zag optical lattices". In: *Physical Review A* 87.3 (2013), p. 033609.

[39] M. Azimi et al. "Helical multiferroics for electric field controlled quantum information processing". In: *Physical Review B* 89.2 (2014), p. 024424.

[40] T. Mishra, S. Greschner, and L. Santos. "Polar molecules in frustrated triangular ladders". In: *Physical Review A* 91.4 (2015), p. 043614.

[41] T. Mishra, S. Greschner, and L. Santos. "Frustration-induced supersolids in the absence of inter-site interactions". In: *Physical Review B* 92.19 (2015), p. 195149.

[42] M. Piraud et al. "Vortex and Meissner phases of strongly interacting bosons on a two-leg ladder". In: *Physical Review B* 91.14 (2015), p. 140406.

[43] S. Greschner et al. "Spontaneous increase of magnetic flux and chiral-current reversal in bosonic ladders: Swimming against the tide". In: *Physical Review Letters* 115.19 (2015), p. 190402.

[44] Á. Rapp, X. Deng, and L. Santos. "Ultracold lattice gases with periodically modulated interactions". In: *Physical Review Letters* 109.20 (2012), p. 203005.

[45] M. Di Liberto et al. "Quantum simulation of correlated-hopping models with fermions in optical lattices". In: *Physical Review A* 89.1 (2014), p. 013624.

[46] S. Greschner, L. Santos, and D. Poletti. "Exploring Unconventional Hubbard Models with Doubly Modulated Lattice Gases". In: *Physical Review Letters* 113.18 (2014), p. 183002.

[47] S. Greschner et al. "Density-Dependent Synthetic Gauge Fields Using Periodically Modulated Interactions". In: *Physical Review Letters* 113.21 (2014), p. 215303.

[48]   S. Greschner and L. Santos. "Anyon Hubbard Model in One-Dimensional Optical Lattices". In: *Physical Review Letters* 115.5 (2015), p. 053002.

[49]   S. Greschner et al. "Density-dependent synthetic magnetism for ultracold atoms in optical lattices". In: *Physical Review B* 92 (11 2015), p. 115120.

[50]   J. Jaramillo, S. Greschner, and T. Vekua. "Band-to-Mott-insulator transformations in four-component alkali-metal fermions at half-filling". In: *Physical Review A* 88.4 (2013), p. 043616.

[51]   R. Grimm, M. Weidemüller, and Y. B. Ovchinnikov. "Optical Dipole Traps for Neutral Atoms". In: *Advances in Atomic Molecular and Optical Physics* 42 (2000), pp. 95–170.

[52]   M. Cazalilla et al. "One dimensional bosons: From condensed matter systems to ultracold gases". In: *Reviews of Modern Physics* 83.4 (2011), p. 1405.

[53]   E. H. Lieb and W. Liniger. "Exact analysis of an interacting Bose gas. I. The general solution and the ground state". In: *Physical Review* 130.4 (1963), p. 1605.

[54]   H. Feshbach. "Unified theory of nuclear reactions". In: *Annals of Physics* 5.4 (1958), pp. 357–390.

[55]   E. Tiesinga, B. Verhaar, and H. Stoof. "Threshold and resonance phenomena in ultracold ground-state collisions". In: *Physical Review A* 47.5 (1993), p. 4114.

[56]   P. Courteille et al. "Observation of a Feshbach resonance in cold atom scattering". In: *Physical Review Letters* 81.1 (1998), p. 69.

[57]   S. Inouye et al. "Observation of Feshbach resonances in a Bose–Einstein condensate". In: *Nature* 392.6672 (1998), pp. 151–154.

[58]   P. Fedichev, M. Reynolds, and G. Shlyapnikov. "Three-body recombination of ultracold atoms to a weakly bound s level". In: *Physical Review Letters* 77.14 (1996), p. 2921.

[59]   M. Theis et al. "Tuning the scattering length with an optically induced Feshbach resonance". In: *Physical Review Letters* 93.12 (2004), p. 123001.

[60]   W. D. Phillips. "Nobel Lecture: Laser cooling and trapping of neutral atoms". In: *Reviews of Modern Physics* 70.3 (1998), p. 721.

[61]   B. DeMarco and D. S. Jin. "Onset of Fermi degeneracy in a trapped atomic gas". In: *Science* 285.5434 (1999), pp. 1703–1706.

[62]   K. Aikawa et al. "Reaching Fermi degeneracy via universal dipolar scattering". In: *Physical Review Letters* 112.1 (2014), p. 010404.

[63]   A. Leanhardt et al. "Cooling Bose-Einstein condensates below 500 picokelvin". In: *Science* 301.5639 (2003), pp. 1513–1515.

[64]   D. McKay and B. DeMarco. "Cooling in strongly correlated optical lattices: prospects and challenges". In: *Reports on Progress in Physics* 74.5 (2011), p. 054401.

[65]   M. Fattori et al. "Demagnetization cooling of a gas". In: *Nature Physics* 2.11 (2006), pp. 765–768.

[66]   C. Becker et al. "Ultracold quantum gases in triangular optical lattices". In: *NJP* 12 (2010).

[67]   G.-B. Jo et al. "Ultracold atoms in a tunable optical kagome lattice". In: *Physical Review Letters* 108.4 (2012), p. 045305.

[68]   L. Tarruell et al. "Creating, moving and merging Dirac points with a Fermi gas in a tunable honeycomb lattice". In: *Nature* 483.7389 (2012), pp. 302–305.

[69]   W. S. Bakr et al. "A quantum gas microscope for detecting single atoms in a Hubbard-regime optical lattice". In: *Nature* 462.7269 (2009), pp. 74–77.

[70]   N. D. Mermin and H. Wagner. "Absence of ferromagnetism or antiferromagnetism in one- or two-dimensional isotropic Heisenberg models". In: *Physical Review Letters* 17.22 (1966), p. 1133.

[71]   J. Freericks and H. Monien. "Strong-coupling expansions for the pure and disordered Bose-Hubbard model". In: *Physical Review B* 53.5 (1996), p. 2691.

[72]   T. D. Kühner, S. R. White, and H. Monien. "One-dimensional Bose-Hubbard model with nearest-neighbor interaction". In: *Physical Review B* 61.18 (2000), p. 12474.

[73] B. Capogrosso-Sansone et al. "Monte Carlo study of the two-dimensional Bose-Hubbard model". In: *Physical Review A* 77.1 (2008), p. 015602.

[74] V. L. Berezinskii. "Destruction of long-range order in one-dimensional and two-dimensional systems with a continuous symmetry group. II. Quantum systems". In: *Sov. Phys. JETP* 34 (1972), p. 610.

[75] J. M. Kosterlitz and D. J. Thouless. "Ordering, metastability and phase transitions in two-dimensional systems". In: *Journal of Physics C* 6 (1973), p. 1181.

[76] M. Cazalilla. "Bosonizing one-dimensional cold atomic gases". In: *Journal of Physics B: Atomic, Molecular and Optical Physics* 37.7 (2004), S1.

[77] E. Altman, E. Demler, and M. D. Lukin. "Probing many-body states of ultracold atoms via noise correlations". In: *Physical Review A* 70.1 (2004), p. 013603.

[78] M. Greiner et al. "Exploring phase coherence in a 2D lattice of Bose-Einstein condensates". In: *Physical Review Letters* 87.16 (2001), p. 160405.

[79] M. Köhl et al. "Fermionic atoms in a three dimensional optical lattice: Observing Fermi surfaces, dynamics, and interactions". In: *Physical Review Letters* 94.8 (2005), p. 080403.

[80] J. F. Sherson et al. "Single-atom-resolved fluorescence imaging of an atomic Mott insulator". In: *Nature* 467.7311 (2010), pp. 68–72.

[81] M. Endres et al. "Observation of correlated particle-hole pairs and string order in low-dimensional Mott insulators". In: *Science* 334.6053 (2011), pp. 200–203.

[82] M. Cheneau et al. "Light-cone-like spreading of correlations in a quantum many-body system". In: *Nature* 481.7382 (2012), pp. 484–487.

[83] A. Imambekov, M. Lukin, and E. Demler. "Spin-exchange interactions of spin-one bosons in optical lattices: Singlet, nematic, and dimerized phases". In: *Physical Review A* 68.6 (2003), p. 063602.

[84] D. M. Stamper-Kurn and M. Ueda. "Spinor Bose gases: Symmetries, magnetism, and quantum dynamics". In: *Reviews of Modern Physics* 85.3 (2013), p. 1191.

[85] K. Rodríguez. "Non-equilibrium Dynamics and Quantum Magnetism in 1D Optical Lattices". PhD thesis. Technische Informationsbibliothek und Universitätsbibliothek Hannover, 2011.

[86] M. A. Cazalilla and A. M. Rey. "Ultracold Fermi gases with emergent SU (N) symmetry". In: *Reports on Progress in Physics* 77.12 (2014), p. 124401.

[87] T. Lahaye et al. "The physics of dipolar bosonic quantum gases". In: *Reports on Progress in Physics* 72.12 (2009), p. 126401.

[88] M. Baranov et al. "Condensed matter theory of dipolar quantum gases". In: *Chemical Reviews* 112.9 (2012), pp. 5012–5061.

[89] A. Griesmaier et al. "Bose-Einstein condensation of chromium". In: *Physical Review Letters* 94.16 (2005), p. 160401.

[90] M. Lu et al. "Strongly dipolar Bose-Einstein condensate of dysprosium". In: *Physical Review Letters* 107.19 (2011), p. 190401.

[91] K. Aikawa et al. "Bose-Einstein condensation of erbium". In: *Physical Review Letters* 108.21 (2012), p. 210401.

[92] T. F. Gallagher and P. Pillet. "Dipole–dipole interactions of Rydberg atoms". In: *Advances in Atomic, Molecular, and Optical Physics* 56 (2008), pp. 161–218.

[93] J. Balewski et al. "Coupling a single electron to a Bose-Einstein condensate". In: *Nature* 502.7473 (2013), pp. 664–667.

[94] A. De Paz et al. "Nonequilibrium quantum magnetism in a dipolar lattice gas". In: *Physical Review Letters* 111.18 (2013), p. 185305.

[95] L. Santos, G. Shlyapnikov, and M. Lewenstein. "Roton-maxon spectrum and stability of trapped dipolar Bose-Einstein condensates". In: *Physical Review Letters* 90.25 (2003), p. 250403.

[96] T. Lahaye et al. "d-wave collapse and explosion of a dipolar Bose-Einstein condensate". In: *Physical Review Letters* 101.8 (2008), p. 080401.

[97] H. Kadau et al. "Observing the Rosensweig instability of a quantum ferrofluid". In: *arXiv preprint arXiv:1508.05007* (2015).

[98]   E. Dalla Torre, E. Berg, and E. Altman. "Hidden order in 1D bose insulators". In: *Physical Review Letters* 97.26 (2006), p. 260401.

[99]   E. Berg et al. "Rise and fall of hidden string order of lattice bosons". In: *Physical Review B* 77.24 (2008), p. 245119.

[100]   X. Deng et al. "Polar bosons in one-dimensional disordered optical lattices". In: *Physical Review B* 87.19 (2013), p. 195101.

[101]   W. Chen, K. Hida, and B. Sanctuary. "Ground-state phase diagram of S= 1 XXZ chains with uniaxial single-ion-type anisotropy". In: *Physical Review B* 67.10 (2003), p. 104401.

[102]   M. F. Maghrebi, Z.-X. Gong, and A. V. Gorshkov. "Continuous symmetry breaking and a new universality class in 1D long-range interacting quantum systems". In: *arXiv preprint arXiv:1510.01325* (2015).

[103]   H. Büchler, A. Micheli, and P. Zoller. "Three-body interactions with cold polar molecules". In: *Nature Physics* 3.10 (2007), pp. 726–731.

[104]   F. Verstraete, M. M. Wolf, and J. I. Cirac. "Quantum computation and quantum-state engineering driven by dissipation". In: *Nature physics* 5.9 (2009), pp. 633–636.

[105]   Y. Lin et al. "Dissipative production of a maximally entangled steady state of two quantum bits". In: *Nature* 504.7480 (2013), pp. 415–418.

[106]   A. Daley et al. "Atomic three-body loss as a dynamical three-body interaction". In: *Physical Review Letters* 102.4 (2009), p. 40402.

[107]   M. Mark et al. "Preparation and Spectroscopy of a Metastable Mott-Insulator State with Attractive Interactions". In: *Physical Review Letters* 108.21 (2012), p. 215302.

[108]   N. Syassen et al. "Strong dissipation inhibits losses and induces correlations in cold molecular gases". In: *Science* 320.5881 (2008), pp. 1329–1331.

[109]   C. Cohen-Tannoudji et al. "Atom-Photon Interactions: Basic Processes and Applications". In: *Physics Today* 45 (1992), p. 115.

[110]   I. Titvinidze et al. "Magnetism and domain formation in SU (3)-symmetric multi-species Fermi mixtures". In: *New Journal of Physics* 13.3 (2011), p. 035013.

[111]   L. Bonnes and S. Wessel. "Pair superfluidity of three-body constrained bosons in two dimensions". In: *Physical Review Letters* 106.18 (2011), p. 185302.

[112]   Y.-C. Chen, K.-K. Ng, and M.-F. Yang. "Quantum phase transitions in the attractive extended Bose-Hubbard model with a three-body constraint". In: *Physical Review B* 84.9 (2011), p. 092503.

[113]   D. Petrov. "Elastic multibody interactions on a lattice". In: *Physical Review A* 90.2 (2014), p. 021601.

[114]   A. J. Daley and J. Simon. "Effective three-body interactions via photon-assisted tunneling in an optical lattice". In: *Physical Review A* 89.5 (2014), p. 053619.

[115]   A. Polkovnikov et al. "*Colloquium*: Nonequilibrium dynamics of closed interacting quantum systems". In: *Reviews of Modern Physics* 83 (3 2011), pp. 863–883.

[116]   T. Kinoshita, T. Wenger, and D. S. Weiss. "A quantum Newton's cradle". In: *Nature* 440.7086 (2006), pp. 900–903.

[117]   M. Gring et al. "Relaxation and prethermalization in an isolated quantum system". In: *Science* 337.6100 (2012), pp. 1318–1322.

[118]   M. Rigol, V. Dunjko, and M. Olshanii. "Thermalization and its mechanism for generic isolated quantum systems". In: *Nature* 452.7189 (2008), pp. 854–858.

[119]   P. W. Anderson. "Absence of diffusion in certain random lattices". In: *Physical review* 109.5 (1958), p. 1492.

[120]   J. Billy et al. "Direct observation of Anderson localization of matter waves in a controlled disorder". In: *Nature* 453.7197 (2008), pp. 891–894.

[121]   M. Robert-De-Saint-Vincent et al. "Anisotropic 2d diffusive expansion of ultracold atoms in a disordered potential". In: *Physical Review Letters* 104.22 (2010), p. 220602.

[122]   L. Barbiero et al. "Out-of-equilibrium states and quasi-many-body localization in polar lattice gases". In: *Physical Review B* 92 (18 2015), p. 180406.

[123] T. W. Kibble. "Topology of cosmic domains and strings". In: *Journal of Physics A: Mathematical and General* 9.8 (1976), p. 1387.

[124] W. Zurek. "Cosmological experiments in superfluid helium?" In: *Nature* 317.6037 (1985), pp. 505–508.

[125] W. H. Zurek, U. Dorner, and P. Zoller. "Dynamics of a quantum phase transition". In: *Physical Review Letters* 95.10 (2005), p. 105701.

[126] V. Ruutu et al. "Vortex formation in neutron-irradiated superfluid 3He as an analogue of cosmological defect formation". In: (1996).

[127] S. Ulm et al. "Observation of the Kibble–Zurek scaling law for defect formation in ion crystals". In: *Nature communications* 4 (2013).

[128] C. N. Weiler et al. "Spontaneous vortices in the formation of Bose–Einstein condensates". In: *Nature* 455.7215 (2008), pp. 948–951.

[129] G. Lamporesi et al. "Spontaneous creation of Kibble-Zurek solitons in a Bose-Einstein condensate". In: *Nature Physics* 9.10 (2013), pp. 656–660.

[130] P. Würtz et al. "Experimental demonstration of single-site addressability in a two-dimensional optical lattice". In: *Physical Review Letters* 103.8 (2009), p. 080404.

[131] S. Natu, K. R. Hazzard, and E. J. Mueller. "Local versus global equilibration near the bosonic Mott-insulator–superfluid transition". In: *Physical Review Letters* 106.12 (2011), p. 125301.

[132] W. Bakr et al. "Probing the superfluid–to–mott insulator transition at the single-atom level". In: *Science* 329.5991 (2010), pp. 547–550.

[133] H. Lignier et al. "Dynamical control of matter-wave tunneling in periodic potentials". In: *Physical Review Letters* 99.22 (2007), p. 220403.

[134] A. Eckardt, C. Weiss, and M. Holthaus. "Superfluid-insulator transition in a periodically driven optical lattice". In: *Physical Review Letters* 95.26 (2005), p. 260404.

[135] E. Kierig et al. "Single-particle tunneling in strongly driven double-well potentials". In: *Physical Review Letters* 100.19 (2008), p. 190405.

[136] A. Zenesini et al. "Coherent control of dressed matter waves". In: *Physical Review Letters* 102.10 (2009), p. 100403.

[137] J. Struck et al. "Tunable Gauge Potential for Neutral and Spinless Particles in Driven Optical Lattices". In: *Physical Review Letters* 108.22 (2012), p. 225304.

[138] C. V. Parker, L.-C. Ha, and C. Chin. "Direct observation of effective ferromagnetic domains of cold atoms in a shaken optical lattice". In: *Nature Physics* 9.12 (2013), pp. 769–774.

[139] J. Gong, L. Morales-Molina, and P. Hänggi. "Many-body coherent destruction of tunneling". In: *Physical Review Letters* 103.13 (2009), p. 133002.

[140] G. Floquet. "Sur les équations différentielles linéaires à coefficients périodiques". In: *Annales scientifiques de l'École Normale Supérieure* 12 (1883), pp. 47–88.

[141] J. H. Shirley. "Solution of the Schrödinger equation with a Hamiltonian periodic in time". In: *Physical Review* 138.4B (1965), B979.

[142] P. Hänggi. "Driven quantum systems". In: *Quantum Transport and Dissipation, Wiley-VCH, Weinheim* (1998), pp. 249–286.

[143] P. Hauke. "Quantum simulations with ultracold atoms: Beyond standard optical lattices". PhD thesis. ICFO - The Institute of Photonic Sciences, 2014.

[144] R. Ma et al. "Photon-assisted tunneling in a biased strongly correlated Bose gas". In: *Physical Review Letters* 107.9 (2011), p. 095301.

[145] G. Jotzu et al. "Experimental realization of the topological Haldane model with ultracold fermions". In: *Nature* 515.7526 (2014), pp. 237–240.

[146] N. Goldman and J. Dalibard. "Periodically driven quantum systems: Effective hamiltonians and engineered gauge fields". In: *Physical Review X* 4.3 (2014), p. 031027.

[147] M. Aidelsburger. "Artificial gauge fields with ultracold atoms in optical lattices". PhD thesis. Ludwig Maximilian University, 2015.

[148] M. Aidelsburger et al. "Measuring the Chern number of Hofstadter bands with ultracold bosonic atoms". In: *Nature Physics* 11.2 (2015), pp. 162–166.

[149] M. M. Maricq. "Application of average Hamiltonian theory to the NMR of solids". In: *Physical Review B* 25.11 (1982), p. 6622.

[150] A. Eckardt and M. Holthaus. "AC-induced superfluidity". In: *EPL (Europhysics Letters)* 80.5 (2007), p. 50004.

[151] D. Poletti and C. Kollath. "Slow quench dynamics of periodically driven quantum gases". In: *Physical Review A* 84.1 (2011), p. 013615.

[152] W. H. Press. *Numerical recipes 3rd edition: The art of scientific computing*. Cambridge university press, 2007.

[153] *LAPACK - Linear Algebra PACKage*. URL: http://www.netlib.org/lapack/.

[154] A. Weiße and H. Fehske. "Exact Diagonalization Techniques". In: *Computational Many-Particle Physics* (2008), pp. 529–544.

[155] K. Okamoto and K. Nomura. "Fluid-dimer critical point in S= 12 antiferromagnetic Heisenberg chain with next nearest neighbor interactions". In: *Physics Letters A* 169.6 (1992), pp. 433–437.

[156] P. Nataf and F. Mila. "Exact Diagonalization of Heisenberg SU (N) Models". In: *Physical Review Letters* 113.12 (2014), p. 127204.

[157] E. K. Gross and R. M. Dreizler. *Density functional theory*. Vol. 337. Springer Science & Business Media, 2013.

[158] R. B. Laughlin. "Anomalous quantum Hall effect: an incompressible quantum fluid with fractionally charged excitations". In: *Physical Review Letters* 50.18 (1983), p. 1395.

[159] D. S. Rokhsar and B. Kotliar. "Gutzwiller projection for bosons". In: *Physical Review B* 44.18 (1991), p. 10328.

[160] G. Vidal. "Efficient simulation of one-dimensional quantum many-body systems". In: *Physical Review Letters* 93.4 (2004), p. 040502.

[161] F. Verstraete and J. I. Cirac. "Renormalization algorithms for quantum-many body systems in two and higher dimensions". In: *arXiv preprint cond-mat/0407066* (2004).

[162] F. Verstraete, J. J. Garcia-Ripoll, and J. I. Cirac. "Matrix product density operators: simulation of finite-temperature and dissipative systems". In: *Physical Review Letters* 93.20 (2004), p. 207204.

[163] I. P. McCulloch. "From density-matrix renormalization group to matrix product states". In: *Journal of Statistical Mechanics: Theory and Experiment* 2007.10 (2007), P10014.

[164] F. Verstraete and J. I. Cirac. "Continuous matrix product states for quantum fields". In: *Physical Review Letters* 104.19 (2010), p. 190405.

[165] N. Schuch, D. Pérez-García, and I. Cirac. "Classifying quantum phases using matrix product states and projected entangled pair states". In: *Physical Review B* 84.16 (2011), p. 165139.

[166] I. Affleck et al. "Rigorous results on valence-bond ground states in antiferromagnets". In: *Physical Review Letters* 59.7 (1987), pp. 799–802.

[167] C. K. Majumdar and D. K. Ghosh. "On Next-Nearest-Neighbor Interaction in Linear Chain. I". In: *Journal of Mathematical Physics* 10.8 (1969), pp. 1388–1398.

[168] S. R. White. "Density matrix formulation for quantum renormalization groups". In: *Physical Review Letters* 69.19 (1992), p. 2863.

[169] S. Rommer and S. Östlund. "Class of ansatz wave functions for one-dimensional spin systems and their relation to the density matrix renormalization group". In: *Physical Review B* 55.4 (1997), pp. 2164–2181.

[170] S. R. White and D. A. Huse. "Numerical renormalization-group study of low-lying eigenstates of the antiferromagnetic S= 1 Heisenberg chain". In: *Physical Review B* 48.6 (1993), p. 3844.

[171] M. P. Zaletel et al. "Chiral bosonic Mott insulator on the frustrated triangular lattice". In: *Physical Review B* 89.15 (2014), p. 155142.

[172] P. Calabrese and J. Cardy. "Entanglement entropy and quantum field theory". In: *Journal of Statistical Mechanics: Theory and Experiment* 2004.06 (2004), P06002.

[173] F. Pollmann et al. "Entanglement spectrum of a topological phase in one dimension". In: *Physical Review B* 81.6 (2010), p. 064439.

[174] X. Deng and L. Santos. "Entanglement spectrum of one-dimensional extended Bose-Hubbard models". In: *Physical Review B* 84.8 (2011), p. 085138.

[175] I. P. McCulloch. "Infinite size density matrix renormalization group, revisited". In: *arXiv preprint arXiv:0804.2509* (2008).

[176] E. Jeckelmann. "Density-Matrix Renormalization Group Algorithms". In: *Computational Many-Particle Physics* (2008), pp. 597–618.

[177] P. Pippan, S. R. White, and H. G. Evertz. "Efficient matrix-product state method for periodic boundary conditions". In: *Physical Review B* 81.8 (2010), p. 081103.

[178] G. Vidal. "Classical simulation of infinite-size quantum lattice systems in one spatial dimension". In: *Physical Review Letters* 98.7 (2007), p. 070201.

[179] S. Yan, D. A. Huse, and S. R. White. "Spin-liquid ground state of the S= 1/2 Kagome Heisenberg antiferromagnet". In: *Science* 332.6034 (2011), pp. 1173–1176.

[180] S. Depenbrock, I. P. McCulloch, and U. Schollwoeck. "Nature of the spin-liquid ground state of the s= 1/2 Heisenberg model on the kagome lattice". In: *Physical Review Letters* 109.6 (2012), p. 067201.

[181] E. S. Sørensen. "Parity, precision and spin inversion within the density matrix renormalization group". In: *Journal of Physics: Condensed Matter* 10.47 (1998), p. 10655.

[182] I. P. McCulloch and M. Gulácsi. "The non-Abelian density matrix renormalization group algorithm". In: *EPL (Europhysics Letters)* 57.6 (2002), p. 852.

[183] S. Singh, H.-Q. Zhou, and G. Vidal. "Simulation of one-dimensional quantum systems with a global SU (2) symmetry". In: *New Journal of Physics* 12.3 (2010), p. 033029.

[184] D. Porras, F. Verstraete, and J. I. Cirac. "Renormalization algorithm for the calculation of spectra of interacting quantum systems". In: *Physical Review B* 73.1 (2006), p. 014410.

[185] G. Vidal. "Efficient classical simulation of slightly entangled quantum computations". In: *Physical Review Letters* 91.14 (2003), p. 147902.

[186] A. J. Daley et al. "Time-dependent density-matrix renormalization-group using adaptive effective Hilbert spaces". In: *Journal of Statistical Mechanics: Theory and Experiment* 2004.04 (2004), P04005.

[187] S. Furukawa, M. Sato, and S. Onoda. "Chiral order and electromagnetic dynamics in one-dimensional multiferroic cuprates". In: *Physical Review Letters* 105.25 (2010), p. 257205.

[188] A. E. Feiguin and S. R. White. "Finite-temperature density matrix renormalization using an enlarged Hilbert space". In: *Physical Review B* 72.22 (2005), p. 220401.

[189] C. Karrasch and J. Moore. "Luttinger liquid physics from the infinite-system density matrix renormalization group". In: *Physical Review B* 86.15 (2012), p. 155156.

[190] C. Karrasch, J. Bardarson, and J. Moore. "Finite-temperature dynamical density matrix renormalization group and the drude weight of spin-1/2 chains". In: *Physical Review Letters* 108.22 (2012), p. 227206.

[191] C. Karrasch, D. Kennes, and F. Heidrich-Meisner. "Spin and thermal conductivity of quantum spin chains and ladders". In: *Physical Review B* 91.11 (2015), p. 115130.

[192] T. Oguchi. "A theory of antiferromagnetism, II". In: *Progress of Theoretical Physics* 13.2 (1955), pp. 148–159.

[193] D. Huerga, J. Dukelsky, and G. E. Scuseria. "Composite boson mapping for lattice boson systems". In: *Physical Review Letters* 111.4 (2013), p. 045701.

[194] D. Huerga et al. "Chiral phases of two-dimensional hard-core bosons with frustrated ring exchange". In: *Physical Review B* 89.9 (2014), p. 094401.

[195] J. Zhao et al. "Composite fermion-boson mapping for fermionic lattice models". In: *Journal of Physics: Condensed Matter* 26.45 (2014), p. 455601.

[196] R. Suzuki and A. Koga. "Cluster mean-field approach with density matrix renormalization group: Application to the hard-core bosonic Hubbard model on a triangular lattice". In: *JPS Conf. Proc.* 3 (2013), p. 016005.

[197]   L. Amico et al. "Entanglement in many-body systems". In: *Reviews of Modern Physics* 80 (2008), p. 517.

[198]   P. Hyllus et al. "Fisher information and multiparticle entanglement". In: *Physical Review A* 85.2 (2012), p. 022321.

[199]   J. Eisert, M. Cramer, and M. Plenio. "Area laws for the entanglement entropy — a review". In: *Rev. Mod. Phys* 82 (2010), p. 277.

[200]   H. Li and F. D. M. Haldane. "Entanglement spectrum as a generalization of entanglement entropy: Identification of topological order in non-abelian fractional quantum hall effect states". In: *Physical Review Letters* 101.1 (2008), p. 010504.

[201]   D. Poilblanc. "Entanglement spectra of quantum Heisenberg ladders". In: *Physical Review Letters* 105.7 (2010), p. 077202.

[202]   G. De Chiara et al. "Entanglement spectrum, critical exponents, and order parameters in quantum spin chains". In: *Physical Review Letters* 109.23 (2012), p. 237208.

[203]   A. Y. Kitaev. "Unpaired Majorana fermions in quantum wires". In: *Physics-Uspekhi* 44.10S (2001), p. 131.

[204]   C. V. Kraus et al. "Majorana edge states in atomic wires coupled by pair hopping". In: *Physical Review Letters* 111.17 (2013), p. 173004.

[205]   M. Hastings. "Entropy and entanglement in quantum ground states". In: *Physical Review B* 76.3 (2007), p. 035114.

[206]   A. Kitaev and J. Preskill. "Topological entanglement entropy". In: *Physical Review Letters* 96.11 (2006), p. 110404.

[207]   H.-C. Jiang, Z. Wang, and L. Balents. "Identifying topological order by entanglement entropy". In: *Nature Physics* 8.12 (2012), pp. 902–905.

[208]   C. Holzhey, F. Larsen, and F. Wilczek. "Geometric and renormalized entropy in conformal field theory". In: *Nuclear Physics B* 424.3 (1994), pp. 443–467.

[209]   J. Latorre and A. Riera. "A short review on entanglement in quantum spin systems". In: *Journal of Physics A: Mathematical and Theoretical* 42.50 (2009), p. 504002.

[210]   F. Pollmann et al. "Theory of finite-entanglement scaling at one-dimensional quantum critical points". In: *Physical Review Letters* 102.25 (2009), p. 255701.

[211]   P. Chen et al. "Entanglement entropy scaling of the XXZ chain". In: *Journal of Statistical Mechanics: Theory and Experiment* 2013.10 (2013), P10007.

[212]   P. Zanardi and N. Paunković. "Ground state overlap and quantum phase transitions". In: *Physical Review E* 74.3 (2006), p. 031123.

[213]   W.-L. You, Y.-W. Li, and S.-J. Gu. "Fidelity, dynamic structure factor, and susceptibility in critical phenomena". In: *Physical Review E* 76.2 (2007), p. 022101.

[214]   S.-J. Gu. "Fidelity approach to quantum phase transitions". In: *International Journal of Modern Physics B* 24.23 (2010), pp. 4371–4458.

[215]   J. Sirker. "Finite-Temperature Fidelity Susceptibility for One-Dimensional Quantum Systems". In: *Physical Review Letters* 105.11 (2010), p. 117203.

[216]   L. C. Venuti and P. Zanardi. "Quantum critical scaling of the geometric tensors". In: *Physical Review Letters* 99.9 (2007), p. 095701.

[217]   G. Sun, A. Kolezhuk, and T. Vekua. "Fidelity at Berezinskii-Kosterlitz-Thouless quantum phase transitions". In: *Physical Review B* 91.1 (2015), p. 014418.

[218]   B. Shastry and B. Sutherland. "Twisted boundary conditions and effective mass in Heisenberg-Ising and Hubbard rings". In: *Physical Review Letters* 65.2 (1990), pp. 243–246.

[219]   M. Rigol and B. Sriram Shastry. "Drude weight in systems with open boundary conditions". In: *Physical Review B: Condensed Matter and Materials Physics* 77.16 (2008), pp. 161101–161104.

[220]   F. Essler, F. Gebhard, and E. Jeckelmann. "Excitons in one-dimensional Mott insulators". In: *Physical Review B* 64.12 (2001), p. 125119.

[221]   E. Jeckelmann. "Dynamical density-matrix renormalization-group method". In: *Physical Review B* 66.4 (2002), p. 045114.

[222]   H. Mikeska and W. Pesch. "Boundary effects on static spin correlation functions in the isotropic X—Y chain at zero temperature". In: *Zeitschrift für Physik B Condensed Matter* 26.4 (1977), pp. 351–353.

[223]   T. Hikihara and A. Furusaki. "Correlation amplitudes for the spin-1 2 XXZ chain in a magnetic field". In: *Physical Review B* 69.6 (2004), p. 064427.

[224]   F. H. Essler et al. *The one-dimensional Hubbard model*. Cambridge University Press, 2005.

[225]   M. Hase et al. "Magnetic properties of Rb 2 Cu 2 Mo 3 O 12 including a one-dimensional spin-1/ 2 Heisenberg system with ferromagnetic first-nearest-neighbor and antiferromagnetic second-nearest-neighbor exchange interactions". In: *Physical Review B* 70.10 (2004), p. 104426.

[226]   T. Masuda et al. "Spin waves and magnetic interactions in Li Cu 2 O 2". In: *Physical Review B* 72.1 (2005), p. 014405.

[227]   S.-L. Drechsler et al. "Frustrated Cuprate Route from Antiferromagnetic to Ferromagnetic Spin-1 2 Heisenberg Chains: Li 2 ZrCuO 4 as a Missing Link near the Quantum Critical Point". In: *Physical Review Letters* 98.7 (2007), p. 077202.

[228]   F. Haldane. "Spontaneous dimerization in the s=1/2 heisenberg antiferromagnetic chain with competing interactions". In: *Physical Review B* 25.7 (1982), p. 4925.

[229]   K. Okamoto and K. Nomura. "Fluid-dimer critical point in S=1/2 antiferromagnetic Heisenberg chain with next nearest neighbor interactions". In: *Physics Letters A* 169.6 (1992), pp. 433–437.

[230]   A. K. Kolezhuk. "Quantum chiral phases in frustrated easy-plane spin chains". In: *Physical Review B* 62.10 (2000), R6057.

[231]   T. Vekua, G. Japaridze, and H.-J. Mikeska. "Phase diagrams of spin ladders with ferromagnetic legs". In: *Physical Review B* 67 (2003), p. 064419.

[232]   T. Hikihara et al. "Ground state phase diagram of frustrated S= 1 XXZ chains: Chiral ordered phases". In: *JPSJ* 69.1 (2000).

[233]   T. Hikihara. "Ground-State Phase Diagram of Frustrated Antiferromagnetic S=1 Chain with Uniaxial Single-Ion-Type Anisotropy". In: *Journal of the Physical Society of Japan* 71.1 (2002), pp. 319–325.

[234]   T. Hikihara, M. Kaburagi, and H. Kawamura. "Ground-state phase diagrams of frustrated spin-S XXZ chains: Chiral ordered phases". In: *Physical Review B* 63.17 (2001).

[235]   T. Hikihara et al. "Vector chiral and multipolar orders in the spin-1 2 frustrated ferromagnetic chain in magnetic field". In: *Physical Review B* 78.14 (2008), p. 144404.

[236]   A. Eckardt et al. "Frustrated quantum antiferromagnetism with ultracold bosons in a triangular lattice". In: *EPL (Europhysics Letters)* 89 (2010).

[237]   R. Schmied et al. "Quantum phases of trapped ions in an optical lattice". In: *New Journal of Physics* 10.4 (2008), p. 045017.

[238]   S. D. Huber and E. Altman. "Bose condensation in flat bands". In: *Physical Review B* 82.18 (2010), p. 184502.

[239]   P. Lecheminant, T. Jolicoeur, and P. Azaria. "Phase transitions in the one-dimensional spin-S J 1-J 2 XY model". In: *Physical Review B* 63.17 (2001), p. 174426.

[240]   A. A. Nersesyan, A. O. Gogolin, and F. H. Eßler. "Incommensurate spin correlations in spin-1/2 frustrated two-Leg heisenberg ladders". In: *Physical Review Letters* 81.4 (1998), p. 910.

[241]   A. Kitazawa, K. Nomura, and K. Okamoto. "Phase diagram of S= 1 bond-alternating XXZ chains". In: *Physical Review Letters* 76.21 (1996), p. 4038.

[242]   A. Dhar et al. "Bose-Hubbard model in a strong effective magnetic field: Emergence of a chiral Mott insulator ground state". In: *Physical Review A* 85 (2012), p. 041602.

[243]   A. Dhar et al. "Chiral Mott insulator with staggered loop currents in the fully frustrated Bose-Hubbard model". In: *Physical Review B* 87 (2013), p. 174501.

[244]   M. Dalmonte et al. "Homogeneous and inhomogeneous magnetic phases of constrained dipolar bosons". In: *Physical Review B* 83.15 (2011), p. 155110.

[245]   M. Kaburagi, H. Kawamura, and T. Hikihara. "Spin and chiral orderings of frustrated quantum spin chains". In: *Journal of the Physical Society of Japan* 68.10 (1999), pp. 3185–3188.

[246]   W. Chen, K. Hida, and B. Sanctuary. "Ground-state phase diagram of S= 1 XXZ chains with uniaxial single-ion-type anisotropy". In: *Physical Review B* 67.10 (2003), p. 104401.

[247]   A. Auerbach. *Interacting electrons and quantum magnetism*. Springer-Verlag NY, 1994.

[248]   L. Tagliacozzo et al. "Scaling of entanglement support for matrix product states". In: *Physical Review B* 78.2 (2008), p. 024410.

[249]   P. Hauke et al. "Non-Abelian gauge fields and topological insulators in shaken optical lattices". In: *Physical Review Letters* 109.14 (2012), p. 145301.

[250]   J. Struck et al. "Engineering Ising-XY spin-models in a triangular lattice using tunable artificial gauge fields". In: *Nature Physics* 9.11 (2013), pp. 738–743.

[251]   I. Dzyaloshinsky. "A thermodynamic theory of "weak" ferromagnetism of antiferromagnetics". In: *Journal of Physics and Chemistry of Solids* 4.4 (1958), pp. 241–255.

[252]   T. Moriya. "New mechanism of anisotropic superexchange interaction". In: *Physical Review Letters* 4.5 (1960), p. 228.

[253]   H. Katsura, N. Nagaosa, and A. V. Balatsky. "Spin current and magnetoelectric effect in non-collinear magnets". In: *Physical Review Letters* 95.5 (2005), p. 057205.

[254]   H. Schmid. "Multi-ferroic magnetoelectrics". In: *Ferroelectrics* 162.1 (1994), pp. 317–338.

[255]   S. Park et al. "Ferroelectricity in an S= 1/2 chain cuprate". In: *Physical Review Letters* 98.5 (2007), p. 057601.

[256]   F. Schrettle et al. "Switching the ferroelectric polarization in the S= 1/ 2 chain cuprate Li Cu V O 4 by external magnetic fields". In: *Physical Review B* 77.14 (2008), p. 144101.

[257]   J. Sudan, A. Lüscher, and A. M. Läuchli. "Emergent multipolar spin correlations in a fluctuating spiral: The frustrated ferromagnetic spin-1 2 Heisenberg chain in a magnetic field". In: *Physical Review B* 80.14 (2009), p. 140402.

[258]   L. Kecke, T. Momoi, and A. Furusaki. "Multimagnon bound states in the frustrated ferromagnetic one-dimensional chain". In: *Physical Review B* 76.6 (2007), p. 060407.

[259]   K. P. Schmidt, J. Dorier, and A. M. Läuchli. "Solids and supersolids of three-body interacting polar molecules on an optical lattice". In: *Physical Review Letters* 101.15 (2008), p. 150405.

[260]   B. Capogrosso-Sansone et al. "Phase diagram of one-dimensional hard-core bosons with three-body interactions". In: *Physical Review B* 79.2 (2009), p. 020503.

[261]   T. Mishra et al. "Quantum phases and phase transitions of frustrated hard-core bosons on a triangular ladder". In: *Physical Review B* 87.17 (2013), p. 174504.

[262]   K. P. Schmidt et al. "Supersolid phase induced by correlated hopping in spin-1/2 frustrated quantum magnets". In: *Physical Review Letters* 100.9 (2008), p. 090401.

[263]   F. Mila, J. Dorier, and K. P. Schmidt. "Supersolid phases of hardcore bosons on the square lattice: Correlated hopping, next-nearest neighbor hopping and frustration". In: *Progress of Theoretical Physics Supplement* 176 (2008), pp. 355–374.

[264]   H. Weimer. "String order in dipole-blockaded quantum liquids". In: *New Journal of Physics* 16.9 (2014), p. 093040.

[265]   L. Landau. "On the theory of superfluidity". In: *Physical Review* 75.5 (1949), p. 884.

[266]   L. Santos, G. Shlyapnikov, and M. Lewenstein. "Roton-maxon spectrum and stability of trapped dipolar Bose-Einstein condensates". In: *Physical Review Letters* 90.25 (2003), p. 250403.

[267]   W. Meissner and R. Ochsenfeld. "Ein neuer Effekt bei Eintritt der Supraleitfähigkeit". In: *Naturwissenschaften* 21.44 (1933), pp. 787–788.

[268]   A. Abrikosov. "The magnetic properties of superconducting alloys". In: *Journal of Physics and Chemistry of Solids* 2.3 (1957), pp. 199–208.

[269]   D. R. Hofstadter. "Energy levels and wave functions of Bloch electrons in rational and irrational magnetic fields". In: *Physical Review B* 14 (1976), pp. 2239–2249.

[270]   Y. Hatsugai. "Topological aspects of the quantum Hall effect". In: *Journal of Physics: Condensed Matter* 9.12 (1997), p. 2507.

[271]   D. Thouless et al. "Quantized Hall conductance in a two-dimensional periodic potential". In: *Physical Review Letters* 49.6 (1982), p. 405.

[272] C. R. Dean et al. "Hofstadter's butterfly and the fractal quantum Hall effect in moiré super-lattices". In: *Nature* 497 (2013), 598–602.

[273] M. Mancini et al. "Observation of chiral edge states with neutral fermions in synthetic Hall ribbons". In: *Science* 349.6255 (2015), pp. 1510–1513.

[274] A. Fetter. "Rotating trapped bose-einstein condensates". In: *Reviews of Modern Physics* 81.2 (2009), p. 647.

[275] N. Goldman et al. "Light-induced gauge fields for ultracold atoms". In: *Reports on Progress in Physics* 77.12 (2014), p. 126401.

[276] M. Matthews et al. "Vortices in a Bose-Einstein condensate". In: *Physical Review Letters* 83.13 (1999), p. 2498.

[277] K. Madison et al. "Vortex formation in a stirred Bose-Einstein condensate". In: *Physical Review Letters* 84.5 (2000), p. 806.

[278] J. Abo-Shaeer et al. "Observation of vortex lattices in Bose-Einstein condensates". In: *Science* 292.5516 (2001), pp. 476–479.

[279] V. Schweikhard et al. "Rapidly rotating Bose-Einstein condensates in and near the lowest Landau level". In: *Physical Review Letters* 92.4 (2004), p. 040404.

[280] D. Jaksch and P. Zoller. "Creation of effective magnetic fields in optical lattices: the Hofstadter butterfly for cold neutral atoms". In: *New Journal of Physics* 5.1 (2003), p. 56.

[281] M. Aidelsburger et al. "Experimental realization of strong effective magnetic fields in an optical lattice". In: *Physical Review Letters* 107.25 (2011), p. 255301.

[282] A. R. Kolovsky. "Creating artificial magnetic fields for cold atoms by photon-assisted tunneling". In: *EPL (Europhysics Letters)* 93.2 (2011), p. 20003.

[283] H. Miyake. "Probing and Preparing Novel States of Quantum Degenerate Rubidium Atoms in Optical Lattices". PhD thesis. Massachusetts Institute of Technology, 2013.

[284] Y.-J. Lin, K. Jimenez-Garcia, and I. Spielman. "Spin-orbit-coupled Bose-Einstein condensates". In: *Nature* 471.7336 (2011), pp. 83–86.

[285] A. Celi et al. "Synthetic gauge fields in synthetic dimensions". In: *Physical Review Letters* 112 (2014), p. 043001.

[286] B. K. Stuhl et al. "Visualizing edge states with an atomic Bose gas in the quantum Hall regime". In: *Science* 349.6255 (2015), pp. 1514–1518.

[287] A. van Oudenaarden and J. E. Mooij. "One-dimensional Mott insulator formed by quantum vortices in Josephson junction arrays". In: *Physical Review Letters* 76 (1996), pp. 4947–4950.

[288] A. van Oudenaarden, S. J. K. Várdy, and J. E. Mooij. "One-dimensional localization of quantum vortices in disordered Josephson junction arrays". In: *Physical Review Letters* 77 (1996), pp. 4257–4260.

[289] D. Roditchev et al. "Direct observation of Josephson vortex cores". In: *Nature Phys.* 11 (2015), p. 332.

[290] M. Kardar. "Josephson-junction ladders and quantum fluctuations". In: *Physical Review B* 33 (1986), pp. 3125–3128.

[291] E. Granato. "Phase transitions in Josephson-junction ladders in a magnetic field". In: *Physical Review B* 42 (1990), pp. 4797–4799.

[292] J. J. Mazo, F. Falo, and L. M. Floria. "Josephson junction ladders: Ground state and relaxation phenomena". In: *Physical Review B* 52 (1995), pp. 10433–10440.

[293] C. Denniston and C. Tang. "Phases of Josephson junction ladders". In: *Physical Review Letters* 75.21 (1995), p. 3930.

[294] E. Orignac and T. Giamarchi. "Meissner effect in a bosonic ladder". In: *Physical Review B* 64 (2001), p. 144515.

[295] A. Petrescu and K. Le Hur. "Bosonic Mott insulator with Meissner currents". In: *Physical Review Letters* 111 (2013), p. 150601.

[296] A. Tokuno and A. Georges. "Ground states of a Bose-Hubbard ladder in an artificial magnetic field: field-theoretical approach". In: *New Journal of Physics* 16 (2014), p. 073005.

[297] A. Petrescu and K. Le Hur. "Chiral Mott insulators, Meissner effect, and Laughlin states in quantum ladders". In: *Physical Review B* 91 (2015), p. 054520.

[298] R. Wei and E. J. Mueller. "Theory of bosons in two-leg ladders with large magnetic fields". In: *Physical Review A* 89 (2014), p. 063617.

[299] S. Uchino and A. Tokuno. "Population-imbalance instability in a Bose-Hubbard ladder in the presence of a magnetic flux". In: *Physical Review A* 92.1 (2015), p. 013625.

[300] S. T. Carr, B. N. Narozhny, and A. A. Nersesyan. "Spinless fermionic ladders in a magnetic field: Phase diagram". In: *Physical Review B* 73.19 (2006), p. 195114.

[301] G. Roux et al. "Diamagnetism of doped two-leg ladders and probing the nature of their commensurate phases". In: *Physical Review B* 76.19 (2007), p. 195105.

[302] S. Barbarino et al. "Magnetic crystals and helical liquids in alkaline-earth fermionic gases". In: *Nature communications* 6 (2015).

[303] S. Barbarino et al. "Synthetic gauge fields in synthetic dimensions: Interactions and chiral edge modes". In: *arXiv preprint arXiv:1510.05603* (2015).

[304] Y. Nishiyama. "Finite-size-scaling analyses of the chiral ordert in the Josephson-junction ladder with half a flux quantum per plaquette". In: *The European Physical Journal B-Condensed Matter and Complex Systems* 17.2 (2000), pp. 295–299.

[305] M.-C. Cha and J.-G. Shin. "Two peaks in the momentum distribution of bosons in a weakly frustrated two-leg optical ladder". In: *Physical Review A* 83.5 (2011), p. 055602.

[306] R. B. Griffiths and W. Chou. "Effective potentials: a new approach and new results for one-dimensional systems with competing length scales". In: *Physical Review Letters* 56.18 (1986), p. 1929.

[307] I. Shyiko et al. "Double zigzag spin chain in a strong magnetic field close to saturation". In: *Physical Review B* 88.1 (2013), p. 014403.

[308] M. Di Dio et al. "Persisting Meissner state and incommensurate phases of hard-core boson ladders in a flux". In: *Physical Review B* 92.6 (2015), p. 060506.

[309] F. Kolley et al. "Strongly interacting bosons on a three-leg ladder in the presence of a homogeneous flux". In: *New Journal of Physics* 17.9 (2015), p. 092001.

[310] F. Abdullaev, P. Kevrekidis, and M. Salerno. "Compactons in Nonlinear Schrödinger Lattices with Strong Nonlinearity Management". In: *Physical Review Letters* 105.11 (2010), p. 113901.

[311] L. Arrachea and A. Aligia. "Exact solution of a Hubbard chain with bond-charge interaction". In: *Physical Review Letters* 73.16 (1994), p. 2240.

[312] L. Arrachea, A. Aligia, and E. Gagliano. "Anomalous flux quantization in a Hubbard ring with correlated hopping". In: *Physical Review Letters* 76.23 (1996), p. 4396.

[313] L. Arrachea, E. Gagliano, and A. Aligia. "Ground-state phase diagram of an extended Hubbard chain with correlated hopping at half-filling". In: *Physical Review B* 55.2 (1997), p. 1173.

[314] A. Aligia and L. Arrachea. "Triplet superconductivity in quasi-one-dimensional systems". In: *Physical Review B* 60.22 (1999), p. 15332.

[315] A. Aligia et al. "Phase diagrams from topological transitions: The Hubbard chain with correlated hopping". In: *Physical Review B* 61.12 (2000), p. 7883.

[316] W. Kohn. "Theory of the insulating state". In: *Physical review* 133.1A (1964), A171.

[317] A. Ovchinnikov et al. "Antiferromagnetic Ising chain in a mixed transverse and longitudinal magnetic field". In: *Physical Review B* 68.21 (2003), p. 214406.

[318] J. Simon et al. "Quantum simulation of antiferromagnetic spin chains in an optical lattice". In: *Nature* 472.7343 (2011), pp. 307–312.

[319] A. Albuquerque et al. "The ALPS project release 1.3: Open-source software for strongly correlated systems". In: *Journal of Magnetism and Magnetic Materials* 310.2 (2007), pp. 1187–1193.

[320] B. Bauer et al. "The ALPS project release 2.0: open source software for strongly correlated systems". In: *Journal of Statistical Mechanics: Theory and Experiment* 2011.05 (2011), P05001.

[321] A. Moreno, A. Muramatsu, and S. R. Manmana. "Ground-state phase diagram of the one-dimensional t-J model". In: *Physical Review B* 83.20 (2011), p. 205113.

[322] H.-C. Nägerl. "Dynamics of ultracold bosons under strong confinement". Bose-Einstein Condensation 2015 - Frontiers in Quantum Gases. 2015. URL: http://bec2015.sciencesconf.org/76075.

[323] A. Rapp and L. Santos. In: (2015), in preparation.

[324] J. Dalibard et al. "Colloquium: Artificial gauge potentials for neutral atoms". In: *Reviews of Modern Physics* 83.4 (2011), p. 1523.

[325] M. Levin and X.-G. Wen. "Colloquium: photons and electrons as emergent phenomena". In: *Reviews of Modern Physics* 77.3 (2005), p. 871.

[326] J. B. Kogut. "The lattice gauge theory approach to quantum chromodynamics". In: *Reviews of Modern Physics* 55.3 (1983), p. 775.

[327] E. Zohar and B. Reznik. "Confinement and lattice quantum-electrodynamic electric flux tubes simulated with ultracold atoms". In: *Physical Review Letters* 107.27 (2011), p. 275301.

[328] E. Kapit and E. Mueller. "Optical-lattice Hamiltonians for relativistic quantum electrodynamics". In: *Physical Review A* 83.3 (2011), p. 033625.

[329] E. Zohar, J. I. Cirac, and B. Reznik. "Simulating compact quantum electrodynamics with ultracold atoms: probing confinement and nonperturbative effects". In: *Physical Review Letters* 109.12 (2012), p. 125302.

[330] D. Banerjee et al. "Atomic quantum simulation of dynamical gauge fields coupled to fermionic matter: from string breaking to evolution after a quench". In: *Physical Review Letters* 109.17 (2012), p. 175302.

[331] E. Zohar, J. I. Cirac, and B. Reznik. "Simulating (2+ 1)-dimensional lattice QED with dynamical matter using ultracold atoms". In: *Physical Review Letters* 110.5 (2013), p. 055302.

[332] D. Banerjee et al. "Atomic quantum simulation of U (N) and SU (N) non-Abelian lattice gauge theories". In: *Physical Review Letters* 110.12 (2013), p. 125303.

[333] E. Zohar, J. I. Cirac, and B. Reznik. "Cold-atom quantum simulator for SU (2) yang-mills lattice gauge theory". In: *Physical Review Letters* 110.12 (2013), p. 125304.

[334] S. Zhang, T. H. Hansson, and S. Kivelson. "Effective-field-theory model for the fractional quantum Hall effect". In: *Physical Review Letters* 62.1 (1989), p. 82.

[335] S. J. B. Rabello. "1D generalized statistics gas: A gauge theory approach". In: *Physical Review Letters* 76.21 (1996), p. 4007.

[336] E. Fradkin. "Jordan-Wigner transformation for quantum-spin systems in two dimensions and fractional statistics". In: *Physical Review Letters* 63.3 (1989), p. 322.

[337] U. Aglietti et al. "Anyons and chiral solitons on a line". In: *Physical Review Letters* 77.21 (1996), p. 4406.

[338] T. Keilmann et al. "Statistically induced phase transitions and anyons in 1D optical lattices". In: *Nature communications* 2 (2011), p. 361.

[339] M. J. Edmonds et al. "Simulating an interacting gauge theory with ultracold Bose gases". In: *Physical Review Letters* 110.8 (2013), p. 085301.

[340] Y. Hao, Y. Zhang, and S. Chen. "Ground-state properties of hard-core anyons in one-dimensional optical lattices". In: *Physical Review A* 79.4 (2009), p. 043633.

[341] G. Tang, S. Eggert, and A. Pelster. "Ground-state properties of anyons in a one-dimensional lattice". In: *arXiv preprint arXiv:1509.01888* (2015).

[342] H. Kikuchi et al. "Magnetic Properties of the Diamond Chain Compound Cu3 (CO3) 2 (OH) 2". In: *Progress of Theoretical Physics Supplement* 159 (2005), pp. 1–10.

[343] A. Del Campo. "Fermionization and bosonization of expanding one-dimensional anyonic fluids". In: *Physical Review A* 78.4 (2008), p. 045602.

[344] Y. Hao and S. Chen. "Dynamical properties of hard-core anyons in one-dimensional optical lattices". In: *Physical Review A* 86.4 (2012), p. 043631.

[345] L. Wang, L. Wang, and Y. Zhang. "Quantum walks of two interacting anyons in one-dimensional optical lattices". In: *Physical Review A* 90.6 (2014), p. 063618.

[346] F. Andraschko and J. Sirker. "Propagation of a single-hole defect in the one-dimensional Bose-Hubbard model". In: *Physical Review B* 91 (2015), p. 235132.

[347] A. Bermudez and D. Porras. "Interaction-dependent photon-assisted tunneling in optical lattices: a quantum simulator of strongly-correlated electrons and dynamical Gauge fields". In: *New Journal of Physics* 17.10 (2015), p. 103021.

[348] K. Eckert et al. "Ultracold atomic Bose and Fermi spinor gases in optical lattices". In: *New Journal of Physics* 9.5 (2007), p. 133.

[349] M. Hermele, V. Gurarie, and A. M. Rey. "Mott insulators of ultracold fermionic alkaline earth atoms: Underconstrained magnetism and chiral spin liquid". In: *Physical Review Letters* 103.13 (2009), p. 135301.

[350] H. Nonne et al. "Haldane charge conjecture in one-dimensional multicomponent fermionic cold atoms". In: *Physical Review B* 81.2 (2010), p. 020408.

[351] H. Nonne et al. "Competing orders in one-dimensional half-filled multicomponent fermionic cold atoms: The Haldane-charge conjecture". In: *Physical Review B* 84.12 (2011), p. 125123.

[352] Y. Dong and H. Pu. "Spin mixing in spinor Fermi gases". In: *Physical Review A* 87.4 (2013), p. 043610.

[353] C. Wu. "Hidden symmetry and quantum phases in spin-3/2 cold atomic systems". In: *Modern Physics Letters B* 20.27 (2006), pp. 1707–1738.

[354] S. Capponi et al. "Confinement versus deconfinement of Cooper pairs in one-dimensional spin-3/2 fermionic cold atoms". In: *Physical Review B* 75.10 (2007), p. 100503.

[355] G. Roux et al. "Spin 3/2 fermions with attractive interactions in a one-dimensional optical lattice: phase diagrams, entanglement entropy, and the effect of the trap". In: *The European Physical Journal B-Condensed Matter and Complex Systems* 68.3 (2009), pp. 293–308.

[356] K. Rodriguez et al. "Mott-insulator phases of spin-3/2 fermions in the presence of quadratic Zeeman coupling". In: *Physical Review Letters* 105.5 (2010), p. 50402.

[357] F. Paschen and E. Back. "Liniengruppen magnetisch vervollständigt". In: *Physica* 1 (1921), pp. 261–273.

[358] G. Breit and I. Rabi. "Measurement of nuclear spin". In: *Physical Review* 38.11 (1931), p. 2082.

[359] E. Jeckelmann and S. R. White. "Density-matrix renormalization-group study of the polaron problem in the Holstein model". In: *Physical Review B* 57.11 (1998), p. 6376.

[360] H. Schulz. "Phase diagrams and correlation exponents for quantum spin chains of arbitrary spin quantum number". In: *Physical Review B* 34.9 (1986), p. 6372.

[361] T. Mishra, S. Greschner, and L. Santos. "Density-induced geometric frustration of ultra-cold bosons in optical lattices". In: *arXiv preprint arXiv:1512.01138* (2015).

[362] D. Raventós et al. "Topological phases of lattice bosons with a dynamical gauge field". In: *arXiv preprint arXiv:1507.03500* (2015).

Acknowledgements

Curriculum Vitae

Address	:	Helmkestr. 4, 30165 Hannover, Germany
Phone	:	+49(0)511 762 247
Email	:	sebastian.greschner@itp.uni-hannover.de
Homepage	:	http://www.itp.uni-hannover.de/sgresch/

Personal profile

Date of Birth	:	6th of December 1984
Place of Birth	:	Quakenbrück, Germany
Gender	:	Male
Marital Status	:	Married, 1 son
Nationality	:	German
Language	:	German, English

Education

2011 - 2016	:	PhD, Leibniz Universität Hannover, Germany
2012 - 2015	:	Member of Research Training Group 1729: *Fundamentals and applications of ultracold matter*
2008 - 2009	:	Academic exchange year at the University of Granada, Spain with the Erasmus programme
2005 - 2011	:	Diploma in physics, Leibniz Universität Hannover, Germany
2004	:	High school graduation (Abitur) at the Gymnasium Lohne, Germany

Publications

1. T. Mishra, S. Greschner, and L. Santos. Frustration-induced supersolids in the absence of inter-site interactions. *Phys. Rev. B 92, 195149 (2015)*.

2. S. Greschner, M. Piraud, F. Heidrich-Meisner, I. P. McCulloch, U. Schollwöck, and T. Vekua. Spontaneous increase of magnetic flux and chiral-current reversal in bosonic ladders: Swimming against the tide. *Phys. Rev. Lett. 115, 190402 (2015)*.

3. S. Greschner, D. Huerga, G. Sun, D. Poletti, and L. Santos. Density-dependent synthetic magnetism for ultracold atoms in optical lattices. *Phys. Rev. B 92, 115120 (2015)*.

4. S. Greschner, and L. Santos. The Anyon Hubbard Model in One-Dimensional Optical Lattices. *Phys. Rev. Lett. 115, 053002 (2015)*.

5. T. Mishra, S. Greschner, and L. Santos. Polar molecules in frustrated triangular ladders. *Phys. Rev. A 91, 043614 (2015)*.

6. M. Piraud, F. Heidrich-Meisner, I. P. McCulloch, S. Greschner, T. Vekua, and U. Schollwöck. Vortex and Meissner phases of strongly-interacting bosons on a two-leg ladder. *Phys. Rev. B 91, 140406(R), 2015*.

7. S. Greschner, L. Santos, and D. Poletti. Exploring unconventional Hubbard models with doubly-modulated lattice gases. *Phys. Rev. Lett. 113, 183002 (2014)*.

8. S. Greschner, G. Sun, D. Poletti, and L. Santos. Dynamical synthetic gauge fields using periodically modulated interactions. *Phys. Rev. Lett. 113, 215303 (2014)*.

9. M. Azimi, L. Chotorlishvili, S. K. Mishra, S. Greschner, T. Vekua, and J. Berakdar. Helical multiferroics for electric field controlled quantum information processing. *Phys. Rev. B 89, 024424 (2014)*.

10. S. Greschner, A. K. Kolezhuk, and T. Vekua. Fidelity susceptibility and conductivity of the current in one-dimensional lattice models with open or periodic boundary conditions. *Phys. Rev. B 88, 195101 (2013)*.

11. J. Jaramillo, S. Greschner, and T. Vekua. Magnetic field induced band insulator to Mott insulator transformations in 4-component alkali fermions at half-filling. *Phys. Rev. A 88, 043616 (2013)*

12. S. Greschner, L. Santos, and T. Vekua. Ultra-cold bosons in zig-zag optical lattices. *Phys. Rev. A 87, 033609 (2013)*

13. A.K. Kolezhuk, F. Heidrich-Meisner, S. Greschner, and T. Vekua. Frustrated spin chains in strong magnetic field: dilute two-component Bose gas regime. *Phys. Rev. B 85, 064420 (2012)*.

Chapter 4 of this thesis is based on 10. Results of chapter 5 have been presented in 13, 12, 9, 5 and 1. Chapter is discussed in 6 and 2. The results of chapter 7 have been published in 7. Chapter 8 is based on 8, 4 and 3. Finally chapter 9 is discussed in 11.

Other publications of the author:

14. T. Mishra, S. Greschner, and L. Santos Density-induced geometric frustration of ultra-cold bosons in optical lattices. *arXiv preprint arXiv:1512.01138 (2015)*.

15. C. Lukas, B. Bellenberg, O. Köster, S. Greschner, and H. K. Hahn. A new sulcus-corrected approach for assessing cerebellar volume in spinocerebellar ataxia. *Psychiatry Research: Neuroimaging (2011)*.

Selbständigkeitserklärung

Hiermit versichere ich, die vorliegende Doktorarbeit selbstständig und unter ausschließlicher Verwendung der angegebenen Hilfsmittel angefertigt zu haben.

Hannover, Dezember 2015

_____

Sebastian Greschner